n-Type Thermoelectric Oxide Ceramics for High Temperature Power Generation

By

Adindu Cyril Iyasara
Registration number: 140264964

A thesis submitted for the degree of Doctor of Philosophy, PhD

The University of Sheffield
Faculty of Engineering
Department of Materials Science and Engineering

Supervisors:
Professor Ian M. Reaney
Professor Derek C. Sinclair

March 2019

Publications and Conferences (in whole/ part) from the Thesis

i. Whitney L. Schmidt, Gregory D. Lewin, **Adindu C. Iyasara**, Derek C. Sinclair, Ian M. Reaney, “Thermoelectric Property of Reduced $Sr_{1-3x/2}RE_xTiO_{3-\delta}$”, Electronic and Advanced Materials, EAM **2018**, Orlando, Fla, USA.

ii. **Adindu C Iyasara**, Whitney L Schmidt, Rebecca Boston, Derek C Sinclair, Ian M Reaney, “La and Sm Co-Doped $SrTiO_{3-\delta}$ Thermoelectric Ceramics”, Materials Today: Proceedings 4(12), **2017**, 12360-12367.

iii. **Adindu C. Iyasara**, Derek C Sinclair, Ian M. Reaney, “Thermoelectric Performance of Strontium Titanate Oxide Ceramics for Energy Harvesting”, Energy Research Symposium (Energy 2050), **2017**, The University of Sheffield, United Kingdom.

iv. **Adindu C. Iyasara**, Whitney L. Schmidt, Rebecca Boston, Derek C. Sinclair, Ian M. Reaney, “La and Sm Co-doped $SrTiO_{3-\delta}$ Thermoelectric Ceramics”, European Materials Research Society (EMRS) Spring Meeting, **2017**, Strasbourg, France.

v. **Adindu C. Iyasara**, Whitney L. Schmidt, Rebecca Boston, Derek C. Sinclair, Ian M. Reaney, “$SrTiO_3$-Based Thermoelectrics for Energy Harvesting”, Thermoelectric Network UK Meeting, **2017**, Manchester, United Kingdom.

vi. R. Boston, W. L Schmidt, G. D Lewin, **A. C Iyasara**, Z. Lu, H. Zhang, D. C Sinclair, I. M Reaney, “Protocols for the Fabrication, Characterization, and Optimization of n-Type Thermoelectric Ceramic Oxides”, *Chemistry of Materials*, **2016**, 29 (1), 265–280.

vii. Whitney L. Schmidt, **Adindu C. Iyasara**, Zhilun Lu, Gregory D. Lewin, Derek C. Sinclair, Ian M. Reaney, “Thermoelectric Properties of n-type Reduced Rare-Earth Doped $SrTiO_3$”, International Symposium on the Applications of Ferroelectrics (ISAF), European Conference on Applications of Polar Dielectrics (ECAPD), Work on Piezoresponse Force Microscopy (PFM); **2016**, Darmstadt, Germany.

viii. Whitney L. Schmidt, Zhilun Lu, **Adindu C. Iyasara**, Lewin, Derek C. Sinclair, Ian M. Reaney, The Road to All Oxide Thermoelectric Generators”, Sustainable Functional Materials (SFM), **2016**, Scarborough, United Kingdom.

Certification

I, Adindu Cyril Iyasara declare that this Thesis submitted in partial fulfilment of the requirements for the award of Doctor of Philosophy, PhD in the Department of Materials Science and Engineering, The University of Sheffield is wholly my work unless otherwise referenced or acknowledged. The document has not been submitted for qualifications at any other academic institution.

Adindu Cyril Iyasara
March 2019.

Acknowledgments

I would like to express my immense gratitude to my supervisors, Professor Ian M. Reaney and Professor Derek C. Sinclair who is recently appointed the Head of Department, Materials Science and Engineering for their excellent supervision, support and advice throughout my research. I want to thank Professor Ian M. Reaney particularly for providing me with the great encouragement and support in various ways during my PhD studies.

It is my wish to thank Dr. Rebecca Boston, Dr. Whitney Schmidt and Dr. Zhilun Lu for giving me the training, and direction in ceramic processing, fabrication and characterisation. All I learnt from them formed the basis for the success achieved in my PhD program. I thank you very much. I would also like to thank my colleagues and all the members of Functional Materials and Devices (FMD) Group, Department of Materials Science and Engineering, University of Sheffield. The educative discussions and academic presentations we had regarding my research area in particular and ceramics in general helped me grow and flourish to the success of my PhD study.

I gratefully thank all the academic, non-academic and technical staff of Materials Science and Engineering Department and Sorby Centre, University of Sheffield especially the immediate past Head of Department, Professor Neil C Hyatt for his immense support, Dr Nik Reeves-McLaren, Mr. Andrew Mould, Dr. Le Ma and Dr. Cheryl Shaw for the training and assistance in making use of the facilities. My internal examiners, Dr Martin C. Stennett and Dr Amy Gandy require my commendation for the academic drive and unbiased assessment that contributed to the success of the doctoral program.

I will not end this acknowledgement without recognising my family. My father, Mr. Eleazar Aniche Iyasara and mother, Mrs. Angela Ngozi Iyasara have been the source of my ultimate support and inspiration since my childhood. They laid my academic foundation, trained me to stand out in the crowd and sacrificed all they have for me to be the best. I pray God to keep them hale and hearty to ripe the fruits of their labour. Special thanks go to my siblings and other relatives for their love and respect for me. My lovely wife, Mrs Jessica Oluchi Iyasara and delightful children (Mmesomachukwu, Chisom, Ekperebuike, Nwasinachi and Kamsiyochukwu) are not left out. I sincerely thank them for their patience, love, support, prayers and the enabling environment that led to the successful completion of the PhD study.

Finally, I return all thanks and praises to God. The journey was not a bed of roses, but full of ups and downs. As a human, when the journey became tough and future turned bleak, God whispered to me saying "Son! Wake up for you are a divine child, you are undergoing a divine project, and therefore, I am there with you". Let him alone take all the glory, Amen.

Dedication

I dedicate this work to my parents, Mr and Mrs Eleazer A. Iyasara for laying the foundation of my academic pursuit.

Table of Content

List of Figures

List of Tables

Nomenclatures

Abbreviations

CN	Coordination Number
CS	Crystallographic Shear
CTM	Conventional Thermoelectric Material
EDX	Energy-Dispersive X-Ray Spectroscopy
ESTO	Electron La-Sm Doped $SrTiO_3$
HSXD	High Speed Xenon Discharge
LFD	Laser Flash Diffusivity
LTO	$La_2Ti_2O_7$ (Lanthanum dititanate)
MFP	Mean Free Path
NTM	Novel Thermoelectric Material
PF	Power Factor
PGEC	Phonon-Glass and Electron-Crystal
PSA	Particle Size Analysis
PSD	Particle Size Distribution
RE	Rare Earth Ion
SBN	Strontium Barium Niobate
SEM	Scanning Electron Microscopy
SLTN	$Sr_5LaTi_3Nb_7O_{30}$
SLTNe	Electron Sm-doped $Sr_5LaTi_3Nb_7O_{30}$
SLTNv	Vacancy Sm-doped $Sr_5LaTi_3Nb_7O_{30}$
SSR	Solid State Reaction
STO	Strontium Titanate ($SrTiO_3$)
TE	Thermoelectric Material
TEG	Thermoelectric Power Generator
TGA	Thermogravimetric Analysis
TPS	Transient Plane Source
TTB	Tetragonal Tungsten Bronze
VSTO	Vacancy La-Sm Doped $SrTiO_3$
VSTO-A	Vacancy La-Sm doped $SrTiO_3$ calcined in air

Abbreviations

VSTO-H	Vacancy La-Sm doped $SrTiO_3$ calcined in 5% H_2/N_2
XRD	X-Ray Diffraction
YSZ	Yttria-Stabilized Zirconia
1300A	$SrLa_{0.1}Sm_{0.1}TiO_3$, calcined at 1300 ^{o}C in air
1300H	$Sr_{0.7}La_{0.1}Sm_{0.1}TiO_3$, calcined at 1300 ^{o}C in 5% H_2/N_2
1350H	$Sr_{0.7}La_{0.1}Sm_{0.1}TiO_3$, double calcined at 1300-1350 ^{o}C in 5% H_2/N_2
1400H	$Sr_{0.7}La_{0.1}Sm_{0.1}TiO_3$, double calcined at 1300-1400 ^{o}C in 5% H_2/N_2

Symbols

C	Specific heat capacity
C_{el}	Electronic specific heat
h	Planck’s constant
I	Current
k	Total thermal conductivity
K_B	Boltzmann constant
k_E	Electronic thermal conductivity
k_L	Lattice thermal conductivity
L	Lorentz number
l	Mean free path of phonons
N	Carrier’s number
n	Carrier concentration
q (or e)	Charge carrier
Q_H	Heat rate at high temperature
Q_L	Heat rate at low temperature
r_A	Ionic radius of atom “A”
r_B	Ionic radius of atom “B”
r_O	Ionic radius of oxygen
S	Seebeck coefficient
$\lvert S \rvert$	Absolute Seebeck coefficient
S_e	Negative thermopower

Symbols

S_p	Positive thermopower
t	Tolerance factor
ΔT	Temperature difference
T_C	Temperature at cold side
T_H	Temperature at hot side
ΔV	Voltage difference
V_g	Group velocity of phonons
W_e	Electrical power output
ZT	Dimensionless figure of merit
σ	Electrical conductivity
η_C	Carnot process
η_T	Efficiency of TEG
η_{max}	Maximum conversion efficiency
μ	Carrier mobility
τ	Scattering time
m^*	Effective mass
λ_S	Scattering distance
ρ	Density
θ_D	Debye temperature
P	Fraction of pores in a material
π_{AB}	Peltier coefficient of A-B circuit
α	Thermal diffusivity
k_O	Thermal conductivity of material without pores

Abstract

Conventional non-oxide materials utilised in thermoelectric devices have unfavourable properties such as instability at high temperatures with scarce and toxic raw materials that constitute an environmental hazard. Transition metal oxide thermoelectric materials are stable at high temperatures, abundant, less toxic and have been suggested as potential alternatives given improvements in thermoelectric figures of merit (ZT). La-Sm co-doped $SrTiO_3$, Sm-doped $Sr_5LaTi_3Nb_7O_{30}$ and Nb-doped $La_2Ti_2O_7$ n-type oxide ceramics synthesised using solid state reaction technique, sintered in air and 5% H_2/N_2 have thus been investigated.

For La-Sm co-doped $SrTiO_3$ ceramics, the following aliovalent doping mechanisms were adopted; $Sr_{1-x}La_{x/2}Sm_{x/2}TiO_3$ (electron donor-doping), $Sr_{1-3x/2}La_{x/2}Sm_{x/2}TiO_3$ (A-site vacancies or ionic donor-doping) which were calcined in air or 5% H_2/N_2 and sintered in air or 5% H_2/N_2 at 1773 K. La-Sm co-doped $SrTiO_3$ pellets sintered in air were white/pale yellow in colour, indicating they were stoichiometric with respect to oxygen concentration hence electrical insulators. All La-Sm co-doped 5% H_2/N_2 sintered ceramics were black single-phase pellets up to 15 mol% (x = 0.15) doping concentration for electron donor-doped compositions. For the A-site vacancy, La-Sm doped $SrTiO_3$, the single-phase materials spanned across all the compositions ($x \geq 0.30$). This indicates that processing in reducing atmosphere improves the electronic conduction by generating oxygen vacancies (V_O) in the lattice with a lower La-Sm solid solubility limit observed in electron donor-doped samples. Vacancy doping with a double calcination in 5% H_2/N_2 at elevated temperatures optimised the ZT values. x = 0.20 (1400H) doubled calcined (at 1573 and 1673 K) and sintered in 5% H_2/N_2 for 8 hours showed the highest ZT (0.35 at 973 K) reported for RE co-doped n-type $SrTiO_3$ ceramics. The result shows that La-Sm co-doping of $SrTiO_3$ through creation of V_{Sr} with processing in 5% H_2/N_2 opens a new window for the synthesis, fabrication and characterisation of oxide thermoelectrics.

For Sm-doped $Sr_5LaTi_3Nb_7O_{30}$ ceramics, $Sr_5La_{1-x}Sm_xTi_3Nb_7O_{30}$ and $Sr_{5-3x/2}Sm_xLaTi_3Nb_7O_{30}$ were sintered in air and 5% H_2/N_2 at 1673 K for 6 hours. The Sm-doped $Sr_5LaTi_3Nb_7O_{30}$ air sintered ceramics showed single-phase, homogenous ceramics with dense microstructures and a white/pale yellow appearance. The white or pale yellow colour shows the samples are electrical insulators, hence were not characterized for TE performance. In contrast, Sm-doped $Sr_5LaTi_3Nb_7O_{30}$ sintered in 5% H_2/N_2 were identified with secondary phases consisting of $SrTiO_3$ (Sm doped) and an Nb-rich oxide (most likely Nb_2O_5). The A-site vacancy samples ($Sr_{5-3x/2}Sm_xLaTi_3Nb_7O_{30}$) exhibited lower thermal conductivity when compared to its electron doped counterpart ($Sr_5La_{1-x}Sm_xTi_3Nb_7O_{30}$), indicating that secondary phase mixtures present in the microstructure and the vacancy defects (V_{Sr} and V_O) created in the lattice contributed in shortening the mean free path (MFP) of phonons, resulting in a maximum ZT (0.21) at 973 K for x = 0.30.

Nb-doped $La_2Ti_2O_7$ ceramics with an electron compensation mechanism were also investigated. All compositions were single-phase with porous microstructures consistent with their low experimental densities. The thermoelectric results showed improved properties in comparison to pure $La_2Ti_2O_7$ but PF and ZT values were too low and not useful for thermoelectric applications. However, the high Seebeck coefficient and glass-like (low) thermal conductivity values achieved have established $La_2Ti_2O_7$ as a potential thermoelectric material.

Chapter 1: Introduction

1.1 Background

Non-renewable energy sources based on fossil fuels, e.g. petroleum, natural gas, coal, etc. currently remain the most widely used sources of electricity generation. Study on the reserves of the world fossil fuel has revealed a probable decrease and eventual total depletion of hydrocarbon production [1], [2]. Despite the global call for a switch to greener and sustainable energy sources, fossil fuels still provide over 80 % of the world energy usage [3]. The high cost of fossil fuels and their attendant environmental effects such as global climate changes, environmental pollution and the emissions of greenhouse gases have resulted in research and development of alternative energy sources [4], [5]. These alternative energy sources include solar power (photovoltaic), wind power, biofuels (biomass), geothermal, nuclear power and thermoelectrics.

Thermoelectric (TE) materials amongst these promising renewable energy sources have received significant attention. TE materials are expected to play a dual role; power generation and energy conversion, and the performance of these roles rely on the efficiency of the materials [6]. Thermoelectric power generators (TEGs) are solid-state devices that directly convert waste-heat (thermal energy) into useable electrical energy using the Seebeck effect [7]–[14]. It has been calculated that if 20 % of waste heat from automobiles, power and incineration plants could be converted to electricity, 35,000GWh of power will be obtained in a year [2], [15]. Recent statistics suggest that about 60 % of the energy produced in US is not reused or recycled but released into the environment as heat [16]

The performance of TEGs are controlled by two main factors; functionality and efficiency. The functionality is based on a heavily doped p-type and n-type semiconducting TE materials with a high carrier concentration, n ($n \sim 10^{19}$-10^{21} cm^{-3}) [17] and with bandgap of ~ $10k_BT$ [18] connected electrically in series (to allow the flow of the same quantity of current along the thermoelements) and thermally in parallel (to restrict the flow of heat) [18]. The efficiency depends on the dimensionless figure of merit, ZT. The low energy conversion efficiency (~ 5 %) associated with TEGs has limited their use for electricity generation and viable only in specialized areas [19]. However, the low energy conversion efficiency is not a major hindrance since energy harvesting (gathering of energy) is from waste heat sources. The fundamental challenge is to optimize the power factor (PF) for effective electricity generation [19]. Apart from low energy efficiency, TEGs suffer from slow technology progression, limited applications, and lack of customer and/or industry education [20]

Presently the most studied thermoelectric semiconducting materials with optimised ZT values of 1 or higher are primarily non-oxides such as $(Bi,Sb)_2(Te,Se)_3$, SiGe, PbTe and $LaFe_3CoSb_{12}$ and their corresponding alloys [21] mainly because they possess small phonon group velocity and low *k*, desirable for thermoelectric applications. The broad application of these materials is limited, however, due to toxicity, scarcity, cost, and limited operational temperature range [22]. There is evidence, however, that transition-metal oxide thermoelectric materials are viable alternatives that if given improvements in ZT, may surmount the challenges associated with non-oxides [23]–[25]. Among these oxide based TE materials, p-type layered cobaltates such as $NaCo_2O_4$, $(Sr,Ca)_3Co_4O_9$, $Bi_{2-x}Pb_xCo_2O_8$ ($0 \leq x \leq 0.4$), $Tl_{0.4}[Sr_{0.9}O]_{1.12}CoO_2$ and $[Pb_{0.7}Hg_{0.4}Sr_{1.9}Co_{0.2}][CoO_2]_{1.8}$ are promising with ZT = 0.8 – 1.0 at 800 – 1000 K [26]. n-type oxides are considered inferior when compared to these p-type oxides as a result of their lower ZT values. Potential thermoelectric n-type oxides include $SrTiO_3$, $CaMnO_3$, In_2O_3 and ZnO. The highest ZT values so far reported for polycrystalline n-type oxides are 0.47 at 1000 K [27], [28] and 0.65 at 1247 K [27] for Al-Ga co-doped ZnO $[Zn_{0.96}Al_{0.02}Ga_{0.02}O]$ and recently ZT ≥ 0.60 at 1000 – 1100 K for 10 mol % La and 10 mol% Nb co-doped $SrTiO_3$ [29].

Most of the TE research reported for reduced RE-doped $SrTiO_{3-\delta}$ relate to electronic compensation mechanism [13], [30], [31], while ionic compensation mechanism (cation vacancy) mostly on A-site are reported only by Kovalevsky *et al* [13], Lu *et al* [31], Popuri *et al* [32] and recently by Han *et al* [33]. Moreover, there are several reported studies of dual doped $SrTiO_3$ with La and Dy or Yb [21], [22],

[33]–[37] La and Ba [38], La and Nb or W [29], [31], [32]. There is no report in the literature for $SrTiO_3$ dual doped with Sm and a second cation.

$Sr_5RTi_3Nb_7O_{30}$ (SLTN) (R = rare earth elements mainly La, Sm, Nd, Eu, Gd and Dy) tetragonal tungsten bronze (TTB) oxide ceramics have been studied widely in terms of crystal structure [39], [40], dielectric and /or ferroelectric properties [39], [41] and phase transition [42]–[46] for various applications. SLTN and other TTBs are significant due to their complex and tunable structures with many interstitial sites in which substitution of various cations are possible [41], [45], [46] However, no literature has reported the thermoelectric properties and potentials of SLTN despite intrinsic characteristics that favour thermoelectric applications. Recent investigation of oxygen-deficient strontium barium niobate (SBN), $Sr_xBa_{1-x}Nb_2O_{6-\delta}$ ferroelectric single crystals as a potential n-type thermoelectrics opens the window for the study of other TTB compounds for thermoelectric applications [47]. Lee *et al* in this study reported a high power factor (PF) of 2000 $\mu W/m. K^2$ at 516 K parallel to c-axis [48], [49] and a figure of merit, ZT > 0.5 at 550 K along the c-direction [50].

$La_2Ti_2O_7$ (LTO) is a perovskite-like layered structure compound whose piezoelectric, dielectric, electro-optic and photocatalytic properties have been widely researched [51]. LTO possesses multiple layers of perovskite units resulting in a large unit cell, crystal anisotropy and a complex structure, hence they exhibit low thermal conductivity [52]. As a complex structured material, it shows a high flexibility for tuning through cation/anion substitution which together with intrinsic low k are vital constituents required for a thermoelectric material.

1.2 Aim of Research

The major aim of this research is to study the structure-property relationships of co-doped rare earth, RE (La and Sm) $SrTiO_{3-\delta}$ perovskite, Samarium (Sm) doped $Sr_5LaTi_3Nb_7O_{30-\delta}$ (SLTN) tetragonal tungsten bronze (TTB) and niobium (Nb) doped $La_2Ti_2O_7$ (LTO) perovskite-like layered n-type ceramics based on the aliovalent doping mechanisms and sintered in 5% H_2/N_2 gas mixtures to reduce the oxides and engender greater conductivity.

The purpose of co-doping in the case of $SrTiO_3$ instead of single doping is an attempt to enhance the phonon scattering and therefore reduce total thermal conductivity without significantly affecting the PF. To do this, we selected lanthanum (La) as the largest RE ion (La^{3+} = 1.36 Å in co-ordination number, CN 12) and samarium (Sm) as an intermediate sized RE ion (Sm^{3+} = 1.24 Å in CN 12) dissimilar to strontium, Sr ion (Sr^{2+} = 1.44 Å in CN 12) [53] to give a significant variation in the ionic radius and mass of these A-site doping ions compared to Sr. In SLTN and LTO study, Sm and Nb, respectively are chosen as donor dopants with a view to increasing the carrier concentration and enhancing phonon scattering thereby optimizing the thermoelectric properties.

References

[1] Alfred J. Cavallo, "Hubbert's Petroleum Production Model: An Evaluation and Implications for World Oil Production Forecasts," *Nat. Resour. Res.*, Vol. 13, No. 4, Pp. 211–221, 2004.

[2] Ryoji Funahashi and Saori Urata, "Development of a Small-Size Cogeneration System using Thermoelectric Power Generation," *Syntheisology. English Ed.*, Vol. 1, No. 2, Pp. 85–92, 2008.

[3] William J. Pike, "The Reality of Alternative Energy ," *World Oil*, Vol. 237, No. 6, P. 13, 2016.

[4] U.S Energy Information Administration, "International Energy Outlook 2013," accessed August 20, 2017.

[5] Jarman T. Jarman, Essam E. Khalil, and Elsayed Khalaf, "Energy Analyses of Thermoelectric Renewable Energy Sources," *Open J. Energy Effic.*, Vol. 2, No. 4, Pp. 143–153, 2013.

[6] Cronin B Vining, "An Inconvenient Truth about Thermoelectrics," *Nature. Mater.*, Vol. 8, No. 2, Pp. 83–85, 2009.

[7] Basel Ismail and Wael Ahmed, "Thermoelectric Power Generation using Waste-Heat Energy as an Alternative Green Technology," *Recent Patents Electr. Eng.*, Vol. 2, No. 1, Pp. 27–39, 2009.

[8] A. J. Minnich, M. S. Dresselhaus, Z. F. Ren, and G. Chen, “Bulk Nanostructured Thermoelectric Materials: Current Research and Future Prospects,” *Energy Environ. Sci.*, Vol. 2, No. 5, P. 466, 2009.

[9] Joseph R. Sootsman, Duck Young Chung, and Mercouri G. Kanatzidis, “New and Old Concepts in Thermoelectric Materials,” *Angew. Chemie - Int. Ed.*, Vol. 48, No. 46, Pp. 8616–8639, 2009.

[10] Kunihito Koumoto, Yifeng Wang, Ruizhi Zhang, Atsuko Kosuga, and Ryoji Funahashi, “Oxide Thermoelectric Materials: A Nano Structuring Approach,” *Annu. Rev. Mater. Res.*, Vol. 40, Pp. 363–394, 2010.

[11] Jeffrey W. Fergus, “Oxide Materials for High Temperature Thermoelectric Energy conversion,” *J. Eur. Ceram. Soc.*, Vol. 32, No. 3, Pp. 525–540, 2012.

[12] Koumoto Kunihito, Funahashi Ryoji, Guilmeau Emmanuel, Miyazaki Yuzuru, Weidenkaff Anke, Wang Yifeng, and Wan Chunlei, “Thermoelectric Ceramics for Energy Harvesting,” *J. Am. Ceram. Soc.*, Vol. 96, No. 1, Pp. 1–23, 2013.

[13] A. V. Kovalevsky, A. A. Yaremchenko, S. Populoh, A. Weidenkaff, and J. R. Frade, “Effect of A-Site Cation Deficiency on the Thermoelectric Performance of Donor-Substituted Strontium Titanate,” *J. Phys. Chem. C*, Vol. 118, No. 9, Pp. 4596–4606, 2014.

[14] Kanishka Biswas, Jiaqing He, Ivan D. Blum, Chun I. Wu, Timothy P. Hogan, David N. Seidman, Vinayak P. Dravid, and Mercouri G. Kanatzidis, “High-Performance Bulk Thermoelectrics with All-Scale Hierarchical Architectures,” *Nature*, Vol. 489, No. 7416, Pp. 414–418, 2012.

[15] Okuma K et al, “Collection of Papers of Thermoelectric Symposium 99,” 1999.

[16] A. Shakouri, “Recent Developments in Semiconductor Thermoelectric Physics and Materials,” *Annu. Rev. Mater. Res.*, Vol. 41, Pp. 399–431, 2011.

[17] G J Snyder and E S Toberer, “Complex Thermoelectric Materials,” *Nat Mater,* Vol. 7, No. 2, Pp. 105–114, 2008.

[18] Abanti Nag and V. Shubha, “Oxide Thermoelectric Materials: A Structure-Property Relationship,” *J. Electron. Mater.*, Vol. 43, No. 4, Pp. 962–977, 2014.

[19] D.M. Rowe and Gao Min, “Evaluation of thermoelectric modules for power generation,” *J. Power Sources*, vol. 73, no. 2, pp. 193–198, 1998.

[20] Dharmik Patel , Prof Shruti B Mehta, and Divyesh Patel, “Review of Use of Thermoelectricity as Renewable Energy Source,” J*ournal of Emerging Technologies and Innovative Research*, Vol.2, No.3, Pp.835–839, 2015.

[21] Zhiting Tian, S Lee, and G Chen, “A Comprehensive Review of Heat Transfer in Thermoelectric Materials and Devices,” *Annu. Rev. Heat Transf.*, Pp.1–64, 2014.

[22] J. Liu, C. L. Wang, Y. Li, W. B. Su, Y. H. Zhu, J. C. Li, and L. M. Mei, “Influence of Rare Earth Doping on Thermoelectric Properties of $SrTiO_3$ Ceramics,” *J. Appl. Phys.*, Vol.114, No.22, 2013.

[23] Kunihito Koumoto and Ichiro Terasaki, “Complex Oxide Materials for Thermoelectric Applications,” *MRS Bull.*, Vol.31, No. March, Pp.206–210, 2006.

[24] Jing Feng Li, Wei Shu Liu, Li Dong Zhao, and Min Zhou, “High-Performance Nanostructured Thermoelectric Materials,” *NPG Asia Mater.*, Vol.2, No.4, Pp. 152–158, 2010.

[25] Ti R Ta, R R Sun, X Y Qin, L L Li, D Li, N N Wang, J Zhang, and Q Q Wang, “Transport and Thermoelectric Properties of $Sr_3(Ti_{0.95}R_{0.05})_2O_7$ (R = Ta, Nb, W) oxides,” Vol.3, Pp.0–8, 2012.

[26] Zhilun Lu, “La Doped $SrTiO_3$ Based Oxide Thermoelectrics.,” PhD Thesis, University of Sheffield, 2016.

[27] Mateja Košir, Matejka Podlogar, Nina Daneu, Aleksander Rečnik, Emmanuel Guilmeau, and Slavko Bernik, “Phase Formation, Microstructure Development and Thermoelectric Properties of $(ZnO)_kIn_2O_3$ Ceramics,” *J. Eur. Ceram. Soc.*, Vol.37, No.8, Pp.2833–2842, 2017.

[28] Michitaka Ohtaki, Kazuhiko Araki, and Kiyoshi Yamamoto, “High Thermoelectric Performance of Dually Doped ZnO Ceramics,” *J. Electron. Mater.*, Vol.38, No.7, Pp.1234–1238, 2009.

[29] Jun Wang, Bo Yu Zhang, Hui Jun Kang, Yan Li, Xinba Yaer, Jing Feng Li, Qing Tan, Shuai Zhang, Guo Hua Fan, Cheng Yan Liu, Lei Miao, Ding Nan, Tong Min Wang, and Li Dong Zhao, “Record High Thermoelectric Performance in Bulk $SrTiO_3$ Via Nano-scale Modulation Doping,” *Nano Energy*, Vol.35, No. April, Pp.387–395, 2017.

[30] A. V. Kovalevsky, A. A. Yaremchenko, S. Populoh, P. Thiel, D. P. Fagg, A. Weidenkaff, and J. R. Frade, “Towards a High Thermoelectric Performance in Rare-Earth Substituted $SrTiO_3$: Effects Provided by Strongly-Reducing Sintering Conditions,” *Phys. Chem. Chem. Phys.*, Vol.16, No.48, Pp. 26946–26954, 2014.

[31] Zhilun Lu, Huairuo Zhang, Wen Lei, Derek C. Sinclair, and Ian M. Reaney, "High-Figure-of-Merit Thermoelectric La-Doped A-Site-Deficient $SrTiO_3$ Ceramics," *Chem. Mater.*, Vol.28, No.3, Pp.925–935, 2016.

[32] S. R. Popuri, A. J. M. Scott, R. A. Downie, M. A. Hall, E. Suard, R. Decourt, M. Pollet, and J.-W. G. Bos, "Glass-like Thermal Conductivity in $SrTiO_3$ Thermoelectrics Induced by A-Site Vacancies," *RSC Adv.*, Vol.4, No.64, Pp. 33720–33723, 2014.

[33] Jiao Han, Qiu Sun, Wenxu Li, and Ying Song, "Microstructure and Thermoelectric Properties of $La_{0.1}Dy_{0.1}Sr_xTiO_3$ Ceramics," *Ceram. Int.*, Vol. 43, No.7, Pp.5557–5563, 2017.

[34] Jiao Han, Qiu Sun, and Ying Song, "Enhanced thermoelectric properties of La and Dy Co-doped, Sr-Deficient $SrTiO_3$ Ceramics," *J. Alloys Compd.*, Vol.705, Pp.22–27, 2017.

[35] H C Wang, C L Wang, W B Su, J Liu, Y Zhao, H Peng, J L Zhang, M L Zhao, J C Li, N Yin, and L M Mei, "Enhancement of Thermoelectric Figure of Merit by Doping Dy in $La_{0.1}Sr_{0.9}TiO_3$ Ceramic," *Mater. Res. Bull.*, Vol.45, No.7, Pp.809–812, 2010.

[36] Hong Chao Wang, Chun Lei Wang, Wen Bin Su, Jian Liu, Yi Sun, Hua Peng, and Liang Mo Mei, "Doping Effect of La and Dy on the Thermoelectric Properties of $SrTiO_3$," *J. Am. Ceram. Soc.*, Vol.94, No.3, Pp.838–842, 2011.

[37] Hongchao Wang and Chunlei Wang, "Thermoelectric Properties of Yb-Doped $La_{0.1}Sr_{0.9}TiO_3$ Ceramics at High Temperature," *Ceram. Int.*, Vol.39, No.2, Pp. 941–946, 2013.

[38] Hiroaki Muta, Ken Kurosaki, and Shinsuke Yamanaka, "Thermoelectric Properties of Doped $BaTiO_3$-$SrTiO_3$ Solid Solution," *J. Alloys Compd.*, Vol. 368, No.1–2, Pp.22–24, 2004.

[39] Bao Li Deng, Xiao Li Zhu, Xiao Qiang Liu, and Xiang Ming Chen, "Effects of Oxygen-Deficiency on Crystal Structure, Dielectric and Ferroelectric Properties in $Sr_5SmTi_{3+2x}Nb_{7-2x}O_{30-x}$ with Tungsten Bronze Structure," *RSC Adv.*, Vol.7, No.44, Pp.27370–27376, 2017.

[40] Xiao Li Zhu, Xiao Qiang Liu, and Xiang Ming Chen, "Crystal Structure and Dielectric Properties of $Sr_5RTi_3Nb_7O_{30}$ (R=La, Nd, Sm, and Eu) Tungsten Bronze Ceramics," *J. Am. Ceram. Soc.*, Vol.94, No.6, Pp.1829–1836, 2011.

[41] Gebru Zerihun, Gaoshang Gong, Shuai Huang, and Songliu Yuan, "Dielectric and Relaxor Ferroelectric Properties of $Sr_4CaLaTi_3Nb_7O_{30}$ Tetragonal Tungsten Bronze Ceramics," *Ceram. Int.*, Vol.41, No.9, Pp.12426–12431, 2015.

[42] X. Zhu, M. Fu, M. C. Stennett, P. M. Vilarinho, I. Levin, C. A. Randall, J. Gardner, F. D. Morrison, and I. M. Reaney, “A Crystal-Chemical Framework for Relaxor Versus Normal Ferroelectric Behavior in Tetragonal Tungsten Bronzes,” *Chem. Mater.*, Vol.27, No.9, Pp.3250–3261, 2015.

[43] Xiao Li Zhu and Xiang Ming Chen, “Ferroelectric Transition of $Sr_5SmTi_3Nb_7O_{30}$ Tungsten Bronze Ceramics Investigated Using Differential Scanning Calorimetry and Raman Scattering,” *J. Am. Ceram. Soc.*, Vol.95, No.10, pp. 3185–3191, 2012.

[44] V. Bovtun, S. Kamba, S. Veljko, D. Nuzhnyy, K. Knížek, M. Savinov, and J. Petzelt, “Relaxor-like Behavior of Lead-free $Sr_2LaTi_2Nb_3O_{15}$ Ceramics with Tetragonal Tungsten Bronze Structure,” *J. Appl. Phys.*, Vol.101, No.5, pp. 1–7, 2007.

[45] M R Ranga Raju, R N P Choudhary, and H R Rukmini, “Diffuse Phase Transition in $Sr_5RTi_3Nb_7O_{30}$ (R = La, Nd, Sm, Gd and Dy) Ferroelectric Ceramics,” *Ferroelectrics*, Vol.325, No.1, Pp. 25–32, 2005.

[46] M R Ranga Raju and R N P Choudhary,“Diffuse Phase Transition in $Sr_5RTi_3Nb_7O_{30}$ (R=La, Nd and Sm),” *J. Phys. Chem. Solids*, Vol.64, No.5, Pp. 847–853, 2003.

[47] Soonil Lee, Jonathan A. Bock, Susan Trolier-McKinstry, and Clive A. Randall, “Ferroelectric-Thermoelectricity and Mott Transition of Ferroelectric Oxides with High Electronic Conductivity,” *J. Eur. Ceram. Soc.*, Vol.32, No.16, Pp. 3971–3988, 2012.

[48] Soonil Lee, Rudeger H.T. Wilke, Susan Trolier-Mckinstry, Shujun Zhang, and Clive A. Randall, “$Sr_xBa_{1-x}Nb_2O_{6-\delta}$ Ferroelectric- Thermoelectrics: Crystal Anisotropy, Conduction Mechanism, and Power Factor,” *Appl. Phys. Lett.*, Vol.96, No.3, Pp. 4–7, 2010.

[49] Yi Li, Jian Liu, Chun-Lei Wang, Wen-Bin Su, Yuan-Hu Zhu, Ji-Chao Li, and Liang-Mo Mei, “Thermoelectric Properties of $Sr_{0.61}Ba_{0.39}Nb_2O_{6-\delta}$ Ceramics in Different Oxygen-reduction Conditions,” *Chinese Phys. B*, Vol.24, No.4, P. 47201, 2015.

[50] Jason H. Chan, Jonathan A. Bock, Hanzheng Guo, Susan Trolier-McKinstry, and Clive A. Randall, “Filled Oxygen-deficient Strontium Barium Niobates,” *J. Am. Ceram. Soc.*, Vol.100, No.2, Pp.774–782, 2017.

[51] N. Zhang, Q. J. Li, S. G. Huang, Y. Yu, J. Zheng, C. Cheng, and C. C. Wang, “Dielectric Relaxations in Multiferroic $La_2Ti_2O_7$ ceramics,” *J. Alloys Compd.*, Vol.652, Pp.1–8, 2015.

[52] Jibran Khaliq, Li Chunchun, Chen Kan, Shi Baogui, Ye Haitao, Antonio M. Grande, Haixue Yan, and Michael J. Reece, “Reduced Thermal Conductivity by Nanoscale Intergrowths in Perovskite like layered Structure $La_2Ti_2O_7$,” *J. Appl. Phys.*, Vol.117, No.7, Pp.2–8, 2015.

[53] R. D Shannon, “Revised Effective Ionic Radii and Systematic Studies of Interatomie Distances in Halides and Chaleogenides,” *Acta Cryst.*, Vol.A32, Pp.751–767, 1976.

Chapter 2: Literature Review

2.1 Principle of Thermoelectric Power Generator

In a thermoelectric power generator (TEG), several doped p-type and n-type semiconductors are configured within the thermoelectric module such that they are arranged electrically in series and thermally in parallel. This arrangement forms the p-n junctions through which the charge carriers (holes for p-type and electrons for n-type) are transported as shown in Figure 2.1 [1]. When a temperature gradient, ΔT (heat) is applied across the thermoelectric (TE) module, the charge carriers become thermally activated. The applied temperature gradient causes a diffusion of heat and charge carriers along the thermal gradient from the hot junction to the cold junction which leads to generating a Seebeck voltage (electrostatic potential, ΔV) across the module. Owing to the generated Seebeck voltage, electric current flows within the circuit leading to the production of electrical DC power. Diffusion, phonon-electron interactions and entropic contributions (e.g. spin entropy) control the transport of the charge carriers [2]. Diffusion of the charge carriers and their flow (carrier mobility) are the parameters that regulate the thermoelectric transport [1].

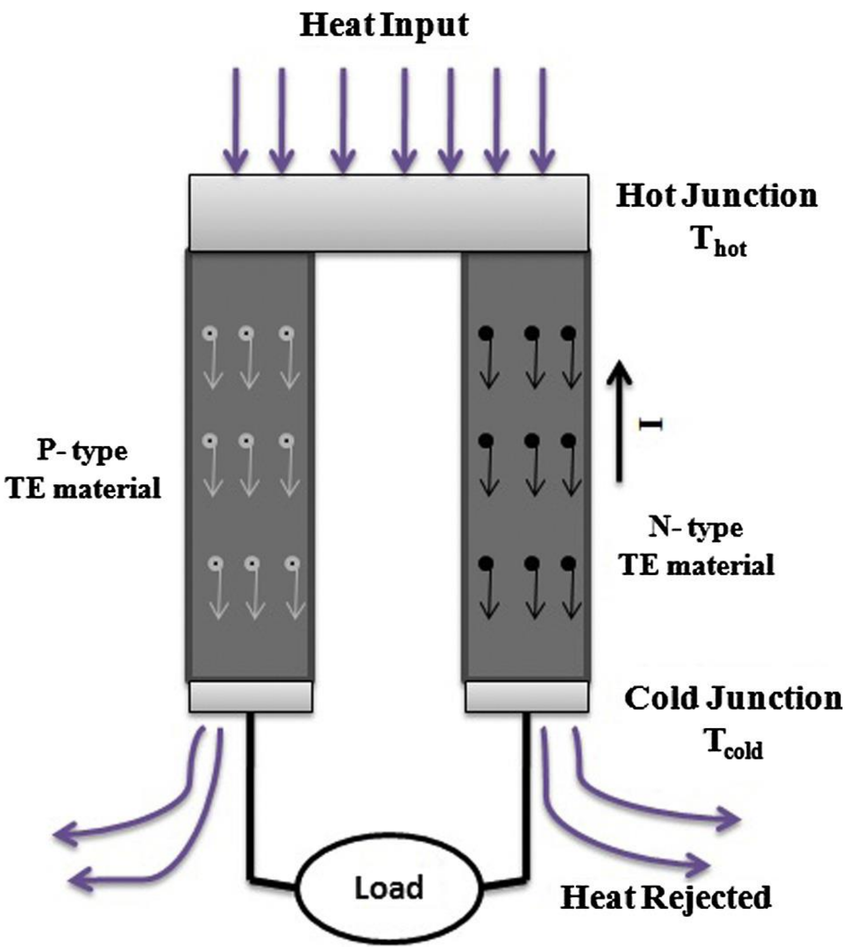

Figure 2.1. A schematic showing the thermoelectric modules operating across a temperature gradient for power generation [1].

In a typical TEG (Figure 2.2), heat is transferred from the high temperature heat source which is maintained at a temperature, T_H at a given heat rate, Q_H [3], [4]. Consequently, the heat is dissipated to the sink sustained at a low temperature, T_L at a rate of Q_L via the cold junction. Owing to the generated voltage or Seebeck voltage, electric current flows within the TE module (circuit) which leads to the production of electrical power. This is attributed to the heat supplied at the hot junction and supported by the first law of thermodynamics [3];

$$Q_H - Q_L = W_e \qquad 2.1$$

where W_e is the electrical power.

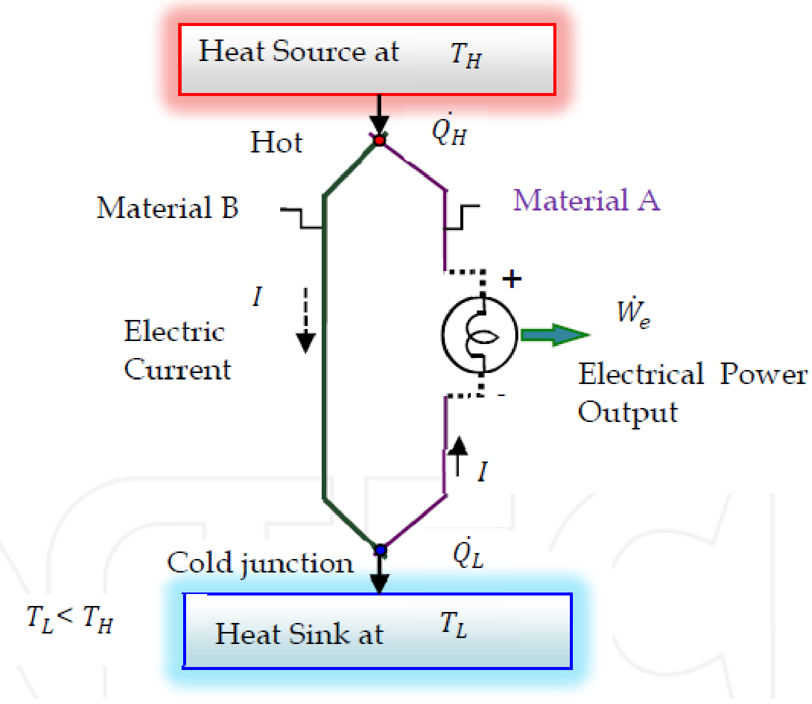

Figure 2.2. Schematic of the operating principle of Thermoelectric Power Generator (TEG) based on the Seebeck effect [4] . Q_H is high temperature heat transfer, T_H is high temperature, Q_L is low temperature heat transfer, and W_e is the output energy (Electrical power output).

A conventional single-stage TEG is made up of two ceramic plates or substrates which serve as foundation, mechanical support, and electrical insulation for the thermoelements/TE materials (p- and n- types) [3]–[5] . These ceramic plates are of ZnO or Al_2O_3 and at times BeO or AlN when large heat transfer is required. The edges of the thermoelements are interconnected with metallic strips of high electrical conduction such as copper. A diagram of a typical single stage TEG showing the arrangement of major components is represented in Figure 2.3. The merits of a TEG over other conventional power generation devices are as outlined below [3]–[9]:

i. TEG is a solid-state device with no moving mechanical parts, hence noiseless, and requires less maintenance
ii. It is a reliable source of green energy and capable of exceeding 100,000 hours of steady-state operation
iii. TEG is relatively small in size (scalability) and light weight thereby making it suitable for small-scale and rural power supply
iv. It is simple, safe, and environmentally friendly; and
v. Operates at both low and high temperatures.

Despite the low energy conversion efficiency, niche applications and slow technological progression associated with TEG, it is paramount to state that TEGs are still in their developmental stage with numerous potential applications [10]. Outside power generation, TE materials have attracted potential applications in solid state cooling or thermoelectric refrigeration using the Peltier effect. The effect of low energy conversion efficiency has constrained the use of TEGs to specialised areas where reliability other than cost is a major consideration [4]. These specialised applications include providing power for cathodic protection systems in gas well casings and pipelines [10], [11]¸ self-powered systems for wireless data communications or gatherings [11], [12], powering of automotive and deep space explorations [12] , ventilation fans, navigation equipment and landing lights in airports [11].

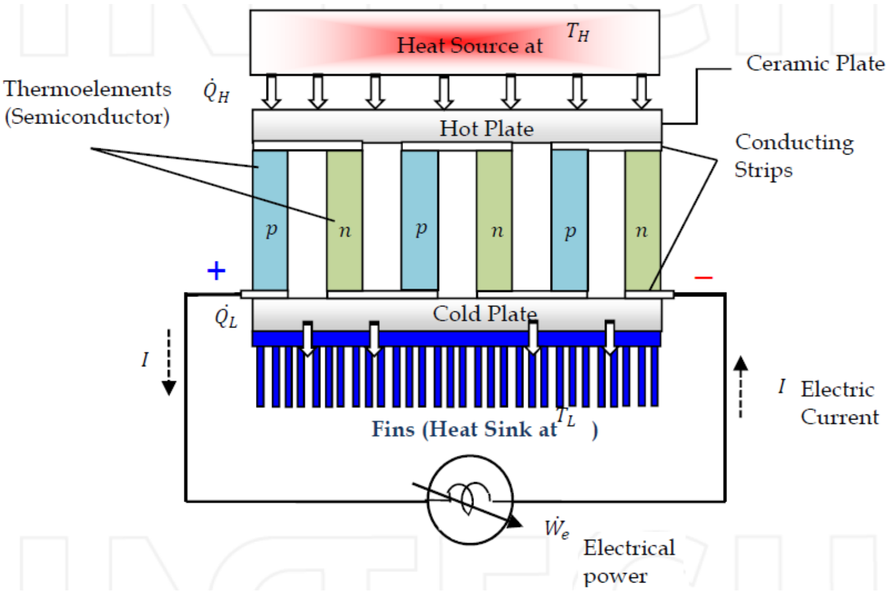

Figure 2.3. Schematic of a typical TEG showing the arrangement of the major components [4]. The thermoelements are heavily doped n- and p-type materials.

2.2 Thermoelectric Phenomena

Electrically conductive materials exhibit three types of effects, namely the: Seebeck; Peltier and Thomson effects. These effects are collectively known as thermoelectric effects [10]. The functionality of power generation and solid-state refrigeration thermoelectrics are fundamentally dependent on the Seebeck effect and Peltier effect, respectively. The focus of this research is on the Seebeck effect as applied in TEGs.

Seebeck effect is the establishment of a thermal gradient across a material which leads to generation of a voltage. It involves the conversion of temperature differences across a conductive material directly into electricity and vice versa [10]

; and was discovered in 1821 by a German physicist, Thomas John Seebeck [13]–[15]. Seebeck in his experiment observed that when two different conductors are joined together, and the junctions are held at different temperatures such as T_1 and T_2, a voltage difference, ΔV is developed. The ratio of the ΔV to temperature difference, ΔT ($T_2 - T_1$) is given as;

$$-\frac{\Delta V}{\Delta T} = S \qquad 2.2$$

where, S is the constant of proportionality called the Seebeck coefficient (thermopower), while ΔV and ΔT are the voltage and temperature differences, respectively between the hot and cold junctions. The negative sign in equation 2.2 is a representation of electron as a negative charge and the convention of current flow in a circuit.

At the atomic scale, Seebeck effect is dominated by charge carrier diffusion. This diffusion therefore pushes the majority charge carriers towards the cold junction of the material leading to a build-up of a compensating voltage [10]. This situation leads to p-type materials (valence holes dominated) to have a positive S values while n-type materials (electrons dominated) possess negative S values. The minority charge carriers move at a slower rate in the opposite direction which can be attributed to an increase in effective mass (electrons and holes) interacting with crystal lattice (known as phonon drag) and charge carrier diffusion rates [16].

2.2.1 Seebeck Effect

When two different conducting materials such as A and B are joined to create an open circuit (Figure 2.4a) and kept at different temperatures, T_1 and T_2 at the junctions, ΔV will be generated between the open ends. If the open ends are closed as illustrated in Figure 2.4b, an electric current, I will be developed which flows along the loop. As ΔT between T_1 and T_2 approaches zero, a linear relationship between ΔT and ΔV is established [17]:

$$\mathrm{S_{AB}} = \frac{\Delta \mathrm{V}}{\Delta \mathrm{T}} \qquad 2.3$$

Considering equation 2.2, equation 2.3 can be re-written as;

$$S_{AB} = S_A - S_B = \frac{\Delta V_A}{\Delta T} - \frac{\Delta V_B}{\Delta T} \qquad 2.4$$

where, S_{AB} is the constant of proportionality called the relative Seebeck coefficient (expressed in units of μV/K or μV/°C) of the A-B circuit., S_A and S_B are the absolute Seebeck coefficients of materials A and B, respectively. A similar Seebeck effect associated with two dissimilar joined materials also occurs in a single conducting material (Figure 2.5).

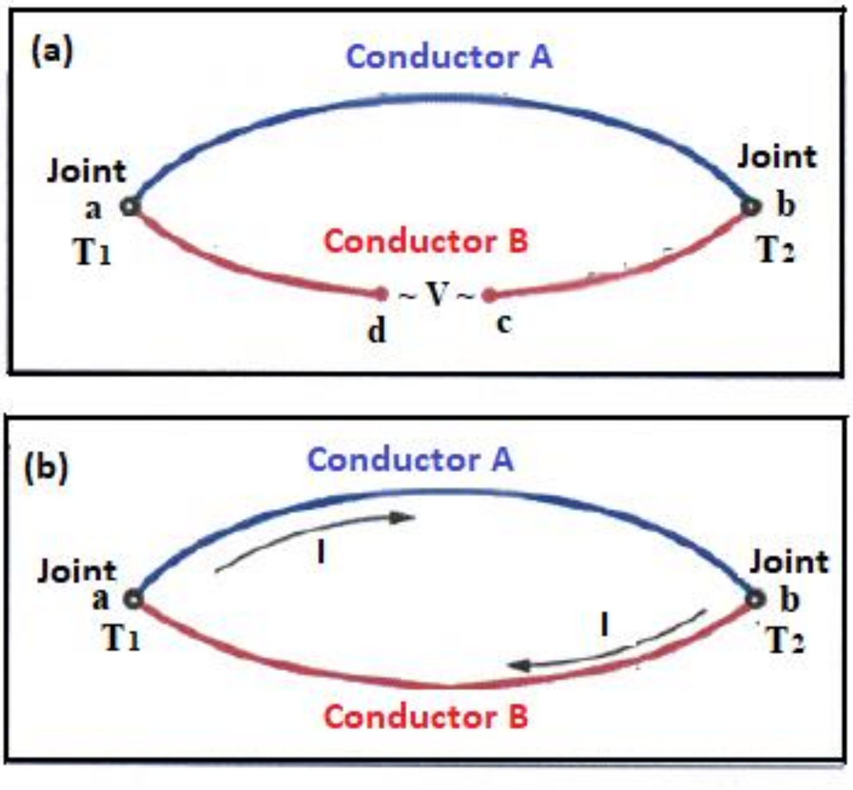

Figure 2.4. A diagram illustrating the Seebeck effect in (a) an open circuit, and (b) a closed circuit with different conducting materials (A and B) and temperatures (T_1 and T_2) maintained at the joints (a and b) [17].

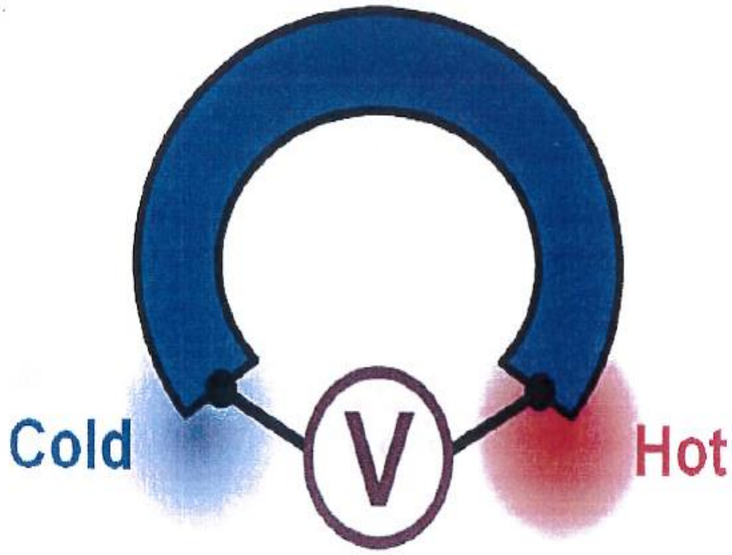

Figure 2.5. The Seebeck effect in a single conducting material [18] showing the hot and cold junctions.

2.2.2 Peltier Effect

The Peltier effect is the presence of heating or cooling at the junction of two dissimilar electrical conducting materials [10]. It is the basis for thermoelectric cooling and was discovered in 1834 by a French physicist, Jean Charles Athanase Peltier [18]–[21]. Peltier in his study observed that an electrical current would produce a temperature gradient at the junction of two different conducting materials. When an external electromotive force (emf) source is applied across the open ends of the two coupled materials (Figure 2.6), current, I flow in a clockwise direction around the circuit. Therefore, a temperature difference, dT is developed, while heat is absorbed or generated, dQ/dt (known as rate of heating) at one junction and at other junction, heat is released or removed, -dQ/dt (known as rate of cooling). The heat absorbed at the junction is proportional to the electric current, I and as shown in equation 2.5.

$$\frac{dQ}{dt} = \pi_{AB} . I \qquad 2.5$$

where, π_{AB} is the Peltier coefficient of the A-B circuit and it is measured in W/A or V according to Kelvin relationship [13],

$$\pi_{AB} = S.T \qquad 2.6$$

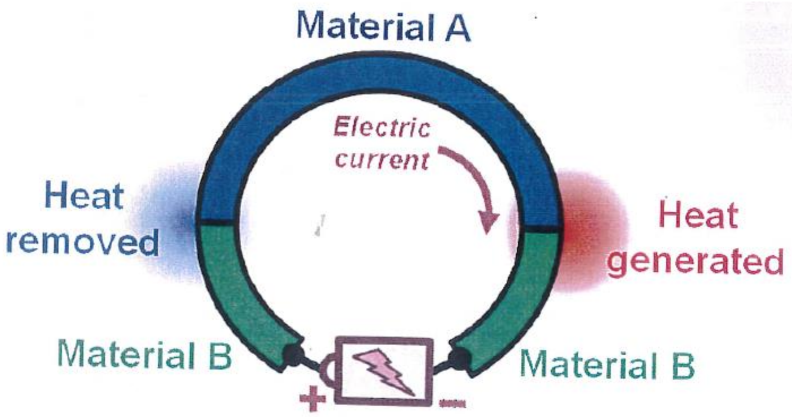

Figure 2.6. Schematic illustration of Peltier effect [18].

2.2.3 Thomson Effect

In 1854, about three decades after the discovery of Seebeck effect, Thomson, a British physicist who later became Lord Kelvin [22], analysed the correlation between Seebeck and Peltier effects, and found what becomes the Thomson effect. In this study, heat is absorbed or released when a current flow in a conducting material with a temperature gradient, dT/dx. The rate of the heat absorbed or released (dQ/dt) is proportional to the electric current (I) and dT/dx. This is demonstrated in equation 2.7.

$$\frac{dQ}{dt} = \mu . I . \frac{dT}{dx} \qquad 2.7$$

where, μ is the Thomson coefficient measured in V/K. The value of Thomson coefficient is positive when current flows from the hot end to the cold end (heat liberation) and negative when current flows in a reverse direction (heat absorption). Thomson effect with a negative Thomson coefficient is shown in Figure 2.7.

Thermoelectric effect (Seebeck, Peltier and Thomson effects) is interrelated in Kelvin's relations as derived from thermodynamics;

$$\mathrm{\pi_{AB}} = \frac{\Delta \mathrm{V}}{\Delta \mathrm{T}}\mathrm{T} = \mathrm{S_{AB}T} \qquad 2.8$$

$$\mathrm{\mu_A} - \mathrm{\mu_B} = -\mathrm{T}\frac{\Delta}{\Delta \mathrm{T}}\left(\frac{\mathrm{\pi_{AB}}}{\mathrm{T}}\right) = -\mathrm{T}\frac{\Delta \mathrm{S_{AB}}}{\Delta \mathrm{T}} = -\mathrm{T}\frac{\Delta^2 \mathrm{V}}{\Delta \mathrm{T}^2} \qquad 2.9$$

$$\frac{\Delta \mathrm{S_{AB}}}{\Delta \mathrm{T}} = \frac{\mathrm{\mu_B} - \mathrm{\mu_A}}{\mathrm{T}} \qquad 2.10$$

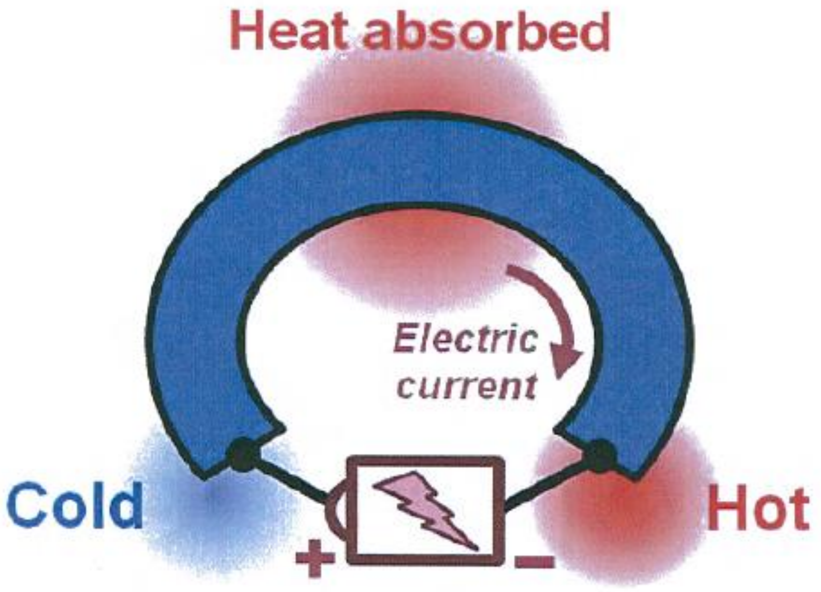

Figure 2.7. Schematic illustration of Thomson effect with a negative Thomson coefficient [18]. This implies that electric current flows from cold end to hot junction.

2.3 Thermoelectric Performance

About 90 % of the world's electricity is generated by heat energy which on average operates at 30-40 % efficiency thereby losing an approximate of 15 terawatts (1.5 x 10^{13} Watts) of power (in form of heat) per year to the surroundings [23], [24]. Thermoelectric devices convert some of this heat into useful electricity [24] . From laws of thermodynamics, the efficiency of a TEG is related to the properties of the TE materials.

The performance of TE devices including TEG depends on the combined effects of efficiency of the Carnot process (η_C), efficiency of thermoelectric generator (η_T) and the dimensionless figure of merit (ZT) resulting to a maximum conversion efficiency (η_{max}) [13], [25]–[27];

$$\eta_{max} = \frac{W}{Q_H} = \eta_C . \eta_T = \eta_C [\frac{\sqrt{(1+ZT_{avg})-1}}{\sqrt{(1+ZT_{avg})+\left(\frac{T_C}{T_H}\right)}}] \quad 2.11$$

$$\eta_C = \frac{T_H - T_C}{T_H} = 1 - \frac{T_C}{T_H} \quad 2.12$$

where W is the power generated, Q_H is the net heat flow, T_H and T_C are the temperatures at the hot and cold sites, respectively, and T_{avg} is the average temperature $(\frac{T_H+T_C}{2})$. Equation 2.12 shows that for an increased efficiency to be obtained, high ZT_{avg} values and large temperature gradients are required.

ZT contains both electrical and thermal contributions to the properties of the TE materials and is given as:

$$ZT = \frac{S^2 \sigma \, T}{K} \quad 2.13$$

where S is the Seebeck coefficient, σ is the electrical conductivity, T is the absolute temperature at which the properties are measured and $k = k_L + k_E$ [28] is the total thermal conductivity. k_L and k_E are the lattice thermal conductivity and electronic thermal conductivity, respectively. ZT describes the material's performance, hence is a prerequisite for a good thermoelectric material. As Dehkordi [29] puts it, "ZT is a measure of the competition between electronic transport (power factor) and thermal transport (total thermal conductivity) in a material". The higher the ZT, the better the efficiency of the TE materials to convert heat energy into useable electricity. In equation 2.13, $S^2\sigma$ is known as the power factor (PF) and is another important TE performance factor. PF is the determination of the capacity of electronic transport in a material for thermoelectric applications [30]. It is the electric power through which the heat flows between the hot and cold sides per unit temperature gradient [31]. Therefore, PF is a measure of the power anticipated from a TEG [32].

2.3.1 Characteristics of Thermoelectric (TE) Materials

A good TE material as already stated is required to exhibit a high dimensionless figure of merit (ZT). The concept of ZT was first used in1949 by Abram Fedororich Ioffe, a Russian physicist when he developed the modern theory of thermoelectricity [33], [34]. For a high ZT to be achieved, the following parameter are essential [28], [35]–[40]:

i. Large Seebeck coefficient to produce a required high voltage for a given temperature difference.
ii. High electrical conductivity to minimise losses through electrical heating (Joule heating), and
iii. Low thermal conductivity to restrict diffusion of heat across the device by maintaining a large thermal gradient.

Unfortunately, nature does not provide materials with these expected properties for thermoelectric applications. For instance, metals have very high electrical and thermal conductivities with low Seebeck coefficient, while glasses, polymers, and insulators in general exhibit very low electrical and thermal conductivities [41]. This therefore gave rise to the notion “phonon-glass and electron-crystal (PGEC) properties” [41]. This concept implies that outstanding thermoelectric materials require crystalline solids with low total thermal conductivity (k) such as glass and scatter phonons without significantly hindering the electrical conductivity (σ) but maintains charge carriers of high mobility or electronic transport (conduction of electricity) as expected of a crystal [41]–[44]. It is observed that S, σ and k in ZT are tied to carrier concentration. Hence, increasing σ (which is desired) decreases S (which is undesirable). Thus, TE materials with high σ are essential for high performance but tend to have very low S and very high k which leads to low ZT and poor efficiency. As carrier concentration increases, σ and k simultaneously increase with a decrease in S thereby decreasing the overall ZT [30].

A mutual correlation must be established amongst a large Seebeck coefficient, high electrical conductivity, and a low thermal conductivity to optimise the figure of merit. The balance lies on the carrier concentration, hence a good TE material requires a high carrier concentration, $10^{19} – 10^{21}$ cm^{-3} [45]. Figure 2.8 illustrates the dependence of ZT, σ, S and k on carrier concentration for a TE material.

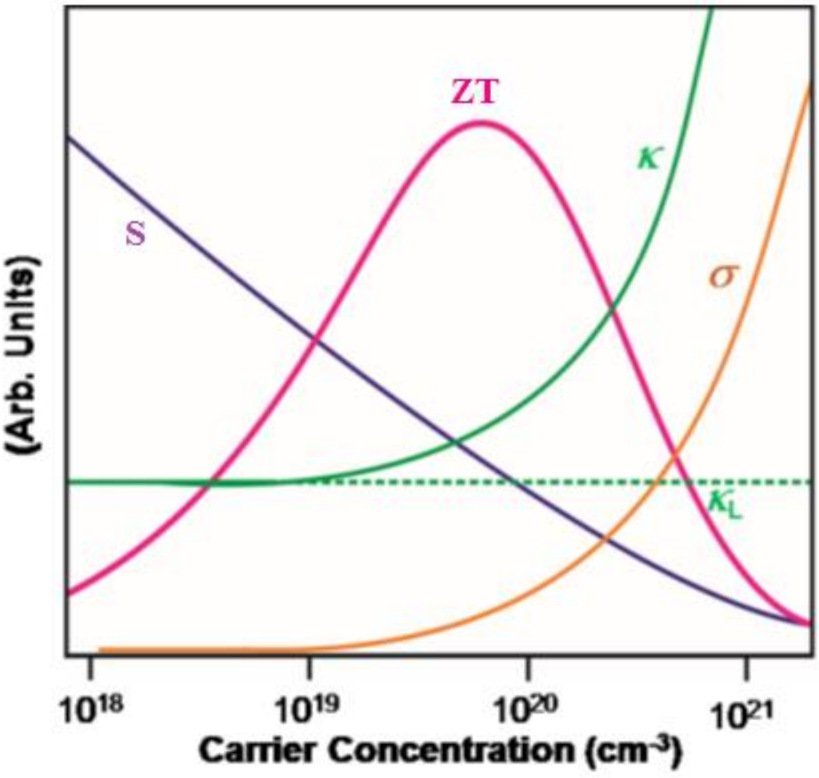

Figure 2.8. A schematic illustrating optimising ZT through a carrier concentration tuning. Maximising the efficiency (ZT) of a thermoelectric material involves a compromise between thermal conductivity (k) and Seebeck coefficient (S) with electrical conductivity (σ) [45].

2.3.2 Seebeck coefficient

Seebeck coefficient is an important property for evaluating the performance of TE materials as shown in equation 2.2. It is the measure of the quantity of potential difference for a given temperature difference generated across a material [46]. Seebeck coefficient, S can also be defined as the heat (entropy) per carrier with respect to temperature ($S \simeq \frac{C}{q}$), where C is the specific heat, and q is the charge of the carrier [47]. Different materials have different Seebeck coefficients. Therefore, the magnitude and mechanism of Seebeck coeffcient and Seebeck effect, respectively for metals are different with that of semiconductors and other materials. In metals, S is given as the product of electronic specific heat (C_{el}) and the temperature (T) divided by the carriers' number (N) [48] ;

$$\mathrm{S} = \frac{\mathrm{C_{el}T}}{\mathrm{N}} \qquad 2.14$$

Equation 2.14 holds because carrier concentration and the position of fermi level of metals are unchanged relative to temperature, hence;

$$S \simeq \frac{C_{el}}{q} = \left(\frac{K_B}{e}\right)\frac{K_B T}{E_F} \qquad 2.15$$

where K_B is the Boltzmann constant, E_F is the Fermi energy, $\frac{\mathrm{K_B}}{\mathrm{e}} = 87\mu\mathrm{VK}^{-1}$ is the thermopower of a classical electron gas. For metals, $S < 87$ µV/K and increases with increasing temperature and vice versa.

In a semiconductor, the charge carriers in the hot joint possess more thermal energy than those in the cold joint leading to the diffusion of the carriers. This implies that the charged particles will excite across the energy, E_G, thus [48];

$$S = \frac{C_{el}}{q} \approx \left(\frac{K_B}{e}\right)\frac{E_G}{K_B T} \tag{2.16}$$

For semiconductors, $S > 87\mu VK^{-1}$ and decreases with increasing temperature and vice versa. Semiconducting materials exhibit either electron conductivity, σ_e (electron dominated charge carrier) with negative thermopower (S_e) or hole conductivity, σ_p (hole dominated charge carrier) with positive thermopower (S_p). These Seebeck coefficients and their corresponding electrical conductivities are related as follows:

$$S \approx \frac{S_e\sigma_e + S_p\sigma_p}{\sigma_e + \sigma_p} \tag{2.17}$$

Typical values of Seebeck coefficient, S required of a good TE materials are 150 -250 µV/K or greater with a corresponding electrical conductivity, σ values of 500-2000 S/cm [29]. Ideally, insulators and semiconductors by nature exhibit large Seebeck coefficients because they possess low carrier concentrations [26]. For a large S to be obtained, only majority carriers (either holes or electrons) devoid of bipolar contributions (mixture of majority and minority carriers) are required in the lattice [49]. Mixed carrier system (existence of n-type and p-type carriers) weakens the Seebeck voltage because of increase of the mixed charge carriers at the cold end. This leads to a total Seebeck coefficient, S_t of both n- and p-type carriers.

$$S_{total} = S_n + S_p \tag{2.18}$$

where S_n is the thermopower of n-type carrier with a negative value, while S_p is the thermopower of p-type carrier with a positive value.

The Boltzmann transport theory describes electronic and thermal transport of most solids. In this theory, the concept of Seebeck coefficient is expressed in the Mott equation [25], [50]:

$$S = \frac{\pi^2}{3}\frac{K_B^2}{e}\, d\ln\frac{\sigma(E)}{dE}\ \Big|\ E = E_f \qquad 2.19$$

where e is the charge electron, and σ (E) is the electrical conductivity determined as a function of the Fermi energy, $E_{f..}$ The relationship between the Seebeck coefficient in the simple model of electron transport as stated below [51]:

$$s = \frac{9\pi^2 K_B^2}{3eh^2}\, m^{*}\, T\left(\frac{\pi}{3n}\right)^{\frac{2}{3}}\left[1 + \left(\frac{d\ln\lambda_s}{d\ln E}\right) E_f\right] \qquad 2.20$$

where h is the Planck’s constant, n is the carrier concentration, m* is the effective mass and λ_s is the scattering distance [52]. It has been shown that large carrier effective mass materials correspond to high Seebeck coefficient, hence desirable for TE applications. On another end, large effective mass leads to low carrier mobility, μ [29] resulting to low electrical conductivity.

This implies that carrier mobility is inversely related to effective mass as shown below:

$$\mu = \frac{e\tau}{m^{*}} \qquad 2.21$$

where τ is the scattering time or the mean scattering between collisions of carriers (carrier lifetime).

2.3.3 Electrical Conductivity

Electrical conductivity (σ) is an important property in TE applications since current flow is required to provide the needed electrical power. Electrical conductivity is the inverse of electrical resistivity and a measure of the ability of a material to conduct an electric current or to allow the passage of electric current. It is related to carrier concentration, n, and its mobility, μ as follows [45]:

$$\sigma = ne\mu \qquad 2.22$$

Using the Drude model [18], [48] which involves combination of equations 2.21 and 2.22, σ can be defined as:

$$\sigma = \frac{ne^2\tau}{m^\star} \qquad 2.23$$

where e is the charge carrier with positive for a hole and negative for an electron.

In metals, electrical conductivity results from the constant motion of the ions and decreases with increase in temperature. σ of metals is very high because they possess optimum charge carriers, about $n \approx 10^{22}$ Carriers/cm^3. The electrical conductivity of semiconductors lies between metals and insulators. For electrical conduction to occur in semiconductors, the charge carriers must be excited across a gap and by the contributions of electrons and holes.

$$\sigma \approx \sigma_0 \exp\left(+\frac{E_G}{K_BT}\right) \qquad 2.24$$

$$\sigma = ne\mu_e + pe\mu_h \qquad 2.25$$

where n, p, μ_e and μ_h are the electron concentration, hole concentration, electron mobility and hole mobility, respectively. Unlike metals, the electrical conductivity of semiconductors increases with increase in temperature. Generally, semiconductors and insulators exhibit low electrical conductivity with high Seebeck coefficient due to possession of low carrier concentration. Two basic methods applicable for achieving high electrical conductivity in semiconductors involves creation of a very small gap for excitation of charge carriers ($E_G < K_BT$) or having a very high mobility carrier [48].

2.3.4 Thermal Conductivity

Thermal conductivity, k is the description of energy transport in the form of heat through a material because of temperature gradient. In thermoelectrics or solid state in general, thermal conductivity is the transfer of heat via a material either by charge carriers (electrons and holes) or by phonons travelling through the lattice. Therefore, total thermal conductivity, k is associated with carrier or electronic thermal conductivity (k_E) and lattice thermal conductivity (k_L) [28], hence;

$$\mathrm{k} = \mathrm{k_E} + \mathrm{k_L} \qquad 2.26$$

In metals, the total thermal conductivity is dominated by k_E which is attributed to presence of high carrier concentration. Therefore, metals are the best electrical and thermal conducting materials. Unlike metals, k_L dominates the total thermal conductivity in insulators and semiconductors. According to Wiedemann-Franz law, the ratio of the electronic contribution of the total thermal conductivity (κ_E) to the electrical conductivity (σ) of the majority of TE materials is proportional to the temperature (T) [45], [50], [53]:

$$k_E = L\sigma T \qquad 2.27$$

Theoretically, the constant of proportionality, L is known as Lorentz number (factor) and is given by:

$$L = \frac{\pi^2}{3}\left(\frac{K_B}{e}\right)^2 = 2.45 \times 10^{-8}\ W\Omega K^{-2} \qquad 2.28$$

The Wiedemann-Franz law exposes the impediment for a TE material to achieve high temperature efficiency by simultaneously increasing σ and decreasing k_E. An attempt to suppress k_E affects the electrical conductivity, leading to low ZT. Therefore, TE materials with k_L dominated are desirable since the σ will be preserved while k can be reduced through other techniques. The lattice contribution to the total thermal conductivity is given by a classical kinetic theory as [16], [27]:

$$K_L = \frac{C_V l\, V_s}{3} \qquad 2.29$$

where C is the specific heat capacity, l is the mean free path of the phonons and V_g is the group velocity of the phonons. Equation 2.29 shows that not only k_L depends on the electronic structure of the material. For a low k to be obtained, low C, short l and a low V_g are required [27].

Heat capacity (C) is a measure of the ability of a material to absorb thermal energy. It is represented as the ratio of heat added (dQ) or removed from a material or system relative to a change in temperature, dT (equation 2.30).

$$C = \frac{dQ}{dT} \tag{2.30}$$

From Debye theory, heat capacity has a weak temperature dependence above Debye temperature (θ_D) (at high temperature) [54]. At θ_D, the highest normal mode of vibration of the material is achieved [54], above which the vibrational modes of the material are occupied and heat capacity approaches the Dulong-Petit limit [27].

Mean free path (MFP) of the phonons is the average distance through which phonons travel between two scattering centres [27]. An introduction of scattering centres (defects) into the lattice can modify the thermal conductivity of a material. These lattice defects (vacancies, substitutions, dopings, etc.) shorten the MFP, cause a decrease in k and consequently improve the ZT of TE materials [27], [55]. It has been observed that at high temperature ($T > \sim 300$ K), V_g and C are temperature independent in typical materials [28], thus only MFP of phonons determine the size and temperature-dependence of k_L. Three basic approaches required to reduce k_L without lowering σ involve introduction of point defects (rattling structures) [56]–[59], designing of complex structures with the intention of scattering phonons without disrupting electron transport [60]–[69], and creation of nanostructures to decrease MFP of phonons [27]. These approaches give rise to 2D structures (superlattices), 1D structures (nanowires), 0D structures or quantum dots and thin film materials [24], [70]–[76].

2.4 Classification of Thermoelectric Materials

Thermoelectric materials are classified into two; conventional (non-oxide) and novel (oxide) thermoelectrics [77].

2.4.1 Conventional Thermoelectric Materials (CTMs)

CTMs basically composed of Bi_2Te_3/Se_3, Sb_2Te_3, PbTe/Se, SiGe, etc. and their corresponding alloys [78]. Conventional thermoelectric materials were first investigated and identified in the 1950s [77]–[81] for commercial and practical applications in TE power generation with attendant high ZT [13], [51]. Due to the their framework structures with large voids filled with heavy elements in most CTMs, they possess low phonon group velocity and thus low k which are desirable for optimised ZT [27]. The broad application of these materials is limited, however, due to toxicity, scarcity, cost, and limited operational temperature range [13]. Non-oxide thermoelectric materials (CTMs) are grouped into three based on operational temperature ranges; low temperature, intermediate temperature and high temperature CTMs [3], [13], [45].

2.4.1.1 Low Temperature (≤ 500 K) CTMs

This class of non-oxide thermoelectrics is primarily based on bismuth (Bi) combined with antimony (Sb), tellurium (Te) or selenium (Se) e.g. Bi_2Te_3, Sb_2Te_3. These alloys are the most widely used TE alloys. Bi_2Te_3 and its alloys e.g p-type $Bi_xSb_{2-x}Te_3$, n-type $Bi_2Te_{1-x}Se$ possess high ZT (≥ 1) at near-room temperature up to 500 K applicable in TE refrigeration and power generation [35], [45], [79], [82]–[84].

2.4.1.2 Intermediate or Mid Temperature (500-900 K) CTMs

They are non-oxide alloys mainly based on group IV tellurides, e.g. PbTe, GeTe, SnTe and $AgSbTe_2$ [35], [82], [84]–[86]. ZT values of ~ 1 have been reported for p-type $PbTe_{1-x}Se_x$ and n-type $Pb_{1-x}Sn_xTe$ (PbTe alloys) with a corresponding reduction in k at 300 K [87], [88]. Current reports on p-type $PbTe_{1-x}Se_x$ show a high

ZT ≥ 2 with optimised PF and reduced k_L [5], [47], [89], [90]. $AgSbTe_2$ alloys such as $(AgSbTe_2)_{1-x}(GeTe)_x$ have shown ZT values of > 1 for n-type and p-type materials, respectively [25], [35], [45], [91].

2.4.1.3 High Temperature (> 900 K) CTMs

High temperature CTMs are fabricated typically using silicon-germanium (SiGe) alloys as the thermoelements of TE power generating devices. The ZT of these materials are still low particularly the p-types despite their high operational temperature. This is attributed in part to its diamond structure (SiGe alloys) with high k_L [45]. Reports have shown a ZT values of ~ 1 and ~ 0.6 for n-type and p-type $Si_{0.8}Ge_{0.2}$, respectively[47], [92]. A further improvement on the material ($Si_{0.8}Ge_{0.2}$) by the application of nano-structuring techniques has optimised the n-type ZT to 1.3 [74] and the p-type to 0.9 – 1.0 [75]. The graph showing the ZT variations of selected conventional thermoelectric materials (CTMs) with their corresponding operational temperatures is represented in Figure 2.9 [93].

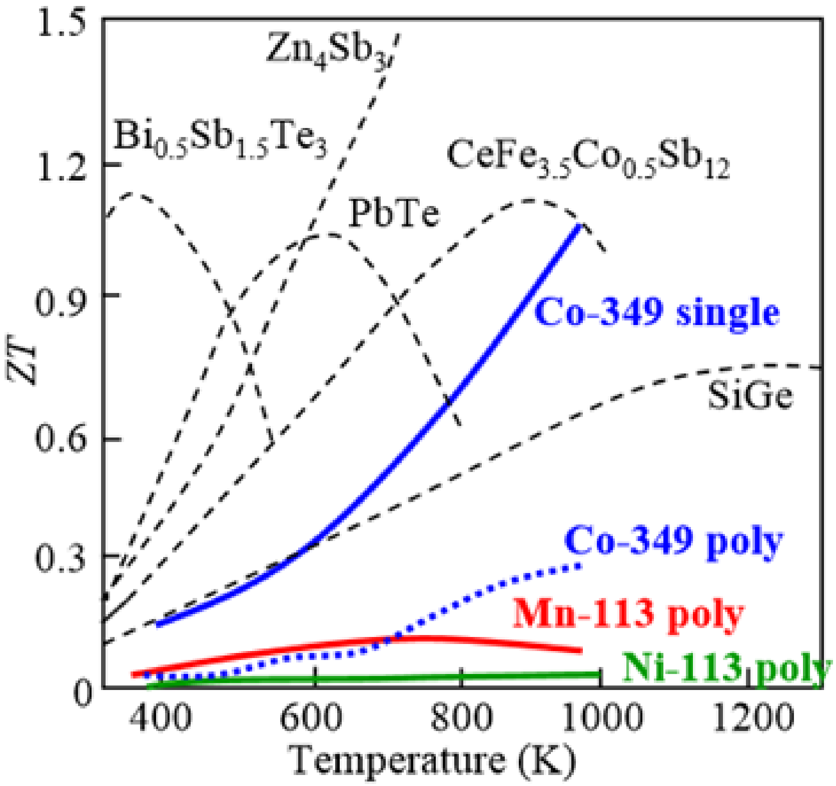

Figure 2.9. Thermoelectric figure of merit (ZT) as a function of temperature (K) for selected conventional thermoelectric materials (CTMs) [93].

2.4.2 Novel Thermoelectric Materials (NTMs)

According to Ioffe's theory, oxides are unsuitable for TE applications due to their strong, mixed ionic and covalent bonds, possession of high k_L and lower carrier mobilities resulting in low electrical conductivity [94]. However, there is strong evidence that oxide thermoelectrics containing transition-metal oxides are novel alternative materials to the current intermetallic (conventional) TE materials. Generally, oxides are inert, non-toxic, light weight, cheap, possess small thermal expansion with high melting point, hence promising TE candidates for high temperature applications [93], [95], [96].

Novel thermoelectric materials are expected to exhibit increased ZT and large PF compared to CTMs. Principal NTMs include p-type $Na_xCo_2O_4$ [comparable to $(Bi, Sb)_2(Te, Se)_3$] and n-type rare-earth (RE) doped $SrTiO_3$ based compositions that have been reduced in N_2/5 % H_2 gas mixtures [96]. The recognition of NTMs as potential TE materials particularly p-type oxides was in 1997 when Terasaki *et al* [96]–[98] in their study showed that layered cobalt oxide, $Na_xCo_2O_4$ exhibited a high electrical conductivity ($\sigma \approx 500$ S/m) and a large Seebeck coefficient ($S \approx 100$ µV/K). This landmark opened the window for further investigations of other oxides for TE applications.

In terms of crystal structure, transition metal-oxides for TE applications are classified into wide-band-gap semiconductor, perovskite-based, layered cobalt oxides and oxychalcogenides [97] and recently oxides with adaptive structures [27] . A brief understanding of structures and properties of some of these promising classes of TE oxides will be reviewed.

2.4.2.1 Na_xCoO_2 ($NaCo_2O_4$)

The short MFP associated with layered structured materials due to phonon scattering at the interfaces between the layers result in low k, hence better candidates for TE applications. Therefore, there is a prospect for layered-structure cobalt oxides as TE materials. Prime p-type oxides for thermoelectric applications are alkaline based layered cobalt oxides [53], [99]–[101]. They are found to exhibit large Seebeck coefficients due to low spin state of Co^{3+} [99], [102]. These layered cobaltites derive a path for conduction due to the presence of CoO_2 planes while the interconnected points or interfaces between the layers and other parts of the structure inhibit heat flow via lattice phonons. Prominent amongst these layered cobaltites are $Ca_3Co_4O_9$ [99], [100], [103]–[108], and Na_xCoO_2 [53], [109]–[112].

The crystal structure of Na_xCoO_2 is a hexagonal layered structure with an alternating stack of Na^+ ions and sheets of CoO_2 along the c-axis (Figure 2.10) [97]. The CoO_2 sheets serve as electronic crystal thereby maintaining high electrical conductivity while the Na^+ ion blocks function as phonon scattering boundaries resulting in low k [97] . Due to the phonon glass-electron crystal (PGEC) behaviour of Na_xCoO_2, its structure type is known as nano-block integration [97]. The large Seebeck coefficients at high temperatures associated with Na_xCoO_2 and other layered cobalt oxides due to the low spin state of Co^{3+} and Co^{4+} are as a result of the CoO_2 sheets in the structure [102], [113].

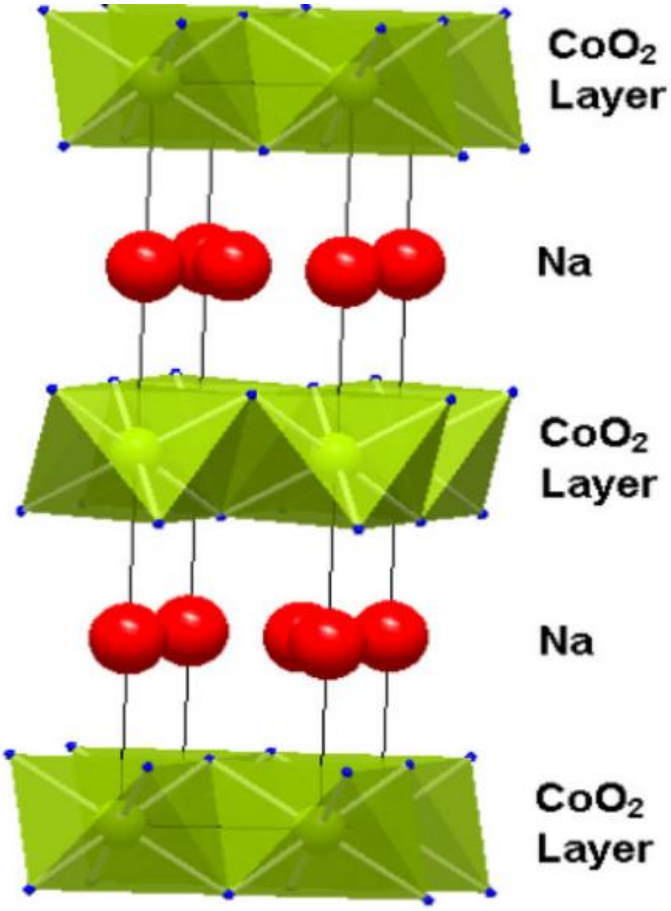

Figure 2.10. Hexagonal crystal structure of Na_xCoO_2 layered cobalt oxide [97].

Single crystal Na_xCoO_2 shows a thermal conductivity between 4 and 5 W/m.K at 300 K with large Seebeck coefficient (100 µV/K), low resistivity (200 µΩcm) and a resulting PF value of 50 µW/K^2.cm [96], [97], [114], [115]. A high ZT ≈ 1 at 800 K has been reported for a single crystal Na_xCoO_2 sample with a high PF and a low thermal conductivity [97], [99]. Unlike single crystal Na_xCoO_2, the polycrystalline ceramic Na_xCoO_2 shows a high resistivity which results in ZT = 0.8 at 1000 K [116]–[118]. It is observed that at high temperatures, Na_xCoO_2 becomes unstable because it tends to absorb moisture in air (a situation known as hygroscopy) while the constituent Na vaporises (degrades) at above 800 ^{o}C. This, therefore, limits the TE application of Na_xCoO_2 at elevated temperatures. This drawback notwithstanding, the huge success recorded in TE study of Na_xCoO_2 has led to the exploitation of other layered cobalt oxides such as $Ca_3Co_4O_9$ and $Bi_2Sr_2Co_2O_9$. The crystal structure of $Ca_3Co_4O_9$ is similar to Na_xCoO_2 except that its CoO_2 planes are separated with layers of a distorted rock-like structure (CaO) as shown in Figure 2.11. ZT values of 1.2 to 2.9 at 873 K [64] and ZT ≥ 1.1 at 1000 K [66] have been reported for $Ca_3Co_4O_9$ single crystals and $Bi_2Sr_2Co_2O_9$ whiskers , respectively.

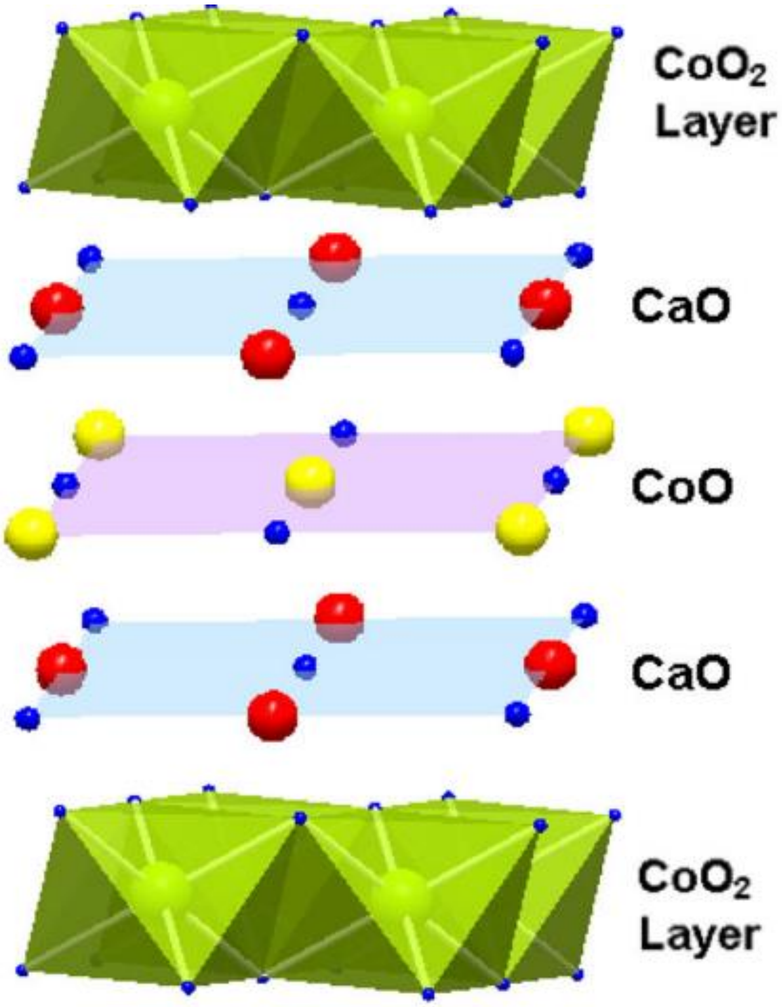

Figure 2.11. Crystal structure of layered $Ca_3Co_4O_9$ oxide [97] .

2.4.2.2 ZnO

Zinc (II) oxide (ZnO) is a wide band gap semiconductor and a promising candidate for TE applications. It is also known as a transparent conducting oxide, TCO [119] with a wurtzite crystal structure belonging to a hexagonal system [120]. In the hexagonal lattice of ZnO (Figure 2.12), each Zn ion is surrounded by four O^{2-} ions in a tetrahedral configuration to form ZnO_4 groups. It possesses a wide band gap of 3.44 eV at low temperature [121], [122]. Stoichiometric ZnO is an intrinsic semiconductor (insulator) but exhibits n-type conductivity due to excess Zn atoms [120].

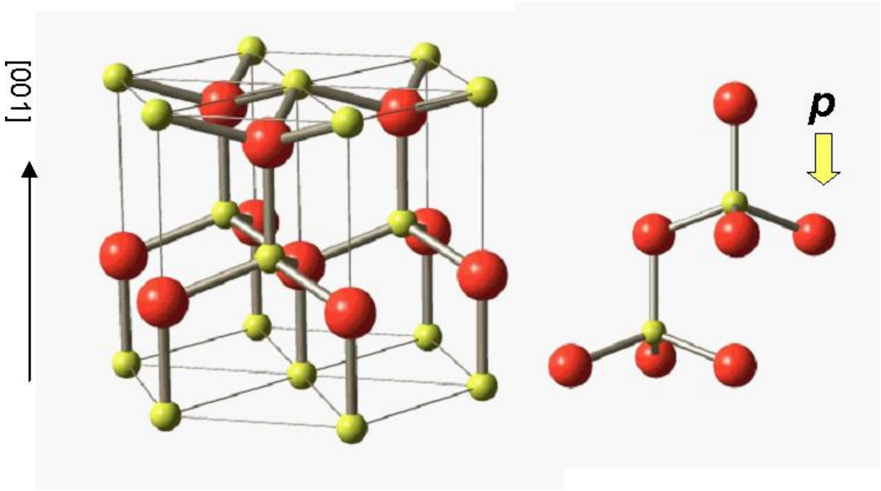

Figure 2.12. Crystal structure (Wurtzite) of ZnO [120]. Zn^{2+} ions are in red and O^{2-} in yellow.

The strategy to enhance the TE efficiency of zinc (II) oxide lies in the reduction of the Zn-O ionic bonds to increase the carrier mobility. A single crystal ZnO and Al-doped ZnO samples were found to possess a carrier mobility of ~ 200 cm^2/Vs and 80 cm^2/Vs, respectively at room temperature [123]. A study of $ZnO_{0.98}Al_{0.02}O$ thin films showed a ZT ~ 0.3 at 1273 K with a PF of 1.5 x 10^{-3} W/m. K^2 [119], [124]. An improved ZT (0.4) at 773 K [125] was obtained in Al-doped ZnO using nanoparticles of carbon or organic polymer (void forming agent). The enhancement of the TE performance of the Al-doped ZnO is attributed to the compression of the c/a lattice ratio of crystal due to the Al doping [126].

Co-doping has been identified as an effective mechanism in the promotion of TE performance of ZnO. A reported research has shown ZT = 0.47 and 0.65 at 1000 and 1273 K, respectively for an Al-Ga dual doped ZnO ($Zn_{0.96}Al_{0.02}Ga_{0.02}O$) [127]. As stated in the introductory part of this work, these ZT values (0.47 and 0.65) so far remain the highest reported ZT values for bulk n-type oxides.

ZnO possesses a very high thermal conductivity when compared to other thermoelectric oxides. It has k = 54 W/m.K for single crystals [124] and k = 40 W/m.K for polycrystalline samples [123] at room temperature. Therefore, the effective means of reducing this high thermal conductivity without compromising the power factor, PF is a fundamental research challenge.

2.4.2.3 BiCuSeO

BiCuSeO is a potential p-type TE material, and the oxide with highest known ZT [128]. It is a non-toxic quaternary oxychalcogenide with a tetragonal crystal structure (space group P4/nmm) [129], [130]. The crystal structure is composed of alternately stacked layers of insulating oxide $(Bi_2O_2)^{2+}$ and the conductive selenide $(CuSe_2)^{2-}$ [18], [128], [130] as shown in Figure 2.13 [130] . The layered crystal structure enhances phonon scattering at the interface (leading to low k), exhibits weak bonding, and contains heavy elements [101], [128]. BiCuSeO possesses k of 0.4 – 0.5 W/m.K at 900 K [128], [129], [131] and $k \leq 1$ at room temperature [128], [132], [133].

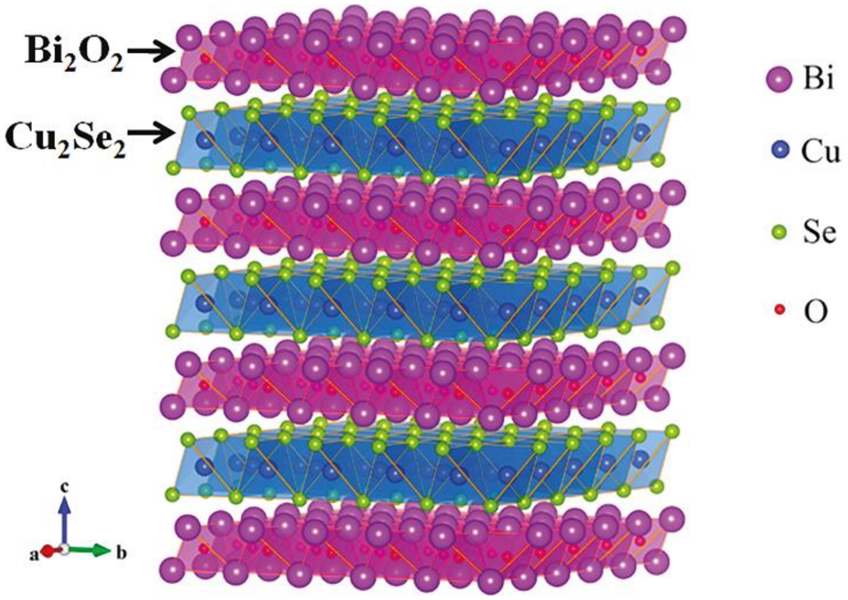

Figure 2.13. Tetragonal crystal structure of BiCuSeO (space group P4/nmm) [130].

Research has shown that BiCuSeO has a good TE properties with $\sigma \geq 4000$ S/m, $S \geq 200$ µV/K and k = 0.5 W/m. K with a ZT = 0.7 at 773 K [101] [128] [130], [132]. A high ZT (0.76) has been reported in BiCuSeO in which the Sr^{2+} is substituted for Bi^{3+} in $(Bi_2O_2)^{2+}$ layer [131]. Liu *et al* [130] enhanced the TE of BiCuSeO properties by introducing Cu deficiencies or holes into the $(CuSe_2)^{2-}$ selenide layers. In this study, Cu deficient $BiCu_{0.975}SeO$ gave an $\sigma = 3000$ S/m, S = 273 µV/K, k = 0.5 W/m. K and a high ZT = 0.81 at 923 K. A further study was reported for a heavily Ba-doped BiCuSeO ($Bi_{1-x}Ba_xCuSeO$) [101], [134] in which a ZT ~ 1.1 at 923 K was obtained. Finally the authors of refs [135]–[138] achieved a ZT ≈ 1.4 at 923 K which remains to date the highest reported for p-type TE oxides.

2.4.2.4 $SrTiO_3$

Strontium titanate, $SrTiO_3$ (STO) is the n = 1 end member of the Ruddlesden-Popper (RP) phases with formula $SrO_{n-1}(SrTiO_3)_n$ (n = integer) and particularly when doped with Nb has received considerable attention as a thermoelectric n-type oxide [139]. Bhattacharya *et al* [49] highlighted notable transport properties of $SrTiO_3$ to include quantum paraelectricity, induced ferroelectricity, superconductivity, correlation between superconductivity and ferromagnetism, piezoelectricity, photo-catalytic activity, and thermoelectricity. Moreover, strontium titanate was the first discovered superconducting ternary oxide [140]. It is a non-toxic, chemically stable in air with a high melting temperature (2080 ^oC) thereby making it a promising candidate for TE applications at high temperatures [139].

Doped $SrTiO_3$ Ceramics

Doped and/or reduced $SrTiO_3$ ceramic materials have recently shown increased conductivity sufficient for thermoelectric applications [140]. Upon doping either at A-site or B-site and/or creation of oxygen vacancies, $SrTiO_3$ undergoes a transformation to semiconductor [49] producing n-type carriers and if sufficient O is removed it becomes metallic in character. Doped and oxygen deficient strontium titanate ($SrTiO_{3-\delta}$) has been reported to exhibit Seebeck coefficients ($|S| \sim 200 - 300\ \mu V/K$), low resistivity ($\rho < 5\ \mu\Omega/cm$) at 750 K due to the carrier electrons possessing high effective mass, m* of (~ 6-10)m_e attributed to its d-band nature and significant high PF ~ 0.8 – 1.3 W/m. K^2 [49], [139], [141]. For example, n-type La-doped $SrTiO_3$ single crystals are reported to have high PF of 3.6 x 10^{-3} W/m. K^2 at room temperature attributed to high carrier concentration, comparable to Bi-Te alloys [101]. However, at 773 K, a decrease in ZT (0.15) occurs in the doped $SrTiO_3$ single crystals because of its inherent high thermal conductivity [142]–[145]. The high thermal conductivity in $SrTiO_3$ and other oxides emanates from the contribution of the lattice thermal conductivity (k_L). $SrTiO_3$ and other related oxides are also susceptible to oxygen uptake (reoxidation) in air when reduced and oxygen-loss in reducing atmospheres at high temperatures [146]. Nonetheless, promising n-type thermoelectric properties have been reported in $SrTiO_3$ doped with Nb, W, La, Ce, Pr, Nd, Sm, Gd, Dy and Yb [27].

There is great interest in developing n-type $SrTiO_3$ despite its low TE properties when compared to state-of-the-art non-oxides [49], [145], [147], [148]. Doped $SrTiO_3$ exhibits high carrier mobility and large effective mass due to its d-band structure [27] thereby causing the observed high electrical conductivity and Seebeck coefficient. Despite the reported high S, high σ and large PF, the ZT remains low due to its high k compared with non-oxide TE materials [148]. It has been widely studied in terms of different dopants, doping mechanisms, and processing conditions [149]. ZT value of 0.27 at 1073 K was obtained in the study of La- and Nb-doped $SrTiO_3$ single crystals [144]. $Sr_{1-x}La_xTiO_3$ ($0 \leq x \leq 0.1$) single crystals were studied by Okuda *et al* [143] and a large PF of 3600 $\mu W/m.\ K^2$ was observed at room temperature. Improved TE properties (k ~ 3 W/m. K, ZT = 0.37) at 1000 K have been reported in an epitaxial Nb-doped strontium titanate ($SrTi_{0.8}Nb_{0.2}O_3$) films [142], [150]. Kovalevsky *et al* [151] studied RE-doped $Sr_{0.9}R_{0.1}TiO_{3-\delta}$ (R = Dy, Sm, Nd) ceramics in reduced atmosphere and obtained an optimised ZT of 0.42 at 1190-1225 K. Recently, Lu *et al* obtained a similar result with a ZT = 0.41 at 973 K from their La-doped, A-site deficient strontium titanate sample ($Sr_{1-3x/2}La_xTiO_3$; x = 0.15) processed in 5% H_2/N_2 reduced atmosphere [135], [152].

Co-doping has been suggested to enhance thermoelectric properties of $SrTiO_3$ ceramics. La-doped and Dy-doped $SrTiO_3$ ceramics ($La_{0.1}Sr_{0.9}TiO_3$ and $Dy_{0.1}Sr_{0.9}TiO_3$) showed maximum ZTs of 0.17 at 673 K (k ~ 3.4 W/m.K, 1073 K) and 0.22 at 573 K (k ~ 2.2 W/m.K), respectively [153], [154]. Co doping with La and Dy ($La_{0.1}Sr_{0.83}Dy_{0.07}TiO_3$) [147], [155] resulted in a reduced k (2.5 W/m.K) and a high ZT = 0.36 at 1045 K. Enhanced thermoelectric properties have been reported for La-Nb doped $SrTiO_3$ ceramics. Wang *et al* [156] in the study of La-Nb co-doped $SrTiO_3$ obtained a significant improved power factor and Seebeck coefficient when compared to La-doped $SrTiO_3$ which is attributed to energy filtering effect of grain boundaries. An increase in electrical conductivity is observed in the study of Nb-doped $La_{0.05}Sr_{0.95}TiO_3$ [142]. Overall, the improvement of the PF and ZT is significant because σ is not much enhanced while Seebeck coefficient is reduced. Muta *et al* [157] investigated the effect of Ba-La co-doping on $SrTiO_3$ ($Ba_{0.9-x}Sr_xLa_{0.1}TiO_3$) and observed an improved PF due to a shorter Ti-Ti distance and a change in lattice parameter according to Vegard's law. Though the ZT obtained is not high (3 x 10^{-4} K^{-1}), further reduction of thermal conductivity and Ti-Ti distance is advocated.

Liu *et al* [148] in their investigation on the TE properties of RE-doped $SrTiO_3$ ceramics suggested that $SrTiO_3$ doped with large RE ions (e.g. La, Nd) exhibit large PF [148], while those doped with mid-sized or small RE ions (Sm, Gd, Dy, Er, Yb) show low thermal conductivity without disrupting the electrical properties [140], [148]. The excess positive charge from the RE ions (normally doped at A-site) is balanced with Sr vacancies in oxidising conditions while some of the Ti^{4+} ions are reduced to Ti^{3+} ions in reducing conditions [140].

A study of La-Dy co-doped Sr-deficient $SrTiO_3$ ceramics strongly upholds the potency of dual doping and Sr vacancies in improving the efficiency of ceramics. $La_{0.1}Dy_xSr_{1-1.25(0.1+x)}TiO_3$ (x = 0, 0.05, 0.075, 0.1) ceramics were prepared using sol-gel method and sintered in 5% H_2-95% N_2 reducing gas [154]. Increase in carrier concentration due to the La-Dy co-doping improved the electrical conductivity. Sr vacancies and the generated second phase ($Dy_2Ti_2O_7$) led to promotion of phonon scattering and decrease in total thermal conductivity (k). A very low k (1.92 W/m.K at 773 K) and improved ZT = 0.29 at 773 K were obtained in x = 0.1 ceramics [154]. Although the ZT of doped $SrTiO_3$ is less than one which is attributed to its large thermal conductivity, La-Nb co-doped $SrTiO_3$ ceramics have shown to be one of the best n-type oxide thermoelectric materials (Figure 2.14). Recently, a ZT ≥ 0.6 at 1000 – 1100 K for 10 mol% La and 10 mol% Nb (La10Nb10) co-doped bulk $SrTiO_3$ ceramics has been reported [158] which remains the highest value for bulk $SrTiO_3$ to date.

Co-doping of $SrTiO_3$ involving other transition elements (e.g. V, Ta, W, etc.) for thermoelectric applications are also reported in the literature. The effect of vanadium (V) co-doping of Nb-$SrTiO_3$ was investigated by full-potential density functional theory [159]. The results indicate that Nb and V concentrations linearly increased the carrier density, hence a potential tool for improving the ZT. Wang *et al* [160] studied the thermoelectric performance of $Sr_{0.9}La_{0.1}Ti_{1-x}Ta_xO_3$; $0.0 \leq x \leq 0.05$, synthesised by conventional solid state reaction method. Substitution with Ta decreased the power factor due to reduction in Seebeck coefficient. Although the thermal conductivity was reduced, resulting in a minimal value of 2.9 W/m.K at 1074 K for x = 0.03, the overall thermoelectric performance is reduced with Ta doping. The highest ZT (0.29) at 1046 K is observed in $Sr_{0.9}La_{0.1}TiO_3$ Ta-free ceramic. In another development, the thermoelectric properties of W-Nb co-doped $SrTiO_3$ ceramics were investigated [161]. Reduction in k and relative high Seebeck coefficient were observed due to carrier scattering, leading to a maximum ZT value of 0.28 at 1270 K for $Sr_{0.97}Ti_{0.8}Nb_{0.17}W_{0.03}O_{3\pm\delta}$.

Generally, Sintering conditions also play important role in the improved electronic properties of doped or co-doped $SrTiO_3$ ceramics. Sintering in reducing atmosphere such as N_2/H_2 gas at high temperature improves the electrical conductivity [162] but this is at the expense of a decrease in S and an increase in k [49], [139]. To make radical breakthrough in ZT, reducing the high k without altering the electronic transport properties is required.

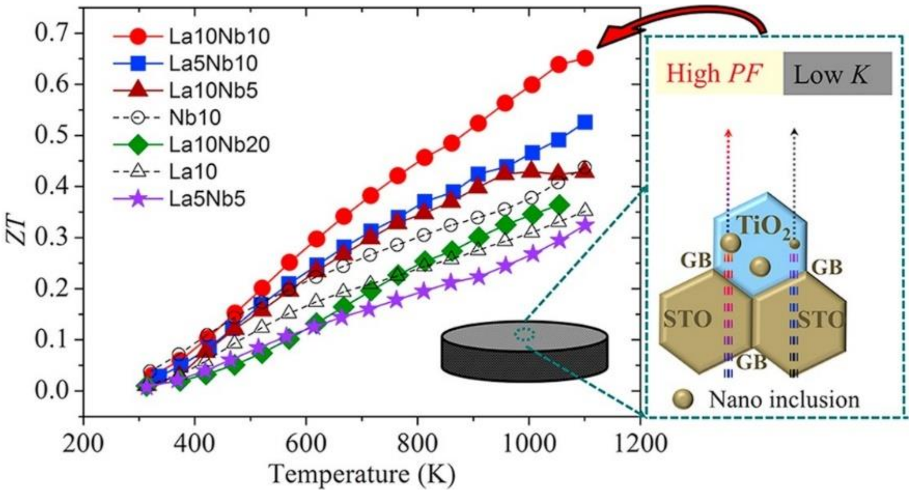

Figure 2.14. Temperature dependence of figure of merit (ZT) values for La, Nb and La-Nb co-doped $SrTiO_3$ ceramics. [158]. The values (5, 10 and 20) attached to La and Nb indicate the mol% of the dopant elements in $SrTiO_3$.

Doped $SrTiO_3$ with Graphene Derivatives or Metallic Inclusions

Apart from A and/or B-site doping, co-doping, ionic doping mechanism (A/B-site cation vacancy), generation of oxygen vacancies and processing under reducing conditions, incorporation of graphene or graphene oxide (GO), metallic elements or creation of second phases have been suggested as potential routes in improving the thermoelectric properties of doped $SrTiO_3$ based ceramics.

Improvement in TE performance due to addition of graphene have been observed in conventional materials (non-oxides) [163], [164], organic (polymeric) materials [165]–[168] and RE-doped $SrTiO_3$ ceramics [169], [170]. In the study by Lin *et al* [169], incorporation of small amount of graphene into La-doped $SrTiO_3$ (LSTO) composites and sintered in Ar/H_2 reducing gas produced final materials with multiphase structures and nano grains. As a result of the reduced thermal conductivity and improved power factor, the highest ZT (0.36 at 1023 K) was achieved by adding 0.6 wt % graphene, which is adjudged to be over 280 % higher when compared to pure LSTO. Recently, TE performance of Nb-doped $SrTiO_3$ (STN) ceramics mixed with 0.6 wt % graphene oxide (GO), prepared by Humer-based method and sintered in 10 % H_2 - 90 % /N_2 high reducing gas mixture was investigated [171]. The study shows that Sr deficiency with GO addition results in a high power factor (~ 1.98 mW/K^2m) at 332 K and a maximum ZT (0.29 at 1160 K) for Sr-deficient, 10 wt % Nb-doped $SrTiO_3$ (nSTN10 + rGO) as shown in Figure 2.15. ZT progressed from 0.17 at 1160 K for stoichiometric STN10 ceramics without GO to 0.24 at 1160 K when GO was added without Sr deficiency (STN10 + rGO) to 0.29 at 1160 K when GO and Sr deficiency were created (nSTN10 + rGO).

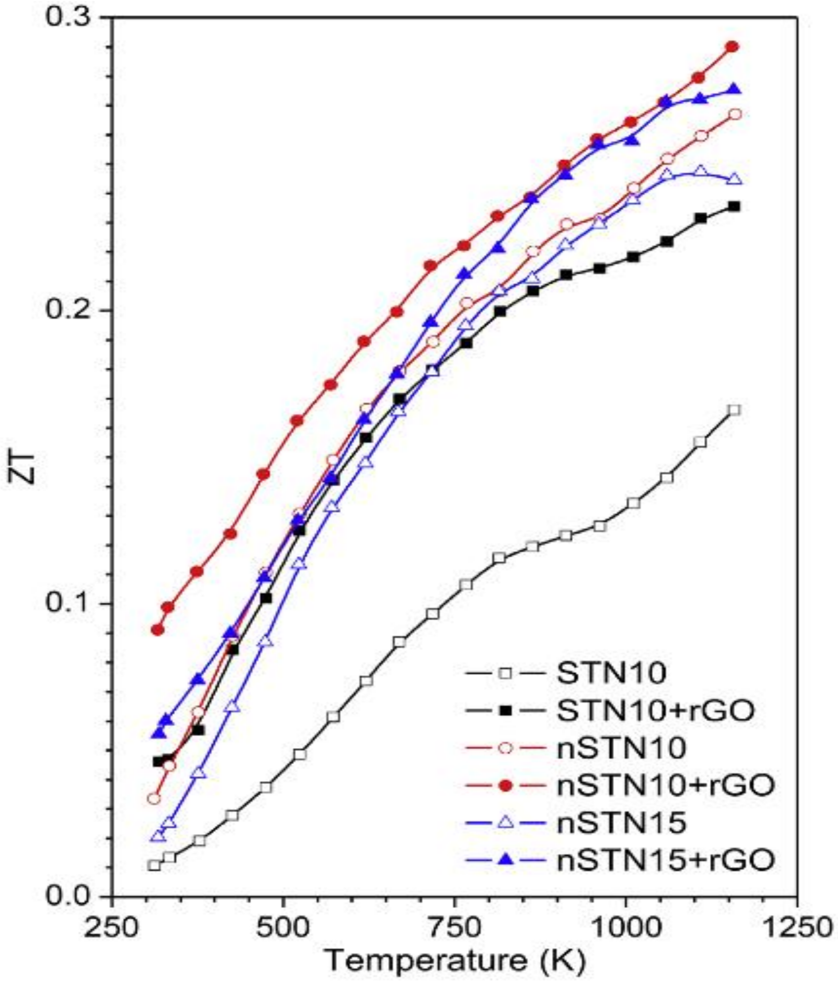

Figure 2.15. Temperature dependence of figure of merit, ZT of stoichiometric STNx and Niobium doped with 2% Sr deficient nSTNx ceramics sintered in 10% H_2/90% N_2 gas with Nb content x = 10 and 15% and their composites with rGO[171]. r implies addition of GO in reduced atmosphere.

Thermoelectric properties of $Sr_{0.9}La_{0.1}TiO_3$ ceramics with silver (Ag) metallic inclusions up to 15 %, prepared by hydrothermal method have been investigated [172], [173]. In these different but similar studies, increased electrical conductivity, enhanced Seebeck coefficient and reduced thermal conductivity, leading to improved figure of merit, ZT are observed. The decrease in thermal conductivity is attributed to an increased phonon scattering centres emanating from the precipitated second phase grain boundaries. Similarly, Qin *et al* [174] prepared $Sr_{0.9}La_{0.1}TiO_3$/xAg compound (x = 5 wt. %, 10 wt. %, 15 wt. %, 20 wt. %) via conventional solid state reaction method and sintered in Ar reducing atmosphere. The results revealed that addition of Ag increased the carrier concentration and accumulated at the grain boundaries (Figure 2.16), forming a complex percolating network. The network acts as electrical connections between the grains, leading to an increase in electrical conductivity, a decrease in thermal conductivity (1.4 – 3.4 W/m.K) and a maximum ZT value of 0.30 at 883 K for x = 20 wt% composition. The k (1.4 – 3.4 W/m.K) value obtained in the study is smaller than the k (3.0 – 9.5 W/m.K) observed in $Sr_{0.9}La_{0.1}TiO_3$/xAg composites synthesized via hydrothermal method [173] and that for pure $Sr_{0.9}La_{0.1}TiO_3$ (3.5 – 6.0 W/m.K) [174].

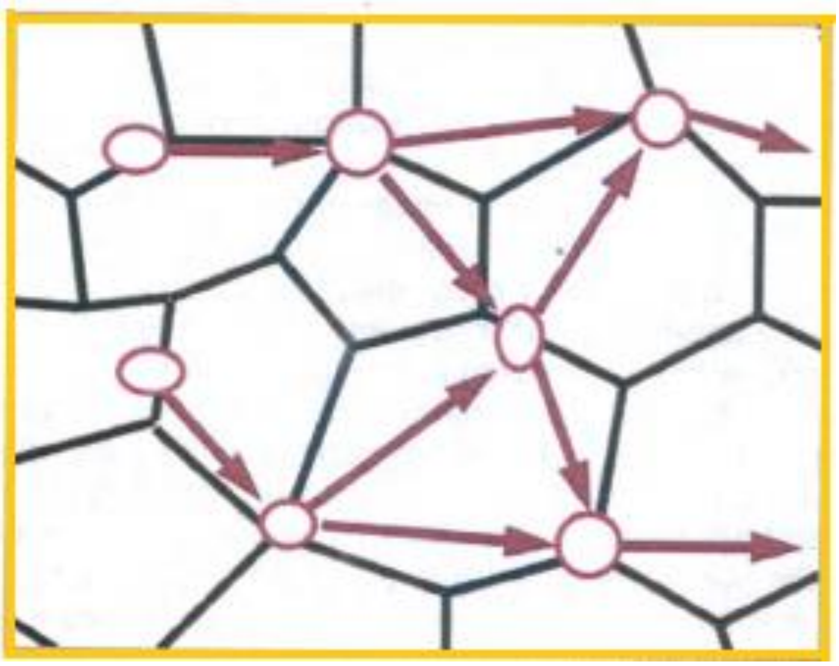

Figure 2.16. the schematic diagram of the complex percolating network formed by the accumulated Ag additive at the grain boundaries [174]. The network acts electrical connections between grains, causing an increase in electrical conductivity.

The limitation of Ag as a metallic additive in some materials have been reported in the literature [175], [176]. Diffusion along grain boundaries and consequent degradation of properties are seen in $Bi_{1/2}Na_{1/2}O_3$ ceramics when Ag is utilized as an electrode [175]. The low melting point (1235 K) of Ag is considered to propagate diffusion especially during sintering , thereby hindering microstructural control [176]. In attempt to overcome the challenges associated with the use of Ag metallic additive and improve the thermoelectric performance, $Sr_{0.8}La_{0.067}Ti_{0.8}Nb_{0.2}O_{3-\delta}$ containing Cu or Fe inclusions were investigated under reducing conditions [176]. The high melting points of Cu (1358 K) and Fe (1811 K) are considered advantageous in restricting diffusion, thereby paving way for microstructural control. The Cu and Fe metallic inclusions therefore increased the carrier concentration and carrier mobility resulting in an increase in σ and PF up to 75 % [176]. A progressive increase in ZT from 0.25 at 1000 K for the control sample (composition without metallic inclusion), to ZT of 0.36 at 900 K for Cu-containing composition and to an optimal ZT value of 0.38 at 1000 K for Fe-containing composition.

Thermoelectric properties of Ti-doped $Sr_{0.9}La_{0.1}TiO_3$ ceramics have been previously studied [177]. Titanium (Ti) as an electrically conductive, and chemical stable transition metal is expected to improve the electrical properties of the La-doped $SrTiO_3$. The results showed that the titanium was oxidized to form TiO_2 during the initial heat treatment (calcination), hence unable to form a Ti-metal inclusion after sintering. Therefore, the TiO_2 secondary phase co-existed with the $Sr_{0.9}La_{0.1}TiO_3$ matrix in the sintered ceramics. The Seebeck coefficients increased from -163 (at 350 K) to -259 μV/K (at 1073 K) with a maximum ZT value of 0.144 at 1073 K for 5 wt% Ti-doping.

2.5 Structure of $SrTiO_3$

Pure $SrTiO_3$ (STO) crystallizes in an ideal cubic perovskite structure at room temperature with a lattice parameter, a ~ 3. 905 Å (space group = Pm-3m) and a wide band gap, E_g of ~ 3.2 eV [49], [178]. STO undergoes a phase transformation from cubic (Pm-3m) to tetragonal (I4/mcm) structure at a temperature below 105 K as a result of the rotation of the TiO_6 octahedra within the structure [49], [140], [179].

2.5.1 Crystal Structure of $SrTiO_3$

Perovskites are ternary compounds with the general formula ABX_3 where "A" and "B" are two different cations in equal ratio (with A > x2 the ionic radius of B) and "X" is an anion, which is usually oxygen (O). In an ideal cubic $SrTiO_3$ structure, "A" represents Sr^{2+} and "B" is the smaller Ti^{4+} ion. Sr^{2+} ions occupy the corner positions of the cube, while the Ti^{4+} ions occupy the centre with O^{2-} (X) anions located at the edge centres of the cubic unit cell [180]. The schematic of cubic perovskite structure of $SrTiO_3$ is shown in Figure 2.17. As shown in the structure of $SrTiO_3$ (Figure 2.17), Sr^{2+} cations are arranged in cubo-octahedral coordination and are surrounded by twelve O^{2-} anions. The Ti^{4+} ions are surrounded by six O^{2-} anions which leads to the formation of TiO_6 octahedra. By the introduction of dopant into the lattice, distortions from cubic to lower symmetries (size incompatibility) may occur. The measure of stability (degree of distortion) within the structure of perovskite-type ABO_3 is defined by the Goldschmidt tolerance factor, t [180]–[183]:

$$t = \frac{r_A + r_O}{\sqrt{2(r_B + r_O)}} \qquad 2.31$$

where r_A, r_B and r_O are the ionic radii of atoms "A", "B" and oxygen, respectively. For an ideal cubic perovskite such as $SrTiO_3$, $t = 1$, $r_A = 1.44$ Å, $r_B = 0.605$ Å and $r_O = 1.40$ Å. Lower symmetries are adopted when $t < 1$ or $t > 1$ [180]. This deviation from $t = 1$ results in distortion from the ideal perovskite structure. For example, if the A ion is too small for the octahedral cage ($t < 1$) as dictated by the radius of the "B" ion, tilting occurs with the intent to fill the unused space, thereby lowering the symmetry of the crystal structure [184]. For compounds with very low values of t, an orthorhombic perovskite structure is formed, e.g. $CaZrO_3$ (t = 0.914). When t >1, tetragonal ($BaTiO_3$, t = 1.062) distortions occur or the ABC close packed stacking sequence is altered to create a family of hexagonal perovskite structures, such as $BaMnO_3$ and $BaNiO_3$ (t = 1.13). These distortions often occur due to doping or through the formation of solid solutions and can be used to tune properties of interest.

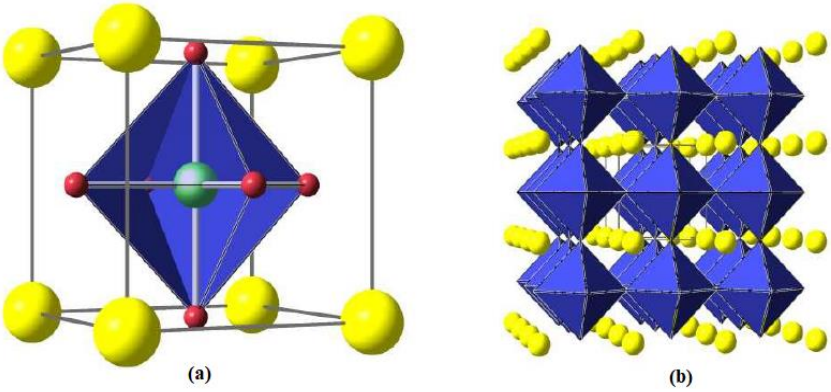

Figure 2.17. Crystal structure of cubic perovskite $SrTiO_3$ at room temperature showing the (a) octahedral coordination of Ti^{4+} cation and (b) corner sharing array of TiO_6 octahedra [180]. Sr^{2+} ions are in yellow, Ti^{4+} ions in green and O^{2-} ions in red.

2.5.2 Electronic structure of $SrTiO_3$

The Ti^{4+} ion in $SrTiO_3$ is a typical transition metal oxide having a d^0 electron configuration. Donor doping of $SrTiO_3$ is thought to partially fill its conduction band with electrons which results in a transition from d^0 state to d^1 electron configuration (Ti^{3+}) thereby increasing the carrier concentration of the lattice. Undoped $SrTiO_3$ is a band insulator at room temperature with a large band gap (3.2 eV) separating the valence from the conduction band [185]. Due to the six-fold coordination of Ti^{4+} ions by O^{2-} anions, octahedral field splitting of Ti-3d states (five degenerate d-band) occurs [186], [187]. Figure 2.18 shows the schematic spatial (three-dimensional) distribution of the octahedral crystal field [186].

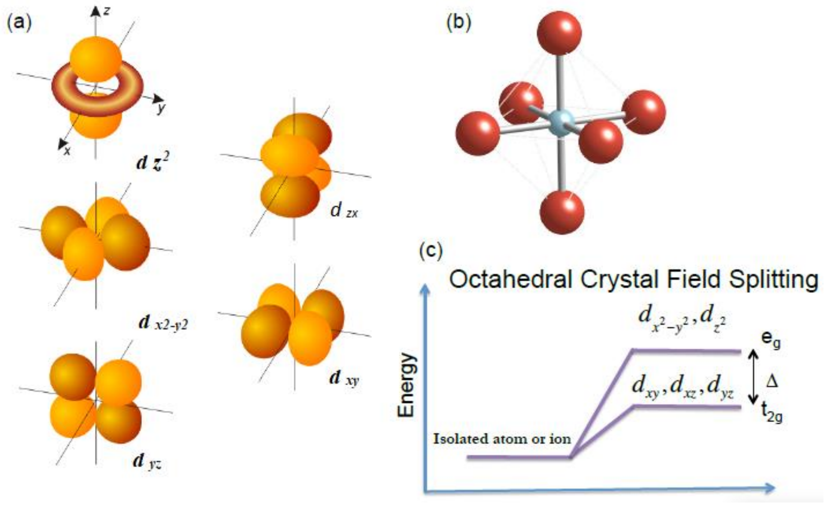

Figure 2.18. Diagrammatic representation of (a) spatial distribution of d-orbitals (b) oxygen octahedral cage around Ti^{4+} (c) d-band energy splitting due to the octahedral crystal field [186].

Studies have shown that the large PF exhibited by $SrTiO_3$ which is comparable to the conventional TE materials is attributed to the large orbital degeneracy of the Ti – d conduction band [187]. From band theory, the valence band is formed by the oxygen 2s and 2p state and it corresponds to the highest occupied molecular orbitals. The conduction band originates from the Ti – d states (mainly Ti – 3d t_{2g}) and it corresponds to the lowest unoccupied molecular orbitals [187].

2.6 Oxides with Adaptive Structures

Magneli phases have recently been explored as potential TE materials. In Ti oxides, they constitute an homologous series of reduced titanium oxides [27]. The oxygen deficiency in the homologous series such as Ti_nO_{2n-1} ($4 \leq n \leq 11$) leads to the formation of crystallographic shear (CS) planes [27], [188]. CS planes act as phonon scattering centres within the lattice which contribute to the decrease of thermal conductivity.

Tetragonal tungsten bronze (TTB) structure materials such as $Nb_{8-x}W_{9+x}O_{47}$ [189]–[192] and W-Nb-O alloy systems [193], [194] have been found to share similar structures with Magneli oxides. Na_xWO_3 was first reported in 1824 by Wöhler [195] but Magneli was the first to determine its structure using x-ray diffraction [196], [197]. Since this discovery, numerous compounds have been shown to crystallise with the TTB structure. The main elements or cations common in TTBs include alkali/alkali earth, rare earth, and transition metals [198], [199].

2.6.1 Tetragonal Tungsten Bronze (TTB) Oxides

Tetragonal tungsten bronze (TTB) oxide ceramics are the largest class of dielectrics after perovskites [197], [200], [201]. The TTB structure is a complex framework lattice with a distorted, corner-sharing oxygen-octahedra ($B1O_6$ and $B2O_6$) which forms three different interstices/tunnels or sites [197], [199], [200], [202], [203], [204]. These tunnels are square (also called perovskite), A1 with a coordination number of 12, pentagonal, A2 with 15-coordinated sites and trigonal/triangular (which is the smallest channel) C containing 9-coordinated sites. A typical TTB structure is represented with the general formula:

$$[A1_2A2_4C_4][B1_2B2_8]O_{30} \tag{2.32}$$

Generally, the A1 and A2 sites are occupied by metal cations of alkali/alkaline earth elements, p-block elements (e.g. Pb, Bi) or RE elements. C-sites are narrow and can be empty in most TTB compounds or occupied by small cations like Li^+. B octahedra sites are often occupied by Ti^{4+}, Nb^{5+} and Ta^{5+}. Because of the capacity to accommodate large cations and possession of great flexibility (or degrees offreedom) for tuning the chemical composition, the TTB family shows excellent properties for diverse applications [197], [202], [203]. These include electro-optic, pyroelectric, piezoelectric, semiconductivity (and metallic conductivity), superconductivity and high permittivity. A prototype TTB crystal structure showing the sites and the corner-sharing oxygen octahedra is presented in Figure 2.19 [200].

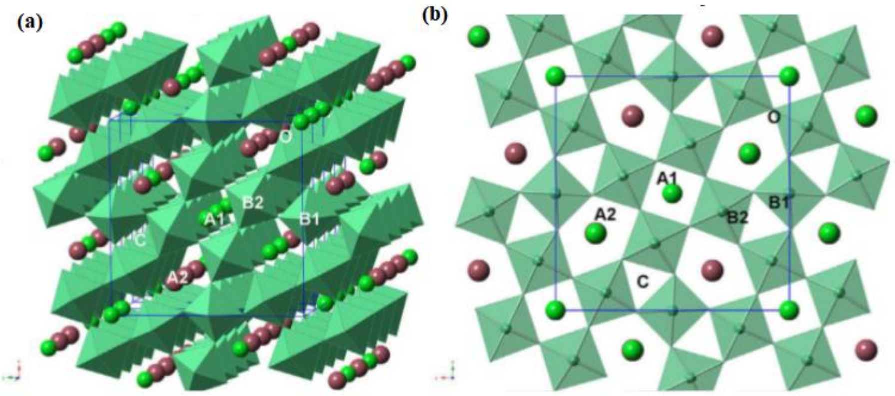

Figure 2.19. (a) Tilted view of a prototype tetragonal tungsten bronze (TTB) structure showing multiple unit cells and the corner-sharing oxygen octahedra (b) a-b plane projection (// c-axis) illustrating the tunnels described by the corner-sharing oxygen octahedra [200].

2.6.2 Classification of TTB Oxides

Tungsten bronze structures exist in cubic, tetragonal (type I and type II), hexagonal and orthorhombic crystal systems [205]. Tetragonal -I and tetragonal-II differs only in the rotation of the oxygen corner-sharing within the unit cell (Figure 2.20) [206]. In this research, only tetragonal tungsten bronzes (type I with prototype symmetry, P4/mbm) will be studied in terms of structure-property relations since they are the focus of part of this thesis [198].

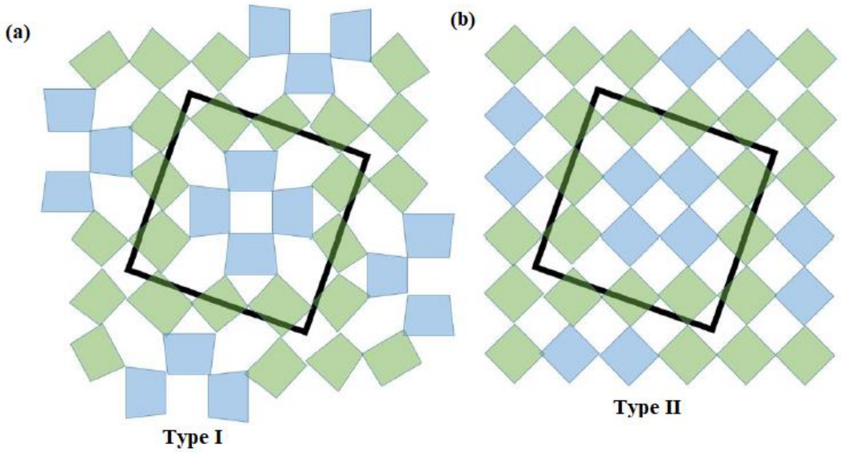

Figure 2.20. Schematic of planar projection (a-b plane view) showing the difference between type I (a) and type II (b) tetragonal tungsten bronzes [206]. The blue octahedra depict the portions that can be rotated to move from type-I to type-II.

TTBs are classified into three; stuffed, filled and unfilled based on the sites (A1, A2 and C) occupied by cations [197], [200], [207] .

2.6.2.1 Stuffed TTB

This class of TTB results when all the A (A1 and A2) and C sites are occupied by cations, e.g. $K_6Li_4Nb_{10}O_{30}$.

2.6.2.2 Filled TTB

In filled TTBs, all the 6 A-sites $[A1_2A2_4]$ are occupied while C site remains empty. With this, the general formula reverts to:

$$[A1_2A2_4][B1_2B2_8]O_{30} \qquad 2.32$$

An example of a filled TTB includes $Ba_4Na_2Nb_{10}O_{30}$. Filled TTBs generally forms two distinct compounds; $M_4R_2Ti_4Nb_6O_{30}$ and $M_5RTi_3Nb_7O_{30}$, where M = Sr or Ba, R = alkali/alkaline earth or RE cations such as Na, Ca, La, Sm, etc. [199].

2.6.2.3 Unfilled TTB

For unfilled TTB, some of the A1 and A2 sites are vacant. Normally, 5 out of the 6 A-sites are occupied, e.g. $Sr_xBa_{1-x}Nb_2O_6$, $(Sr_xBa_{1-x})_5Nb_{10}O_{30}$. In some unfilled TTBs, a vacancy (hole) is created within the 5 A-sites occupied by cations, e.g. $Ba_4Dy_{0.67}Nb_{10}O_{30}$ [207] and is refers to as "Empty TTB" [197].

TTB compounds have also been classified using a geometric Goldschmidt tolerance factor, t [197] as stated in equation 2.29. Individual tolerance factors for A1 and A2 sites represented with t_{A1} and t_{A2}, respectively are stated as follows [197], [208]:

$$t_{A1} = \frac{r_{A1}+r_O}{\sqrt{2}(r_B+r_O)} \qquad 2.33$$

$$t_{A2} = \frac{r_{A2}+r_O}{\sqrt{23-12\sqrt{3}}(r_B+r_O)} \qquad 2.34$$

$$t_{TTB} = \frac{t_{A1}+2t_{A2}}{3} \qquad 2.35$$

Equation 2.35 is referred to as the effective tolerance factor for the entire TTB structure (t_{TTB}) and it is obtained by combining equations 2.33 and 2.34. This equation (2.35) is similar for perovskites as stated in equation 2.31. Therefore, t_{TTB} is an index to determine the occurrence of a TTB structure with consideration given to the ions involved [197].

2.6.3 Thermoelectric Properties of TTB Oxides

Oxides are potential TE materials due to their cheapness or abundance, non-toxicity and high chemical and/or physical stability when subjected to high temperatures. However, high crystallographic symmetry (and small unit cells) associated with oxides lead to high thermal conductivity and low ZT [209]. In order to improve the TE efficiency via lowering of the thermal conductivity, materials with intrinsic phonon scattering centres such as Magneli phases and TTBs have recently attracted attention [192], [209]. The CS planes and the natural disorder inherent in Magneli phases and TTBs are regarded as intrinsic nanostructures [27], [209] and serve as barriers to phonon propagation.

The TE properties of $Na_{8-x}W_{9+x}O_{47-\delta}$ (x = 0, 0.075, 0.1, 1, 2) TTB compounds were investigated [27], [209] with compositions exhibiting stability up to 1323 K, low thermal conductivity (1.6-2.0 W/m.K) , and high S = -240 µV/K (indication of n-type) at room temperature. The highest PF = 0.8 µW/cm. K^2 and maximum ZT = 0.043 at 973 K were observed in $Nb_6W_{11}O_{47-\delta}$ (x = 2). The highest ZT (0.043) for $Na_{8-x}W_{9+x}O_{47-\delta}$ obtained in this study is very low compared to other n-type oxides, but the high Seebeck coefficient and very low thermal conductivity recorded show the potential of TTBs for TE applications. Lee *et al* [210] and Li *et al* [211] independently investigated the TE performance of single crystal $Sr_xBa_{1-x}Nb_2O_{6-\delta}$ TTB compounds and reported a high PF (200 µW/m.K^2) at 516 K parallel to c-axis and a ZT > 0.5 along the c-direction [200]. In a related study of TE properties of $Sr_xBa_{1-x}Nb_2O_{6-\delta}$ single crystal and ceramics, k = 1.92 W/m.K (400 K), PF = 40.8 µW/cm.K^2 (550 K), ZT = 1.12 (550 K) for single crystals; and k = 2.28 W/m.K (550 K), PF = 7 µW/cm.K^2 (550 K), ZT = 0.17 (550 K) for ceramics [32]. In the recent study of the TE properties of $Nb_{8-x}W_{9+x}O_{47}$ (0<x<5) TTB ceramics, S = -95 µV/K, k = 2.6 W/m.K and ZT = 0.2 at 1173 K were reported for $Nb_4W_{13}O_{47}$ (x = 4) composition [212].

With these TE results reported for TTB compounds, it is obvious to state that oxides with adaptive structures are potential candidates for TE applications [27]. This is attributed in part but not limited to their complex structure, hence there is the possibility of tuning properties by cation substitution (and oxygen deficiency), [27], [209].

2.7 $RE_2Ti_2O_7$ Oxide Ceramics

Rare earth titanium oxide ceramics ,$RE_2Ti_2O_7$ (where RE = trivalent rare earth ions) have received a significant attention due to their robust crystal chemistry [213], and their thermal, electrical, optical, magnetic, and catalytic properties [214], [215]. RE titanates exhibit potential technological applications in fuel cells [214]–[217]; sensors; fluorescence; catalytic activities [216]; thermal barrier coatings; high permittivity dielectrics, nuclear waste management [217] and other related technological areas [214], [215].

The stability of $RE_2Ti_2O_7$ compounds is determined by the ratio of the RE-(A) and Ti-site (B), r_A/r_B cationic radii. As widely reported in the literature [213], [214], [218], [219], [220], RE titanates form a pyrochlore structure (Fd-3m) if the r_A/r_B range is 1.46-1.78. When the ratio decreases below 1.46, i.e. $r_A/r_B < 1.46$, a disordered fluorite structure (Fd-3m) is formed, while it adopts a monoclinic perovskite layered structure ($P2_1$) if $r_A/r_B > 1.78$. Generally, RE titanates with smaller atomic mass (La^{3+} - Nd^{3+}) form monoclinic perovskite structures while others (Sm^{3+} - Lu^{3+}) form cubic pyrochlore structures [213], [214].

2.7.1 $La_2Ti_2O_7$ Ceramics

The study of electrical properties of lanthanum dititanate, $La_2Ti_2O_7$ (LTO) ferroelectrics started over thirty years ago [221]. LTO exhibits high Curie temperature, Tc >1500 ^oC [218], [221], [222] , excellent piezoelectric properties [213], [218], [221], non-linear optical and photocatalytic properties [213], [218], [221], [222]; and finds application in gas turbines at high temperature (>1000 ^oC) [222].

$La_2Ti_2O_7$ belongs to the perovskite-like layered structure family with a homologous series $A_nB_nO_{3n+2}$, where A = RE elements, B = titanium, and n (= 4 in case of LTO) is the number of octahedral units in the perovskite layers [218], [223]. At room temperature, LTO possesses a monoclinic unit cell with a space group of $P2_1$ and a corresponding lattice parameter a = 13.0150 Å, b = 5.5456 Å, c = 7.8170 Å and β = 98.6^o [223]. Above room temperature (at high temperatures), LTO undergoes a transformation. For instance, at ~ 780 ^oC, it transforms to orthorhombic phase ($CMc2_1$) and changes to a paraelectric phase (CMcm) at 1500 ^oC [221], [222].

The structure of LTO consists of discontinuous layers of corner sharing TiO_6 octahedra in the unit cell [218], [223], with La occupying interstitial positions between the octahedra [218]. Figure 2.21 represents the crystal structure of $La_2Ti_2O_7$ ceramics. Pure LTO has a wide band gap (E_g) of 3-4 eV [224], [225]. The size of E_g is dependent on the microstructure [224], morphology [225] and processing method of $La_2Ti_2O_7$ [225].

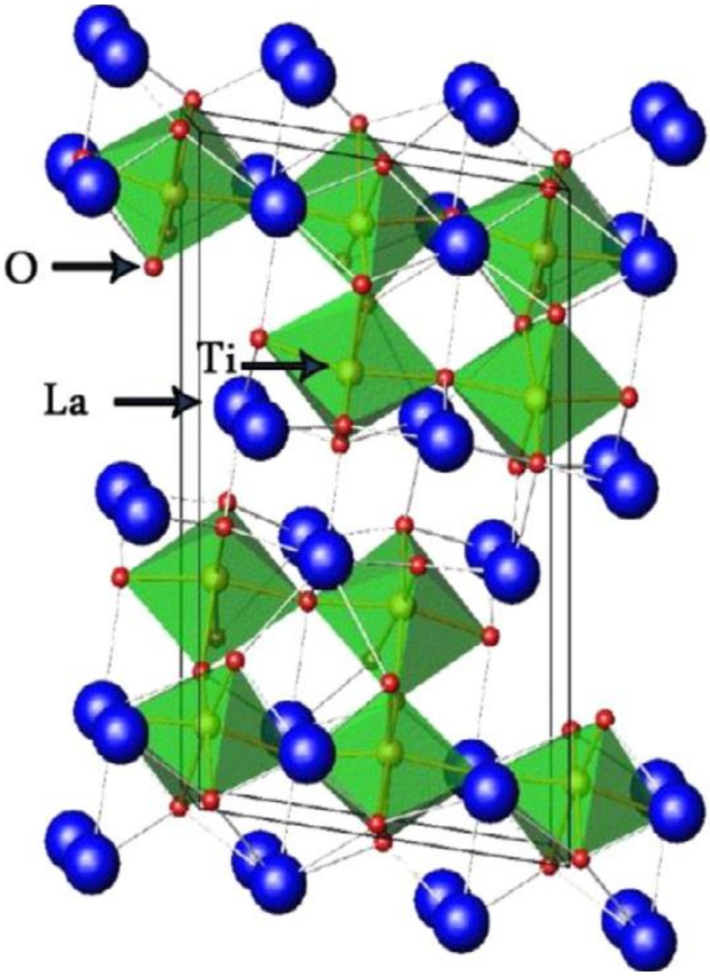

Figure 2.21. Crystal structure of Lanthanum dititanate, $La_2Ti_2O_7$ [218]. Blue, red, and green balls correspond to La^{3+}, O^{2-} and Ti^{4+} ions respectively.

In comparison with many structure types, the thermoelectric properties of LTO and other related layered perovskites have received less attention. Recently, Khaliq *et al* [223] reported a low thermal conductivity, k value (k ~ 1.3 W/m.K at 573 K in pure $La_2Ti_2O_7$, and very low values of ~ 1.12 and ~ 0.93 W/m.K for Sr- and Ta-doped $La_2Ti_2O_7$, respectively at 573 K. These low k values are attributed to its large unit cells, large atomic mass, crystal anisotropy and complex crystal structure.

2.8 Impact of Processing Conditions on TE Properties

Thermoelectric performance of semiconductors, ceramics, organics and other related materials have been widely studied in terms of the effects of different dopants, inclusions/additives, doping mechanisms, processing conditions (and parameters), defect engineering and micro/nanostructural engineering [149], [226]. As already discussed, the essence of utilizing these strategies is to seek the best approach to boost the electronic transport (power factor), minimize or restrict heat flow (phonon scattering) and optimize the efficiency (ZT) necessary for thermoelectric application. Furthermore, researchers have suggested that creation of both cation and anion vacancies in the doped materials with sintering in reducing atmosphere is a promising approach to enhance the TE properties [149], [162], [226].

$SrTiO_3$ ceramic (which is the main focus of this thesis) has a high thermal conductivity and it's detrimental to TE applications. However, $SrTiO_3$ has received a considerable attention due to its high Seebeck coefficient [223]. For example, Kovalevsky *et al* [151] in their study utilized highly reducing conditions and achieved a high ZT (~ 0.42) for RE-doped $SrTiO_3$ ceramics. The optimized ZT obtained is attributed to generated Ti^{3+}, oxygen vacancies, cation (A-site) vacancies and oxygen-rich crystallographic shear planes.

In view of the promising results obtained by Kovalevsky *et al* [151] and other investigators, La-Sm co-doped $SrTiO_3$ (perovskite), Sm-doped $Sr_5LaTi_3Nb_7O_{30}$ (TTB) and Nb-doped $La_2Ti_2O_7$ (PLS) ceramics were prepared via solid state reaction technique and processed under reducing conditions (5% H_2-95% N_2) to create oxygen deficiency [176]. Co-doping (using La^{3+} and Sm^{3+} cations) was utilized to validate the findings that mass contrast (atomic mass difference) and nanoscale intergrowths could influence the thermal conductivity [223]. It is also in furtherance to test the proposition that dopants with mass contrasts and ionic radii dissimilar to the matrix cation (in this case, Sr^{2+}) would enhance phono scattering, thus reduce the thermal conductivity.

The importance of low thermal conductivity in thermoelectrics necessitated the study of TTB and PLS compounds in this research. The inherent crystallographic shear planes in Magneli phases and TTBs are intrinsic phonon scattering centres [27], [209] and thus serve as barriers to phonon propagation. In addition, TTB and PLS compounds possess large unit cells when compared to perovskites which amount to low thermal conductivity. Due to the multiple layers of perovskite units in PLS, it exhibits anisotropy and eventual low thermal conductivity.

References

[1] Gayner Chhatrasal and K.Kar Kamal, “Recent advances in thermoelectric materials,” *Prog. Mater. Sci.*, vol. 83, no. 83, pp. 330–382, 2016.

[2] Deepanshu Srivastava, “Effect of Processing Conditions and Second-Phase Additives on Thermoelectric Properties of $SrTiO_3$ Based Ceramics,” The University of Manchester, 2016.

[3] Basel Ismail and Wael Ahmed, “Thermoelectric Power Generation Using Waste-Heat Energy as an Alternative Green Technology,” *Recent Patents Electr. Eng.*, vol. 2, no. 1, pp. 27–39, 2009.

[4] Basel I Ismail, “Power Generation Using Nonconventional Renewable Geothermal & Alternative Clean Energy Technologies,” *Planet Earth 2011 - Glob. Warm. Challenges Oppor. Policy Pract.*, pp. 399–424, 2011.

[5] Kanishka Biswas, Jiaqing He, Ivan D. Blum, Chun I. Wu, Timothy P. Hogan, David N. Seidman, Vinayak P. Dravid, and Mercouri G. Kanatzidis, “High-performance bulk thermoelectrics with all-scale hierarchical architectures,” *Nature*, vol. 489, no. 7416, pp. 414–418, 2012.

[6] S. B. Riffat and Xiaoli Ma, “Thermoelectrics: A review of present and potential applications,” *Appl. Therm. Eng.*, vol. 23, no. 8, pp. 913–935, 2003.

[7] Siddig A. Omer and David G. Infield, “Design and thermal analysis of a two stage solar concentrator for combined heat and thermoelectric power generation,” *Energy Convers. Manag.*, vol. 41, no. 7, pp. 737–756, 2000.

[8] A. Yadav, K. P. Pipe, and M. Shtein, “Fiber-based flexible thermoelectric power generator,” *J. Power Sources*, vol. 175, no. 2, pp. 909–913, 2008.

[9] Mitsuru Kambe. Tarahiro Jinushi, Masahiro Okahara, Zenzo Ishijima, Hideo Shikata, “Development of the High Performance Thermoelectric Modules for High Temperature Heat Sources,” *Mater. Sci. Forum*, pp. 534-536:1521-1524, 2007.

[10] Dharmik Patel and Prof Shruti B Mehta, “Review of Use of Thermoelectricity as Renewable Energy Source,” *Journal of Emerging Technologies and Innovative Research*, vol. 2, no. 3, pp. 835–839, 2015.

[11] Robert J. Karschinia Swapan Chakraborty, “Pipeline Thermoelectric Generator Assembly,” EP2067183BI, 2013.

[12] D.M Rowe., *CRC Handbook of Thermoelectrics*. Boca Raton: CRC Press., 1995.

[13] Jarman T. Jarman, Essam E. Khalil, and Elsayed Khalaf, “Energy Analyses of Thermoelectric Renewable Energy Sources,” *Open J. Energy Effic.*, vol. 02, no. 04, pp. 143–153, 2013.

[14] H. Goldsmid, “Introduction in Recent Trends in Thermoelectric Materials Research,” in *Semiconductors and Semimetals*, T. Tritt., Ed. New York: Academic, 2006, pp. 1–24.

[15] Euke Liu, Bingheng Zhu, and Jinsheng Luo, *Semiconductors Physics*. Peking: National Defense Industry, 1994.

[16] Kittel Charles, *Introduction to Solid State Physics*, 7th ed. John Wiley and Sons Inc., 1996.

[17] Yifeng Wang, “Study on Thermoelectric Properties of Layered Perovskite-Type Oxide, SRO $(SrTiO_3)_n$ (n = Integer),” Nagoya University, 2008.

[18] Ningyu Wu, “Development and Processing of p-type Oxide Thermoelectric Materials,” PhD Thesis, Technical University of Denmark, 2014.

[19] Warren E. Pickett and Jagadeesh S. Moodera, “Half Metallic Magnets,” *Physics. Today*, vol. 54, no. 5, pp. 39–44, 2001.

[20] D.E Demirocak, “Thermodynamic and Economic Analysis of a Solar Thermal Powered Adsorption Cooling System,” PhD Thesis, Middle East Technical University, Ankara, 2008.

[21] Robert Harry Hyde, “Growth and Characterization of Thermoelectric Ba 8 Ga 16 Ge 30 Type-I Clathrate Thin-Films Deposited by Pulsed Dual-Laser Ablation,” PhD Thesis, University of Florida, 2011.

[22] William Thomson, “On the Dynamical Theory of Heat. Part V. Thermo-electric Currents,”*Transactions of the Royal Society of Edindurgh*, vol. 21, no. 1, pp. 123–171, 1857.

[23] David Ginger. C. Jeffrey Brinker, "Nanotechnology for Sustainability: Energy Conversion, Storage, and Conversation," in *Nanotechnology Research Directions for Societal Needs in 2020*, Volume 1., Series Science Policy Reports, pp. 261–303.

[24] A. I. Hochbaum, R. K. Chen, R. D. Delgado, W. J. Liang, E. C. Garnett, M. Najarian, A. Majumdar, and P. D. Yang, "Enhanced thermoelectric performance of rough silicon nanowires," *Nature*, vol. 451, no. 7175, pp. 163–168, 2008.

[25] Joseph R. Sootsman, Duck Young Chung, and Mercouri G. Kanatzidis, "New and old concepts in thermoelectric materials," *Angew. Chemie - Int. Ed.*, vol. 48, no. 46, pp. 8616–8639, 2009.

[26] Gao Min, D. M. Rowe, and K. Kontostavlakis, "Thermoelectric figure-of-merit under large temperature differences," *Journal of Physics D: Applied Physics.*, vol. 37, no. 8, pp. 1301–1304, 2004.

[27] Gregor Kieslich, Giacomo Cerretti, Igor Veremchuk, Raphaẽl P. Hermann, Martin Panthöfer, Juri Grin, and Wolfgang Tremel, "A chemists view: Metal oxides with adaptive structures for thermoelectric applications," *Phys. Status Solidi Appl. Mater. Sci.*, vol. 213, no. 3, pp. 808–823, 2016.

[28] Terry M Tritt and M a Subramanian, "Thermoelectric Materials, Phenomena, and Applications : A Bird's Eye View," *MRS Bull.*, vol. 31, pp. 188–198, 2006.

[29] Arash Mehdizadeh Dehkordi, "An Experimental Investigation Towards Improvement of Thermoelectric Properties of Strontium Titanate Ceramics," PhD Thesis, Clemson University, 2014.

[30] Arash Mehdizadeh Dehkordi, Sriparna Bhattacharya, Taghi Darroudi, Husam N. Alshareef, and Terry M. Tritt, "New insights on the synthesis and electronic transport in bulk polycrystalline Pr-doped $SrTiO_{3-\delta}$," *J. Appl. Phys.*, vol. 117, no. 5, 2015.

[31] J. P. Carmo, Joaquim Antunes, M. F. Silva, J. F. Ribeiro, L. M. Goncalves, and J. H. Correia, "Characterization of thermoelectric generators by measuring the load-dependence behavior," *Meas. J. Int. Meas. Confed.*, vol. 44, no. 10, pp. 2194–2199, 2011.

[32] Soonil Lee, Jonathan A. Bock, Susan Trolier-McKinstry, and Clive A. Randall, "Ferroelectric-thermoelectricity and Mott transition of ferroelectric oxides with high electronic conductivity," *Journal of the European Ceramic Society*, vol. 32, no. 16, pp. 3971–3988, 2012.

[33] "Brief History of Thermoelectrics." Materials Science, Division of Engineering & Applied Science, California Institute of Technology, 2016. Retrieved from *www.thermoelectrics.caltech.edu/thermoelectrics/history.html*

[34] E.K. Vedernikov, M.V.; Iordanishvili, “A . F . Ioffe and Origin of Modern Semiconductor Thermoelectric Energy Conversion,” in *17th International Conference on Thermoelectrics*, 1998, vol. 1, no. 1 998, pp. 37–42.

[35] C. Wood, “Materials for thermoelectric energy conversion,” R*eports on Progress in Physics*, vol. 51. pp. 459–539, 1988.

[36] B C Sales, “Electron Crystals and Phon lLasses: A new Path to Improved Thermoelectric Materials,” *MRS Bull.*, vol. 23, no. 1, pp. 15–21, 1998.

[37] George S Nolas and Joe Poon, “Recent Developments Thermoelectric Materials,” *MRS Bull.*, vol. 31, no. March, pp. 1–7, 2006.

[38] D.M. Rowe, “Thermoelectrics, an environmentally-friendly source of electrical power,” *Renew. Energy*, vol. 16, no. 1–4, pp. 1251–1256, 1999.

[39] Gael Sebald, Daniel Guyomar, and Amen Agbossou, “On thermoelectric and pyroelectric energy harvesting,” *Smart Mater. Struct.*, vol. 18, no. 12, 2009.

[40] David Nemir and Jan Beck, “On the significance of the thermoelectric figure of merit Z,” *J. Electron. Mater.*, vol. 39, no. 9, pp. 1897–1901, 2010.

[41] A. J. Minnich, M. S. Dresselhaus, Z. F. Ren, and G. Chen, “Bulk nanostructured thermoelectric materials: current research and future prospects,” *Energy Environ. Sci.*, vol. 2, no. 5, p. 466, 2009.

[42] S. R. Popuri, A. J. M. Scott, R. A. Downie, M. A. Hall, E. Suard, R. Decourt, M. Pollet, and J.-W. G. Bos, “Glass-like thermal conductivity in $SrTiO_3$ thermoelectrics induced by A-site vacancies,” *RSC Adv.*, vol. 4, no. 64, pp. 33720–33723, 2014.

[43] G. Slack, *CRC Handbook of Thermoleectrics*. Boca Raton: CRC Press, 1995.

[44] G.D Mahan., “Solid State Physics.” Advances in Research and Applications 51, p. 81, 1998.

[45] G J Snyder and E S Toberer, “Complex thermoelectric materials,” *Nat Mater*, vol. 7, no. 2, pp. 105–114, 2008.

[46] Jean-Pierre Fleurial, “Thermoelectric power generation materials: technology and application opportunities,” *J. Miner. Met. Mater. Soc.*, vol. 61, no. 4, pp. 79–85, 2009.

[47] Chaiken P.M., “An Introduction To Thermopower For Those Who Might Want To Use It To Study Organic Conductors and Superconductors,” in *Organic Superconductors*, L. W. A. Kreszin V.Z, Ed. New York: Plenum Press, 1990, pp. 101–105.

[48] T.M. Tritt, “Thermoelectric Materials : Principles , Structure , Properties , and Applications,” *Encycl. Mater. Sci. Technol.*, pp. 1–11, 2002.

[49] S. Bhattacharya, A. Mehdizadeh Dehkordi, S. Tennakoon, R. Adebisi, J. R. Gladden, T. Darroudi, H. N. Alshareef, and T. M. Tritt, “Role of phonon

scattering by elastic strain field in thermoelectric $Sr_{1-x}Y_xTiO_{3-\delta}$,” *J. Appl. Phys.*, vol. 115, no. 22, 2014.

[50] H. Jones. N.F Mott, *The Theory of the Properties of Metals and Alloys*. New York: Dover Publications, 1958.

[51] R.L Fitzpatrick. M.Cutter, J.F Leavy, “Electronic Transport in Semi Mettalic Cerium Sulphide,” *Phys. Rev.*, vol. 133, pp. A1143–A1152, 1964.

[52] A.H Wilson, *The Theory of Metals*, 2nd ed. New York London: Cambrige University Presss, 1953.

[53] J. P. Doumerc, M. Blangero, M. Pollet, D. Carlier, J. Darriet, R. Berthelot, C. Delmas, and R. Decourt, “Transition-metal oxides for thermoelectric generation,” *J. Electron Mater.*, vol. 38, no. 7, pp. 1078–1082, 2009.

[54] Hill T.L, *Introduction to Statistical Thermodynamics*. New York: Dover, 1986.

[55] G. H. Zheng, Z. X. Dai, Y. Q. Dong, F. L. Zan, D. Zou, Y. Q. Ma, and G. Li, “Low thermal conductivity for $Sr_{1-x}La_xTiO_3$,” *Mater. Res. Innov.*, vol. 16, no. 6, pp. 438–441, 2012.

[56] Holger Kleinke, “New bulk materials for thermoelectric power generation: clathrates and complex antimonides,” *Chem. Mater.*, vol. 22, no. 3, pp. 604–611, 2010.

[57] B. C. Sales, B. C. Chakoumakos, D. Mandrus, and J. W. Sharp, “Atomic displacement parameters and the lattice thermal conductivity of clathrate-like thermoelectric compounds,” *J. Solid State Chem.*, vol. 146, no. 2, pp. 528–532, 1999.

[58] Jianjun Dong, Otto F. Sankey, Ganesh K. Ramachandran, and Paul F. McMillan, “Chemical trends of the rattling phonon modes in alloyed germanium clathrates,” *J. Appl. Phys.*, vol. 87, no. 11, pp. 7726–7734, 2000.

[59] B. C. Sales, B. C. Chakoumakos, and D. Mandru, “Thermoelectric properties of thallium-filled skutterudites,” *Phys. Rev. B*, vol. 61, no. 4, pp. 2475–2481, 2000.

[60] Kunihito Koumoto and Ichiro Terasaki, “Complex Oxide Materials for Thermoelectric Applications,” *MRS Bull.*, vol. 31, no. March, pp. 206–210, 2006.

[61] C.M Bhandari and D.M Rowe, “Boundary scattering of phonons,” *J. Phys. C Solid State Phys.*, vol. 11, no. 9, pp. 1787–1794, 1978.

[62] S. Li, R. Funahashi, I. Matsubara, K. Ueno, and H. Yamada, “High temperature thermoelectric properties of oxide $Ca_9Co_{12}O_{28}$,” *J. Mater. Chem.*, vol. 9, pp. 1659–1660, 1999.

[63] Masahiro Shikano and Ryoji Funahashi, “Electrical and thermal properties of single-crystalline $(Ca_2CoO_3)_{0.7}CoO_2$ with a $Ca_3Co_4O_9$ structure,” *Appl. Phys. Lett.*, vol. 82, no. 12, pp. 1851–1853, 2003.

[64] R. Funahashi, I. Matsubara, H. Ikuta, T. Takeuchi, U. Mizutani, and S. Sodeoka, “An oxide single crystal with high thermoelectric performance in air.,” *Jpn. J. Appl. Phys.*, vol. 39, no. Part 2, No. 11B, p. L1127–L1129., 2000.

[65] Ryoji Funahashi, Ichiro Matsubara, and Satoshi Sodeoka, “Thermoelectric properties of $Bi_2Sr_2Co_2O_x$ polycrystalline materials,” *Appl. Phys. Lett.*, vol. 76, no. 17, pp. 2385–2387, 2000.

[66] Ryoji Funahashi and Masahiro Shikano, “$Bi_2Sr_2Co_2O_y$ whiskers with high thermoelectric figure of merit,” *Appl. Phys. Lett.*, vol. 81, no. 8, pp. 1459–1461, 2002.

[67] Ryoji Funahashi and Ichiro Matsubara, “Thermoelectric properties of Pb- and Ca-doped $(Bi_2Sr_2O_4)_xCoO_2$ whiskers,” *Appl. Phys. Lett.*, vol. 79, no. 3, pp. 362–364, 2001.

[68] J. J. Shen, X. X. Liu, T. J. Zhu, and X. B. Zhao, “Improved thermoelectric properties of La-doped $Bi_2Sr_2Co_2O_9$-layered misfit oxides,” *J. Mater. Sci.*, vol. 44, no. 7, pp. 1889–1893, 2009.

[69] R. Venkatasubramanian, E. Siivola, T. Colpitts, and B. O’Quinn, “Thin-film thermoelectric devices with high room-temperature figures of merit,” *Nature*, vol. 413, no. 6856, pp. 597–602, 2001.

[70] T. C. Harman, “Quantum Dot Superlattice Thermoelectric Materials and Devices,” *Science (80-.).*, vol. 297, no. 5590, pp. 2229–2232, 2002.

[71] Akram I. Boukai, Yuri Bunimovich, Jamil Tahir-Kheli, Jen Kan Yu, William A. Goddard, and James R. Heath, “Silicon nanowires as efficient thermoelectric materials,” *Nature*, vol. 451, no. 7175, pp. 168–171, 2008.

[72] B. Poudel, Q. Hao, Y. Ma, Y. Lan, A. Minnich, B. Yu, X. Yan, D. Wang, A. Muto, D. Vashaee, X. Chen, J. Liu, M. S. Dresselhaus, G. Chen, and Z. Ren, “High-Thermoelectric Performance of Nanostructured Bismuth Antimony Telluride Bulk Alloys,” *Science (80-.).*, vol. 320, no. 5876, pp. 634–638, 2008.

[73] Yi Ma, Qing Hao, Bed Poudel, Yucheng Lan, Bo Yu, Dezhi Wang, Gang Chen, and Zhifeng Ren, “Enhanced thermoelectric figure-of-merit in p-type nanostructured bismuth antimony tellurium alloys made from elemental chunks,” *Nano Lett.*, vol. 8, no. 8, pp. 2580–2584, 2008.

[74] X. W. Wang, H. Lee, Y. C. Lan, G. H. Zhu, G. Joshi, D. Z. Wang, J. Yang, A. J. Muto, M. Y. Tang, J. Klatsky, S. Song, M. S. Dresselhaus, G. Chen, and Z. F. Ren, “Enhanced thermoelectric figure of merit in nanostructured n -type silicon germanium bulk alloy,” *Appl. Phys. Lett.*, vol. 93, no. 19, pp. 1–4, 2008.

[75] G. Joshi, H. Lee, Y. Lan, X. Wang, G. Zhu, D. Wang, R.W. Gould, D.C. Cuff, M.Y. Tang, Klatsky J, Song S, M.S. Dresselhaus, G. Chen, and Z. Ren, "Enhanced thermoelectric figure of merit in nanostructured p-type silicon germanium bulk alloy," *Appl. Phys. Lett.*, vol. 93, no. 19, p. 193121, 2008.

[76] Mildred S. Dresselhaus, Gang Chen, Ming Y. Tang, Ronggui Yang, Hohyun Lee, Dezhi Wang, Zhifeng Ren, Jean Pierre Fleurial, and Pawan Gogna, "New directions for low-dimensional thermoelectric materials," *Adv. Mater.*, vol. 19, no. 8, pp. 1043–1053, 2007.

[77] D.M Rowe., "Review, Thermoelectric Waste Heat Recovery as a Renewable Energy Source," *Int. J. Innov. Energy Syst. Power*, vol. 1, no. 1, pp. 13–23, 2006.

[78] Zhiting Tian, S Lee, and G Chen, "A Comprehensive Review of Heat Transfer in Thermoelectric Materials and Devices," *Annu. Rev. Heat Transf.*, pp. 1–64, 2014.

[79] H.J. Goldsmid and R.W Douglas, "The use of semiconductors in thermoelectric refrigeration," *Br. J. Appl. Phys.*, vol. 5, pp. 386–390, 1954.

[80] A.F. Ioffe, *Semiconductor Thermoelements and Thermoelectric Cooling*. Infosearch Ltd, 1957.

[81] M. C. Steele and F. D. Rosi, "Thermal conductivity and thermoelectric power of germanium-silicon alloys," *J. Appl. Phys.*, vol. 29, no. 11, pp. 1517–1520, 1958.

[82] R.R. Heikes and R.W. Ure, *Thermoelectricity: Science and Engineering*. New York London: Interscience, 1961.

[83] F.D. Rosi, "Thermoelectricity and thermoelectric power generation," *Solid. State Electronics.*, vol. 11, no. 9, pp. 833–868, 1968.

[84] F.D. Rosi, E.F. Hockings, and N.E. Lindenblad, "Semiconducting Materials for Thermoelectric Power Generation," *RCA (Radio Corp. Am. Rev.*, vol. 22, pp. 82–121, 1961.

[85] Y. Gelbstein, Z. Dashevsky, and M. P. Dariel, "High performance n-type PbTe-based materials for thermoelectric applications," *Phys. B Condens. Matter*, vol. 363, no. 1–4, pp. 196–205, 2005.

[86] R.W. Fritts, *Thermoelectric Materials and Devices*, ed. I.B. Cadoff and E. Miller. New York: Reinhold, pp. 143–162, 1960.

[87] H. Julian Goldsmid, *Introduction to Thermoelectricity*. 2nd ed. vol. 121, United States, NY: Springer , 2010.

[88] G. Chen, M. S. Dresselhaus, G. Dresselhaus, J.-P. Fleurial, and T. Caillat, "Recent developments in thermoelectric materials," *Int. Mater. Rev.*, vol. 48, no. 1, pp. 45–66, 2003.

[89] Yanzhong Pei, Xiaoya Shi, Aaron Lalonde, Heng Wang, Lidong Chen, and G. Jeffrey Snyder, “Convergence of electronic bands for high performance bulk thermoelectrics,” *Nature,* vol. 473, no. 7345, pp. 66–69, 2011.

[90] Qian Zhang, Feng Cao, Weishu Liu, Kevin Lukas, Bo Yu, Shuo Chen, Cyril Opeil, David Broido, Gang Chen, and Zhifeng Ren, “Heavy doping and band engineering by potassium to improve the thermoelectric figure of merit in p-type PbTe, PbSe, and $PbTe_{1-y}Se_y$,” *J. Am. Chem. Soc.*, vol. 134, no. 24, pp. 10031–10038, 2012.

[91] Kuei Fang Hsu, Sim Loo, Fu Guo, Wei Chen, Jeffrey S. Dyck, Ctirad Uher, E. K. Polychroniadis Tim Hogan, and Mercouri G. Kanatzidis1, “Cubic $AgPb_mSbTe_{2+m}$: Bulk Thermoelectric Materials with High Figure of Merit,” *Science* , vol. 303, pp. 818–821, 2004.

[92] Cronin B. Vining, William Laskow, Jack O. Hanson, Roland R. Van Der Beck, and Paul D. Gorsuch, “Thermoelectric properties of pressure-sintered $Si_{0.8}Ge_{0.2}$ thermoelectric alloys,” *J. Appl. Phys.*, vol. 69, no. 8, pp. 4333–4340, 1991.

[93] Ryoji Funahashi, “Oxide thermoelectric power generation,” in 2009 Thermoelectrics Applications Workshop, San Diego, CA, September 29 - October 1, 2009. Retrieved from *https://www.energy.gov/eere/vehicles/2009-thermoelectrics-applications-workshop-1*

[94] Ichiro Terasaki., “Layered Cobalt Oxides: Correlated Electrons for Thermoelectrics,” in *Thermoelectric Nanomaterials: Materials Design and Applications.*, K. Koumoto and T. Mori, (Eds). Berlin Heidelberg: Springer, Springer Series in Materials Science , vol. 182, 2013, pp. 51–70.

[95] Petr Tomeš, Matthias Trottmann, Clemens Suter, Myriam Heidi Aguirre, Aldo Steinfeld, Philipp Haueter, and Anke Weidenkaff, “Thermoelectric oxide modules (TOMs) for the direct conversion of simulated solar radiation into electrical energy,” *Materials (Basel).*, vol. 3, no. 4, pp. 2801–2814, 2010.

[96] I. Terasaki, Y. Sasago, and K. Uchinokura, “Large thermoelectric power in $NaCo_2O_4$ single crystals,” *Phys. Rev. B,* vol. 56, no. 20, pp. R12685–R12687, 1997.

[97] Abanti Nag and V. Shubha, “Oxide thermoelectric materials: A structure-property relationship,” *J. Electron. Mater.*, vol. 43, no. 4, pp. 962–977, 2014.

[98] Lihua Zhang, Tsuyoshi Tosho, Noriyuki Okinaka, and Tomohiro Akiyama, “Thermoelectric Properties of Combustion Synthesized and Spark Plasma Sintered $Sr_{1-X}R_XTiO_3$ ($R = Y$, La, Sm, Gd, Dy, $0<X\leq0.1$),” *Mater. Trans.,* vol. 48, no. 8, pp. 2088–2093, 2007.

[99] Jeffrey W. Fergus, “Oxide materials for high temperature thermoelectric energy conversion,” *J. Eur. Ceram. Soc.*, vol. 32, no. 3, pp. 525–540, 2012.

[100] Hiromichi Ohta, Kenji Sugiura, and Kunihito Koumoto, “Recent Progress in Oxide Thermoelectric Materials: p-Type $Ca_3Co_4O_9$ and n-Type $SrTiO_3$-,” vol. 47, no. 19, pp. 8429–8436, 2008.

[101] Qiang Li, Zhiwei Lin, and Juan Zhou, “Thermoelectric materials with potential high power factors for electricity generation,” *J. Electron. Mater.*, vol. 38, no. 7, pp. 1268–1272, 2009.

[102] W. Koshibae, K. Tsutsui, and S. Maekawa, “Thermopower in cobalt oxides,” *Phys. Rev. B - Condens. Matter Mater. Phys.*, vol. 62, no. 11, pp. 6869–6872, 2000.

[103] Ichiro Matsubara, Ryoji Funahashi, Masahiro Shikano, Kei Sasaki, and Hiroyuki Enomoto, “Cation substituted $(Ca_2CoO_3)_xCoO_2$ films and their thermoelectric properties,” *Appl. Phys. Lett.*, vol. 80, no. 25, pp. 4729–4731, 2002.

[104] Chris D. Ling, Karina Aivazian, Siegbert Schmid, and Paul Jensen, “Structural investigation of oxygen non-stoichiometry and cation doping in misfit-layered thermoelectric $(Ca_2CoO_{3-x})(CoO_2)_\delta$, $\delta \approx 1.61$,” *J. Solid State Chem.*, vol. 180, no. 4, pp. 1446–1455, 2007.

[105] H. Fukutomi, Y. Konno, K. Okayasu, M. Hasegawa, and H. Nakatsugawa, “Texture development of $Ca_3Co_4O_9$ thermoelectric oxide by high temperature plastic deformation and its contribution to the improvement in electric conductivity,” *Mater. Sci. Eng. A*, vol. 527, no. 1–2, pp. 61–64, 2009.

[106] T. A. Tyson, Z. Chen, Q. Jie, Q. Li, and J. J. Tu, “Local structure of thermoelectric $Ca_3Co_4O_9$,” *Phys. Rev. B - Condens. Matter Mater. Phys.*, vol. 79, no. 2, pp. 1–7, 2009.

[107] Y. Morita, J. Poulsen, K. Sakai, T. Motohashi, T. Fujii, I. Terasaki, H. Yamauchi, and M. Karppinen, “Oxygen nonstoichiometry and cobalt valence in misfit-layered cobalt oxides,” *J. Solid State Chem.*, vol. 177, no. 9, pp. 3149–3155, 2004.

[108] Y. Oide, Y. Miyazaki, Y Ono, X Y Huang, and T Kajitani., “Thermogravimetric Study and High-Temperature Thermoelectric Properties of $[Ca_2(Co_{1-x}A_x,)_{03}]_{0.62}CoO_2$,” in *2006 International Conference on Thermoelectrics*, 2006, pp. 402–405.

[109] Shin Ichi Shamoto, Yuki Hasegawa, and Tsuyoshi Kajitani, “Two-Dimensional Sodium Fluctuation at High Temperatures in High-Temperature Thermoelectric Material γ-$Na_{0:7}CoO_2$,” *Japanese J. Appl. Physics, Part 1 Regul. Pap. Short Notes Rev. Pap.*, vol. 45, no. 8 A, pp. 6395–6397, 2006.

[110] Yasuhiko Takahashi, Junji Akimoto, Norihito Kijima, and Yoshito Gotoh, “Structure and electron density analysis of $Na_{0.74}CoO_2$ by single-crystal X-ray diffraction,” *Solid State Ionics*, vol. 172, no. 1–4 SPEC. ISS., pp. 505–508, 2004.

[111] Nan Li, Yang Jiang, Guohua Li, Chun Wang, Jianfeng Shi, and Dabin Yu, "Self-ignition route to Ag-doped $Na_{1.7}Co_2O_4$ and its thermoelectric properties," *J. Alloys Compd.*, vol. 467, no. 1–2, pp. 444–449, 2009.

[112] Biprodas Dutta, Jugdersuren Battogtokh, David Mckewon, Igor Vidensky, Neilanjan Dutta, and Ian L. Pegg, "Thermoelectric Properties of $NaCo_{2-x}Fe_x O_y$," *J. Electron. Mater.*, vol. 36, no. 7, pp. 746–752, 2007.

[113] Yayu Wang, Nyrissa S. Rogado, R. J. Cava, and N. P. Ong, "Spin entropy as the likely source of enhanced thermopower in $Na_xCo_2O_4$," *Nature*, vol. 423, no. 6938, pp. 425–428, 2003.

[114] Janina ; Molenda, Claude ; Delmas, and Paul Hagenmuller, "Electronic and electrochemical properties of Na_xCoO_{2-y} cathode," *Solid State Ionics*, vol. 9/10, pp. 431–435, 1983.

[115] Tomoaki Tanaka, Shin Nakamura, and Shuichi Iida, "Observation of Distinct Metallic Conductivity in $NaCo_2O_4$," *Jpn. J. Appl. Phys.*, vol. 33, no. 4B, pp. L581–L582, 1994.

[116] K. Fujita;, T. Mochida;, and K. Nakamura, "High Temperature Thermoelectric Properties of $Na_xCoO_{2-\delta}$ Single Crystals," *Jpn. J. Appl. Phys.*, vol. 40, p. 4644, 2001.

[117] Mikio Ito, Tomoya Nagira, Daisuke Furumoto, Shigeru Katsuyama, and Hiroshi Nagai, "Synthesis of $Na_xCo_2O_4$ thermoelectric oxides by the polymerized complex method," *Scr. Mater.*, vol. 48, no. 4, pp. 403–408, Feb. 2003.

[118 I Terasaki, "Thermoelectric materials in layered transition-metal oxides," in *24th International Conference on Thermoelectrics*, 2005, pp. 301–306.

[119] Lassi Karvonen;, Petr Tomes;, and Auke Weidenkaff, "Thermoelectric performance of perovskite- type oxide materials Materials," *Mater. \matters*, vol. 6, no. 4, pp. 92–99, 2011.

[120] A. Onodera. and M.Takesada., "Electronic Ferroelectricity in II-VI Semiconductor ZnO," in *Advances in Ferrolectrics*, P.-B. A, Ed. Intech, 2012.

[121] Anderson Janotti and Chris G Van De Walle, "Fundamentals of zinc oxide as a semiconductor," *Reports Prog. Phys.*, vol. 72, no. 126501, p. 29, 2009.

[122] A. Mang, K. Reimann, and St. Riibenacke, "Band Gaps, Crystal-Field Splitting, Spin-Orbit Coupling, and Excition Binding Energies in ZnO under Hydrostatic Pressure," *Solid State Commun.*, vol. 94, no. 4, pp. 251–254, 1995.

[123] P Wanger and R. Helbig, "The Hall Effect and the Anisotropy of the Mobility of the Electrons in ZnO," *J Phys Chem Solids*, vol. 35, pp. 327–335, 1974.

[124] Toshiki Tsubota, Michitaka Ohtaki, Koichi Eguchi, and Hiromichi Arai, "Thermoelectric properties of Al-doped ZnO as a promising oxide material for high- temperature thermoelectric conversion," *J. Mater. Chem.*, vol. 7, pp. 85–90, 1997.

[125] Michitaka Ohtaki, Sayaka Maehara, and Shinichirou Shige, "Thermoelectric Properties of Al-doped ZnO Sintered with Nanosized Void Forming Agents," in *22nd lnternational Conference on Thermoelectrics*, 2003, pp. 171–174.

[126] J P Wiff, Y Kinemuchi, H Kaga, C Ito, and K Watari, "Correlations between thermoelectric properties and effective mass caused by lattice distortion in Al-doped ZnO ceramics," *J. Eur. Ceram. Soc.*, vol. 29, pp. 1413–1418, 2009.

[127] Michitaka Ohtaki, Kazuhiko Araki, and Kiyoshi Yamamoto, "High thermoelectric performance of dually doped ZnO ceramics," *J. Electron. Mater.*, vol. 38, no. 7, pp. 1234–1238, 2009.

[128] S Kumar and U Schwingenschlo, "Lattice thermal conductivity in layered BiCuSeO," *Phys. Chem. Chem. Phys.*, vol. 18, pp. 19158–19164, 2016.

[129] Hezhu Shao, Xiaojian Tan, Guo Qiang Liu, Jun Jiang, and Haochuan Jiang, "A first-principles study on the phonon transport in layered BiCuOSe," *Sci. Rep.*, vol. 6, pp. 1–9, 2016.

[130] Yong Liu, Li-dong Zhao, Yaochun Liu, Jinle Lan, Wei Xu, Fu Li, Bo-ping Zhang, and David Berardan, "Remarkable Enhancement in Thermoelectric Performance of BiCuSeO," *J. Am. Chem. Soc.*, vol. 133, pp. 20112–20115, 2011.

[131] L D Zhao, D Berardan, Y L Pei, C Byl, N Dragoe, L D Zhao, D Berardan, Y L Pei, and C Byl, "$Bi_{1-x}Sr_xCuSeO$ oxyselenides as promising thermoelectric materials," *Appl. Phys. Lett.*, vol. 97, pp. 0921181–0921184, 2010.

[132] Fu Li, Jing-Feng Li, Li-Dong Zhao, Kai Xiang, Yong Liu, Bo-Ping Zhang, Yuan-Hua Lin, Ce-Wen Nana, and Hong-Min Zhu, "Polycrystalline BiCuSeO Oxides as a Potential Thermoelectric Material," *Energy Environ. Sci.*, vol. 5, pp. 7188–7195, 2012.

[133] Jingxuan Ding, Ben Xu, Yuanhua Lin, Cewen Nan, and Wei Liu, "Lattice vibration modes of the layered material BiCuSeO and first principles study of its thermoelectric properties.," *New J. Phys.*, vol. 17, p. 083012, 2015.

[134] Jing Li, Jiehe Sui, Yanling Pei, Celine Barreteau, David Berardan, Nita Dragoe, Wei Cai, Jiaqing He, and Li-Dong Zhao, "A high thermoelectric figure of merit ZT > 1 in Ba heavily doped BiCuSeO oxyselenides," *Energy Environ. Sci.*, vol. 5, no. 9, p. 8543, 2012.

[135] Daniel I Bilc, Calin G Floare, Liviu P Za, Sorina Garabagiu, Sebastien Lemal, and Philippe Ghosez, "First-Principles Modeling of $SrTiO_3$ Based Oxides for Thermoelectric Applications," *J. Phys. Chem. C*, vol. 120, p. 25678−25688, 2016.

[136] Xiao Zhang and Li-dong Zhao, “Thermoelectric materials : Energy conversion between heat and electricity,” *J. Mater.*, vol. 1, no. 2, pp. 92–105, 2015.

[137] Li-dong Zhao, Jiaqing He, David Berardan, Yuanhua Lin, and Jing-feng Li, “BiCuSeO oxyselenides : new promising thermoelectric materials,” *Energy Environ. Sci.*, vol. 7, pp. 2900–2924, 2014.

[138] C Barreteau, L Pan, E Amzallag, L D Zhao, D Bérardan, and N Dragoe., “system as good thermoelectric materials Layered oxychalcogenide in the Bi – Cu – O – Se system as good thermoelectric,” *Semicond. Sci. Technol.*, vol. 29, no. 6, pp. 1–11, 2014.

[139] Kunihito Koumoto, Yifeng Wang, Ruizhi Zhang, Atsuko Kosuga, and Ryoji Funahashi, “Oxide Thermoelectric Materials: A Nano Structuring Approach,” *Annu. Rev. Mater. Res.*, vol. 40, pp. 363–394, 2010.

[140] J. A. Dawson, X. Li, C. L. Freeman, J. H. Hardinga, and D. C. Sinclair., “The application of a new potential model to the rare-earth doping of $SrTiO_3$ and $CaTiO_3$,” *Journal of Materials Chemistry C* , vol. 1, no. 8, pp. 1574–1582, 2013.

[141] Arash Mehdizadeh Dehkordi, Sriparna Bhattacharya, Taghi Darroudi, Jennifer W Gra, Udo Schwingenschlo, Husam N Alshareef, and Terry M Tritt, “Large Thermoelectric Power Factor in Pr-Doped $SrTiO_{3-}$,” *Chem. Mater.*, vol. 26, no. 7, p. 2478−2485, 2014.

[142] H C Wang, C L Wang, W B Su, J Liu, H Peng, J L Zhang, M L Zhao, J C Li, N Yin, and L M Mei, “Substitution effect on the thermoelectric properties of reduced Nb-doped,” *J. Alloys Compd.*, vol. 486, pp. 693–696, 2009.

[143] T Okuda, K Nakanishi, S Miyasaka, and Y Tokura, “Large Thermoelectric Response of Metallic Perovskite: $Sr_{1-x}La_xTiO_3$ ($0 \leq x \leq 0.1$),” *Phys. Rev. B*, vol. 63, pp. 1131041–1131044, 2001.

[144] Shingo Ohta, Takashi Nomura, Hiromichi Ohta, and Kunihito Koumoto, “High-temperature carrier transport and thermoelectric properties of heavily La- or Nb- doped single crystals,” *J. Appl. Phys.*, vol. 97, no. 3, pp. 0341061–0341064, 2005.

[145] Hiroaki Muta, Ken Kurosaki, and Shinsuke Yamanaka, “Thermoelectric properties of reduced and La-doped single-crystalline $SrTiO_3$,” *J. Alloys Compd.*, vol. 392, no. 1–2, pp. 306–309, 2005.

[146] S R Sarath Kumar, Abeer Z Barasheed, and H N Alshareef, “High Temperature Thermoelectric Properties of Strontium Titanate Thin Films with Oxygen Vacancy and Niobium Doping,” *Appl. Mater. Interfaces*, vol. 5, no. 15, pp. 7268–7273, 2013.

[147] H C Wang, C L Wang, W B Su, J Liu, Y Zhao, H Peng, J L Zhang, M L Zhao, J C Li, N Yin, and L M Mei, "Enhancement of thermoelectric figure of merit by doping Dy in $La_{0.1}Sr_{0.9}TiO_3$ ceramic," *Mater. Res. Bull.*, vol. 45, no. 7, pp. 809–812, 2010.

[148] J. Liu, C. L. Wang, Y. Li, W. B. Su, Y. H. Zhu, J. C. Li, and L. M. Mei, "Influence of rare earth doping on thermoelectric properties of SrTiO3ceramics," *J. Appl. Phys.*, vol. 114, no. 22, 2013.

[149] Deepanshu Srivastava, Colin Norman, Feridoon Azough, Marion C. Schafer, Emmanuel Guilmeau, Demie Kepaptsoglou, Quentin M. Ramasse, Giuseppe Nicotrad, and Robert Freer, "Tuning the Thermoelectric Properties of A-site Deficient $SrTiO_3$ Ceramics by Vacancies and Carrier Concentration," *Phys. Chem. Chem. Phys.*, vol. 18, pp. 26475–26486, 2016.

[150] Shingo Ohta, Takashi Nomura, Hiromichi Ohta, Masahiro Hirano, Hideo Hosono, and Kunihito Koumoto, "Large thermoelectric performance of heavily Nb-doped $SrTiO_3$ epitaxial film at high temperature," *Appl. Phys. Lett.*, vol. 87, p. 092108, 2005.

[151] A. V. Kovalevsky, A. A. Yaremchenko, S. Populoh, P. Thiel, D. P. Fagg, A. Weidenkaff, and J. R. Frade, "Towards a high thermoelectric performance in rare-earth substituted $SrTiO_3$: effects provided by strongly-reducing sintering conditions," *Phys. Chem. Chem. Phys.*, vol. 16, no. 48, pp. 26946–26954, 2014.

[152] Zhilun Lu, Huairuo Zhang, Wen Lei, Derek C. Sinclair, and Ian M. Reaney, "High-Figure-of-Merit Thermoelectric La-Doped A-Site-Deficient $SrTiO_3$ Ceramics," *Chem. Mater.*, vol. 28, no. 3, pp. 925–935, 2016.

[153] Hiroaki Muta, Ken Kurosaki, and Shinsuke Yamanaka, "Thermoelectric properties of rare earth doped $SrTiO_3$," *J. Alloys Compd.*, vol. 350, no. 1–2, pp. 292–295, 2003.

[154] Jiao Han, Qiu Sun, and Ying Song, "Enhanced thermoelectric properties of La and Dy co-doped, Sr-deficient $SrTiO_3$ ceramics," *J. Alloys Compd.*, vol. 705, pp. 22–27, 2017.

[155] Hongchao Wang and Chunlei Wang, "Thermoelectric properties of Yb-doped $La_{0.1}Sr_{0.9}TiO_3$ ceramics at high temperature," *Ceram. Int.*, vol. 39, no. 2, pp. 941–946, 2013.

[156] Yifeng Wang, Xiaoyan Zhang, Liming Shen, Ningzhong Bao, Chunlei Wan, Nam Hee Park, Kunihito Koumoto, and Arunava Gupta, "Nb-doped grain boundary induced thermoelectric power factor enhancement in La-doped $SrTiO_3$ nanoceramics," *J. Power Sources*, vol. 241, pp. 255–258, 2013.

[157] Hiroaki Muta, Ken Kurosaki, and Shinsuke Yamanaka, "Thermoelectric properties of doped $BaTiO_3$-$SrTiO_3$ solid solution," *J. Alloys Compd.*, vol. 368, no. 1–2, pp. 22–24, 2004.

[158] Jun Wang, Bo Yu Zhang, Hui Jun Kang, Yan Li, Xinba Yaer, Jing Feng Li, Qing Tan, Shuai Zhang, Guo Hua Fan, Cheng Yan Liu, Lei Miao, Ding Nan, Tong Min Wang, and Li Dong Zhao, "Record high thermoelectric performance in bulk $SrTiO_3$ via nano-scale modulation doping," *Nano Energy*, vol. 35, no. April, pp. 387–395, 2017.

[159] K. Ozdogan, M. Upadhyay Kahaly, H. N. Alshareef, and U. Schwingenschögl, "Anomalous enhancement of the thermoelectric figure of merit by V co- doping of Nb-$SrTiO_3$," *Appl. Phys. Lett.*, vol. 100 , no.19 , pp. 1931101-1931104, 2012.

[160] H C Wang, C L Wang, W B Su, J Liu, H Peng, Y Sun, J L Zhang, M L Zhao, J C Li, N Yin, and L M Mei, "Synthesis and thermoelectric performance of Ta doped $Sr_{0.9}La_{0.1}TiO_3$ ceramics," *Ceramics International*, vol. 37,no. 7, pp. 2609–2613, 2011.

[161] A V Kovalevsky, S Populoh, S G Patricio, P Thiel, M C Ferro, D P Fagg, J R Frade, and A Weidenkaff, "Design of $SrTiO_3$-Based Thermoelectrics by Tungsten Substitution," *Journal of Physical Chemistry C,* vol. 119, no. 9, pp. 4466−4478, 2015.

[162] Dragos Neagu and John T S Irvine, "Structure and Properties of La0.4 Sr0. 4 TiO3 Ceramics for Use as Anode Materials in Solid Oxide Fuel Cells," *Chem. Mater.*, vol. 22, no. 6, pp. 5042–5053, 2010.

[163] Bin Feng, Jian Xie, Gaoshao Cao, Tiejun Zhu, and Xinbing Zhao, "Enhanced thermoelectric properties of p-type $CoSb_3$/graphene nanocomposite," *J. Mater. Chem. A*, vol. 1, no. 42, pp. 13111–13119, 2013.

[164] Jingdu Dong, Wei Liu, Han Li, Xianli Su, Xinfeng Tang, and Ctirad Uher, "In situ synthesis and thermoelectric properties of PbTe-graphene nanocomposites by utilizing a facile and novel wet chemical method," *J. Mater. Chem. A*, vol. 1, no. 40, pp. 12503–12511, 2013.

[165] Fangzhuan Liu, Lingyu Wang, Qinjian Yin, and Bo Jiang, "Optimization of thermoelectric figure of merit in poly(p-phenylenediamine)/exfoliated graphene nanosheets composites," *RSC Adv.*, vol. 4, no. 93, pp. 51558–51568, 2014.

[166] Kongli Xu, Guangming Chen, and Dong Qiu, "Convenient construction of poly(3,4-ethylenedioxythiophene)-graphene pie-like structure with enhanced thermoelectric performance," *Journal of Materials Chemistry A*, vol. 1, no. 40, pp. 12395–12399, 2013.

[167] Begoña Abad, Irene Alda, Pablo Díaz-Chao, Hiroshi Kawakami, Albert Almarza, David Amantia, David Gutierrez, Laurent Aubouy, and Marisol Martín-González, "Improved power factor of polyaniline nanocomposites with exfoliated graphene nanoplatelets (GNPs)," *Journal of Materials Chemistry A* , vol. 1, no. 35, pp. 10450–10457, 2013.

[168] Jinglei Xiang and Lawrence T. Drzal, “Templated growth of polyaniline on exfoliated graphene nanoplatelets (GNP) and its thermoelectric properties,” *Polymer.*, vol. 53, no. 19, pp. 4202–4210, 2012.

[169] Yue Lin, Colin Norman, Deepanshu Srivastava, Feridoon Azough, Li Wang, Mark Robbins, Kevin Simpson, Robert Freer, and Ian A. Kinloch, “Thermoelectric Power Generation from Lanthanum Strontium Titanium Oxide at Room Temperature through the Addition of Graphene,” *ACS Appl. Mater. Interfaces*, vol. 7, no. 29, pp. 15898–15908, 2015.

[170] Olena Okhay, Sebastian Zlotnik, Wenjie Xie, Krzysztof Orlinski, Maria J. Hortiguela Gallo, Gonzalo Otero-Irurueta, Antonio J.S. Fernandes, Dorota A. Pawlak, Anke Weidenkaff, and Alexander Tkach, “Thermoelectric performance of Nb-doped $SrTiO_3$ enhanced by reduced graphene oxide and Sr deficiency cooperation,” *Carbon* ., vol. 143, pp. 215–222, 2018.

[171] Olena Okhay, Sebastian Zlotnik, Wenjie Xie, Krzysztof Orlinski, Maria J. Hortiguela Gallo, Gonzalo Otero-Irurueta, Antonio J.S. Fernandes, Dorota A. Pawlak, Anke Weidenkaff, and Alexander Tkach, “Thermoelectric performance of Nb-doped $SrTiO_3$ enhanced by reduced graphene oxide and Sr deficiency cooperation,” *Carbon* ., vol. 143, pp. 215–222, 2019.

[172] Li Hanbo, Zheng Ganhong, Dai Zhenxiang, Yuan Zhenheng, Wang Haiqiu, and Ma Yongqing, “Thermoelectric properties of Sr0.9La0.1TiO3and $Sr_{2.7}La_{0.3}Ti_2O_7$with 15% Ag addition,” *J. Rare Earths*, vol. 32, no. 4, pp. 314–319, 2014.

[173] G H Zheng , Z X Dai, H B Li, H Q Wang, Y Q Li , X F Xu, B T Huang, Y Q Ma and G Li “Improving the Thermoelectric Properties of $Sr_{0.9}La_{0.1}TiO_3$ by Ag Addition,” *Journal of Low Temperature Physics*, vol. 174, pp. 128–135, 2014.

[174] Mengjie Qin, Feng Gao, Gaogao Dong, Jie Xu, Maosen Fu, Yu Wang, Mike Reece, and Haixue Yan, “Microstructure characterization and thermoelectric properties of $Sr_{0.9}La_{0.1}TiO_3$ ceramics with nano-sized Ag as additive,” *J.Alloys Compd.*, vol. 762, pp. 80–89, 2018.

[175] Naoki Iwagami, Hajime Nagata, Isao Sakaguchi, and Tadashi Takenaka, “Diffusion behavior of Ag electrodes into $(Bi_{1/2}Na_{1/2})TiO_3$ ceramics,” *Journal of the Ceramic Society of Japan*, vol. 124, no. 6 pp. 644–647, 2016.

[176] Deepanshu Srivastava, Colin Norman, Feridoon Azough, Marion C. Schäfer, Emmanuel Guilmeau, and Robert Freer, “Improving the thermoelectric properties of $SrTiO_3$-based ceramics with metallic inclusions,” *J. Alloys Compd.*, vol. 731, no. January, pp. 723–730, 2018.

[177] Mengjie Qin, Feng Gao, An Min Wang, Chaochao Zhang, Qingqing Zhang, and Li Wang, “Fabrication and High-Temperature Thermoelectric Properties of Ti-Doped $Sr_{0.9}La_{0.1}TiO_3$ Ceramics,” *Ceram. Int.*, vol. 42, no. 15, 2016.

[178] Klaus Van Benthem, C. Elsasser, and Roger H French, “Bulk Electronic Structure of $SrTiO_3$: Experiment and Theory,” *J. Appl. Phys.*, vol. 90, pp. 6156–6164, 2001.

[179] A. Migliori, J.L. Sarrao, William M. Visscher, T.M. Bell, Ming Lei, Z Fisk, and R.G. Leisure, “Resonant ultrasound spectroscopic techniques for measurement of the elastic moduli of solids,” *Phys. B*, vol. 1, no. 183, pp. 1–24, 1993.

[180] Ruth Margaret Adams, “Structure-composition-property Relations in B-site Deficient Hexagonal Perovskite Systems,” PhD Thesis, University of Huddersfield, 2010.

[181] V. M Goldschmidt, *Geochemistry*. Oxford, Clarendon Press, 1958.

[182] Adrian P. Jones, C. Terry Williams, and Frances Wall, *Rare Earth Minerals: Chemistry, Origin and Ore Deposits*. United Kingdom: Chapman and Hall, 1996.

[183] U. Müller, *Ionic Compounds, in Inorganic Structural Chemistry*, Second Edi. United Kingdom: John Wiley & Sons, Ltd, Chichester, 2007.

[184] J. Venkatesh and V.R.K. Murthy, “Microwave dielectric properties of (Ba, Sr)$(Zn_{1/3}Ta_{2/3})O_3$ dielectric resonators,” in *Materials Chemistry and Physics 58 (3)*, Elsevier B.V., 1999, pp. 276–279.

[185] Nicola A. Hill, “Density Functional Studies of Multiferroic Magnetoelectrics,” *Annu. Rev. Mater. Res.*, vol. 32, no. 1, pp. 1–37, 2002.

[186] Jayakanth Ravichandran, “Thermal and Electrical Transport in Oxide Heterostrucutures,” PhD, Thesis, University of California, Berkeley, 2011.

[187] Jayakanth Ravichandran, Wolter Siemons, Dong-wook Oh, Justin T Kardel, Arvind Chari, Herman Heijmerikx, Matthew L Scullin, Arun Majumdar, Ramamoorthy Ramesh, and David G Cahill, “High temperature thermoelectric response of double-doped $SrTiO_3$ epitaxial films,” *Sci. Technol.*, p. 6, 2010.

[188] M.-H. Whangbo, E. Canadell, P. Foury, and J.-P. Pouget, “Hidden Fermi surface nesting and charge density wave instability in low-dimensional metals,” *Science (80-.).*, vol. 252, pp. 96–98, 1991.

[189] F. Krumeich, A. Hussain, C. Bartsch, and R. Gruehn, “Preparation and Structure of Niobium Tungsten-Oxides $(Nb,W)_{(17)}O_{-47}$ with Mixed-Valency,” *Zeitschrift fur Anorg. und Allg. Chemie*, vol. 621, no. 5, pp. 799–806, 1995.

[190] F. Krumeich, “Oxidation-Products of $Nb_7W_{10}O_{47}$ - A Transmission Electron-Microscopy Study,” *J. Solid State Chem.*, vol. 119, no. 2, pp. 420–427, 1995.

[191] Frank Krumeich, Michael Wörle, and Altaf Hussain, “Superstructure and twinning in the tetragonal tungsten bronze-type phase $Nb_7W_{10}O_{47}$,” *J. Solid State Chem.*, vol. 149, no. 2, pp. 428–433, 2000.

[192] Frank Krumeich, “Order and Disorder in Niobium Tungsten Oxides of the Tetragonal Tungsten Bronze Type,” *Acta Crystallogr. Sect. B Struct. Sci.*, vol. 54, no. 3, pp. 240–249, 1998.

[193] Michael R. Winter and David R. Clarke, “Oxide materials with low thermal conductivity,” *J. Am. Ceram. Soc.*, vol. 90, no. 2, pp. 533–540, 2007.

[194] Michael W. Gaultois, Jason E. Douglas, Taylor D. Sparks, and Ram Seshadri, “Single-step preparation and consolidation of reduced early-transition-metal oxide/metal n-type thermoelectric composites,” *AIP Adv.*, vol. 5, no. 9, 2015.

[195] P. G. Dickens and M. S. Whittingham, “The tungsten bronzes and related compounds,” *Q. Rev. Chem. Soc.*, vol. 22, no. 1, pp. 30–44, 1968.

[196] A. Magneli, “The Crystal Structure of Tetragonal Potassium,” *Ark Kemi*, vol. 1, no. 3, pp. 213–221, 1949.

[197] X. Zhu, M. Fu, M. C. Stennett, P. M. Vilarinho, I. Levin, C. A. Randall, J. Gardner, F. D. Morrison, and I. M. Reaney, “A Crystal-chemical framework for relaxor versus normal ferroelectric behavior in tetragonal tungsten bronzes,” *Chem. Mater.*, vol. 27, no. 9, pp. 3250–3261, 2015.

[198] Donna C. Arnold and Finlay D. Morrison, “B-cation effects in relaxor and ferroelectric tetragonal tungsten bronzes,” *J. Mater. Chem.*, vol. 19, no. 36, p. 6485, 2009.

[199] Yu Jiao Fang, Gao Shang Gong, Zerihun Gebru, and Song Liu Yuan, “Effects of A1 site occupation on dielectric and ferroelectric properties of $Sr_4CaRTi_3Nb_7O_{30}$ (R = Ce, Eu) tungsten bronze ceramics,” *Chinese Phys. B*, vol. 23, no. 12, 2014.

[200] Jason H. Chan, Jonathan A. Bock, Hanzheng Guo, Susan Trolier-McKinstry, and Clive A. Randall, “Filled oxygen-deficient strontium barium niobates,” *J. Am. Ceram. Soc.*, vol. 100, no. 2, pp. 774–782, 2017.

[201] Xiao Li Zhu, Xiao Qiang Liu, and Xiang Ming Chen, “Crystal Structure and Dielectric Properties of $Sr_5RTi_3Nb_7O_{30}$ (R=La, Nd, Sm, and Eu) Tungsten Bronze Ceramics,” *J. Am. Ceram. Soc.*, vol. 94, no. 6, pp. 1829–1836, 2011.

[202] Kun Lin, Yangchun Rong, Hui Wu, Qingzhen Huang, Li You, Yang Ren, Longlong Fan, Jun Chen, and Xianran Xing, “Ordered Structure and Thermal Expansion in Tungsten Bronze $Pb_2 K_{0.5}Li_{0.5}Nb_5O_{15}$,” *Inorg. Chem.*, vol. 53, no. 17, pp. 9174–9180, 2014.

[203] M R Ranga Raju and R N P Choudhary, “Diffuse phase transition in $Sr_5RTi_3Nb_7O_{30}$ (R=La, Nd and Sm),” *J. Phys. Chem. Solids*, vol. 64, no. 5, pp. 847–853, 2003.

[204] M.; Smirnov and P.; Saint-Grégoire, “An innovative approach to structural instabilities in tetragonal tungsten bronze crystals through the concept of rigid unit modes,” *Condens. Matter*, pp. 1–22, 2013.

[205] K L Ngai and T L Reinecke, “Structural instabilities and superconductivity in the alkali tungsten bronzes,” *J. Phys. F Met. Phys.*, vol. 8, no. 1, pp. 151–160, 1978.

[206] Jason Chan, “Study of Filled Tungsten Bronze Strontium Barium Niobate for Thermoelectric Applications,” M.Sc Thesis, Pennsylvania State University, US, 2015.

[207] Gerhard Henning Olsen, “Ferroelectric Tungsten B ronzes,” Norwagian University of Science and Technology, 2016.

[208] Naoki Wakiya, Jui-kai Wang, Atsushi Saiki, Kazuo Shinozaki, and Nobuyasu Mizutani, “Synthesis and Dielectric Properties of $Ba_{1-x} R_{2x/3}Nb_2O_6$ (R : Rare Earth) with Tetragonal Tungsten Bronze Structure,” *J. Eur. Ceram. Soc.*, vol. 19, pp. 1071–1075, 1999.

[209] Christophe P. Heinrich, Matthias Schrade, Giacomo Cerretti, Ingo Lieberwirth, Patrick Leidich, Andreas Schmitz, Harald Fjeld, Eckhard Mueller, Terje G. Finstad, Truls Norby, and Wolfgang Tremel, “Tetragonal tungsten bronzes $Nb_{8-x}W_{9+x}O_{47-\delta}$: optimization strategies and transport properties of a new n-type thermoelectric oxide,” *Mater. Horizons*, vol. 2, no. 5, pp. 519–527, 2015.

[210] Soonil Lee, Rudeger H.T. Wilke, Susan Trolier-Mckinstry, Shujun Zhang, and Clive A. Randall, “$Sr_xBa_{1-x}Nb_2O_{6-\delta}$ Ferroelectric- thermoelectrics: Crystal anisotropy, conduction mechanism, and power factor,” *Appl. Phys. Lett.*, vol. 96, no. 3, pp. 4–7, 2010.

[211] Yi Li, Jian Liu, Chun-Lei Wang, Wen-Bin Su, Yuan-Hu Zhu, Ji-Chao Li, and Liang-Mo Mei, “Thermoelectric properties of $Sr_{0.61}Ba_{0.39}Nb_2O_{6-\delta}$ ceramics in different oxygen-reduction conditions,” *Chinese Phys. B*, vol. 24, no. 4, p. 047201, 2015.

[212] G. Cerretti, M. Schrade, X. Song, B. Balke, H. Lu, T. Weidner, I. Lieberwirth, M. Panthöfer, T. Norby, and W. Tremel, “Thermal stability and enhanced thermoelectric properties of the tetragonal tungsten bronzes $Nb_{8-x}W_{9+x}O_{47}$ ($0 < x < 5$),” *J. Mater. Chem. A*, vol. 5, no. 20, pp. 9768–9774, 2017.

[213] Sadequa J. Patwe, Vasundhara Katari, Nilesh P. Salke, Sudhanshu K. Deshpande, Rekha Rao, Mayanak K. Gupta, Ranjan Mittal, S. Nagabhusan Achary, and Avesh K. Tyagi, “Structural and electrical properties of layered perovskite type $Pr_2Ti_2O_7$: experimental and theoretical investigations,” *J. Mater. Chem. C*, vol. 3, no. 17, pp. 4570–4584, 2015.

[214] A. Garbout and M. Férid, “Influence of Eu substitution for Gd on the structure and photoluminescent properties of $(Gd_{1-x}Eu_x)_2Ti_2O_7$ pyrochlore solid solutions,” *Adv. Powder Technol.*, vol. 28, no. 5, pp. 1382–1390, 2017.

[215] M. Saif, Magdy Shebl, A. Mbarek, A. I. Nabeel, R. Maalej, and R. Shokry, "Synthesis of non-toxic phosphor material based on pyrochlore-type dititanate ($Eu_{3+/}Y_2Ti_2O_7$)," *J. Photochem. Photobiol. A Chem.*, vol. 301, pp. 1–5, 2015.

[216] Jasmeet Kaur Gill, O. P. Pandey, and K. Singh, "Role of sintering temperature on thermal, electrical and structural properties of $Y_2Ti_2O_7$pyrochlores," *Int. J. Hydrogen Energy*, vol. 36, no. 22, pp. 14943–14947, 2011.

[217] Michel B. Johnson, David D. James, Alex Bourque, Hanna A. Dabkowska, Bruce D. Gaulin, and Mary Anne White, "Thermal properties of the pyrochlore, $Y_2Ti_2O_7$," *J. Solid State Chem.*, vol. 182, no. 4, pp. 725–729, 2009.

[218] Sulgiye Park, Maik Lang, Cameron L. Tracy, Jiaming Zhang, Fuxiang Zhang, Christina Trautmann, Matias D. Rodriguez, Patrick Kluth, and Rodney C. Ewing, "Response of $Gd_2Ti_2O_7$ and $La_2Ti_2O_7$ to swift-heavy ion irradiation and annealing," *Acta Mater.*, vol. 93, pp. 1–11, 2015.

[219] Jacob Shamblin, Cameron L. Tracy, Rodney C. Ewing, Fuxiang Zhang, Weixing Li, Christina Trautmann, and Maik Lang, "Structural response of titanate pyrochlores to swift heavy ion irradiation," *Acta Mater.*, vol. 117, pp. 207–215, 2016.

[220] Katlyn M. Turner, Dylan R. Rittman, Rachel A. Heymach, Cameron L. Tracy, Madison L. Turner, Antonio F. Fuentes, Wendy L. Mao, and Rodney C. Ewing, "Pressure-induced structural modifications of rare-earth hafnate pyrochlore," *J. Phys. Condens. Matter*, vol. 29, no. 25, 2017.

[221] Yuan Jian Zhong, Feridoon Azough, and Robert Freer, "The effect of $La_2Ti_3O_9$ second phase on the microstructure and dielectric properties of $La_2Ti_2O_7$ ceramics," *J. Eur. Ceram. Soc.*, vol. 15, no. 3, pp. 255–263, 1995.

[222] N. Zhang, Q. J. Li, S. G. Huang, Y. Yu, J. Zheng, C. Cheng, and C. C. Wang, "Dielectric relaxations in multiferroic $La_2Ti_2O_7$ ceramics," *J. Alloys Compd.*, vol. 652, pp. 1–8, 2015.

[223] Jibran Khaliq, Li Chunchun, Chen Kan, Shi Baogui, Ye Haitao, Antonio M. Grande, Haixue Yan, and Michael J. Reece, "Reduced thermal conductivity by nanoscale intergrowths in perovskite like layered structure $La_2Ti_2O_7$," *J. Appl. Phys.*, vol. 117, no. 7, pp. 2–8, 2015.

[224] Tanguy Pussacq, Houria Kabbour, Silviu Colis, Hervé Vezin, Sébastien Saitzek, Olivier Gardoll, Cédric Tassel, Hiroshi Kageyama, Christel Laberty Robert, and Olivier Mentré, "Reduction of $Ln_2Ti_2O_7$ Layered Perovskites: A Survey of the Anionic Lattice, Electronic Features, and Potentials," *Chem. Mater.*, vol. 29, no. 3, pp. 1047–1057, 2017.

[225] Junying Zhang, Wenqiang Dang, Zhimin Ao, Scott K Cushing, and Nianqiang Wu, “Band gap narrowing in nitrogen-doped $La_2Ti_2O_7$ predicted by density-functional theory calculations.,” *Phys. Chem. Chem. Phys.*, vol. 17, no. 14, pp. 8994–9000, 2015.

[226] Andrei V. Kovalevsky, Myriam H. Aguirre, Sascha Populoh, Sonia G. Patrício, Nuno M. Ferreira, Sergey M. Mikhalev, Duncan P. Fagg, Anke Weidenkaff, and Jorge R. Frade, “Designing strontium titanate-based thermoelectrics: insight into defect chemistry mechanisms,” *J. Mater. Chem. A*, vol. 5, no. 8, pp. 3909–3922, 2017.

Chapter 3: Experimental Procedure

3.1 Introduction

In this chapter, a description of the experimental procedures used in this work is given. It starts with the processing of the raw materials (starting powders), synthesis of the doped ceramics, followed by the methods used in the sintering and preparation of samples for analysis.

The processing method applied in this project is solid-state reaction (SSR). SSR is one of the oldest and most widely used approaches in preparing polycrystalline solid materials such as oxides. It is an effective industrial processing approach to obtain micro- or meso size powders [1], [2]. For nanoparticles, hydrothermal and wet chemical reactions are required [1]. SSR is a chemical reaction involving the mixture of the starting materials (reactants) as powders at high temperatures in the absence of a solvent. Stoichiometric amounts of the starting powders are mixed, ball milled and subjected to an initial heat treatment, known as calcination. The calcined powders are pressed into pellets and sintered in a furnace to form dense polycrystalline ceramics.

3.2 Ceramic Processing

3.2.1 Powder Preparation

Prior to use, all the starting materials; strontium carbonate, $SrCO_3$ (99.90 %, Sigma-Aldrich, UK), titanium (IV) oxide, TiO_2 (99.90 %, Sigma-Aldrich, UK), lanthanum (III) oxide, La_2O_3 (99.99 %, Sigma-Aldrich, UK), samarium (III) oxide, Sm_2O_3 (99.90 %, Stanford Materials Corporation, USA) and niobium (V) oxide, Nb_2O_5 (99.5 %, Stanford Materials Corporation, USA) were a dried. $SrCO_3$ powder was dried in a chamber furnace at 180 ^oC for 24 hours. TiO_2, La_2O_3, Sm_2O_3, and

Nb_2O_5 powders were dried in a clean chamber furnace at 900 °C for 8 hours and cooled to 200 °C. All dried powders were transferred to a vacuum desiccator and allowed to cool to prevent adsorption of moisture. Table 3.1 shows the starting oxide powders used in this study with their manufacturers, percentage purity and drying temperatures.

Stoichiometric proportions of the dried powders were weighed using a digital analytical weighing balance to a precision of ± 0.0001 g based on compositions shown in Table 3.2. Each composition was mixed using a ball mill in isopropanol (propan-2-ol, C_3H_8O) with 10 mm diameter yttria -stabilized zirconia (YSZ) milling media for 24 hours. After milling, the slurry was dried at 80 °C, sieved through a 250 µm mesh and calcined at 1423 – 1573 K for 6, 8 or 15 hours in air or 5 % H_2/N_2 mixed gas (depending on the composition) in an alumina crucible [3]. Calcination is important in order to decompose any carbonate present in the mixture and drive off absorbed moisture and volatile constituents, thereby obtaining a homogenous mix with smaller particle sizes.

Table 3.1. Starting materials, percentage purity and drying temperatures.

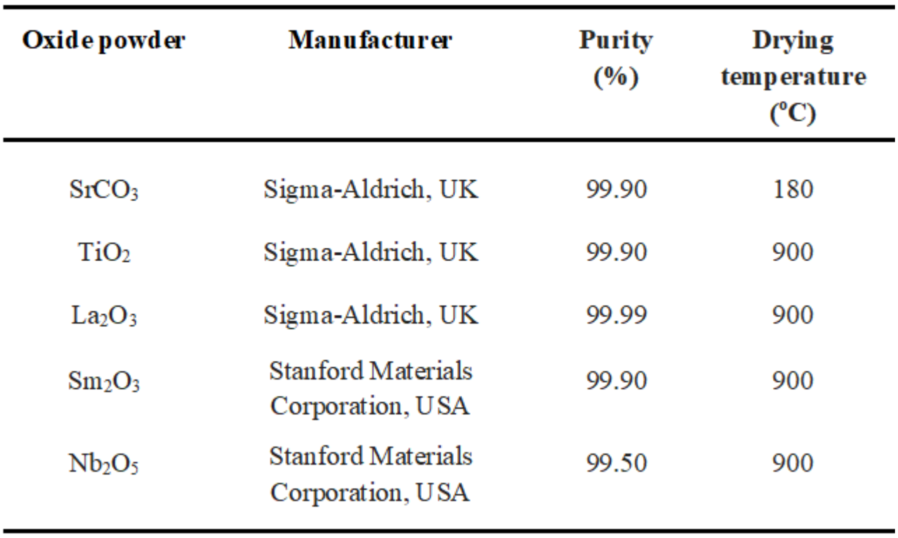

Oxide powder	Manufacturer	Purity (%)	Drying temperature (°C)
$SrCO_3$	Sigma-Aldrich, UK	99.90	180
TiO_2	Sigma-Aldrich, UK	99.90	900
La_2O_3	Sigma-Aldrich, UK	99.99	900
Sm_2O_3	Stanford Materials Corporation, USA	99.90	900
Nb_2O_5	Stanford Materials Corporation, USA	99.50	900

3.2.2 Pellet Preparation and Sintering

The two most common laboratory-based consolidation techniques to obtain a sintered ceramics are uniaxial pressing and/or cold isostatic pressing [3]. In this work, only uniaxial pressing method was used. Uniaxial pressing involves loading of finely grained, calcined powder into a cylindrical or oblong steel die and application of pressure to compact the powder. The pressure is applied along one axis using a hydraulic press handle [3]. Prior to application of the pressure, it needs to be tested in order to select the suitable compaction (low, moderate or high) for each calcined powder. For example, a low pressure compacted powder could lead to weak mechanical green body, hence difficult to be removed from the die, while high compaction leads to end-capping defect in the green body [4]. The calcined powders (~ 2 g per disc or bar pellet) were mixed with 5 wt. % poly vinyl alcohol (PVA) binder, ground and pressed into a 20 mm diameter (≤ 2 mm thickness) disc or 40 x 5 x 3 mm bar pellet in a uniaxial press using 31.2 MPa of applied load for ~ 1 minute.

The green pellets were placed in an alumina narrow boat-shaped crucible and pre-sintered in air at 873 K for 1 hour to burn-off the binder. It was followed by sintering the samples in air or in flowing 5 % H_2/N_2 gas at 1673 or 1773 K for 6 or 8 hours depending on the sample or composition. Heating and cooling rates of 5 ^oC/min and 10 ^oC/min, respectively were used. The calcination conditions (temperature and atmosphere) for the 5 % H_2/N_2 gas sintered compositions are presented in Table 3.3. Air sintered pellets were placed on platinum (Pt) foil in the crucible to prevent the pellets from reacting with the alumina crucible. For samples sintered in 5% H_2/N_2 gas, Pt foil was not used since it melts at high temperature in this atmosphere.

Table 3.2. Fabricated compositions in the La-Sm, Sm and Nb-doped ceramics

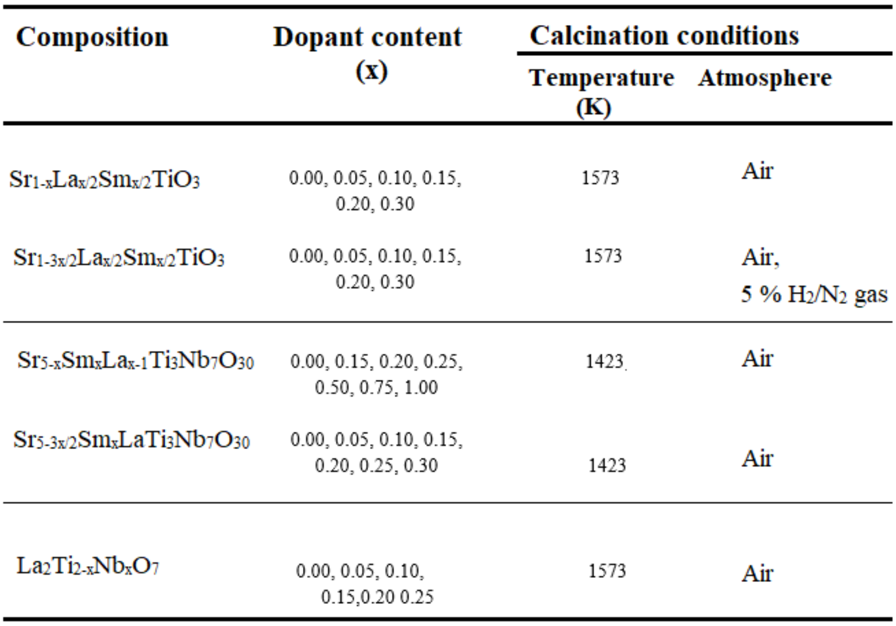

Composition	Dopant content (x)	Calcination conditions	
		Temperature (K)	Atmosphere
$Sr_{1-x}La_{x/2}Sm_{x/2}TiO_3$	0.00, 0.05, 0.10, 0.15, 0.20, 0.30	1573	Air
$Sr_{1-3x/2}La_{x/2}Sm_{x/2}TiO_3$	0.00, 0.05, 0.10, 0.15, 0.20, 0.30	1573	Air, 5 % H_2/N_2 gas
$Sr_{5-x}Sm_xLa_{x-1}Ti_3Nb_7O_{30}$	0.00, 0.15, 0.20, 0.25, 0.50, 0.75, 1.00	1423	Air
$Sr_{5-3x/2}Sm_xLaTi_3Nb_7O_{30}$	0.00, 0.05, 0.10, 0.15, 0.20, 0.25, 0.30	1423	Air
$La_2Ti_{2-x}Nb_xO_7$	0.00, 0.05, 0.10, 0.15,0.20 0.25	1573	Air

3.2.3 Polishing and Density Measurements

The sintered ceramics were wet polished with metallographic abrasive papers (120, 240, 400, 800, and 1200 grits in decreasing order of roughness) to remove surface impurities and produce smooth (and flat) surface samples. In carrying out this simple operation, care was taken to avoid introduction of non-uniformities (inconsistencies) in thickness of the samples.

The density of sintered ceramics is commonly determined using the direct measurement (geometric) method or Archimedes method. The experimental densities of the samples were determined by applying Archimedes principle using an electronic digital density balance (Mettler-Toledo AG Balance, Laboratory & Weighing Technologies, CH-8606 Greifensee, Switzerland) to an accuracy of ±0.0001 g. First, the temperature of the distilled water contained in a beaker used for the measurement was read (and recorded) from the thermometer inserted therein. Each of the samples was weighed in air, removed, and immersed in a distilled water and weighed. The density was automatically calculated using the following equation:

$$\rho_e = \rho_{H_2 0} * \frac{m_1}{m_1 - m_2} \qquad 3.1$$

where: ρ_e is the experimental density (g/cm^3) of the sample; ρ_{H20} is the density (g/cm^3) of distilled water at the experimental temperature; m_1 is the mass (g) of sample weighed in air and m_2 is the mass (g) of sample weighed when immersed in distilled water.

Because direct measurement method relies on the geometry of the sample, any error recorded in the length, width, thickness or radius will be integrated double fold into the volume, thereby inducing a high percentage error (1-2 %). Archimedes method, on the hand is unsuitable to give accurate or reliable result for porous (low density) samples [3]. Uncertainties in density measurement using Archimedes principle method are limited to errors due to measurement of weight of samples. Therefore, accurate measurement of weight could limit these errors. The typical uncertainty in the resultant density value for this method is ±0.05 %.

Table 3.3. Heat treatment conditions for H_2/N_2 gas sintered compositions

Composition	Code	Calcination conditions		Sintering conditions	
		Temperature (K)	Atmosphere	Temperature (K)	Dwell time (h)
$Sr_{1-x}La_{x/2}Sm_{x/2}TiO_3$	ESTO	1573	Air	1773	6
$Sr_{1-3x/2}La_{x/2}Sm_{x/2}TiO_3$	VSTO	1573	Air	1773	6
$Sr_{1-3x/2}La_{x/2}Sm_{x/2}TiO_3$	VSTO-H	1573	H_2/N_2	1773	8
$Sr_{5-x}Sm_xLa_{x-1}Ti_3Nb_7O_{30}$	SLTNe	1423	Air	1673	6
$Sr_{5-3x/2}Sm_xLaTi_3Nb_7O_{30}$	SLTNv	1423	Air	1673	6
$La_2Ti_{2-x}Nb_xO_7$	LTO	1573	Air	1773	6

3.3 Structural and Microstructural Characterisation

3.3.1 Particle Size Analysis (PSA)

Particle size distribution to determine the particle diameters of the raw materials and calcined powders after ball milling was carried out using a Mastersizer 3000 laser particle size analyser (Malvern Instruments Limited, Worcestershire, UK). A typical laser diffraction system such as Mastersizer 3000 is made up of three main systems [5]: optical bench; sample dispersion unit and instrument software. The optical bench is the measurement area through which the dispersed powder sample passes, and the laser beam illuminates the particles while the intensity of scattered light by the particles is accurately measured. The sample unit is designed to hold the sample (either wet or dry) and ensures that the correct concentration of the particles is channelled to the optical bench. The wet sample dispersion unit uses a liquid dispersant, e.g. distilled water, while a dry sample dispersion unit suspends the sample in a flowing gas stream (dry air).

The instrument software controls the system – controls the measurement process, analysis the scattering data generated and calculates the particle size distribution of the sample. A typical optical layout of a laser diffraction instrument is shown in Figure 3.1.

About 0.2 g of each sample powder was dissolved in distilled water. After initializing the analyser, the background was measured, and the dissolved powder was dispersed into a 500 ml beaker filled with distilled water which was placed in the wet sample dispersion unit. The dispersed powder was de-agglomerated for about 30 seconds using the ultrasonic unit of the analyser. Finally, the measurement commenced and automatically measured particle size to an accuracy of ±0.001 μm.

As the beam passes through the dispersed particulate sample, the angular intensity of the scattered light relative to the beam was measured. The scattered data were collected and analysed by the instrument software. The size of the particles that created the scattering pattern was calculated using the Mie theory of light scattering [5]. The Mie theory requires the optical properties (mainly the refractive index) of both the dispersant and the measured sample. Five measurements on each sample were repeated and out of which the average particle diameter was determined. The particle size was reported as a volume equivalent sphere diameter. The uncertainty in the particle size distribution measurements using the laser diffraction Mastersizer 3000 analyser is as low as ±0.6 % while the repeatability in the data is ±0.5 %.

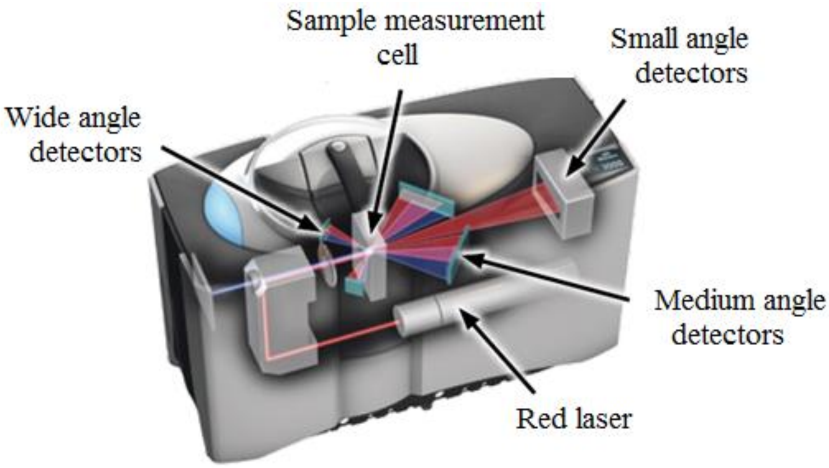

Figure 3.1. Schematic of a typical laser diffraction instrument showing the optical layout [5].

3.3.2 Thermogravimetric Analysis

Thermogravimetric analysis, TGA (or simply thermogravimetry) is a branch of thermal analysis that studies the change in mass of a sample as a function of temperature or time when subjected to a controlled temperature and atmosphere [5], [7]. TGA to determine the rate of oxygen uptake (weight variation) and thermal stability of samples in air at room temperature to 1000 ^{o}C was carried out using PerkinElmer Pyris 1 TGA (PerkinElmer Instruments, Norwalk, USA) computer-controlled analyser.

The sample pan (supported with precision or microbalance) of the analyser operates with a high resolution (sensitivity) and can detect a mass change as small as 0.1 µg up to a maximum capacity of 1300 mg. The furnace uses Pt/30 % Rh elements and change in weight of the ceramic samples were measured in air with a 5 ^{o}C/min heating rate up to 1000 ^{o}C and a 5 ^{o}C/min cooling rate to room temperature.

3.3.3 X-Ray Diffraction

X-ray diffraction (XRD) is a non-destructive technique used for identification of crystalline materials (in powdered and solid forms), qualitative analysis and determination of the phases present [8]. X-rays are electromagnetic radiation with high frequency (~ 10^{18} Hz), low wavelength (~ 10^{-10} m = 1 Å) and energies in the range of 100 eV-1000 KeV. An anode (a major component of x-ray tube where the x-rays are produced) converts the energy of the electrons (electronic energy) into x-rays and dissipates the heat produced in the process. For an effective performance, the anode materials are required to be metallic (i.e. conduct electrons), possess high melting point and produce characteristic wavelengths of about 0.5 to 2.3 Å. Typical anodes are chromium (Cr), iron (Fe), cobalt (Co), copper (Cu) and molybdenum (Mo) (Table 3.3). A Cu anode is the most commonly used in powder diffraction since its wavelength (λ) is comparable with the inter-atomic distances (~ 1.5 Å) required in XRD while Mo is preferred in single crystal diffraction.

Crystal (lattice) planes are described by notations called Miller indices. The Miller indices refer to the reciprocal of the points at which a, b, and c axes of the lattice planes are intersected by the plane, denoted h, k, and l from a defined origin. These lattice planes are arranged in space to form a series of parallel planes which are separated from each other by an interplanar spacing d. When an x-ray beam of wavelength λ is incident on the crystal planes of a crystalline material at an angle θ, a constructive interference of the diffraction occurs when Bragg's law (Figure 3.2) is satisfied, i.e. when AC+BC is equal to a whole number of wavelength (nλ). Bragg's law is expressed as:

$$n\lambda = 2\mathrm{d}\sin\theta \qquad 3.2$$

where n is an integer representing the order of the diffraction peak. The signals generated are then converted into peaks (fingerprints) by the diffractometer.

Table 3.4. Characteristic wavelengths of common anode materials used in XRD operation [9]. Kα is the average value derived from $\lambda_{average} = (2\lambda K\alpha_1 + \lambda K\alpha_2)/3$. Kα1 and Kα2 are two characteristics components of Kα radiation.

Anode	Wavelength (Å)		
	Kα	**$K\alpha_1$**	**$K\alpha_2$**
Cr	2.29105	2.28975(3)	2.293652(2)
Fe	1.93739	1.93608(1)	1.94002(1)
Co	1.79030	1.78900(1)	1.79289(1)
Cu	1.54187	1.5405929(5)	1.54441(2)
Mo	0.71075	0.7093171(4)	0.71361(1)

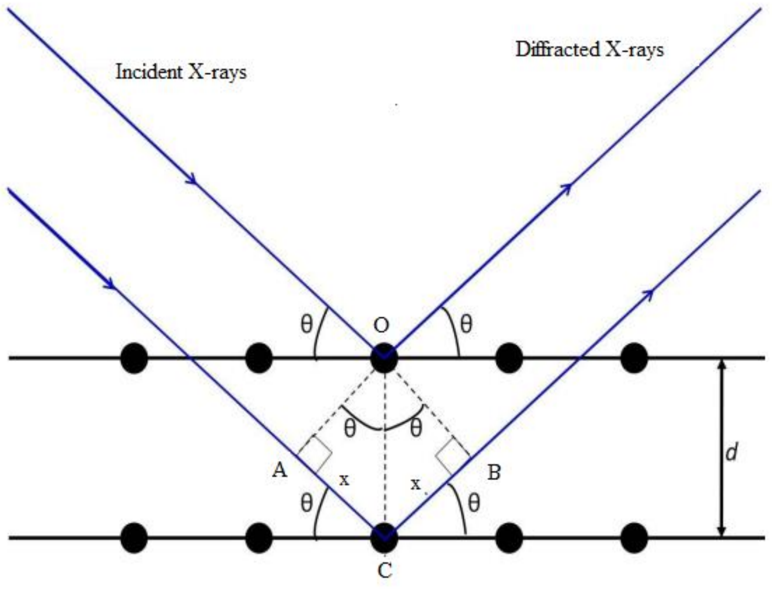

Figure 3.2. Schematic diagram of an X-ray beam interacting with crystal planes and illustrating Bragg’s law.

In this work, the crystal structures of starting materials, calcined powders and the crushed sintered pellets were characterized by powder x-ray diffraction with Cu Kα radiation with λ = 1.5406 Å using Siemens D5000 x-ray diffractometer (Siemens Analytical X-ray Instruments Inc., Madison W1, 53719) and D2 phaser diffractometer (Bruker AXS GmbH, Karlsruhe, Germany) operated with 40 kV voltage, 40 mA current and 30 kV voltage, 10 mA current, respectively.

A specimen holder was filled with the powder sample and gently pressed down with a glass slide so that the top of the sample is on the same level with the top of the specimen holder. This simple precaution is necessary to prevent "specimen height displacement error". After loading the sample into the diffractometer, the scan was conducted across the 2θ range of 20 – 80 degrees with a step size of 0.01° or 0.02° at a scan rate of 1°/min. Phase identity and purity of the collected data were analysed using the "Bruker Eva COD" and "ICDD Sleve+ PDF-4+" software [10], [11]. The theoretical density, ρ_{th} was calculated from the equation below [12]:

$$\rho_{\mathrm{th}} = \frac{(\mathrm{FW} * \mathrm{Z} * 1.66)}{\mathrm{V}} \quad , \qquad 3.3$$

while the relative density, ρ_r (%) was determined from the experimental density over the theoretical density [13];

$$\rho_r = \frac{\rho_e}{\rho_{th}} * 100 \qquad 3.4$$

where: FW is formula weight of the sample (g/mol); Z is the number of atoms per unit cell and V is the cell or lattice volume of the sample ($Å^3$) which was calculated using the lattice parameter constants from XRD data of the crushed pellets. The errors associated with the calculation of lattice parameters are limited by specimen displacement, offset of 2Theta (2θ) degrees and peak position which amount to uncertainties of ±0.001 Å.

3.3.4 Scanning Electron Microscopy (SEM)

A scanning electron microscope, SEM is an instrument used for the observation of solid specimen surfaces. According to Australian Microscopy & Microanalysis Research Facility online learning module [14], SEM is a tool for seeing invisible worlds of microspace (1 micron = 10^{-6} m) and nanospace (1 nanometer = 10^{-9} m). SEM uses a focussed incident electron beam of high energy to generate a variety of emitted signals when it strikes the specimen surface. SEM uses these signals to observe, analyse and interpret information such as microstructure, chemical composition, morphology (texture) and topography (structural shape) of specimens at magnifications ranging from 10x to ~ 300,000x.

When the primary (incident) electron beam strikes the sample, it penetrates to a depth ~ 1 μm forming a limiting interaction volume from which several signals (radiations) are emitted as shown in Figure 3.3(a). These signals include secondary electrons (SEs), backscattered electrons (BSEs), characteristic x-rays, cathodoluminescence (photons) and auger electrons. Secondary electrons (SEs) originate from the atoms of the sample and are released when electron beam interacts inelastically with lower energy shell of sample elements. The electrons are released from topmost regions (~ 15 nm) from the sample surface [14]. SEs have low energy (< 50 eV), and very useful for the inspection of the topography of the sample surface. However, BSEs originate from deeper regions of the sample and are reflected back after elastic interactions between the primary electron beam and the sample nucleus. Backscattered electrons show high sensitivity to atomic number of sample elements. The higher the atomic number (Z) of an element, the brighter the sample image appears. For example, iron, Fe atoms (Z = 26) scatter more electrons back towards the detector than the lighter aluminium, Al (Z =13) atoms, hence shows a brighter SEM image.

Typically, SEM consists of three main components [14]: a microscope column; ancillary equipment unit and the computer device. The microscope column contains the electron gun at the top, followed by the column, magnetic lens system and the specimen chamber at the base. The electron gun generates the electrons, while the "column" is the channel through which the electron beam travels. The magnetic lens system (comprising the condenser lenses, deflection, or scan coils and final or objective lenses) processes the electron beam by controlling its intensity and brings the electron into focus on the specimen. The specimen chamber houses the specimen and maintains a high vacuum condition in order to minimize scattering (attenuation) of the electron before reaching the specimen. Generally, the electron gun, lenses and specimen chamber must be under a high vacuum for an efficient operation of the SEM. This condition is expedient because an electron cannot freely travel through air.

The ancillary equipment unit includes the pump system (to keep the system under vacuum), water chilling system and the electron detectors. The water chilling system maintains the magnetic lenses at a constant temperature of 20 ^{o}C during the operation. When the chiller fails, the lenses heat up and the SEM will automatically shut down. Electron detectors collect the generated signals from the specimen. The collected signals are converted to photons using a scintillator, amplified in a photo multiplier, hence converted to electrical signals [14]. The computer device drives the SEM and displays the image on the viewing screen. A simplified SEM operational set up is shown in Figure 3.3(b). The quality of an image produced in SEM is controlled by the properties of the sample, sample preparation technique and instrumental parameters such as accelerating voltage, scan speed, working distance and spot size.

Samples for microstructural examination were prepared by grinding and polishing to a mirror finish on a diamond polishing wheel. The polished samples were thermally etched at 90 % of the sintering temperature in air or 5 % H_2/N_2 gas (depending on the processing atmosphere) for 30 minutes to reveal the grain structures. Thermally etched samples were mounted on aluminium pin-type stubs with adhesive tapes. Powder samples of the starting materials and calcined powders were dispersed in acetone and deposited on adhesive tape mounted on pin-type stubs and allowed to dry.

Samples prepared for SEM were carbon coated using Edwards vacuum carbon coater (Edwards High Vacuum Ltd, England) to make them conductive and maximise secondary electron signal from the specimen. Conductive samples prevent “charging”. Charging is a build-up of negative charge at the point where the electron beam strikes the sample surface. Charging causes uncommon effects such as abnormal contrast and image deformation. The edges (sides) of the mounted samples are obviously poorly coated. Therefore, conductive silver-based paste (Agar Scientific Ltd, Stansted, UK) was applied on the edges. After carbon coating of the samples, the microstructures were examined using XL 30 S-FEG (Philips/FEI) at an accelerating voltage of 5-20 kV. Secondary electron images were obtained from the sample surfaces.

The average grain size in the samples was calculated using the line-intercept method [15], [16] after Mendelson model [17]. The procedure involves taken measurements from the photomicrograph of the SEM images. A transparent overlay or intersection consisting of one or more test lines of known length and placed over the micrograph. The number of intercepts between the test lines and grain boundaries are counted. Afterwards, the average grain size, Đ is calculated using the following equation [16]:

$$\text{Đ} = 1.56\frac{C}{MN} \qquad 3.5$$

where: C = total length of the test line; N = number of intercepts; M = magnification of the photomicrograph and 1.56 is the constant of proportionality (correction factor). This method, however, is suitable only for a full dense single-phase microstructure. For a multi-phase microstructure, the defects (secondary phase, porosity, etc) may have an effect on the accuracy of the measurement.

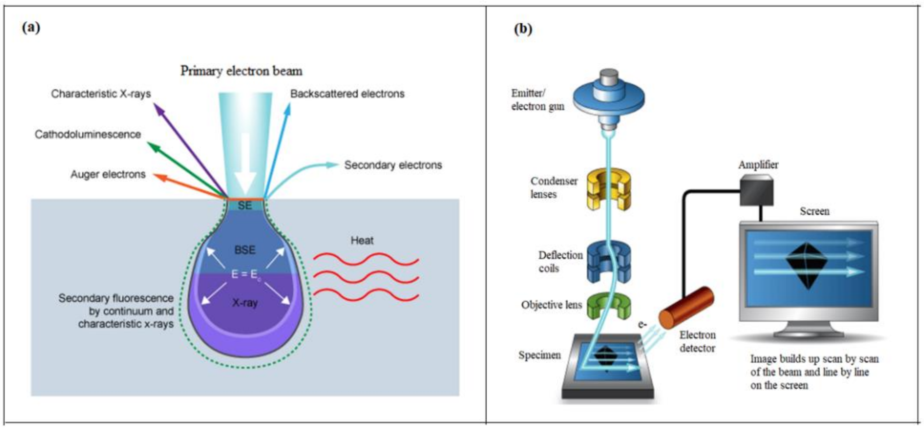

Figure 3.3. Schematics of (a) scanning electron microscope operational set-up and (b) Primary electron beam-Sample interaction [14].

3.3.5 Energy Dispersive X-Ray Spectroscopy (EDX)

Energy dispersive spectroscopy (EDX) is a chemical microanalysis technique linked to SEM to analyse characteristic x-ray spectra by measuring the energies of the x-rays. As the electron beam strikes the sample, the EDX technique detects the x-rays emitted and characterizes the elemental composition of the sample. The x-rays are generated within the whole region of the interaction volume as shown in Figure 3.3(a). As an electron is removed from the inner shell of the atom by the incident primary electron beam, the atom becomes ionized and unstable. The atom regains its stability when an electron from an outer shell fills the inner shell vacancy, and in so doing, x-ray photon is emitted. The energy of the emitted photon is characteristic of the energy difference between the two energy states for the atom [18].

EDX system is made up of three major components; x-ray detector, pulse processor and analyser. The x-ray detector identifies and converts the x-rays into electronic signals while the pulse processor measures the electronic signals. In measuring the electronic signals, the energy of each x-ray is identified. The analyser finally displays and interprets the x-ray data.

The data generated for collection consists of spectra with peaks corresponding to all the different elements that are present in the sample. The software (analyser) enables auto-identification of the peaks and calculation of the atomic percentage of the elements detected. These spectra together with the atomic percent of the elements confirmed in each of the samples are collected.

Sources of errors associated with EDX analysis are related to the sample, SEM, EDX detector and the data software [14]. Therefore, the accuracy of EDX analysis depends on the sum of all these errors, hence difficult to quantify. The combined uncertainties limit the precision of EDX analysis to ±2 % [14]

In this work, the EDX analysis was performed using INCA Energy EDS X-ray Microanalysis System (Oxford Instruments Analytical, UK) comprised of INCA EDS detectors, INCAx-stream pulse processors and INCAEnergy software and linked to Philips XL 30 S-FEG SEM.

3.4 Thermoelectric Characterisation

3.4.1 Electrical Conductivity (σ) and Seebeck Coefficient (S)

The electrical conductivity and Seebeck coefficient of the samples were measured simultaneously by employing the Van der Pauw four-point probe method (commonly known as four-point probe method). The four-point probe method was first proposed in 1916 by Frank Wenner to measure the earth's resistivity [19]. It was later used by Valdes in 1954 for measuring semiconductor wafer resistivity [20]. Four-point probe method is preferable to other conventional methods to measure the resistivity of low resistive (conductive) samples [3]. It provides less internal resistance and a better accuracy. The four-point probe method involves bringing four-independent electrical terminals (probes) in contact with a sample surface of unknown resistance [21]. Two of the terminals (outer probes) are utilized for sourcing current (current contacts). A pre-set electrical current is passed through the outer probes from an external source. The other two terminals (inner probes) are used for measuring the resulting voltage drop (voltage contacts) across the surface of the sample. To obtain reliable data, the four-point probe method requires the sample to be homogeneous (devoid of holes or cavities) and flat (constant thickness) [22].

A rectangular-shaped sample of about 20 mm in length, 3 mm in width and ≤ 2 mm in thickness or a circular-shaped pellet of 16 mm in diameter with ≤ 2 mm thickness was prepared for electrical conductivity and Seebeck coefficient measurements. The Van der Pauw four-point probe method was employed for the simultaneous measurements of the electrical conductivity and Seebeck coefficient under identical conditions using a Netzsch SBA 458 Nemesis (NETZSCH-Geratabau GmbH, Germany) Seebeck coefficient and electrical conductivity analyser. The sample was placed with both ends on a sample support in the carrier system unit of the Nemesis measuring instrument. The carrier system enclosed in a furnace is constructed in such a way to measure simultaneously the Seebeck coefficient and electrical conductivity of solid state materials using two thermocouples and two current pins arranged in a four-linear electrical terminals [23], [24]. The carrier system contains a sample support which has two micro heaters (to generate a temperature gradient, ΔT between both ends of the sample), two current pins (outer probes) and two thermocouples (inner probes) (Figure 3.4). In SBA 458 Nemesis instrument [23], the distance between the current pins is 11.50 mm, while the distance between the thermocouples is 8.25 mm.

To initiate the measurement process, a pre-set program of temperature steps (room temperature to 700 ^{o}C) was set up, and the furnace purged with argon gas. As the furnace was heated, it followed the pre-set temperature steps and measured the electrical conductivity on reaching the temperature using the current pins. Thereafter, the micro heaters generated a temperature gradient within the sample thereby measuring the resulting voltage (ΔU) using the thermocouples and the Seebeck coefficient ($S = \Delta U/ \Delta T$) calculated. This procedure was repeated automatically at every pre-set temperature until the maximum temperature (973 K) was reached. The furnace was allowed to cool down to room temperature before removing the sample.

The uncertainty in the electrical conductivity and Seebeck coefficient measurements using the SBA 458 Nemesis instrument is as high as ±10 % while the repeatability in the data is ±7 % and ±3 % for σ and S, respectively. However, the probes (current pins and thermocouples) of the Netzsch Nemesis risk degradation emanating either from aging or reaction with impurities within the sample or lack of contact with the sample. In order to determine the proper alignment of the data, multiple heating and cooling cycles are undertaken and, in some instances, the probes are properly cleaned or replaced.

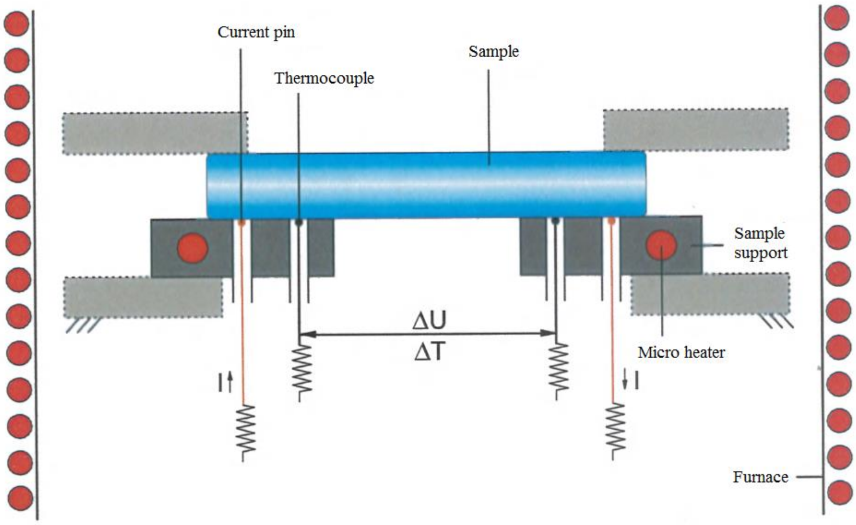

Figure 3.4. Simultaneous electrical conductivity and Seebeck coefficient measurement set up for the SBA 458 Nemesis instrument in the temperature range between room temperature and 700 °C [23]. It allows samples of different geometries (square, rectangle, round/disc and strips) to be measured.

3.4.2 Thermal Conductivity

The commonly used techniques for measuring the thermal conductivity of bulk materials include steady-state absolute method, comparative technique, laser flash diffusivity (LFD) method and transient plane source (TPS) method [25]. In this work, LFD method was used.

Laser flash method utilizes non-contact, non-destructive temperature sensing to achieve a high precision [25]. The LFD method was first introduced by Parker *et al* in 1961 [26] and has remained a preferred method for researchers of thermophysical properties of materials and is the most common method for the determination of thermal conductivity of bulk ceramics [3]. A typical arrangement of LFD method is shown in Figure 3.5. It uses instantaneous heat source (laser or xenon flash) to heat up the sample's front side, and a high infra-red (IR) detector to measure the time-dependent temperature rise at the rear (back) side [25]. Thermal diffusivity values are computed from the temperature rise versus time data curve (Figure 3.5b). The higher the thermal diffusivity of the sample, the faster the heat transfer and temperature rise on the rear side. The heat conduction is one dimensional with the presumption that no lateral heat loss occurs.

For a good detector signal to be obtained in a laser flash system, the test sample must not be transparent to IR radiation and/or reflective to visible light, but required to exhibit excellent emission-absorption capacity [27]. Unfortunately, most materials in nature do not fulfil these important criteria, e.g. most polymers and glasses are transparent to IR radiation while metals are highly reflective to visible light. Therefore, prior to LFD method measurement, all samples are required to be coated in order to improve emission-absorption properties and optimize the signal-to-noise ratio [27]. The sample is either coated with graphite or sputtered with gold. Graphite is commonly preferred as the standard coating film. It is applied by spraying a layer of graphite on both sides of the sample. The graphite layer acts as an absorber on the front side (to prevent the penetration of laser beam into the sample) and acts as an emitter on the rear side (to prevent viewing of the IR detector into the sample) [28].

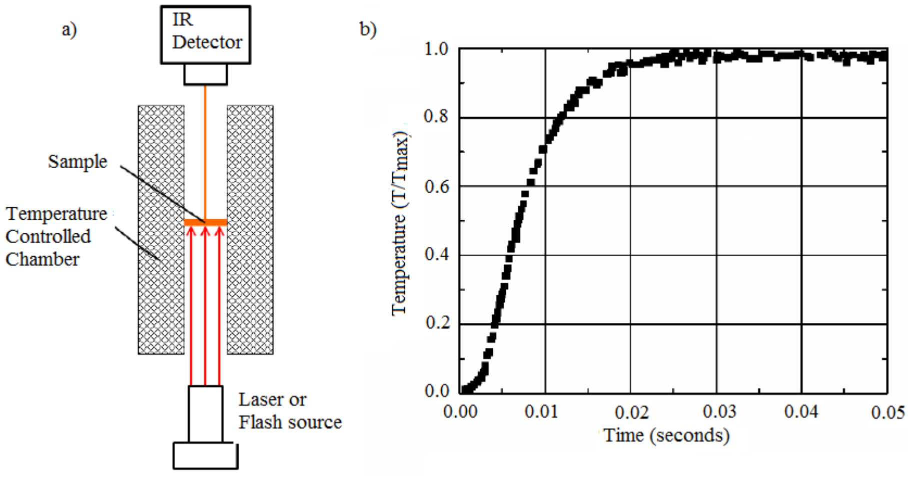

Figure 3.5 (a) Schematic measurement set up for the laser flash diffusivity (LFD) method. A light source (laser or flash) heats the front side of the planar-shaped sample and an IR detector measures the resulting temperature rise of the rear surface of the sample.(b) An exemplary illustration of a measured time-dependent temperature rise data curve [25].

The thermal conductivity measurements were performed using a thermal properties analyser (Anter Flashline TM 3000, Pittsburgh, PA 15235, USA) with High Speed Xenon Discharge (HSXD) pulse source and IR furnace operated with nitrogen gas. A square sample of 10 x 10 mm with ~ 1.5 mm thickness was prepared for the measurements. The density of the sample measured using Archimedes method was keyed into the program software. The sample was cleaned with isopropanol, coated with graphite aerosol on both sides and allowed to dry. The prepared sample and a thermographite reference material were placed in different sample holders and positioned on a sample chamber (carousel) aligned with graphite foil located in the furnace. Thermographite is noted for its stability and well documented thermophysical properties, hence it is used as a common reference material in LFD method.

As the furnace was heated, it followed predetermined temperature steps (room temperature to 700 ^{o}C). At each temperature, the sample surface (front side) was irradiated with energy pulse from the HSXD. The energy pulse in turn resulted in a homogeneous temperature rises at the sample surface. The resulting temperature rise of the sample rear surface was measured by a high speed IR detector. Thermal diffusivity and specific heat values of the samples were then evaluated from the time-dependent temperature rise data (signal) generated. Combining the thermal diffusivity (α), specific heat capacity (C_p) and density (ρ) values, the total thermal conductivity (k) of the sample was calculated using the following equation with expanded uncertainty of ± 4 % for Anter Flashline thermal properties analyser:

$$\mathrm{k(T)} = \alpha(\mathrm{T}) * \mathrm{C_p} * \rho(\mathrm{T}) \qquad 3.6$$

where T is the predetermined temperature.

The determination of k using the laser flash system is the most significant source of error for the calculation of thermoelectric figure of merit. This is obvious because, measurement of k involves the integration of density and specific heat capacity data which have their own errors. To minimize the uncertainty resulting from density measurement via Archimedes principle, use of high density samples are encouraged. Porous samples can absorb the liquid, leading to an overestimation of the density values [29]. In as much as graphite coating of the sample prior to measurement is pertinent to ensure excellent emissivity and absorption of the laser impulse and detector signal [27], [29] , thin coatings are required for reliable diffusivity data. Excess graphite coatings of samples could cause errors [29]. In controlling the errors inherent in C_p measurement, the thickness of the sample should be thin enough to allow the value of $t_{1/2}$ to be ≤ 0.3 s, thereby minimizing heat losses [3]. $t_{1/2}$ is the time required of the temperature to increase to half-maximum, and it is utilized in calculating the thermal diffusivity [29]. With these measures in place, the errors in ZT can be minimized. However, the accuracy and percent errors associated with the individual measurements of σ, S and k lead to a final uncertainty of ±14 % in ZT.

References

[1] Yucheng Lan, Austin Jerome Minnich, Gang Chen, and Zhifeng Ren, "Enhancement of Thermoelectric Figure-of-Merit by a Bulk Nanostructuring Approach," *Adv. Funct. Mater.*, vol. 20, pp. 357–376, 2010.

[2] C. Suryanarayana, "Mechanical alloying and milling," *Prog. Mater. Sci.*, vol. 46, no. 1–2, pp. 1–184, 2001.

[3] R. Boston, W. L. Schmidt, G. D. Lewin, A. C. Iyasara, Z. Lu, H. Zhang, D. C. Sinclair, and I. M. Reaney, "Protocols for the fabrication, characterization, and optimization of n-type thermoelectric ceramic oxides," *Chem. Mater.*, vol. 29, no. 1, pp. 265–280, 2017.

[4] Ajit Singh and Nuclear Fuel Complex, "End-capping and other defects in pressed ceramic compacts," *Indian Journal of Engineering and Materials Sciences*, vol. 3, no.5 , pp. 196–200, October, 1996.

[5] "A Basic Guide to Particle Characterization," Inform White Paper, *Malvern Instruments Ltd.*, pp. 1–26, 2012.

[6] Perkin Elmer, *Pyris Software for Windows*. USA.: Perkin Elmer LLC., 1999.

[7] PerkinElmer, *Thermogravimetric Analysis (TGA) A Beginner ' s Guide*. Waltham, USA: Perkin Elmer Inc., 2010.

[8] B.D Cullity and S.R. Stock, *Elements of X-Ray Diffraction*, Third Edit. New York: Prentice -Hall, 2001.

[9] Vitalij Pecharsky and Peter Zavalij, *Fundamentals of Powder Diffraction and Structural Characterization of Materials.*, Second Edi. New York, USA: Springer+ Business Media Inc., 2005.

[10] Saulius Graulis, Daniel Chateigner, Robert T. Downs, A. F.T. Yokochi, Miguel Quirós, Luca Lutterotti, Elena Manakova, Justas Butkus, Peter Moeck, and Armel Le Bail, "Crystallography Open Database - An open-access collection of crystal structures," *J. Appl. Crystallogr.*, vol. 42, no. 4, pp. 726–729, 2009.

[11] T. G. Fawcett, F. Needham, C.E. Crowder, and S. Kabekkodu, "Advanced Materials Analysis using the Powder Diffraction File," in *10th National Conference on x-ray Diffraction and ICDD Workshop*, 2009, pp. 1–3.

[12] Anthony R. West, *Solid State Chemistry and its Applications*, Second Edi. West Sussex: Willey and Sons Limited, 2014.

[13] Hongchao Wang and Chunlei Wang, “Thermoelectric properties of Yb-doped $La_{0.1}Sr_{0.9}TiO_3$ ceramics at high temperature,” *Ceram. Int.*, vol. 39, no. 2, pp. 941–946, 2013.

[14] Myscope, *Introduction to Scanning Electron Microscopy*. Australian Microscopy & Microanalysis Research Facility, www.ammrf.org.au/MyScope, 2014.

[15] Jason H. Chan, Jonathan A. Bock, Hanzheng Guo, Susan Trolier-McKinstry, and Clive A. Randall, “Filled oxygen-deficient strontium barium niobates,” *J. Am. Ceram. Soc.*, vol. 100, no. 2, pp. 774–782, 2017.

[16] J. C Wurst and J. A Nelson, “Lineal Intercept for Measuring Grain Size in Two-Phase Polycrystalline Ceramics,” *J. Am. Ceram. Soc.*, vol. 55, no. 2, p. 109, 1972.

[17] Mendelson .MI, “Average Grain Size in Polycrystalline Ceramics,” *J. Am. Ceram. Soc.*, vol. 52, no. 8, pp. 443–446, 1969.

[18] David Brandon and Wayne D. Kaplan, *Microstructural characterization of Materials*, Second Edition, New Jersey: Wiley and Sons, *2008*.

[19] F. Wenner, “A method of measuring earth resistivity,” *Bull. Bur. Stand.*, vol. 12, no. 4, p. 469, 1916.

[20] L B Valdes, “Resistivity Measurements on Germanium for Transistors,” in *Proceedings of I-R-E*, 1954, vol. 42, pp. 420–427.

[21] Valentin Garcia-Vazquez, “Biased four-point probe resistance,” *Rev. Sci. Instrum.*, vol. 88, no. 11, 2017.

[22] Johannes De Boor and Volker Schmidt, “Efficient thermoelectric van der Pauw measurements,” *Appl. Phys. Lett.*, vol. 99, no. 2, pp. 5–7, 2011.

[23] Thomas Denner, *Operating Instructions SBA 458 Nemesis.pdf*. Wittelsbacher, Germany: NETZSCH-Geratebau GmbH, http://www.netzsch-thermal-analysis.com, 2015.

[24] Netzsch, *Simultaneous Determination of Seebeck Coefficient and Electrical Conductivity-SBA 458 Nemesis*. Germany: NETZSCH-Geratebau GmbH, 2015.

[25] Dongliang Zhao, Xin Qian, Xiaokun Gu, Saad Ayub Jajja, and Ronggui Yang, “Measurement Techniques for Thermal Conductivity and Interfacial Thermal Conductance of Bulk and Thin Film Materials,” *J. Electron. Packag.*, vol. 138, no. 4, pp. 1–64, 2016.

[26] W. J. Parker, R. J. Jenkins, C. P. Butler, and G. L. Abbott, “Flash method of determining thermal diffusivity, heat capacity, and thermal conductivity,” *J. Appl. Phys.*, vol. 32, no. 9, pp. 1679–1684, 1961.

[27] Fabia Neidhardt, “When and How Must Samples Be Coated During LFA Measurements,” *Appl. Note-Netzsch*, pp. 1–4, 2014.

[28] Mikko Ruoho, Kjetil Valset, Terje Finstad, and Ilkka Tittonen, “Measurement of thin film thermal conductivity using the laser flash method,” *Nanotechnology*, vol. 26, no. 19, 2015.

[29] Kasper A. Borup, Johannes De Boor, Heng Wang, Fivos Drymiotis, Franck Gascoin, Xun Shi, Lidong Chen, Mikhail I. Fedorov, Eckhard Müller, Bo B. Iversen, and G. Jeffrey Snyder, “Measuring thermoelectric transport properties of materials,” *Energy Environ. Sci.*, vol. 8, no. 2, pp. 423–435, 2015.

Chapter 4: Powder Characterisation

4.1 Characterisation of Raw Powders

Solid state reaction technique depends on accurate stoichiometry of the raw materials and even distribution (homogeneity) of the constituent ions [1]. To ensure optimum reproducibility and reliability of experimental data, particle size, phase and microstructural analyses of the raw and calcined powders were carried out.

4.1.1 Strontium Carbonate, $SrCO_3$

The $SrCO_3$ powder with 99.9% purity used in this work was supplied by Sigma-Aldrich Company Ltd, UK. Figure 4.1 depicts the XRD patterns of $SrCO_3$ powder, showing that all diffraction peaks may be indexed as strontium carbonate according to the PDF card No. (PDF# 01-071-2393) with no secondary phases. SEM images and EDX trace of the $SrCO_3$ powder (Figure 4.2) revealed rod-like particles and presence of Sr, C and O elements. No secondary phase was confirmed. The particle diameter distribution is shown in Figure 4.3. The mean particle size (or diameter), d_{50} of $SrCO_3$ was 4.3 μm with a d_{90} (cumulative 90 % point of diameter) of 10.7 μm, i.e. 90 % of sample has particle size $\leq$ 10.7 μm.

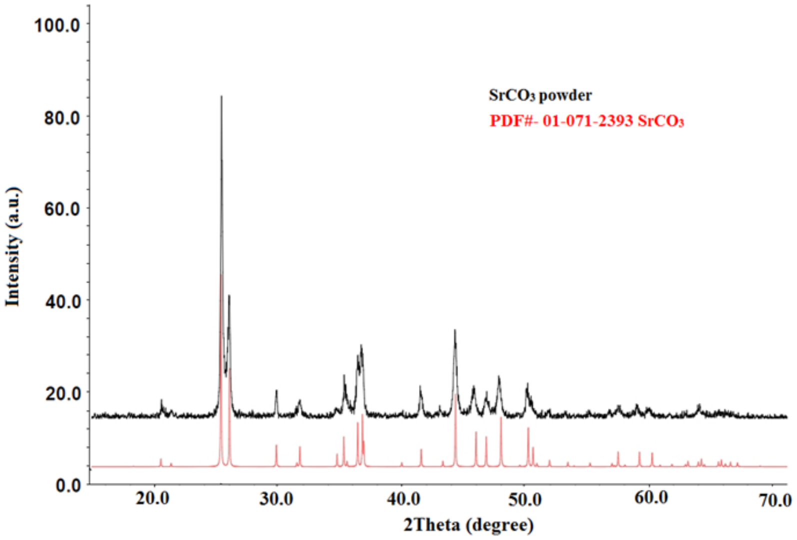

Figure 4.1. XRD pattern of $SrCO_3$ powder.

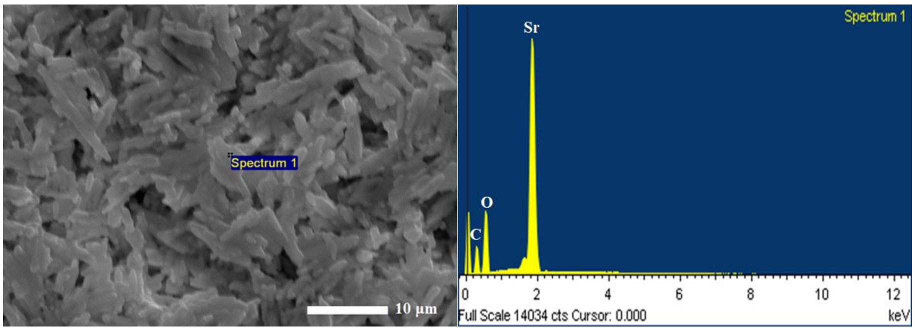

Figure 4.2.SEM image and EDX trace of $SrCO_3$ powder.

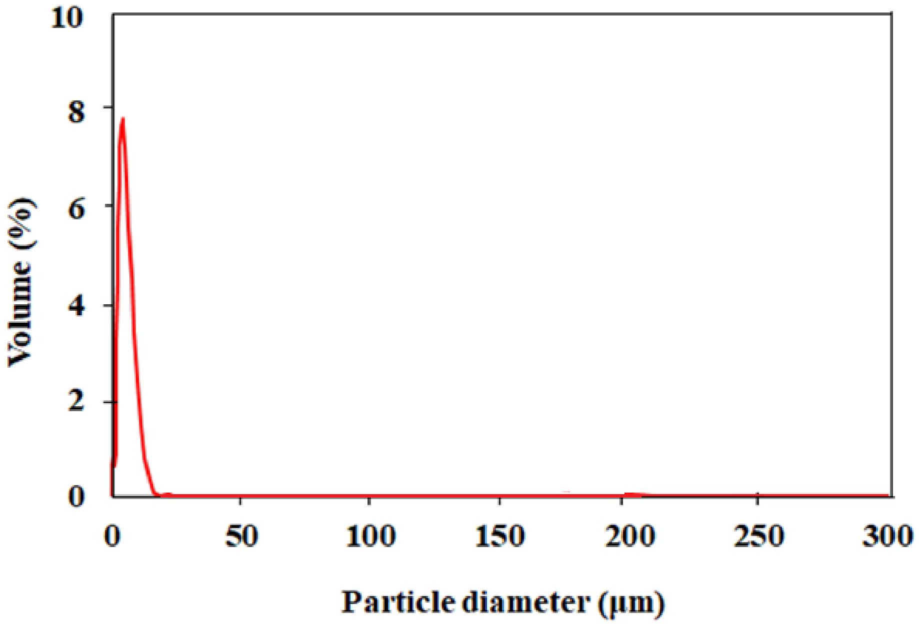

Figure 4.3. Particle size distribution of $SrCO_3$ powder.

4.1.2 Titanium (IV) Oxide, TiO_2

Titanium (IV) oxide powder with 99.9% purity used in this work was obtained from Sigma-Aldrich Company Ltd. UK. As shown in Figure 4.4 (XRD pattern), the all peaks were indexed according to tetragonal TiO_2-rutile with the PDF card No. (PDF# 04-004-4337). SEM images (Figure 4.5) along with EDX, revealed clusters of nanoparticles but no secondary phases. Figure 4.6 represents the particle size distribution of TiO_2 powder. The mean measured particle size (d_{50}) was 6.6 µm and d_{90} = 12.2 µm. This data contradicts the observation of nanoparticles by SEM, suggesting that ultrasonic treatment prior to measurement was insufficient to breakdown the powder to its primary particle size.

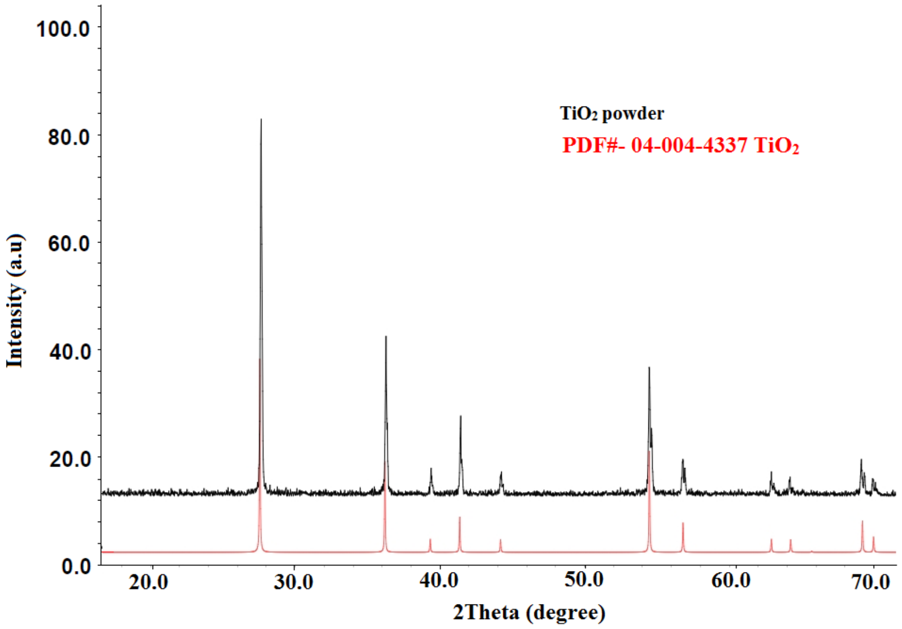

Figure 4.4. XRD pattern of TiO_2 powder.

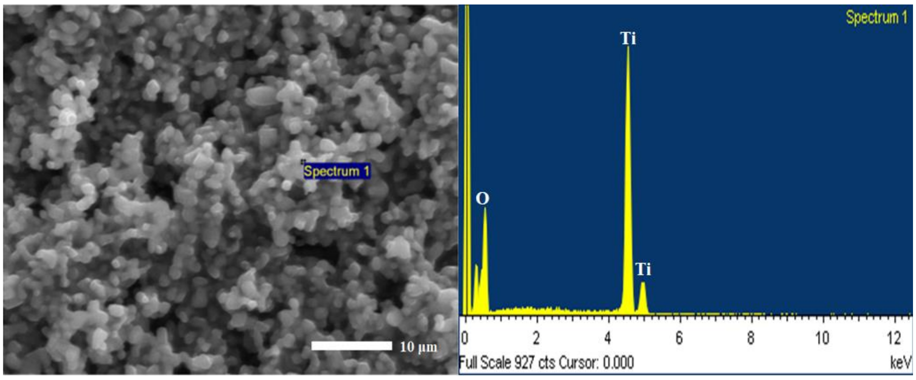

Figure 4.5. SEM image and EDX trace of TiO_2 powder.

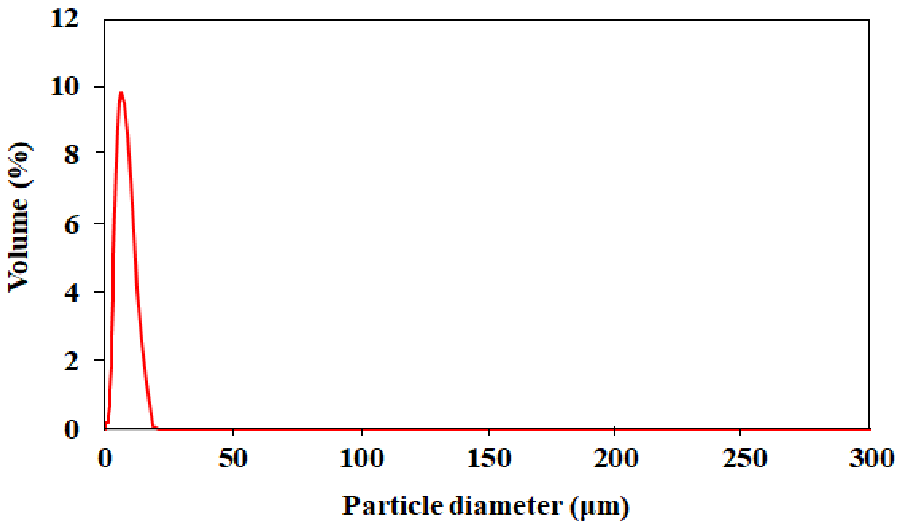

Figure 4.6. Particle size distribution of TiO_2 powder.

4.1.3 Lanthanum (III) Oxide, La_2O_3

The La_2O_3 powder (with 99.99% purity) was supplied by Sigma-Aldrich Company Ltd, UK. All peaks in the XRD pattern were indexed according to hexagonal La_2O_3 (PDF# 01-083-4961), Figure 4.7. As shown in Figure 4.8, the primary particle size was ~ 5 µm and no secondary phases were detected in the SEM image and through EDX analysis. The particle size distribution, Figure 4.9 showed that the particle mean size was large, 25.4 µm with a corresponding large d_{90}, 51.3 µm, indicating significant agglomeration. Ball milling was therefore utilized to reduce the particle size.

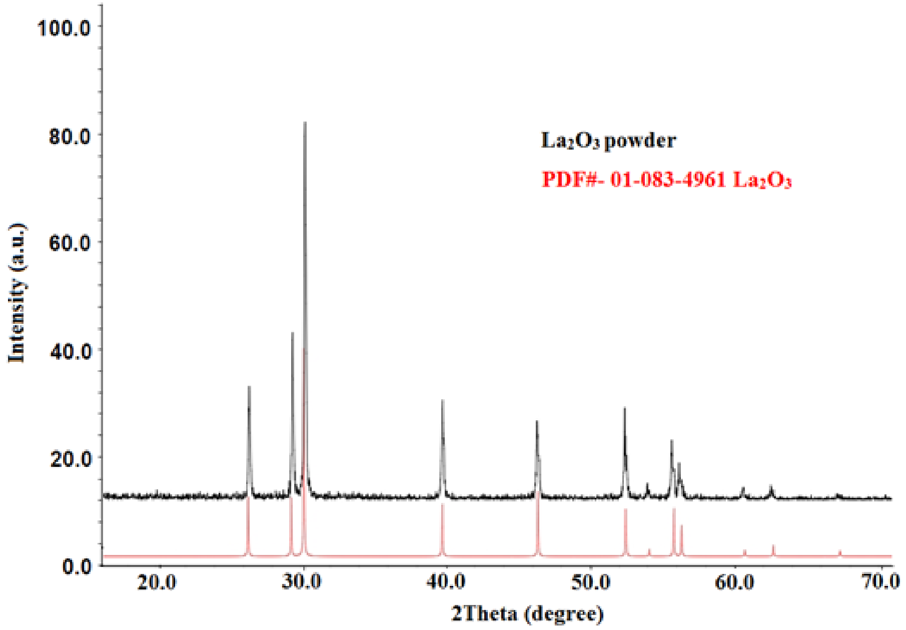

Figure 4.7. XRD pattern of La_2O_3 powder.

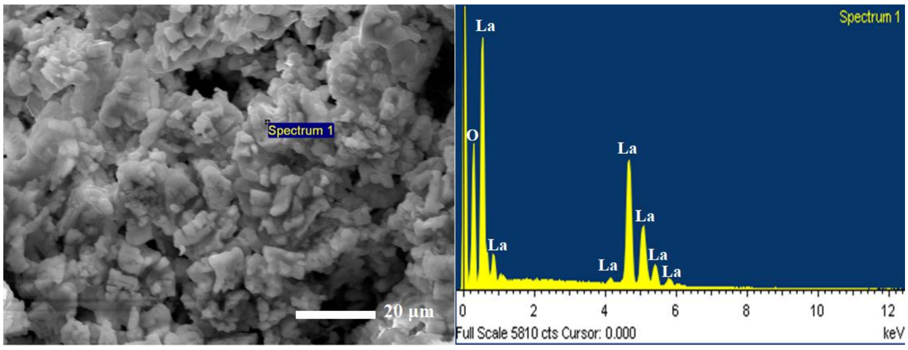

Figure 4.8. SEM image and EDX trace of La_2O_3 powder.

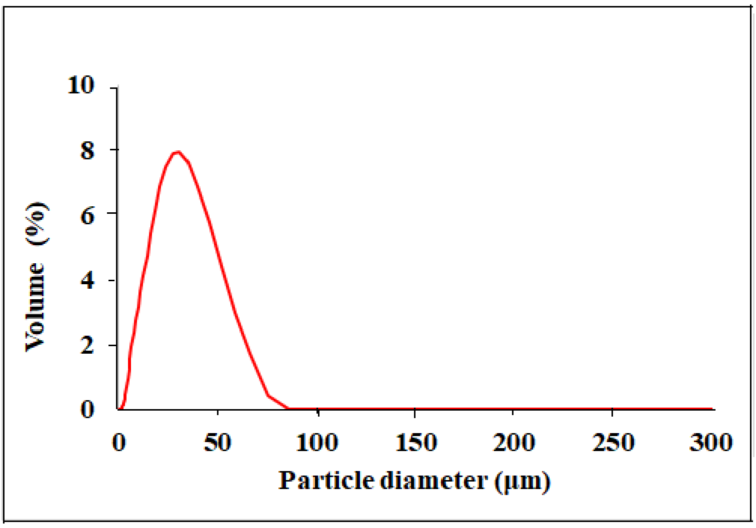

Figure 4.9. Particle size distribution of La_2O_3 powder.

4.1.4 Samarium (III) Oxide, Sm_2O_3

Stanford Materials Corporation, USA supplied the Sm_2O_3 pale yellow powder with 99.90% purity. All peaks in the XRD pattern (Figure 4.10) were indexed as Sm_2O_3 according to the PDF card (PDF# 00-043-1030). SEM images revealed a needle like primary particle geometry (0.5 x 5 µm) but no secondary phases were detected, as shown in Figure 4.11. The particle size distribution is shown in Figure 4.12 with a large mean particle size of 24.1 µm and d_{90} of 54.4 µm, again suggesting agglomeration.

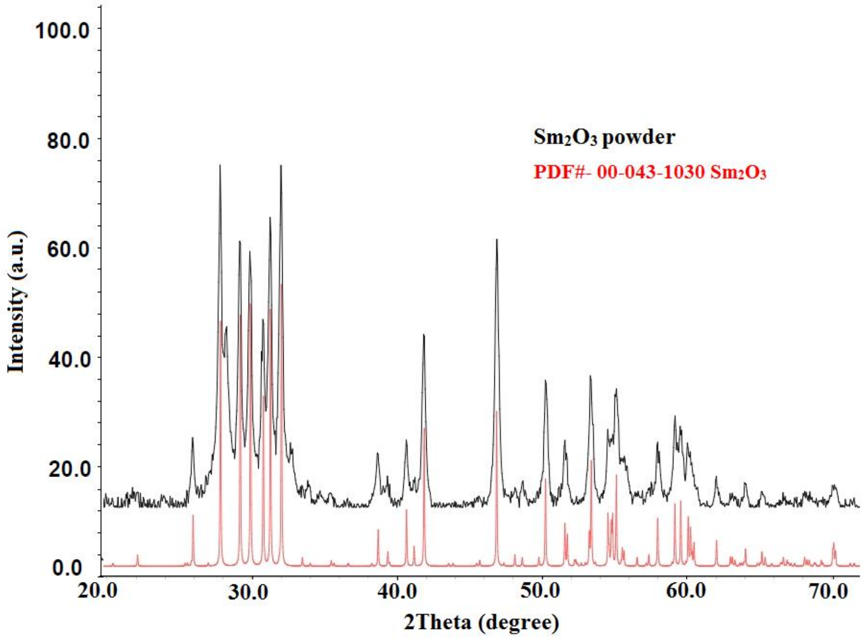

Figure 4.10. XRD pattern of Sm_2O_3 powder.

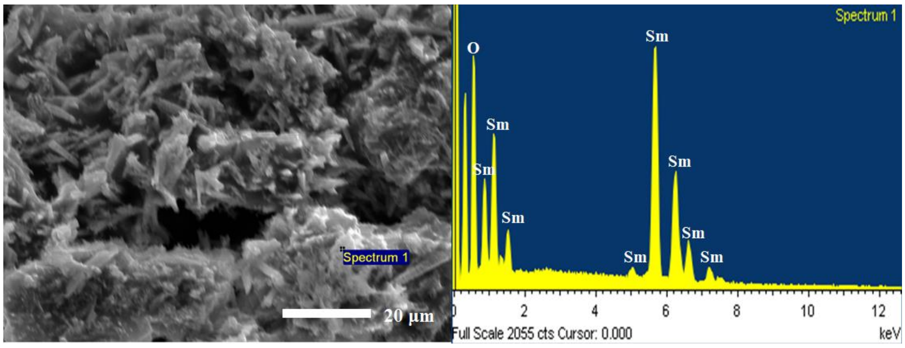

Figure 4.11. SEM image and EDX trace of Sm_2O_3 powder.

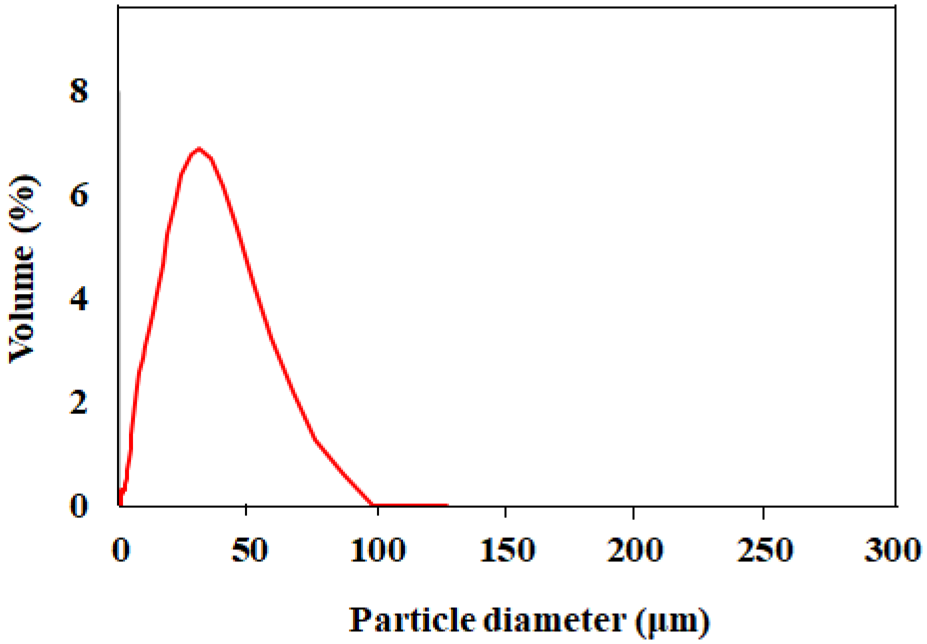

Figure 4.12. Particle size distribution of Sm_2O_3 powder.

4.1.5 Niobium (IV) Oxide, Nb_2O_5

Niobium (IV) oxide powder with 99.5% purity was supplied by Stanford Materials Corporation, USA. All peaks of the XRD pattern were indexed according to a monoclinic Nb_2O_5 crystal system using PDF card No. (PDF# 00-037-1468), Figure 4.13. As shown in Figure 4.14, the particle size showed a homogenous distribution ~1 µm, with no secondary phases. Figure 4.15 shows the particle size distribution of Nb_2O_5 powder. The mean particle size (d_{50}) was 8.8 µm while the d_{90} was 37.2 µm, which indicated that the powders were significantly agglomerated.

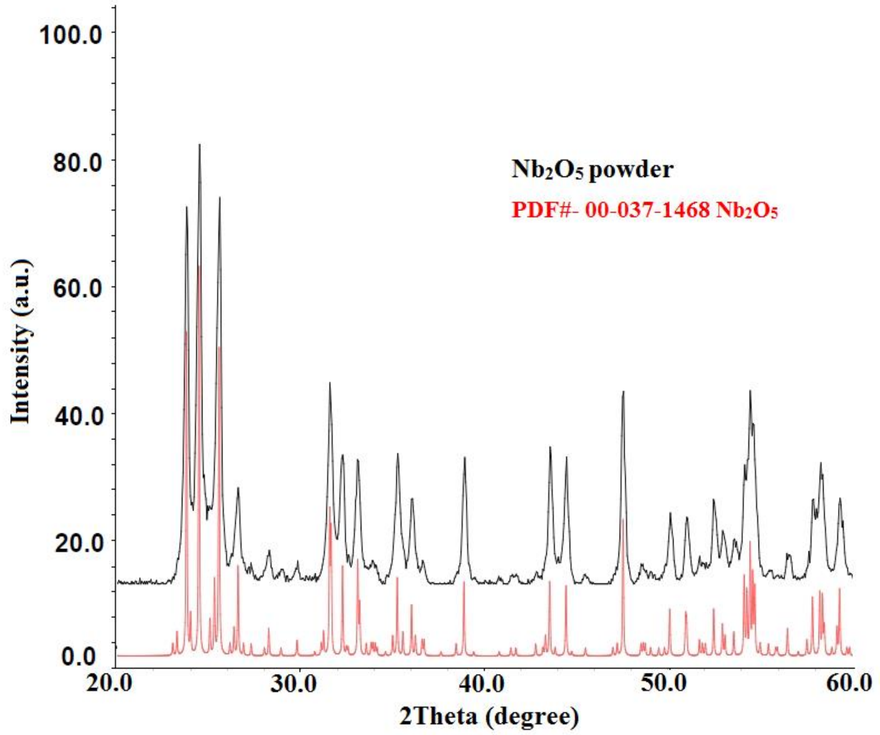

Figure 4.13. XRD pattern of Nb_2O_5 powder.

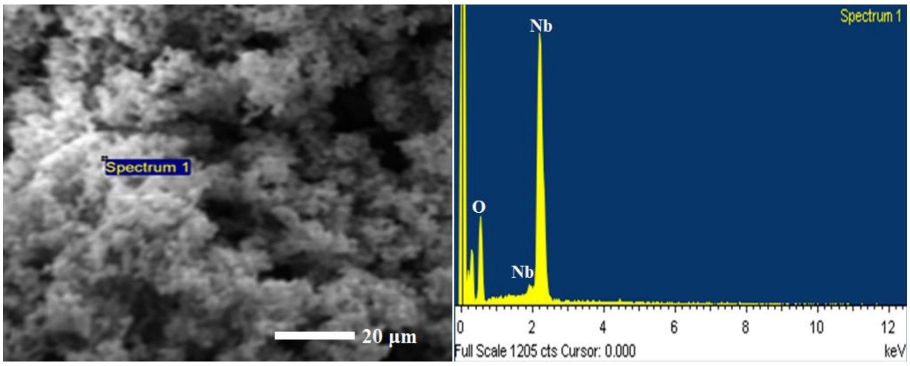

Figure 4.14. SEM image and EDX trace of Nb_2O_5 powder.

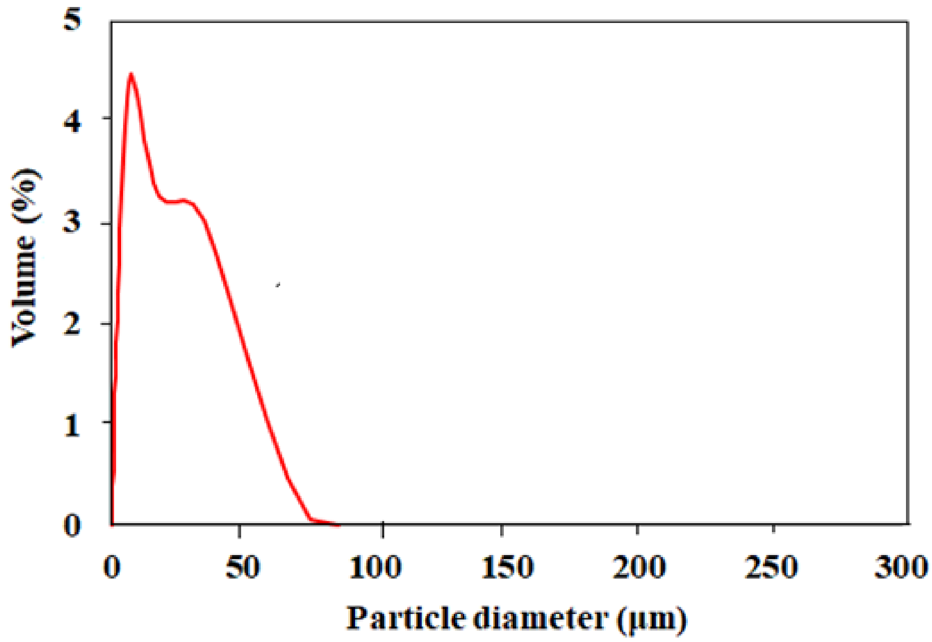

Figure 4.15. Particle size distribution of Nb_2O_5 powder.

4.2 Characterisation of Calcined Powders

4.2.1 La-Sm Co-Doped $SrTiO_3$ Series

Figure 4.16 shows the particle size distribution (PSD) of calcined La-Sm co-doped $SrTiO_3$ powders based on aliovalent doping mechanisms after ball milling.

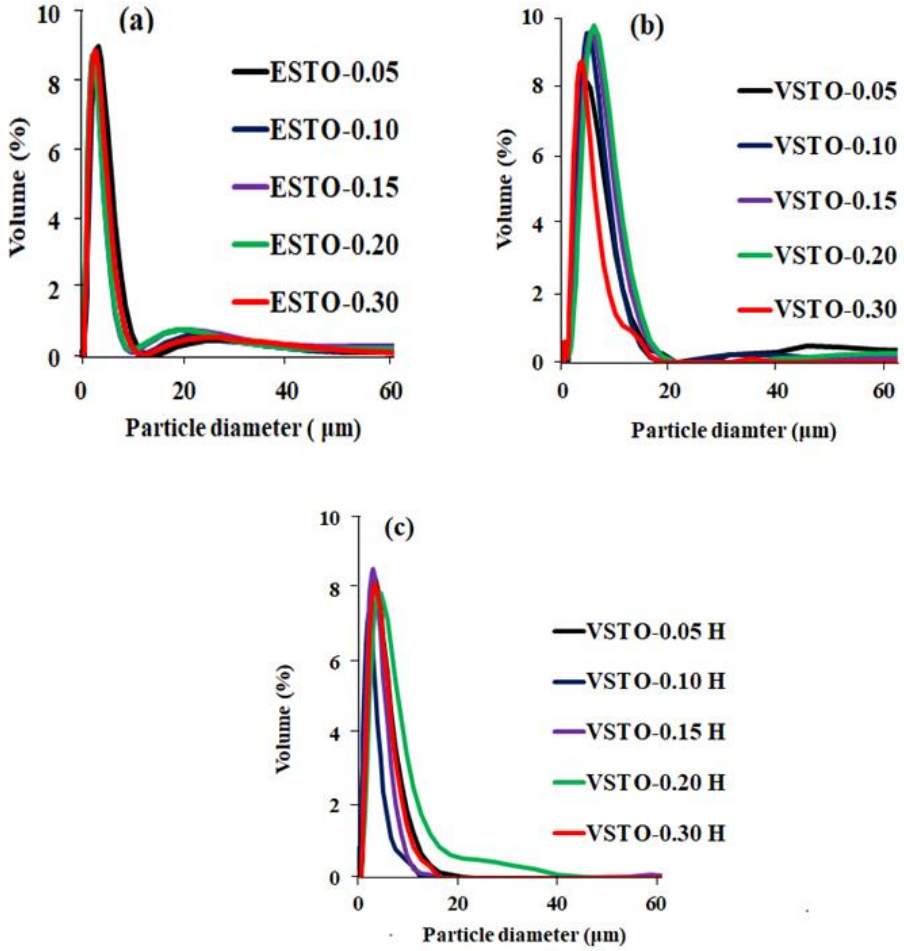

Figure 4.16. Particle size distribution of (a) $Sr_{1-x}La_{x/2}Sm_{x/2}TiO_3$ (ESTO); x = 0.05, 0.10, 0.15, 0.20, 0.30, (b) $Sr_{1-3x/2}La_{x/2}Sm_{x/2}TiO_3$ (VSTO); x = 0.05, 0.10, 0.15, 0.20, 0.30, (c) $Sr_{1-3x/2}La_{x/2}Sm_{x/2}TiO_3$ (VSTO-H); x = 0.05, 0.10, 0.15, 0.20, 0.30 calcined powders after 24 hours of ball milling. VSTO-H represents powders calcined in 5% H_2/N_2 gas.

As shown in Table 4.1, all the ball milled powders had mean particle sizes ≤ 6 µm and $d_{90} \leq 12$ µm. Lu [2] worked on the same powder ($SrTiO_3$) using attrition milling and obtained much smaller particle sizes ($d_{50} \leq 3$ µm and $d_{90} \leq 9$ µm). This confirms the postulation of Boston *et al* [1] that attrition milling utilizing high energy in mixing is more efficient than ball milling in reducing particle size. However, attrition milling has a higher possibility of introducing impurities such as ZrO_2 into the reaction from the milling media [1].

The SEM images together with EDX elemental analysis of selected calcined La-Sm co-doped $SrTiO_3$ powders after ball milling is shown in Figure 4.17. From the SEM images, all the powder particles were homogenous, and no secondary phase was detected. The EDX analysis confirmed that only elements (Sr, La, Sm, Ti, O) of the La-Sm doped $SrTiO_3$ powders were present. ESTO-0.15 ($x = 0.15$) had the smallest powder particles while VSTO-0.15 ($x = 0.15$) exhibited the largest powder particles. This agrees with the PSD results (Table 4.1) where ESTO-0.15 had a mean particle size (d_{50}) of 2.8 µm while VSTO-0.15 and VSTO-0.15H had d_{50} of 5.6 and 3.3 µm, respectively. The result also confirms that processing (calcination) of vacancy co-doped $Sr_{1-3x/2}La_{x/2}Sm_{x/2}TiO_3$ powders in 5% H_2/N_2 gas reduces the particles sizes.

Table 4.1. Particle sizes of calcined La-Sm co-doped $SrTiO_3$ powders based on aliovalent doping mechanisms after 24 hours ball milling. Uncertainty in particle size determination is ±0.6 %.

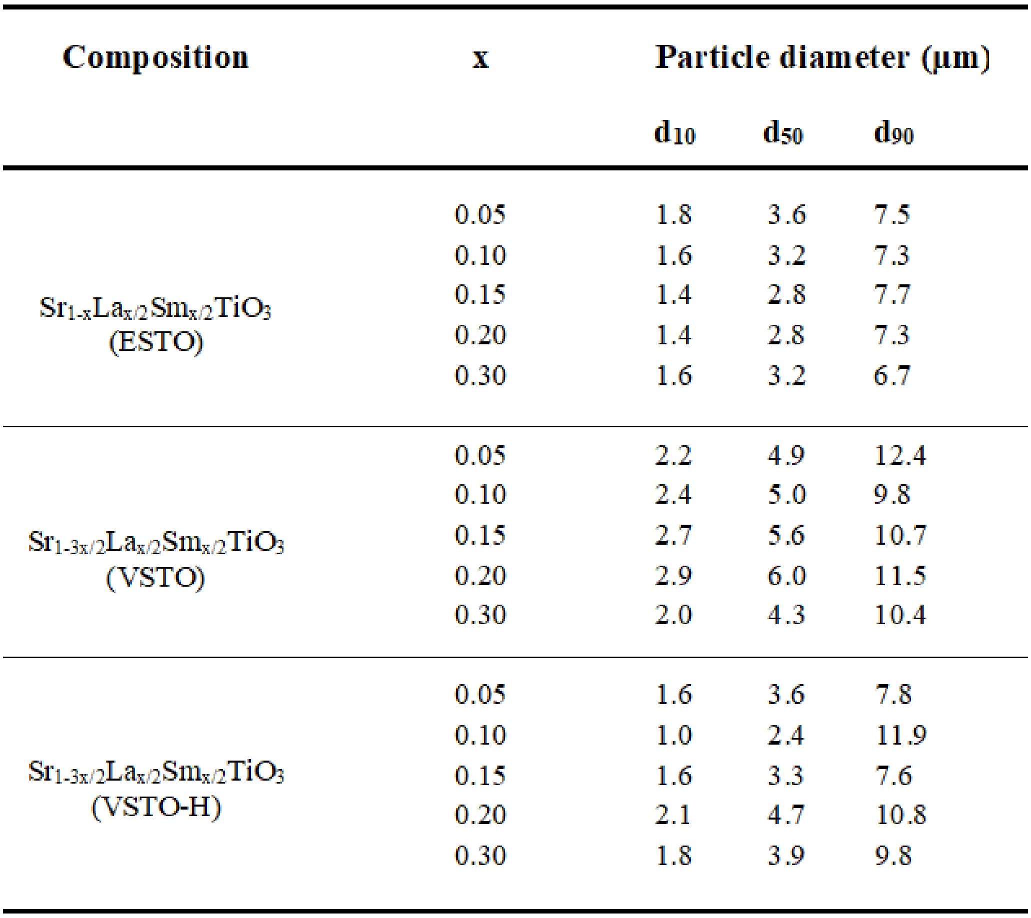

Composition	x	Particle diameter (µm)		
		d_{10}	d_{50}	d_{90}
$Sr_{1-x}La_{x/2}Sm_{x/2}TiO_3$ (ESTO)	0.05	1.8	3.6	7.5
	0.10	1.6	3.2	7.3
	0.15	1.4	2.8	7.7
	0.20	1.4	2.8	7.3
	0.30	1.6	3.2	6.7
$Sr_{1-3x/2}La_{x/2}Sm_{x/2}TiO_3$ (VSTO)	0.05	2.2	4.9	12.4
	0.10	2.4	5.0	9.8
	0.15	2.7	5.6	10.7
	0.20	2.9	6.0	11.5
	0.30	2.0	4.3	10.4
$Sr_{1-3x/2}La_{x/2}Sm_{x/2}TiO_3$ (VSTO-H)	0.05	1.6	3.6	7.8
	0.10	1.0	2.4	11.9
	0.15	1.6	3.3	7.6
	0.20	2.1	4.7	10.8
	0.30	1.8	3.9	9.8

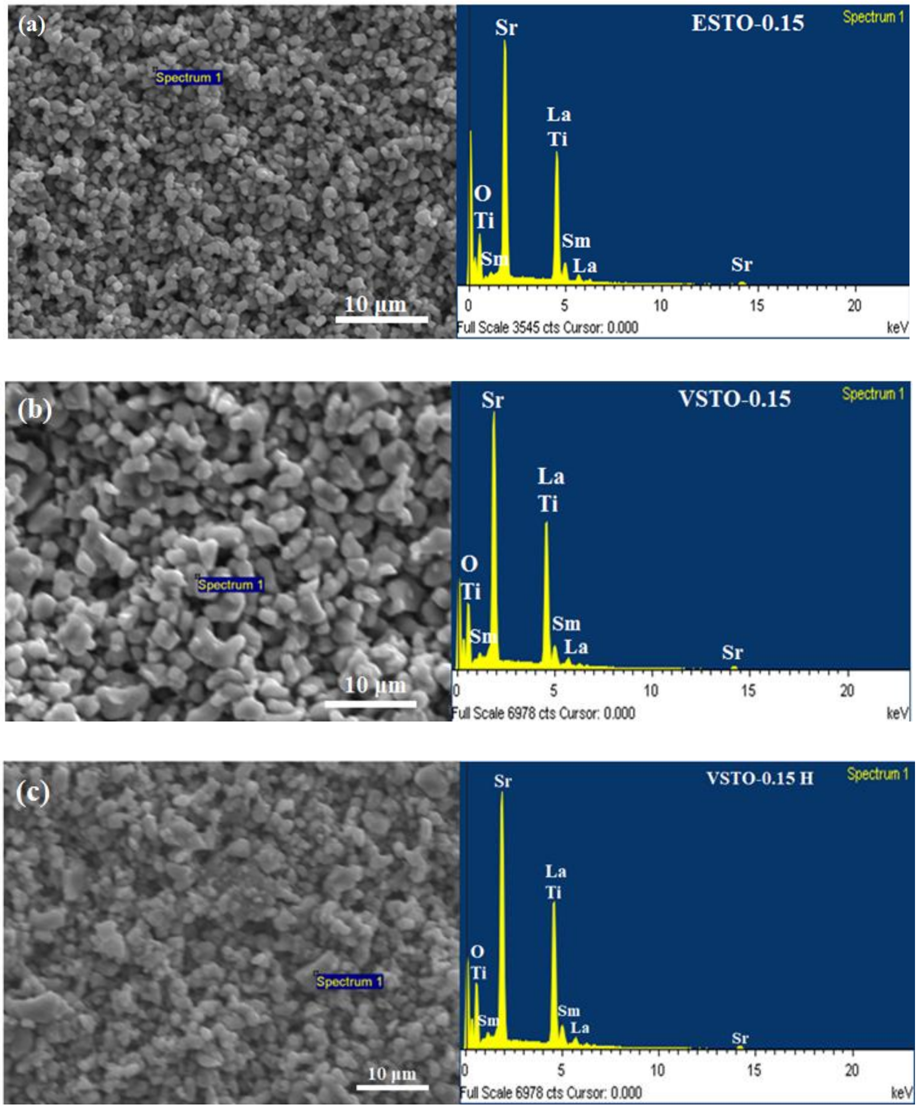

Figure 4.17. SEM image and EDX trace of (a) $Sr_{1-x}La_{x/2}Sm_{x/2}TiO_3$ (ESTO-0.15); x = 0.15, (b) $Sr_{1-3x/2}La_{x/2}Sm_{x/2}TiO_3$ (VSTO-015); x = 0.15, (c) $Sr_{1-3x/2}La_{x/2}Sm_{x/2}TiO_3$ (VSTO-0.15H); x = 0.15 calcined powders after 24 hours of ball milling.

4.2.2 Sm-Doped $Sr_5LaTi_3Nb_7O_{30}$ Series

The particle size distribution of milled Sm-doped $Sr_5LaTi_3Nb_7O_{30}$ powders after calcination based on different compensation mechanisms are shown in Figure 4.18. All as-milled powders showed mean particle sizes of ~ 5 µm and $d_{90} \leq 10$ µm (Table 4.2). These small particle sizes confirmed that ball milling reduced the particles of Sm-doped $Sr_5LaTi_3Nb_7O_{30}$ powders required for thermoelectric applications.

Figure 4.19 shows the SEM image and EDX analysis of $Sr_5La_{x-1}Sm_xTi_3O_{30}$ (SLTNe); x = 0.15 and $Sr_{5-3x/2}LaSm_xTi_3O_{30}$ (SLTNv); x = 0.15 calcined powders after ball milling. All the as-milled powders showed a homogenous particle with no secondary phases. All the x-ray peaks from the EDX matched with O, Sr, La, Sm, and Ti elements as contained in the sample powders. The particle sizes of SLTNe, x = 0.15 were larger than that of SLTNv, x = 0.15, hence in agreement with the PSD results as shown in Table 4.2.

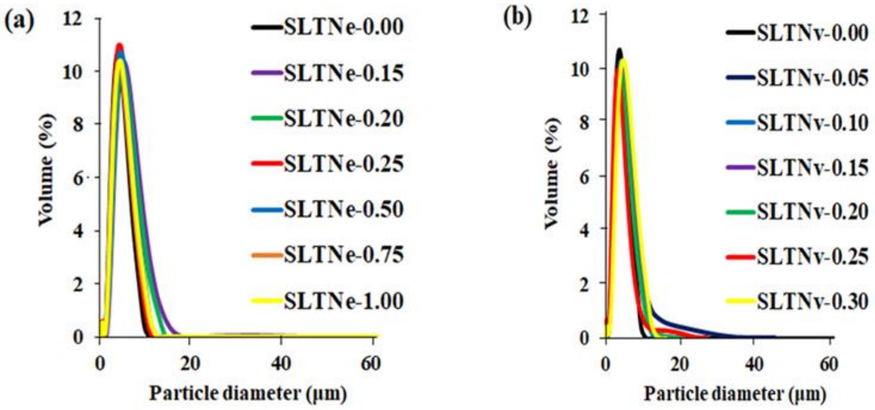

Figure 4.18. Particle size distribution of (a) $Sr_5La_{x-1}Sm_xTi_3O_{30}$ (SLTNe); x = 0.00, 0.15, 0.20, 0.25, 0.50, 0.75, 1.00 (b) $Sr_{5-3x/2}LaSm_xTi_3O_{30}$ (SLTNv); x = 0.05, 0.10, 0.15, 0.20, 0.25, 0.30 calcined powders after 24 hours of ball milling.

Table 4.2. Particle sizes of calcined Sm-doped $Sr_5LaTi_3Nb_7O_{30}$ powders based on different compensation mechanisms after 24 hours ball milling. Uncertainty in particle size determination is ±0.6 %.

Composition	x	Particle diameter (μm)		
		d_{10}	d_{50}	d_{90}
$Sr_5La_{1-x}Sm_xTi_3Nb_7O_{30}$ (SLTNe)	0.00	2.0	4.0	7.0
	0.15	2.8	5.4	9.8
	0.20	2.5	5.0	9.0
	0.25	2.3	4.3	7.5
	0.50	2.4	4.6	8.1
	0.75	2.1	4.2	7.6
	1.00	2.2	4.4	7.9
$Sr_{5-3x/2}La_xSm_xTi_3Nb_7O_{30}$ (SLTNv)	0.00	2.1	4.4	10.3
	0.05	2.0	4.3	9.0
	0.10	2.2	4.5	8.0
	0.15	2.2	4.4	8.2
	0.20	2.0	4.2	7.7
	0.25	1.8	3.6	6.9
	0.30	2.5	4.9	8.8

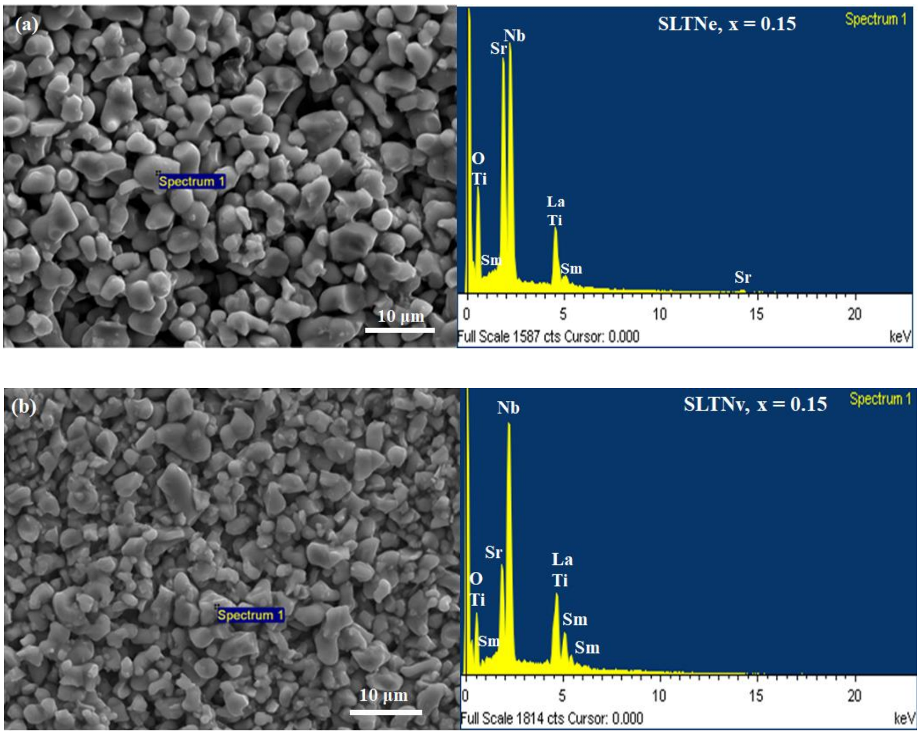

Figure 4.19. SEM image and EDX trace of (a) $Sr_5La_{x-1}Sm_xTi_3O_{30}$ (SLTNe); x = 0.15, (b) $Sr_{5-3x/2}LaSm_xTi_3O_{30}$ (SLTNv); x = 0.15 calcined powders after 24 hours of ball milling.

4.2.3 Nb-Doped $La_2Ti_2O_7$ Series

The particle size distribution of calcined and milled Nb-doped $La_2Ti_2O_7$ powders according to electronic B-site compensation mechanisms are represented in Figure 4.20. All as-milled powders (Table 4.3) showed mean particle sizes of ~ 5 µm and $d_{90} \leq 10$ µm with no significant agglomerations.

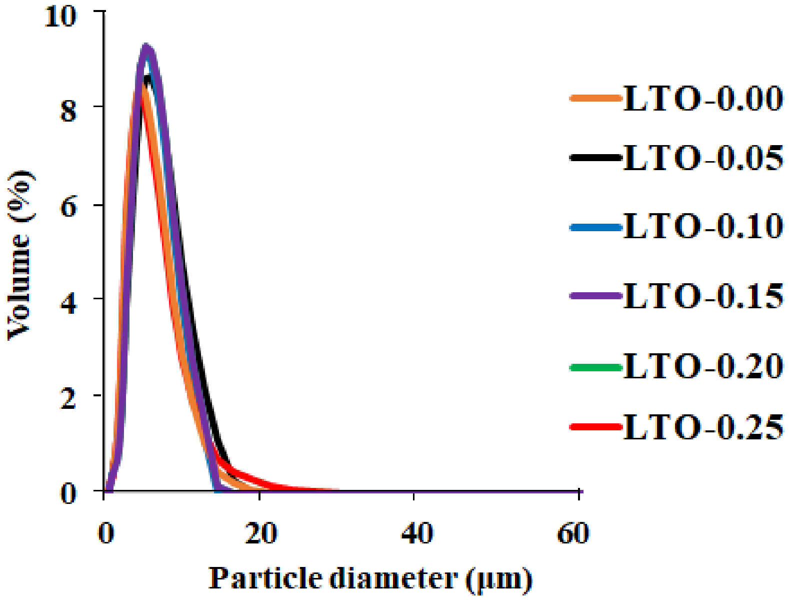

Figure 4.20. Particle size distribution of $La_2Ti_{2-x}Nb_xO_7$ (LTO); x = 0.00, 0.05, 0.10, 0.15, 0.20, 0.25 calcined powders after 24 hours of ball milling.

Figure 4.21 shows the SEM image together with EDX trace of selected calcined Nb-doped $La_2Ti_{2-x}Nb_xO_7$ (LTO) powders after ball milling. The SEM image (LTO, x = 0.00, 0.15) showed homogeneous particles with no secondary phases.

Table 4.3. Particle sizes of calcined Nb-doped $La_2Ti_2O_7$ powders based on B-site electronic compensation mechanisms after 24 hours ball milling. Uncertainty in particle size determination is ±0.6 %.

Composition	x	Particle diameter (μm)		
		d_{10}	d_{50}	d_{90}
$La_2Ti_{2-x}Nb_xO_7$ (LTO)	0.00	1.3	4.4	8.9
	0.05	1.6	5.3	10.3
	0.10	1.4	5.0	9.3
	0.15	1.7	5.2	9.6
	0.20	1.5	4.8	10.4
	0.25	1.3	4.4	9.2

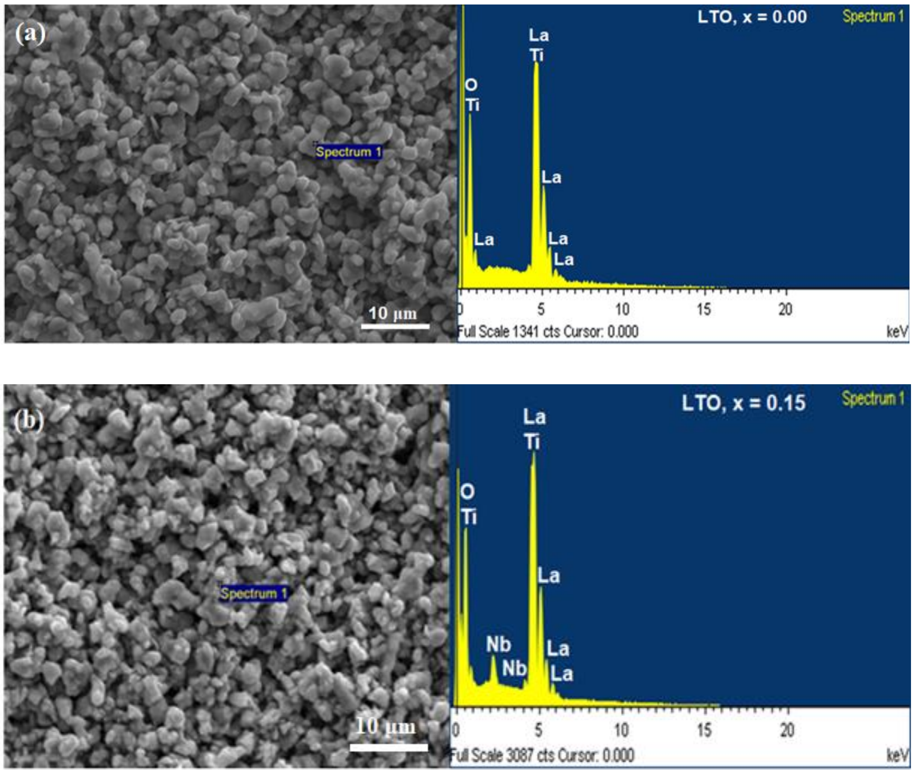

Figure 4.21. SEM image and EDX trace of $La_2Ti_{2-x}Nb_xO_7$ (LTO); x = 0.00, 0.15 calcined powders after 24 hours of ball milling.

4.3 Conclusion

Particle size distribution and quality of starting powders are essential in achieving efficient and high thermoelectric figures of merit [3]. At times this vital processing step is neglected and it leads to unreliable and/or irreproducible results [1].

Based on the foregoing, the particle size distribution, phase and elemental composition (SEM/EDX) analyses were carried out. Results of all powders analysed confirmed homogenous particles and no trace(s) of secondary phase(s) were detected.

References

[1] R. Boston, W. L. Schmidt, G. D. Lewin, A. C. Iyasara, Z. Lu, H. Zhang, D. C. Sinclair, and I. M. Reaney, “Protocols for the fabrication, characterization, and optimization of n-type thermoelectric ceramic oxides,” *Chem. Mater.*, vol. 29, no. 1, pp. 265–280, 2017.

[2] Zhilun Lu, “La doped $SrTiO_3$ Based Oxide Thermoelectrics.,” PhD Thesis, University of Sheffield, 2016.

[3] Jun Wang, Bo Yu Zhang, Hui Jun Kang, Yan Li, Xinba Yaer, Jing Feng Li, Qing Tan, Shuai Zhang, Guo Hua Fan, Cheng Yan Liu, Lei Miao, Ding Nan, Tong Min Wang, and Li Dong Zhao, “Record high thermoelectric performance in bulk $SrTiO_3$ via nano-scale modulation doping,” *Nano Energy*, vol. 35, no. April, pp. 387–395, 2017.

Chapter 5: La-Sm Electron Doped $SrTiO_3$ Ceramics

5.1 Introduction

Reduced rare earth (RE) doped $SrTiO_3$ ceramics have recently been shown to have promising TE properties [1]–[3]. $SrTiO_3$ as an end-member material has been widely studied in terms of the effect of different dopants, doping mechanisms, and processing conditions [4]. The most common RE doping mechanism is based on A-site donor doping via an electronic mechanism, i.e. $RE^{3+} + e^- \rightarrow Sr^{2+}$ (general formula $Sr_{1-x}RE_xTiO_3$) in attempts to increase σ. Despite reported high S, high σ, and large PF, ZT remains low due to high k when compared to non-oxide TE materials [3], [5].

There are a wide range of values reported for RE-doped $SrTiO_3$, the majority of which relate to the same electronic compensation mechanism discussed in this chapter [2], [3], [6], [7]. These reported ZT values for reduced bulk polycrystalline strontium titanates include 0.22 at 573 K for $Sr_{0.9}Dy_{0.1}TiO_3$ and 0.28 at 873 K for $Sr_{0.9}Nd_{0.1}TiO_3$ [2], [6], [7], 0.22 at 800 K for $Sr_{0.92}La_{0.08}TiO_3$ and 0.17 at 1045 K for $SrTi_{0.90}Ta_{0.1}TiO_3$ [6], 0.24 at 1073 K for $Sr_{0.9}Sm_{0.1}TiO_3$ and 0.31 at 1023 K for $Sr_{0.8}La_{0.18}Yb_{0.02}TiO_3$ [2], 0.36 at 1045 K for $La_{0.1}Sr_{0.83}Dy_{0.07}TiO_3$ [2], [7] and $Sr_{0.9}Nd_{0.1}TiO_{3\pm\delta}$, $Sr_{0.9}Sm_{0.1}TiO_{3\pm\delta}$ and $Sr_{0.9}Dy_{0.1}TiO_{3\pm\delta}$ of ZT ~ 0.42 at 1190 –1225 K [2]. However, the recent data with an optimised ZT was presented by Wang *et al* [8] who studied La-Nb electron co-doped $SrTiO_3$ prepared using hydrothermal method. Wang *et al* [8] concluded that the hydrothermal method and high sintering temperature were effective in producing nano-structured bulk ceramics. The net overall result was a high ZT (> 0.6) and low k (~ 2.75) at 1100 K obtained in 10 mol% La and 10 mol% Nb (La10Nb10) co-doped $SrTiO_3$ bulk ceramics.

This chapter studies the structure-property relationships of co-doped RE $SrTiO_{3-\delta}$ ceramics based on the electron doping sintered in 5% H_2/ N_2 gas mixtures. The purpose of co-doping instead of single doping is an attempt to enhance the phonon scattering and therefore reduce k without significantly affecting the PF [3]. La^{3+} (largest RE ion) and Sm^{3+} (intermediate sized RE ion) ions were chosen as co-dopants in this study to test the hypothesis that a range of ions with mass and ionic radius dissimilar to Sr^{2+} ion on the A-site would enhance phonon scattering and decrease k whilst simultaneously acting as a donor dopant, potentially increasing the carrier concentration [3].

5.2 Results and Discussion

5.2.1 Phase Assemblage

Room temperature XRD patterns of the crushed $Sr_{x-1}La_{x/2}Sm_{x/2}TiO_3$ ceramics sintered in air and 5% H_2/N_2 at 1773 K for 6 hours are shown in Figure 5.1. All major peaks are indexed as primitive cubic $SrTiO_3$ perovskite (space group Pm-3m) according to the PDF card (PDF# 04-002-6890). x = 0.20 and 0.30 exhibited weak intensity peaks (< 1% relative intensity) of a secondary phase that corresponded to rutile TiO_2.The absence of a trend for the appearance of a secondary phase as a function of x suggests the residual TiO_2 is most likely due to unreacted starting material [3]. The lattice parameters, cell volumes and theoretical densities were determined from the XRD data by manual indexing and the results for 5%H_2/N_2 sintered compositions are shown in Table 5.1. They were derived from the indices of the main peaks and corresponding angles using Bragg's law. The dopant (La-Sm) concentration dependence of the lattice parameters of both air and 5% H_2/N_2 sintered compositions are presented in Figure 5.2.

The lattice parameter of the ceramics decreases progressively with increasing doping concentration, $0.00 \leq x \leq 0.20$ and then levels off at x = 0.30 (Figure 5.2). The decrease is attributed to the smaller ionic radii of La^{3+} (1.36 Å in coordination number, CN 12) and Sm^{3+} (1.24 Å in CN 12) in the substitution for large Sr^{2+} ions (1.44 Å in CN 12) [6], [9]–[11]. The reason for a sharp increase in lattice parameter after x = 0.20 is unclear. From the suggestion made by Wang and Wang [9], the increase could be that the dopants (in this case, La^{3+} and Sm^{3+}) are no longer incorporated onto the A- site of the lattice. Kovalevsky *et al* [2] in their work obtained a tetragonal phase for 10 mol % Sm doped $SrTiO_{3\pm\delta}$ ceramics and a cubic phase for $Sr_{0.9}La_{0.1}TiO_{3\pm\delta}$ with lattice parameter of 3.9096(3) Å. The data obtained in this work therefore suggests that co-doping inhibits the apparent distortion to the tetragonal phase. Further diffraction analysis (electron, neutron) is recommended to ascertain whether co-doping has suppressed the distortion or reduced its scale length to below the detection limit of the x-ray diffractometer. However, it is concluded that La and Sm are incorporated onto the A-site of the perovskite lattice in respect of the batched stoichiometry. Further crystallographic studies (beyond the scope of this thesis) would provide more insight on the lattice distortions, incorporation of the co-doped elements and clarify the solid solution limit.

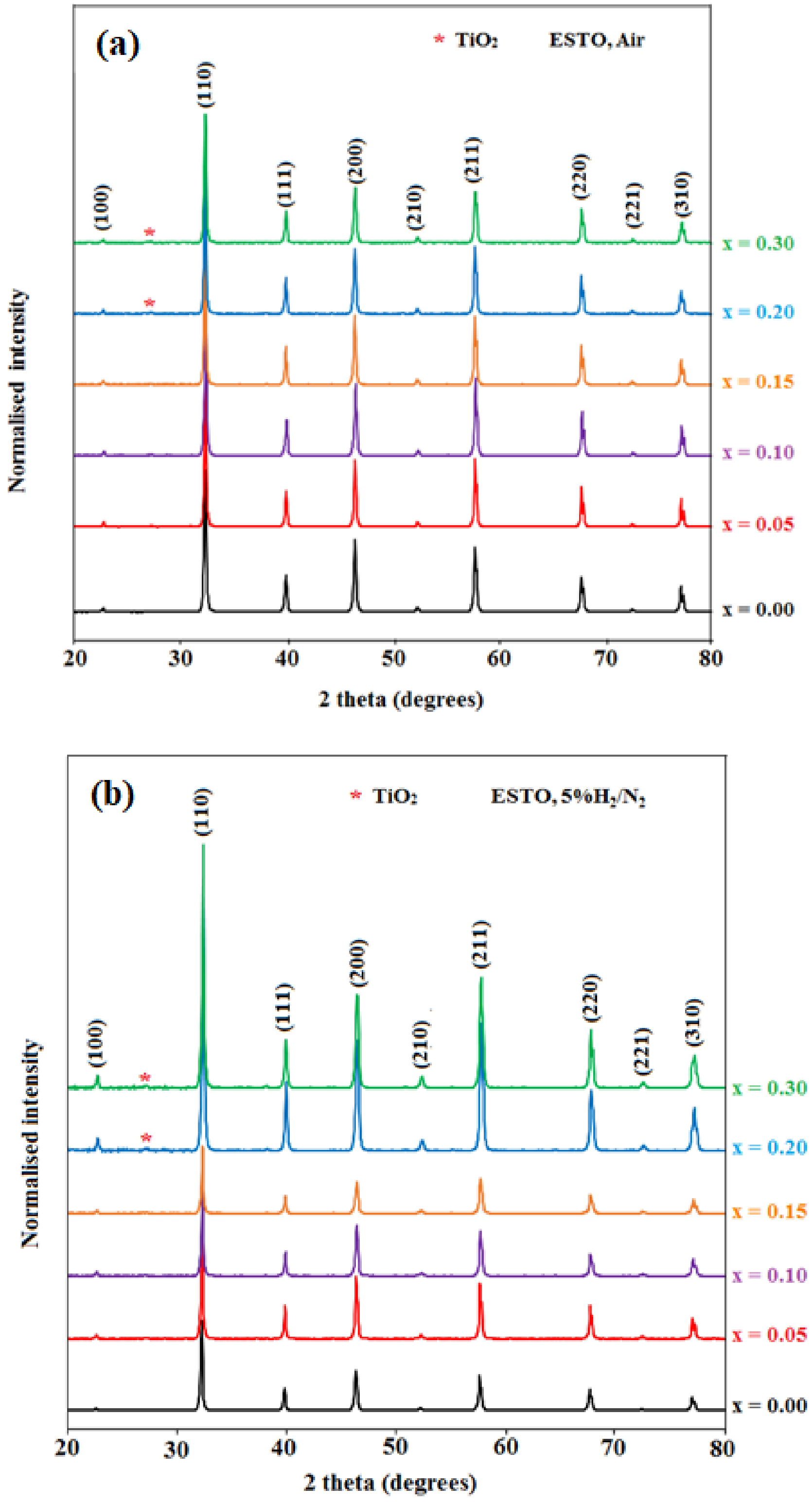

Figure 5.1. Room temperature XRD patterns of crushed $Sr_{x-1}La_{x/2}Sm_{x/2}TiO_3$ Ceramics sintered in (a) air (ESTO, Air) (b) 5% H_2/N_2 (ESTO, 5% H_2/N_2) at 1773 K for 6 hours.

As shown in Figure 5.2, the lattice parameter of pure $SrTiO_3$ sintered in reduced atmosphere is high with a value of 3.912 ±0.001 Å in comparison to air-sintered 3.906 ±0.001 Å which is comparable to the value (3.905 Å) reported in literature [12], [13]. The lattice parameters of the compositions irrespective of sintering atmosphere decreased progressively within $x \leq 0.20$ and levels off at high doping concentration. Sample with $x = 0.20$ possesses the lowest values of 3.902 Å and 3.903 Å for air (ESTO, Air) and 5% H_2/N_2 (ESTO, 5% H_2/N_2) sintered ceramics, respectively. Generally, the lattice parameter of compositions sintered in 5% H_2/N_2 gas are larger than those sintered in air. This is attributed to the decrease in Coulombic force (binding energy) in the lattice due to removal of O^{2-} ions (in form of water, H_2O) from the lattice during the reduction process [14] resulting in the partial reduction of Ti^{4+} ions (0.605 Å in CN 6) to the larger ionic radius of Ti^{3+} (0.670 Å in CN 6) [6], [14]. A similar decrease in lattice parameters on co-doping of $SrTiO_3$ has been reported for $La_{0.1}Sr_{0.9-x}Yb_xTiO_3$; $x \leq 0.1$ [9].

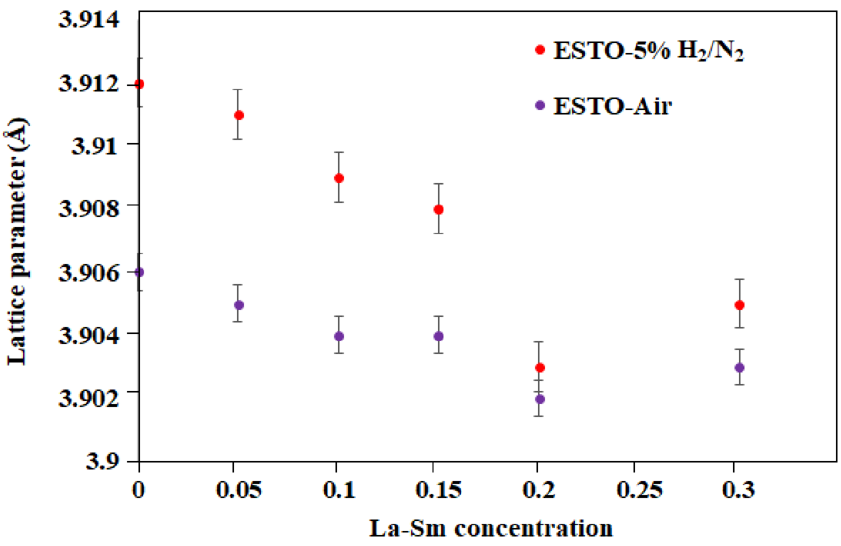

Figure 5.2. Lattice parameters of $Sr_{x-1}La_{x/2}Sm_{x/2}TiO_3$ ceramics sintered in air (ESTO, Air) and 5% H_2/N_2 (ESTO, 5% H_2/N_2) at 1773 K for 6 hours.

Table 5.1. Lattice parameters, cell volumes and theoretical densities of $Sr_{x-1}La_{x/2}Sm_{x/2}TiO_3$ ceramics sintered in 5% H_2/N_2 at 1773 K for 6 hours.

Composition x	Lattice Parameter (Å) (±0.001 Å)	Cell Volume ($Å^3$) (±0.002 $Å^3$)	Relative Density (%) (±0.5 %)
0.00	3.912	59.868	95.1
0.05	3.911	59.822	97.6
0.10	3.909	59.731	97.7
0.15	3.908	59.685	96.4
0.20	3.903	59.456	90.8
0.30	3.905	59.547	89.4

5.2.2 Microstructure

All ceramics after sintering had a relative density of ≥ 89 % as presented in Table 5.1. Secondary electron microscopy (SEM) images of the thermally etched, carbon coated surfaces for $Sr_{x-1}La_{x/2}Sm_{x/2}TiO_3$ ceramics are shown in Figure 5.3. The SEM images of $0.00 \leq x \leq 0.15$ ceramics revealed a homogeneous and dense structures consistent with their high relative density of ≥ 95 %. x = 0.05 ceramics contain smaller irregular shaped grains with average grain size of 3.1μm. For 15 wt. % La-Sm doped sample, a broad grain size distribution was observed. It (x = 0.15) exhibits an oval shaped grain with an average grain size of 9.4 μm. A further increase in the doping level (> 15 wt. %) inhibited grain growth which resulted in small grain sizes (5.2 μm average size for x = 0.30) with significant evidence of porosity and secondary phase (Figure 5.3c-d). This observation is in agreement with the phase structure (XRD) obtained for $x \geq 0.20$ ceramics with a lower relative density of ~ 90 %. The multiphase microstructure observed in $x \geq 0.20$ ceramics due to the presence of pores and secondary phase hindered the accurate determination of the average grain size of x = 0.20 sample. The low density of $x \geq 0.20$ ceramics most likely relates to the more refractory nature of La and Sm oxides in comparison to $SrTiO_3$.

This signals the need for further optimisation sintering techniques to achieve higher density [3]. Increase in La-Sm concentration within the solubility limit ($\geq$ 0.15) of the composition contributes to the expansion of the grain sizes. Enlarged grains have been suggested to provide pathway for carrier mobility, leading to increase in electrical conductivity [15].

The impact of porosity and secondary phase in the heavily doped compositions ($x \geq 0.20$) is not clear. Some researchers suggest the presence of pores and/or secondary phase create discontinuities in the lattice which act as scattering centres, impede carrier mobility, and enhance phonon scattering [8], [16]. In consequence, electrical conductivity is reduced due to the restricted carrier mobility [16], [17] while thermal conductivity is decreased by additional phonon scattering by the pores [16]. Therefore, these pores and secondary phases in the SEM micrographs may contribute to the very low electrical and thermal conductivity values observed in $x \geq 0.20$ ceramics.

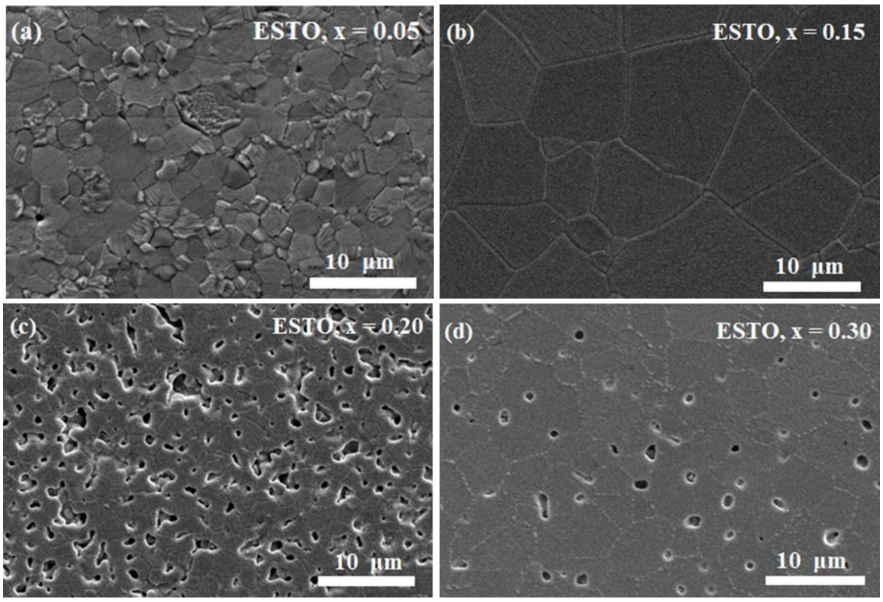

Figure 5.3. SEM images of the surfaces of $Sr_{x-1}La_{x/2}Sm_{x/2}TiO_3$ (ESTO, 5% H_2/N_2) ceramics sintered in 5% H_2/N_2 at 1773 K for 6 hours and thermal etched at 1623 K for 0.5 hour.

5.2.3 Thermogravimetric Analysis (TGA)

The results of the thermogravimetric analysis, TGA of electron doped $Sr_{x-1}La_{x/2}Sm_{x/2}TiO_3$ ceramics sintered in 5% H_2/N_2 at 1773 K for 6 hours are presented in Figure 5.4 and Table 5.2. From the results, $x \leq 0.05$ and $x = 0.10$ compositions were stable in air up to 1000 °C and 960 °C, respectively. This validates the theory that $SrTiO_3$ as a transition oxide is chemically stable in air at high temperatures [18]. When the doping concentration of the ceramics was increased ($x \geq 0.15$), an upward trend with onset temperatures around 770, 550 and 400 °C for x = 0.15, 0.20 and 0.30, respectively was observed. The weight gain (oxidation) continued sharply up to the maximum temperature (1000 °C) for x = 0.15 and 800 °C for $x \geq 0.20$ and stabilised afterwards. The colour of ceramic samples after TGA remained black for $x \leq 0.05$ and turned to brown for $x \leq 0.15$ and white for $x \geq 0.20$.

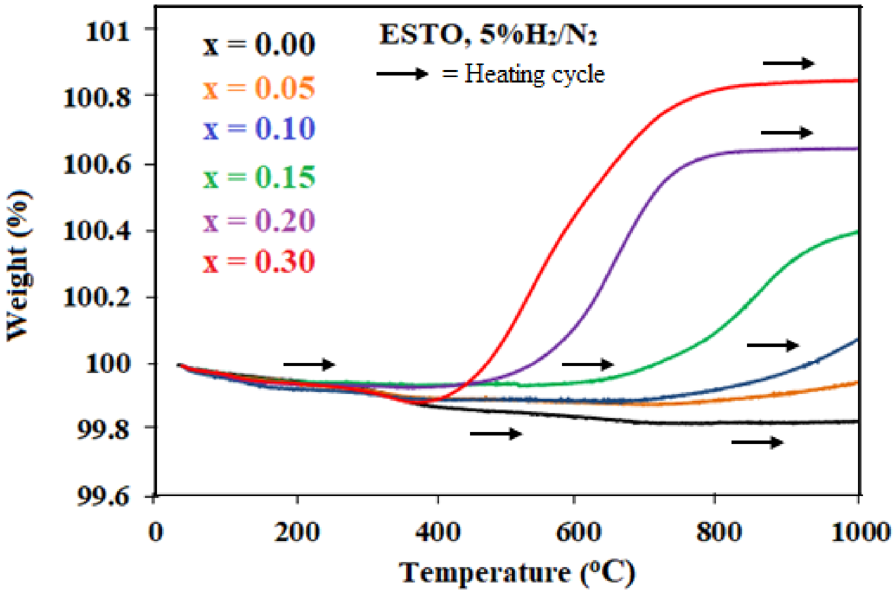

Figure 5.4. Thermogravimetric analysis showing the oxidation (oxygen uptake) in air up to 1000 °C of $Sr_{x-1}La_{x/2}Sm_{x/2}TiO_3$ (ESTO, 5% H_2/N_2, $0.00 \leq x \leq 0.30$) ceramics sintered in 5% H_2/N_2 at 1773 K for 6 hours.

As shown in Table 5.2, the oxygen uptake increased with increasing La-Sm concentration and decreasing oxidation onset temperature for $x \geq 0.10$ ceramics. This concludes that $SrTiO_3$ ceramics at high values of x are not stable in air at high temperatures, hence unsuitable for thermoelectric applications above 300 °C.

Table 5.2. TGA result showing the weight variation and oxidation onset temperature of $Sr_{x-1}La_{x/2}Sm_{x/2}TiO_3$ (ESTO, 5% H_2/N_2, $0.00 \leq x \leq 0.30$) ceramics sintered in 5% H_2/N_2 at 1773 K for 6 hours.

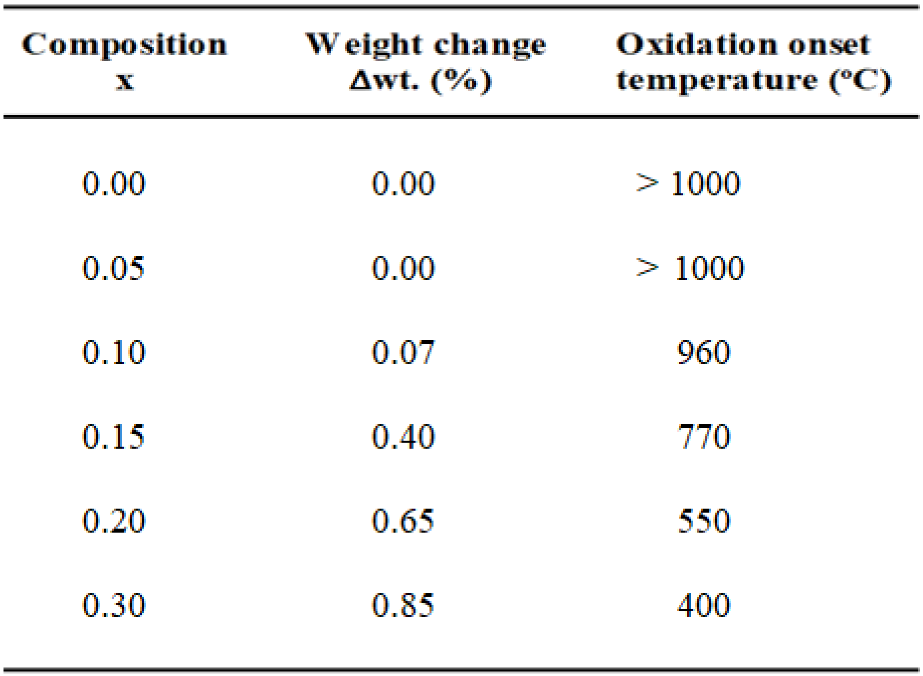

Composition x	Weight change Δwt. (%)	Oxidation onset temperature (°C)
0.00	0.00	> 1000
0.05	0.00	> 1000
0.10	0.07	960
0.15	0.40	770
0.20	0.65	550
0.30	0.85	400

5.2.4 Thermoelectric Properties

The temperature dependence of the thermoelectric properties (σ, │S│, PF, k, k_E, k_L and ZT) of $Sr_{x-1}La_{x/2}Sm_{x/2}TiO_3$ $0.05 \le x \le 0.30$) ceramics sintered in 5% H_2/N_2 at 1773 K for 6 hours are shown in Figures 5.5 to 5.11. As shown in Figure 5.5, the electrical conductivity, σ for $x \le 0.15$ decreases with increasing temperature. This trend shows typical metallic-type behaviour. Further, within this same range of compositions ($x = 0.05$ to 0.15), σ increases as the La-Sm concentration increases, showing that σ depends on carrier concentration and carrier mobility [19]. At high La-Sm concentrations ($x \ge 0.20$), a switch from metallic to semiconducting behaviour was observed. This behaviour is attributed in part to inability of the heavy dopants to be fully incorporated into the lattice, hence more grain boundaries that act as scattering centres to electrons and phonons are created. Therefore, carrier mobility is restricted which leads to decrease in σ [9], [10]. Further, this may relate to structural phase transitions involving the rotation of O-octahedra commonly seen in RE-doped $SrTiO_3$ [2], [3], [6].

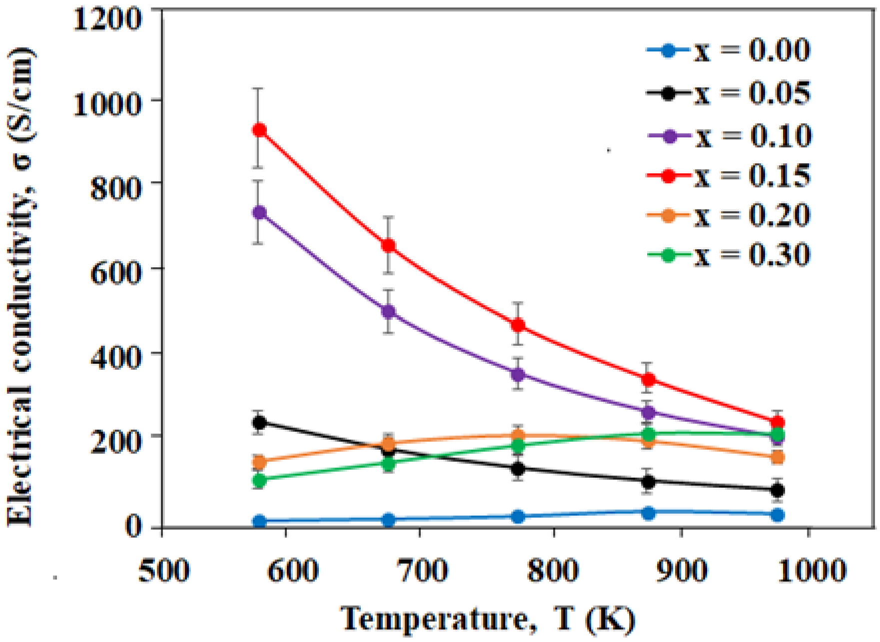

Figure 5.5. Temperature dependence of electrical conductivity, σ for $Sr_{1-x}La_{x/2}Sm_{x/2}TiO_3$ ($0.00 \leq x \leq 0.30$) ceramics sintered in 5% H_2/N_2 at 1773 K for 6 hours.

Han *et al* [20] obtained a similar electrical conduction behaviour in their study of microstructure and thermoelectric properties of $La_{0.1}Dy_{0.1}Sr_xTiO_3$ (x = 0.70, 0.75, 0.78, 0.80) ceramics. At $x \geq 0.78$, the ceramics exhibited semiconducting behaviour with low σ values compared to $x \leq 0.75$ compositions. The authors attributed this trend to generation of defects (Sr and O) and presence of porosity in the microstructure, which restrict the carrier mobility by scattering carriers. Studying the influence of 10 wt% of RE (La, Nd, Sm, Gd, Dy, Y, Er, Yb) doping on TE properties of $SrTiO_3$ ceramics has shown the impact of pores and second phases [5], which supports the σ behaviour obtained in this work. Liu *et al* [5], showed that inherent pores and second phases generated in the microstructure of $Sr_{0.9}Yb_{0.1}TiO_3$ reduced the relative density (91.6%) compared to other compositions, and switched the electrical conduction from metallic to semiconducting behaviour.

The temperature dependence of Seebeck coefficient (S) is shown in Figure 5.6. The Seebeck coefficients of all compositions are negative, suggesting *n*-type electrical conduction. The absolute value of S increases linearly with temperature, and this indicates metallic behaviour [9]–[11]. The │S│ decreases with increasing La-Sm concentration in all the samples. This suggests an inverse relationship between S and carrier concentration. For example, │S│ (~ 393 µV/K) for x = 0.00 at 973 K decreases to ~ 179 µV/K and ~ 119 µV/K at 973 K for x = 0.15 and x = 0.30, respectively. The linear relationship of S with temperature and inversely related with carrier concentration for all the compositions can be expressed as [11]:

$$S = \frac{\pi^2 K_B^2 T}{eE_F} \qquad 5.1$$

where K_B is Boltzmann constant (8.617 x 10^{-5} eV), T, e, and E_F are Temperature, electron charge and Fermi level, respectively. From equation 5.1, S is inversely related to $E_{F.}$ Therefore, increase in doping level (invariably an increase in carrier concentration) causes an upward shift of the energy level resulting to increase in E_F and decrease in S.

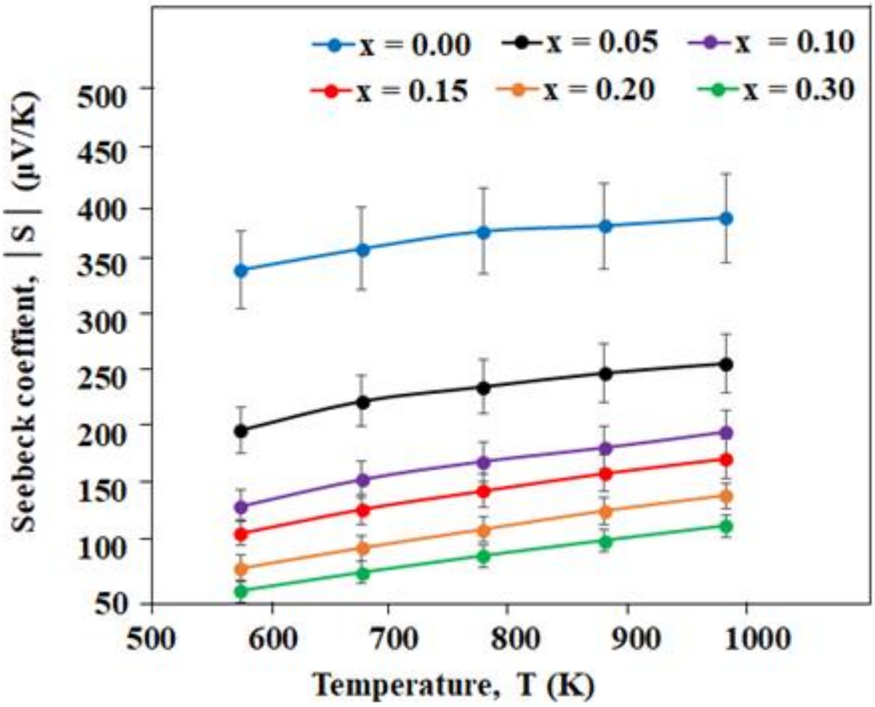

Figure 5.6. Temperature dependence of absolute Seebeck coefficient, |S| for $Sr_{1-x}La_{x/2}Sm_{x/2}TiO_3$ ($0.00 \leq x \leq 0.30$) ceramics sintered in 5% H_2/N_2 at 1773 K for 6 hours.

The power factor, PF was calculated from $S^2\sigma$, and presented in Figure 5.7. PF for $0.05 \leq x \leq 0.15$ ceramics decreases progressively in the entire measured temperature range (573-973 K) with a display of relative larger values. For x = 0.00 and $x \geq 0.20$, the PF increases with increasing temperature over all the measured temperature range but with very low values, hence unsuitable for thermoelectric applications. x = 0.10 exhibits the highest PF of ~ 1400 µW/K^2.m and ~ 865 µW/K^2.m at 573 and 973 K, respectively. The interplay of S and conductivity in reduced oxide compositions and how it gives rise to PF values is complex. The “O” stoichiometry is most likely inhomogeneous with the bulk having higher oxygen concentration than the grain boundary regions [3]. The resulting inhomogeneous electrical microstructure may result in differing Seebeck coefficients and conductivities as a function of distance within the sample, with the macroscopic properties representing average behaviour [3].

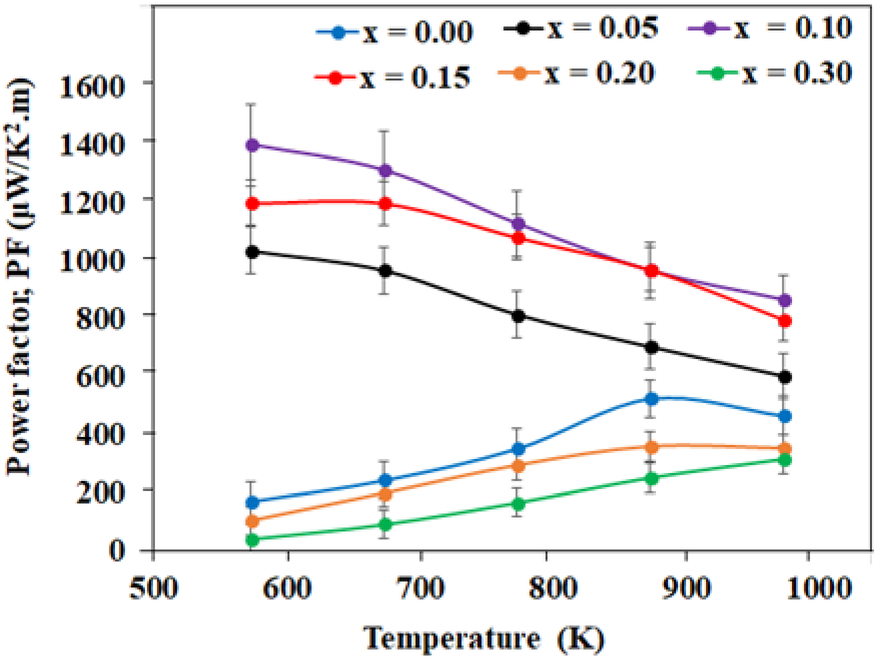

Figure 5.7. Temperature dependence of power factor, PF for $Sr_{1-x}La_{x/2}Sm_{x/2}TiO_3$ ($0.00 \leq x \leq 0.30$) ceramics sintered in 5% H_2/N_2 at 1773 K for 6 hours.

Total thermal conductivity ($k = k_E + k_L$) as a function of temperature is shown in Figure 5.8 and the electronic thermal conductivity, k_E is presented in Figure 5.9. As discussed in the literature review, k_E was calculated from Wiedemann-Franz law (equation 2.27), while lattice thermal conductivity (k_L) shown in Figure 5.10 was determined from k and k_E (equation 2. 26). k decreases with increasing temperature within the measured temperature range. This suggests that heat transfer is controlled by phonon scattering via oxygen deficiency and lattice defects [3], [21], [22]. For example, k for x = 0.00 ceramics decreased linearly from 5.9 W/m.K at 573 K to 4.2 W/m.K at 973 K. As observed from Figures 5.8 and 5.10, the difference between k and k_L is very small, while large differences exist between k and k_E, Figure 5.9. This explains the fact that k_E contributed less to k. Therefore, the decrease in k with temperature of $Sr_{x-1}La_{x/2}Sm_{x/2}TiO_3$ ($0.05 \leq x \leq 0.30$) ceramics is mainly attributed to a reduction in k_L obtained by enhanced phonon scattering.

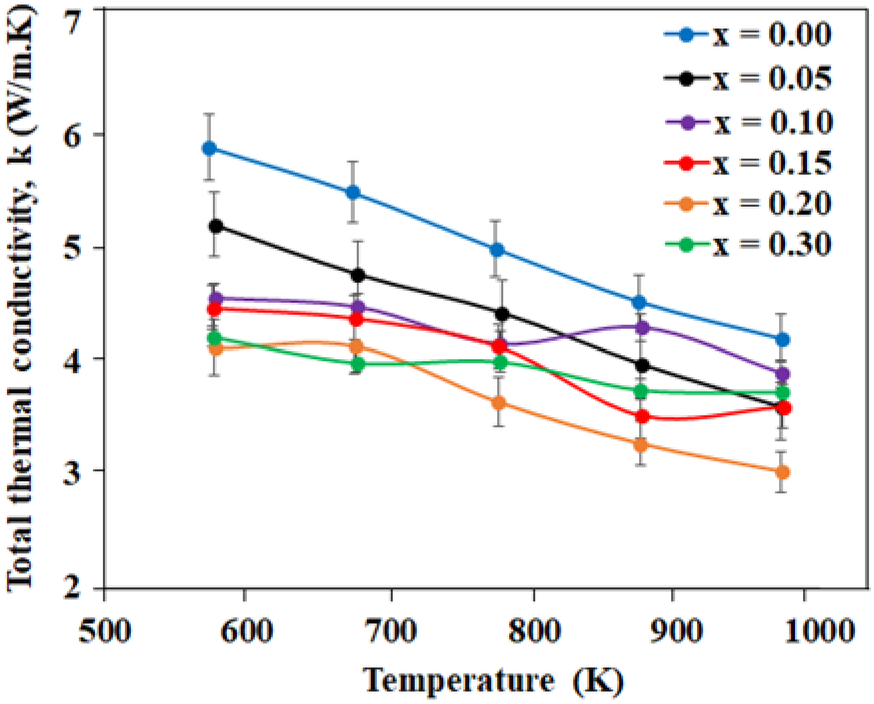

Figure 5.8. Temperature dependence of total thermal conductivity, k for $Sr_{1-x}La_{x/2}Sm_{x/2}TiO_3$ ($0.00 \leq x \leq 0.30$) ceramics sintered in 5% H_2/N_2 at 1773 K for 6 hours.

Enhanced phonon scattering is dependent on the difference between size (ionic radius) and mass of the dopant and the host (matrix) [11]. In this work, the atomic mass of the dopants (La and Sm) is 138.91 and 150.36 g/mol, respectively, while the host (Sr) has a small atomic mass of 87.62 g/mol. However, the ionic radius of the dopants (La = 1.36 Å, Sm = 1.24 Å in CN 12) is slightly smaller than Sr (1.44 Å in CN 12). From this observation, the increase in phonon scattering and resultant decrease in k can be attributed to the large mass difference between the dopants (La and Sm) and host species (Sr). It is noted that an increase in porosity and presence of secondary phases also contribute in reducing k. Thermal conductivity of non-metallic crystals such as ceramics depends mainly on lattice vibration (phonon) [23]. Thus, phonon scattering during transmission by defects, impurities, pores and phase boundaries lead to low k. These effects impede carrier mobility and phonon propagation resulting in low σ [10], [16], [17] and low k [10], [16]. As shown in

Figures 5.1 and 5.3, the pores and phases observed in $x \geq 0.20$ ceramics may have contributed in the low thermal and electrical conductivities. The lowest k is observed for x = 0.20 with a value of ~ 3.0 W/m.K at 973 K.

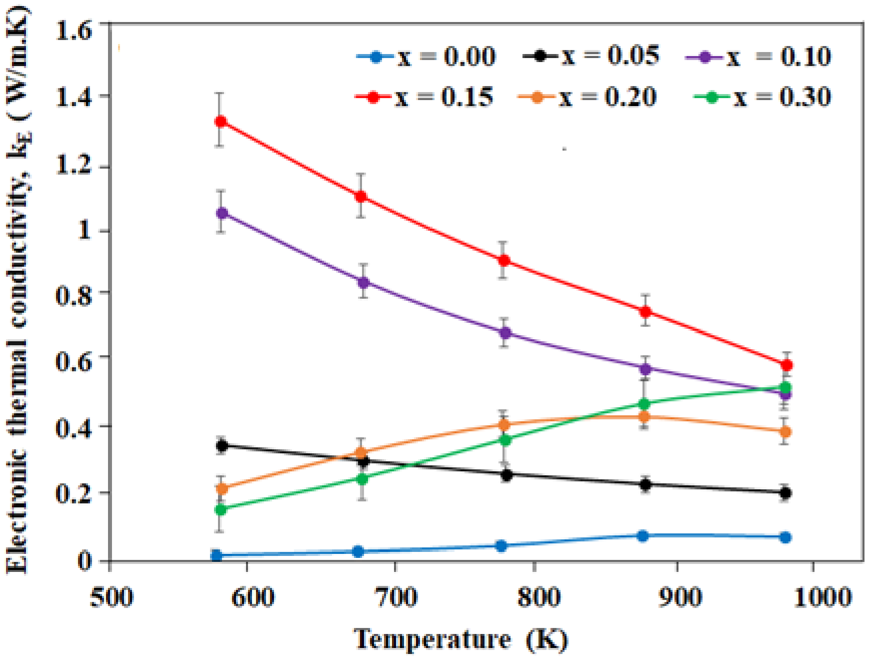

Figure 5.9. Temperature dependence of electronic thermal conductivity, k_E for $Sr_{1-x}La_{x/2}Sm_{x/2}TiO_3$ ($0.00 \leq x \leq 0.30$) ceramics sintered in 5% H_2/N_2 at 1773 K for 6 hours.

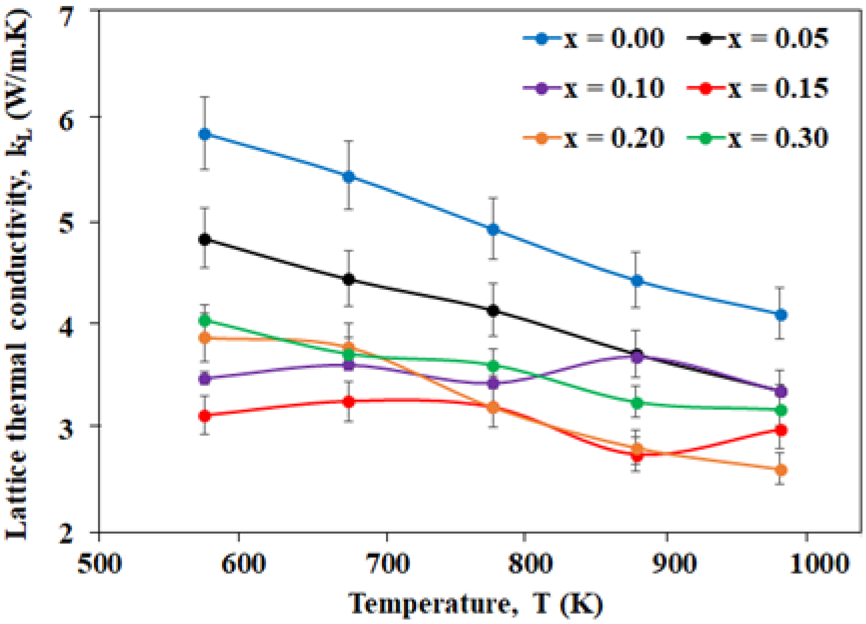

Figure 5.10. Temperature dependence of lattice thermal conductivity, k_L for $Sr_{1-x}La_{x/2}Sm_{x/2}TiO_3$ ($0.00 \leq x \leq 0.30$) ceramics sintered in 5% H_2/N_2 at 1773 K for 6 hours.

Temperature dependence of dimensionless ZT is shown in Figure 5.11. ZT of all ceramic samples increases with temperature over the whole temperature range. However, a “transverse wave” behaviour was observed between x = 0.10 and x = 0.15 ceramics at high temperature range (773 – 973 K) resulting in a crest (maximum point) and trough (minimum point) at 873 K. The effect of heavy doping ($x \geq 0.30$) and consequent porosity on σ and k also influence ZT. The excess scattering centres created in the lattice results in low ZT values for $x \geq 0.30$ ceramics. Overall, x = 0.15 shows the highest ZT value of 0.24 at 873 K. This is due to the relatively high PF and low k exhibited by x = 0.15 ceramics.

The maximum ZT value (0.24) obtained for 15 wt% La-Sm doped sample at 873 K is low due to low σ compared to other RE electron co-doped $SrTiO_3$ in the literature [5], [6], [8], [11], [24]. It is important to state that authors report these high ZT values at elevated temperatures (≥ 1000 K) where the operation of a commercial

TE device is not feasible [25]. Boston *et al* [25], therefore suggests the report of TE properties at intermediate temperatures (573 – 973 K) for easy assessment of the potential and viability of the TE materials. However, the approach applied in this work has shown a pathway to pursue methodologies to improve the power factor, maximise the ZT and utilise the reduction in k as a result of defects and pores.

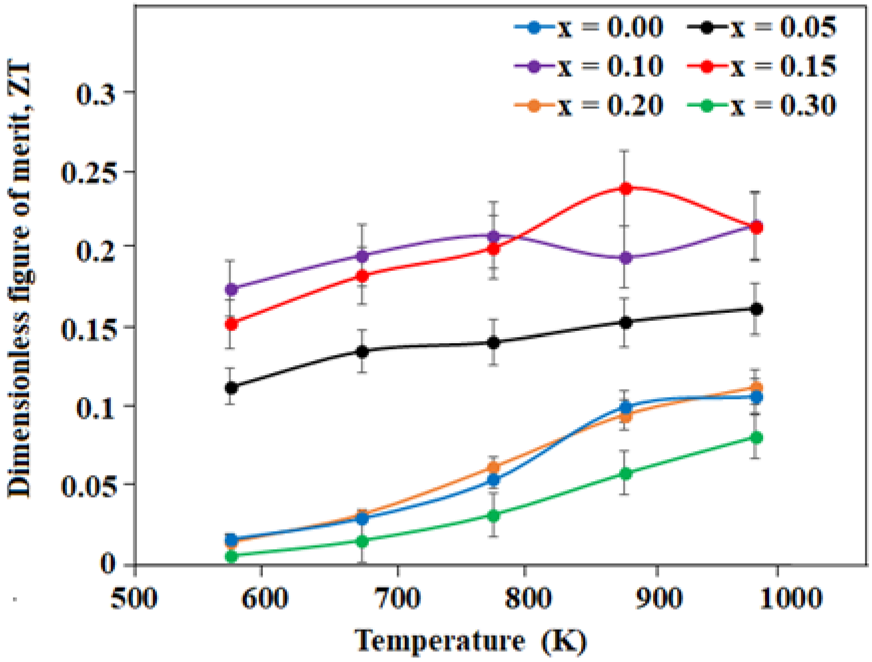

Figure 5.11. Temperature dependence of dimensionless figure of merit, ZT, for $Sr_{1-x}La_{x/2}Sm_{x/2}TiO_3$ (0.00 ≤ x ≤ 0.30) ceramics sintered in 5% H_2/N_2 at 1773 K for 6 hours

5.6 Conclusion

Evidence is presented here that novel electronically co-doped $SrTiO_3$ ceramics with La and Sm enhances the ZT in part through a reduction in k (minimum k = 3.0 W/m.K at 973 for x = 0.20). However, as the La-Sm concentration increases, σ and │S│ decrease with a corresponding decrease in PF. Compositions with x = 0.15 ceramics with the highest ZT (0.24 at 873 K) reflect an optimum comprise between reducing k and maintaining metallic behaviour with high σ.

Further, RE co-doped $SrTiO_3$ with La and Sm decreases the scale length of previously observed tetragonal distortion associated with Sm (and other RE with small ionic radii) as a single dopant [2].

However, overall it is established that electron co-doping had minimal effect on k leading to the conclusion that optimising ZT by this method is of limited merit in the context of this compositional set. In light of the work reported by Lu *et al* [6] and Lu [26], it is suggested that batched stoichiometries with A-site (cation) vacancies are more likely to optimize ZT, at least in part through enhanced phonon scattering and reducing k. This idea informs the aim of the work as presented in chapter six.

References

[1] M. Backhaus-Ricoult, J. Rustad, L. Moore, C. Smith, and J. Brown, "Semiconducting large bandgap oxides as potential thermoelectric materials for high-temperature power generation?," *Appl. Phys. A Mater. Sci. Process.*, vol. 116, no. 2, pp. 433–470, 2014.

[2] A. V. Kovalevsky, A. A. Yaremchenko, S. Populoh, P. Thiel, D. P. Fagg, A. Weidenkaff, and J. R. Frade, "Towards a high thermoelectric performance in rare-earth substituted $SrTiO_3$: effects provided by strongly-reducing sintering conditions," *Phys. Chem. Chem. Phys.*, vol. 16, no. 48, pp. 26946–26954, 2014.

[3] Adindu C. Iyasara, Whitney L. Schmidt, Rebecca Boston, Derek C. Sinclair, and Ian M. Reaney, "La and Sm Co-doped $SrTiO_{3-\delta}$ Thermoelectric Ceramics," *Mater. Today Proc.*, vol. 4, no. 12, pp. 12360–12367, 2017.

[4] Deepanshu Srivastava, Colin Norman, Feridoon Azough, Marion C. Schafer, Emmanuel Guilmeau, Demie Kepaptsoglou, Quentin M. Ramasse, Giuseppe Nicotrad, and Robert Freer, "Tuning the Thermoelectric Properties of A-site Deficient $SrTiO_3$ Ceramics by Vacancies and Carrier Concentration," *Phys. Chem. Chem. Phys.*, vol. 18, pp. 26475–26486, 2016.

[5] J. Liu, C. L. Wang, Y. Li, W. B. Su, Y. H. Zhu, J. C. Li, and L. M. Mei, "Influence of rare earth doping on thermoelectric properties of $SrTiO_3$ ceramics," *J. Appl. Phys.*, vol. 114, no. 22, 2013.

[6] Zhilun Lu, Huairuo Zhang, Wen Lei, Derek C. Sinclair, and Ian M. Reaney, "High-Figure-of-Merit Thermoelectric La-Doped A-Site-Deficient $SrTiO_3$ Ceramics," *Chem. Mater.*, vol. 28, no. 3, pp. 925–935, 2016.

[7] A. V. Kovalevsky, A. A. Yaremchenko, S. Populoh, A. Weidenkaff, and J. R. Frade, "Effect of A-site cation deficiency on the thermoelectric performance of donor-substituted strontium titanate," *J. Phys. Chem. C,* vol. 118, no. 9, pp. 4596–4606, 2014.

[8] Jun Wang, Bo Yu Zhang, Hui Jun Kang, Yan Li, Xinba Yaer, Jing Feng Li, Qing Tan, Shuai Zhang, Guo Hua Fan, Cheng Yan Liu, Lei Miao, Ding Nan, Tong Min Wang, and Li Dong Zhao, "Record high thermoelectric performance in bulk $SrTiO_3$ via nano-scale modulation doping," *Nano Energy*, vol. 35, no. April, pp. 387–395, 2017.

[9] Hongchao Wang and Chunlei Wang, "Thermoelectric properties of Yb-doped $La_{0.1}Sr_{0.9}TiO_3$ ceramics at high temperature," *Ceram. Int.*, vol. 39, no. 2, pp. 941–946, 2013.

[10] Hong Chao Wang, Chun Lei Wang, Wen Bin Su, Jian Liu, Yi Sun, Hua Peng, and Liang Mo Mei, "Doping effect of La and Dy on the thermoelectric properties of $SrTiO_3$," *J. Am. Ceram. Soc.*, vol. 94, no. 3, pp. 838–842, 2011.

[11] H C Wang, C L Wang, W B Su, J Liu, Y Zhao, H Peng, J L Zhang, M L Zhao, J C Li, N Yin, and L M Mei, "Enhancement of thermoelectric figure of merit by doping Dy in $La_{0.1}Sr_{0.9}TiO_3$ ceramic," *Mater. Res. Bull.*, vol. 45, no. 7, pp. 809–812, 2010.

[12] S. Bhattacharya, A. Mehdizadeh Dehkordi, S. Tennakoon, R. Adebisi, J. R. Gladden, T. Darroudi, H. N. Alshareef, and T. M. Tritt, "Role of phonon scattering by elastic strain field in thermoelectric $Sr_{1-x}Y_xTiO_{3-\delta}$," *J. Appl. Phys.*, vol. 115, no. 22, 2014.

[13] Klaus Van Benthem, C. Elsasser, and Roger H French, "Bulk Electronic Structure of $SrTiO_3$: Experiment and Theory," *J. Appl. Phys.*, vol. 90, pp. 6156–6164, 2001.

[14] Dragos Neagu and John T S Irvine, "Structure and Properties of $La_{0.4}Sr_{0.4}$ TiO_3 Ceramics for Use as Anode Materials in Solid Oxide Fuel Cells," *Chem. Mater.*, vol. 22, no. 6, pp. 5042–5053, 2010.

[15] Peng Peng Shang, Bo Ping Zhang, Yong Liu, Jing Feng Li, and Hong Min Zhu, "Preparation and thermoelectric properties of La-doped $SrTiO_3$ ceramics," *J. Electron. Mater.*, vol. 40, no. 5, pp. 926–931, 2011.

[16] Chang Sun Park, Min Hee Hong, Hyung Hee Cho, and Hyung Ho Park, "Effect of mesoporous structure on the Seebeck coefficient and electrical properties of $SrTi_{0.8}Nb_{0.2}O_3$," *Appl. Surf. Sci.*, vol. 409, pp. 17–21, 2017.

[17] Min Hee Hong, Chang Sun Park, Sangwoo Shin, Hyung Hee Cho, Won Seon Seo, Young Soo Lim, Jung Kun Lee, and Hyung Ho Park, "Effect of surfactant concentration variation on the thermoelectric properties of mesoporous ZnO," *J. Nanomater.*, vol. 2013, pp. 1–6, 2013.

[18] Kunihito Koumoto, Yifeng Wang, Ruizhi Zhang, Atsuko Kosuga, and Ryoji Funahashi, "Oxide Thermoelectric Materials: A Nano Structuring Approach," *Annu. Rev. Mater. Res.*, vol. 40, pp. 363–394, 2010.

[19] G J Snyder and E S Toberer, “Complex thermoelectric materials,” *Nature Mater*, vol. 7, no. 2, pp. 105–114, 2008.

[20] Jiao Han, Qiu Sun, Wenxu Li, and Ying Song, “Microstructure and thermoelectric properties of $La_{0.1}Dy_{0.1}Sr_xTiO_3$ ceramics,” *Ceram. Int.*, vol. 43, no. 7, pp. 5557–5563, 2017.

[21] G. H. Zheng, Z. X. Dai, Y. Q. Dong, F. L. Zan, D. Zou, Y. Q. Ma, and G. Li, “Low thermal conductivity for $Sr_{1-x}La_xTiO_3$,” *Mater. Res. Innov.*, vol. 16, no. 6, pp. 438–441, 2012.

[22] Choongho Yu, Matthew L. Scullin, Mark Huijben, Ramamoorthy Ramesh, and Arun Majumdar, “Thermal conductivity reduction in oxygen-deficient strontium titanates,” *Appl. Phys. Lett.*, vol. 92, no. 19, pp. 1–4, 2008.

[23] Mengjie Qin, Feng Gao, Gaogao Dong, Jie Xu, Maosen Fu, Yu Wang, Mike Reece, and Haixue Yan, “Microstructure characterization and thermoelectric properties of $Sr_{0.9}La_{0.1}TiO_3$ ceramics with nano-sized Ag as additive,” *J. Alloys Compd.*, vol. 762, pp. 80–89, 2018.

[24] Jiao Han, Qiu Sun, and Ying Song, “Enhanced thermoelectric properties of La and Dy co-doped, Sr-deficient $SrTiO_3$ ceramics,” *J. Alloys Compd.*, vol. 705, pp. 22–27, 2017.

[25] R. Boston, W. L. Schmidt, G. D. Lewin, A. C. Iyasara, Z. Lu, H. Zhang, D. C. Sinclair, and I. M. Reaney, “Protocols for the fabrication, characterization, and optimization of n-type thermoelectric ceramic oxides,” *Chem. Mater.*, vol. 29, no. 1, pp. 265–280, 2017.

[26] Zhilun Lu, “La doped $SrTiO_3$ Based Oxide Thermoelectrics.,” PhD Thesis, University of Sheffield, 2016.

Chapter 6: A-Site Vacancy La-Sm Co-Doped $SrTiO_3$ Ceramics

6.1 Introduction

As discussed in Chapter 5, a maximum ZT value of 0.24 at 873 K was obtained in electron La-Sm co-doped $SrTiO_3$ ceramics. A conclusion is drawn that this method is of limited effect in optimizing ZT. Introduction of cation vacancies in the A- and/or B-site, doped with RE and/or transition metal cations, followed once again by processing in reduced atmosphere has been suggested as a promising route to achieving optimised thermoelectric properties [1]. The combination of cation and anion vacancies has been shown to improve PF and suppress k [2], [3] by previous researchers and is the basis of the following chapter. There are various approaches so far utilized for optimising the thermoelectric properties in $SrTiO_3$. These include suitable doping (and co-doping), additives (or inclusions), enhanced processing conditions, defect engineering and micro/nanostructural engineering [1], [3]. The highest ZT values achieved in applying these methods for bulk $SrTiO_3$ ceramics remained ≤ 0.4 until recently $ZT \geq 0.6$ at 1000-1100 K was reported in La-Nb co-doped $SrTiO_3$ bulk ceramics [4].

The work reported in this chapter therefore attempts to improve the thermoelectric properties of A-site vacancy La-Sm co-doped $SrTiO_3$ ceramics by modifying the calcination atmosphere, temperature, dwell time, and calcination cycles. Sintering methods and atmospheres (e.g. 5%H_2/N_2) as described in chapter five are utilised. The A-site vacancy La-Sm co-doped $SrTiO_3$ ceramics whose powder were calcined in air will be denoted as VSTO-A while those calcined in 5%H_2/N_2 will be known as VSTO-H (VSTO denotes strontium titanate with compositionally engineered A-site vacancies).

6.2 Results and Discussion

6.2.1 Phase Assemblage

Figure 6.1 shows the room temperature XRD patterns of crushed $Sr_{1-3x/2}La_{x/2}Sm_{x/2}TiO_3$ ($0.05 \leq x \leq 0.30$) ceramics (VSTO-A and VSTO-H) sintered in 5% H_2/N_2 at 1773 K for 6 or 8 hours. All the major peaks can be indexed with the $SrTiO_3$ cubic perovskite structure belonging to the Pm-3m space group (PDF# 04-002-6890). No secondary phase was detected within the limits of the diffractometer. The lattice parameters, cell volumes and theoretical densities were calculated from the XRD data and results are shown in Table 6.1. The dopant (La-Sm) concentration dependence of the lattice parameters of VSTO-A and VSTO-H compositions are presented in Figure 6.2.

The lattice parameters of VSTO-A compositions show a progressive decreasing relationship with increasing La-Sm concentrations (Figure 6.2). The lattice parameters of VSTO-A ceramics contract from 3.910 Å (for $x = 0.05$) to a minimal value of 3.902 Å for $x = 0.30$. The decrease in lattice parameter is attributed to the smaller ionic radii of La^{3+} and Sm^{3+} (La^{3+} = 1. 36 Å; Sm^{3+} = 1.24 Å in CN 12) than that of Sr^{2+} ionic radius (1.44 Å in CN 12) [5]–[8] and in obedience to Vegard's law. In contrast, the lattice parameters of VSTO-H compositions of $0.05 \leq x \leq 0.20$ ceramics increase with increasing La-Sm doping concentrations, from 3.899 Å to 3.910 Å and drops at $x = 0.30$ with a value of 3.902 Å (Table 6.1(b), Figure 6.2). The lattice parameter may expand due to a decrease in Coulombic force in the lattice by the formation of V_O accompanied by partial reduction of Ti^{4+} ions (0.605 Å in CN 6) to a high ionic radius Ti^{3+} ion (0.67 Å in CN 6) [2]. The reason behind the decrease in lattice parameter at high doping level ($x = 0.30$) is unclear but might be related to structural transitions or distortions or solid solution limit. However, as suggested in Chapter 5, subsection 5.2.1, further crystallographic study using electron diffraction would provide more insight.

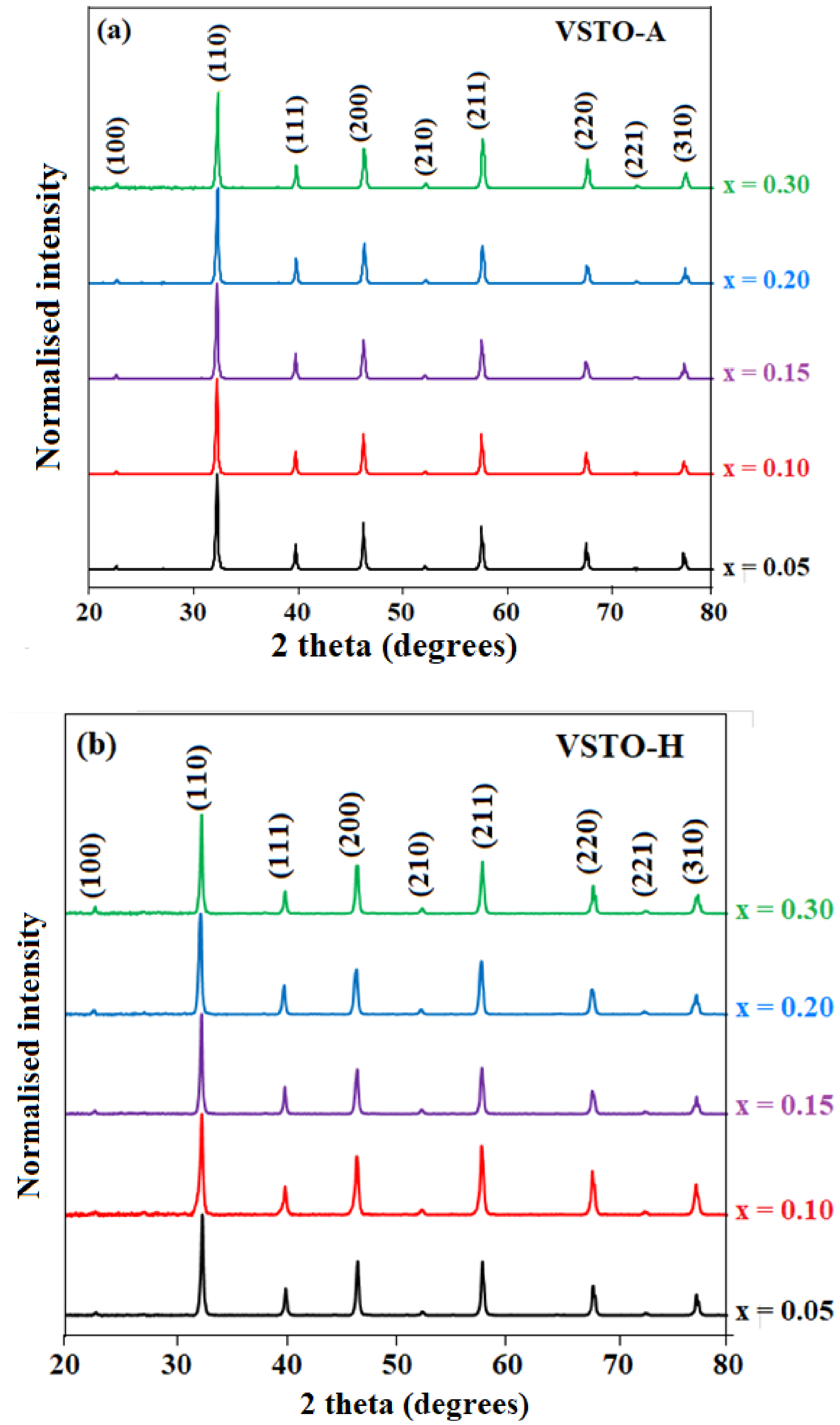

Figure 6.1. Room temperature XRD patterns of crushed $Sr_{1-3x/2}La_{x/2}Sm_{x/2}TiO_3$; $0.05 \leq x \leq 0.30$ ceramics calcined in (a) air (VSTO-A) at 1573 K for 6 hours and (b) 5% H_2/N_2 (VSTO-H) at 1573 K for 6 hours and sintered in 5% H_2/N_2 at 1773 K for 6-8 hours.

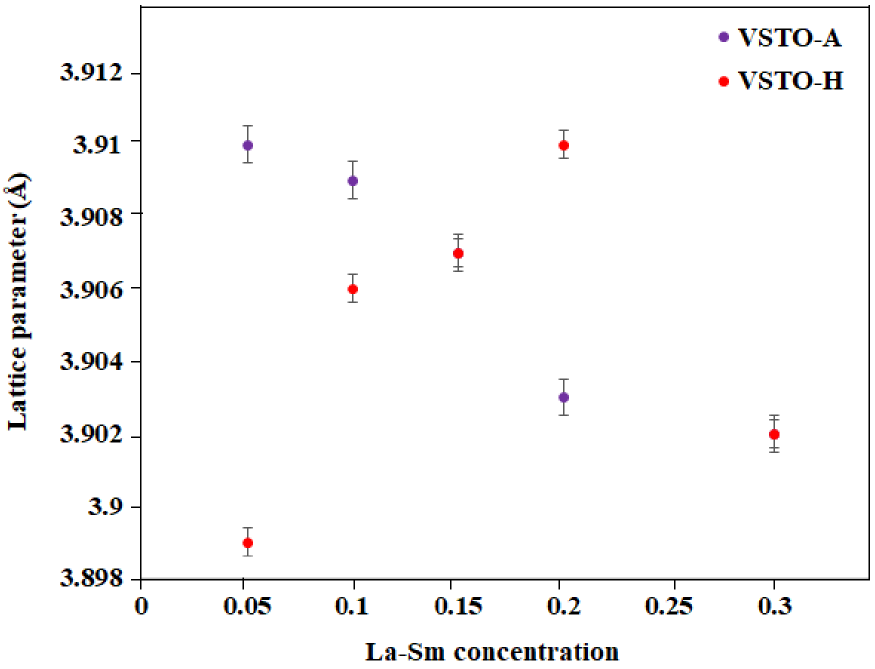

Figure 6.2. Dopant (La-Sm) concentration dependence of the lattice parameters of $Sr_{1-3x/2}La_{x/2}Sm_{x/2}TiO_3$; $0.05 \leq x \leq 0.30$. The lattice parameters merged at x = 0.15 and 0.30 for both VSTO-A and VSTO-H ceramics as represented by double capped (at both ends) uncertainty bar icons.

6.2.2 Microstructure

Secondary electron microscopy (SEM) micrographs of the thermally etched, carbon coated surfaces for $Sr_{1-3x/2}La_{x/2}Sm_{x/2}TiO_3$; $0.05 \leq x \leq 0.30$ ceramics are shown in Figures 6.3 and 6.4. After sintering, all compositions showed a relative density of ≥ 96 % (Table 6.1). All images revealed homogenous and dense microstructures consistent with their high relative density. The average grain size of the compositions was calculated using the line intercept method [9], [10]. All samples exhibited regular polygonal-shaped grain structures, with size increasing with doping concentration. The average grain size of VSTO-A samples increased from 5.1 µm (for x = 0.05) to 9.6, 14.9 and 15.3 µm for x = 0.10, 0.20 and 0.30 ceramics, respectively. VSTO-H samples showed similar trend with VSTO-A compositions, but the grain sizes are smaller especially at high x values.

The average grain size increased from 7.5 µm for x = 0.10 to 10.4 µm for x = 0.15, to 10.8 µm for x = 0.20, and finally to 11.2 µm for x = 0.30. The small average grain size exhibited by VSTO-H compositions compared to that of VSTO-A compositions agrees with the particle size distribution (PSD) results reported in Chapter 4 (Table 4.1) for powders used for VSTO-A and VSTO-H ceramics. VSTO-A powders had a mean particle size (d_{50}) of ≤ 6.04 µm while VSTO-H showed a smaller d_{50} of ≤ 4.70 µm. It can be concluded from these results that processing (calcination and sintering) of vacancy co-doped $Sr_{1-3x/2}La_{x/2}Sm_{x/2}TiO_3$ ceramics in 5% H_2/N_2 gas contributes in the grain size reduction. This assertion is supported by the study undertaken by Srivastava *et al* [3]. The authors revealed that $Sr_{0.8}La_{0.067}Ti_{0.8}Nb_{0.2}O_{3-\delta}$ ceramics when sintered in air showed a grain size of ~ 13 µm, and 7-10 µm when sintered in reducing atmosphere. Therefore, processing in reducing atmosphere creates oxygen vacancies, which contribute to the reduction in grain size. The use of highly reducing processing conditions (calcination and sintering) in 5% H_2/N_2 as applied in this work is postulated to cause stripping of more V_O from the lattice. Reduced grain size (incorporation of large grain boundaries) shortens the mean free path (MFP) of the phonons. Since grain boundaries act as scattering for the phonons [11], k is reduced with consequent increase in ZT [12], [13].

In VSTO-A SEM images, artefacts (labelled with white circles on the images) were observed on the grain and grain boundaries. This abnormal feature is likely deposited onto the ceramics through sample preparations or absorbed dirt or trapped impurities in the furnaces used for the processing. These impurities are more pronounced in x = 0.30, and with enlarged sizes. Since the presence of impurities and defects affect k, these artefacts might have contributed to the low thermal conductivity observed in this composition.

Table 6.1. Lattice parameters, cell volumes and theoretical densities of $Sr_{1-3x/2}La_{x/2}Sm_{x/2}TiO_3$; $0.05 \leq x \leq 0.30$ ceramics calcined in (a) air (VSTO-A) at 1573 K for 6 hours and (b) 5% H_2/N_2 (VSTO-H) at 1573 K for 6 hours and sintered in 5% H_2/N_2 at 1773 K for 6-8 hours.

(a)	Composition x	Lattice parameter (Å) (±0.001 Å)	Cell volume (Å) (±0.002 Å)	Relative density (%) (±0.5 %)
	0.05	3.91	59.776	96.4
	0.10	3.909	59.731	98.9
	0.15	3.907	59.639	98.2
	0.20	3.903	59.456	98.4
	0.30	3.902	59.41	98.9

(b)	Composition x	Lattice parameter (Å) (±0.001 Å)	Cell volume (Å) (±0.002 Å)	Relative density (%) (±0.5 %)
	0.05	3.899	59.273	98.1
	0.10	3.906	59.593	96.1
	0.15	3.907	59.639	99.1
	0.20	3.91	59.776	98.7
	0.30	3.902	59.41	98.2

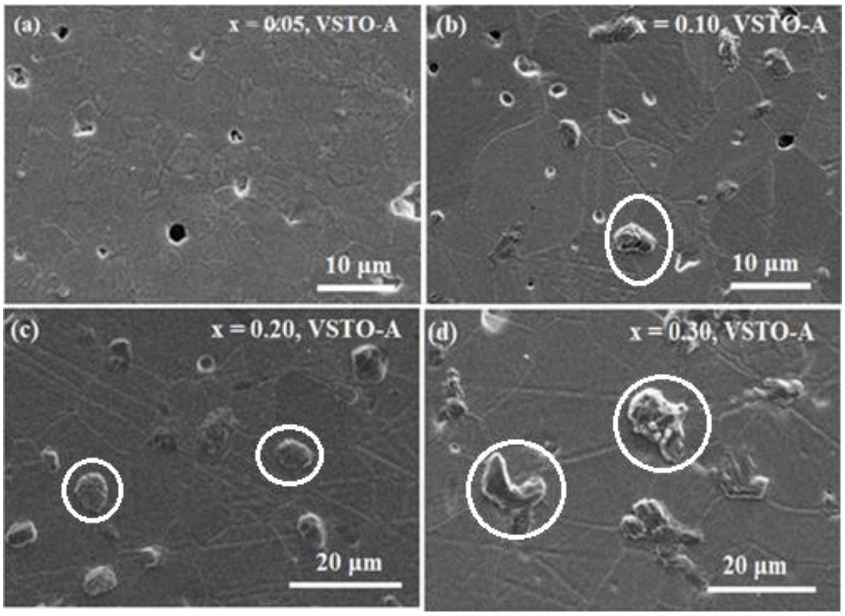

Figure 6.3. SEM micrographs of the surfaces of $Sr_{1-3x/2}La_{x/2}Sm_{x/2}TiO_3$; $0.05 \le x \le 0.30$ ceramics calcined in air (VSTO-A) at 1573 K for 6 hours, sintered at 1773 K for 6 hours and thermally etched at 1623 K for 30 minutes. Observed artefacts are labelled with white circles.

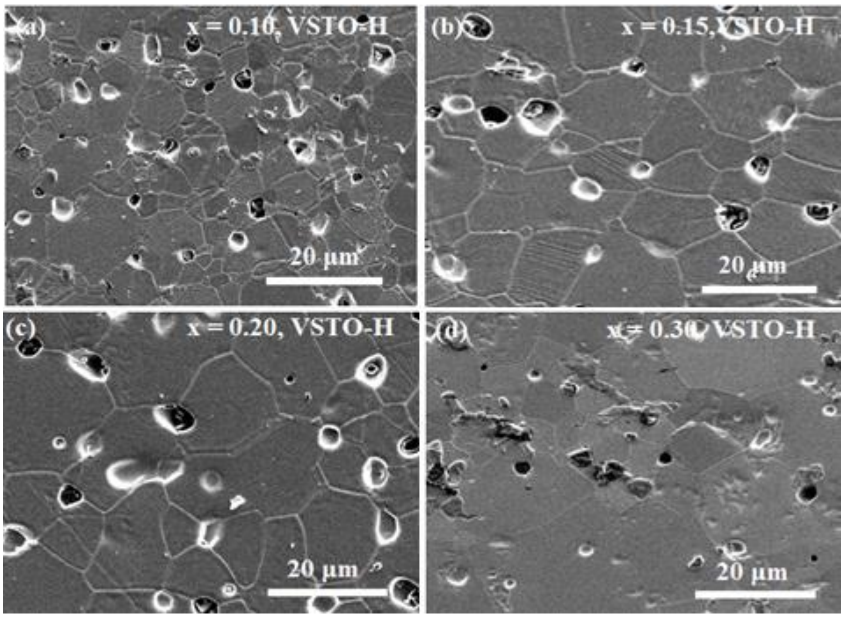

Figure 6.4. SEM micrographs of the surfaces of $Sr_{1-3x/2}La_{x/2}Sm_{x/2}TiO_3$; $0.05 \le x \le 0.30$ ceramics calcined in 5% H_2/N_2 (VSTO-H) at 1573 K for 6 hours, sintered in 5% H_2/N_2 at 1773 K for 8 hours and thermally etched at 1623 K for 30 minutes.

6.2.3 Thermogravimetric Analysis (TGA)

As shown in Figure 6.5, for the VSTO-A and VSTO-H calcined compositions sintered in 5% H_2/N_2 at 1773 K, oxygen uptake increased with increasing La-Sm concentration and decreased with oxidation temperature for all ceramics. $x = 0.05$ were stable in air up to 1000 °C. The colour of VSTO-A ceramics after TGA remained black for $x \leq 0.10$, turned to brown for $x \leq 0.20$ and white for $x = 0.30$, while in VSTO-H compositions, $x = 0.05$ was black and $x \geq 0.10$ turned white.

Table 6.2 shows the variation in weight in 5% H_2/N_2 calcined ceramics (VSTO-H) was larger than air calcined samples (VSTO-A). This indicates that calcination of vacancy doped $Sr_{1-3x/2}La_{x/2}Sm_{x/2}TiO_3$ powders in air and subsequent sintering in 5% H_2/N_2 yields a stable ceramic in air at higher temperatures. However, all the ceramics after TGA remained stable up to 475 °C and this is within the intermediate temperature range (300 -700 °C), suggested as desirable for a ceramic-based TE generator technology [11].

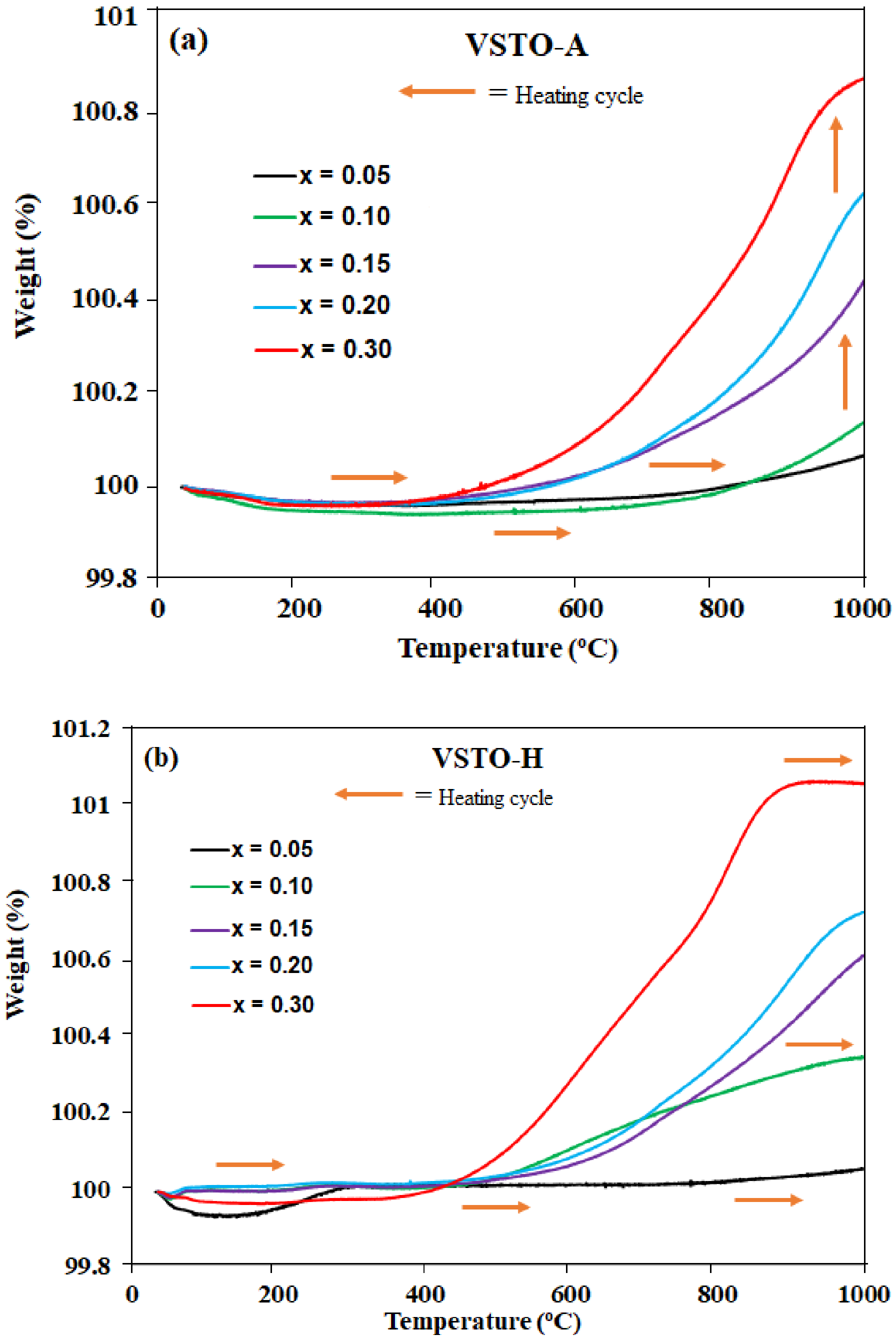

Figure 6.5. Thermogravimetric analysis showing the oxidation in air up to 1000 °C of $Sr_{1-3x/2}La_{x/2}Sm_{x/2}TiO_3$; $0.05 \leq x \leq 0.30$ ceramics calcined in (a) air (VSTO-A) at 1573 K for 6 hours and (b) 5% H_2/N_2 (VSTO-H) at 1573 K for 6 hours and sintered in 5% H_2/N_2 at 1773 K for 6-8 hours.

Table 6.2. TGA result showing the weight variation and oxidation onset temperature of $Sr_{1-3x/2}La_{x/2}Sm_{x/2}TiO_3$; $0.05 \leq x \leq 0.30$ ceramics calcined in (a) air (VSTO-A) at 1573 K for 6 hours and (b) 5% H_2/N_2 (VSTO-H) at 1573 K for 6 hours and sintered in 5% H_2/N_2 at 1773 K for 6-8 hours.

(a)

Composition x	Weight change Δwt. (%)	Oxidation onset temperature (°C)
0.05	0.00	> 1000
0.10	0.12	900
0.15	0.41	600
0.20	0.62	600
0.30	0.87	520

(b)

Composition x	Weight change Δwt. (%)	Oxidation onset temperature (°C)
0.05	0.00	> 1000
0.10	0.34	570
0.15	0.60	570
0.20	0.72	560
0.30	1.06	475

6.2.4 Thermoelectric Properties

6.2.4.1 VSTO-A Series

Figures 6.6 to 6.12 show the temperature dependence of the thermoelectric properties (σ, │S│, PF, k, k_L, k_E and ZT) of the $Sr_{1-3x/2}La_{x/2}Sm_{x/2}TiO_3$ (VSTO-A) ceramics sintered at 1773 K for 6 hours in 5% H_2/N_2 gas mixture. For all samples, electrical conductivity decreases with increasing temperature over the measured temperature range, Figure 6.6. This trend confirms metallic behaviour and also implies the properties share a similar conduction mechanism [6], [14]. σ for $x \leq 0.20$ compositions increases with increasing La-Sm concentration, showing the dependence of σ on carrier concentration and mobility [15]. At $x = 0.30$, the electrical conductivity decreased. The reason for the drop of σ at high La-Sm concentration is unclear, However, this may relate to solid solution limit (though no secondary phase was observed in the XRD and SEM images) or structural phase transitions as a result of rotation of O-octahedra observed in RE-doped $SrTiO_3$ [8], [16], [17]. The highest electrical conductivity obtained was 1184 S/cm at 573 K for $x = 0.20$. From literature, heavily doped La-Sm VSTO-A ceramics ($x \geq 0.15$) in this work show enhanced σ when compared to that of $Sr_{0.9}Nd_{0.1}TiO_3$ with B_2O_3 and Zr_2O_3 additions [18] and La-Nb co-doped $SrTiO_3$ ceramics [4] at the same temperature range (573 - 973 K). The σ result concludes that A-site vacancy has a greater effect on conductivity than electronic compensation in La-Sm doped $SrTiO_3$ (σ_{max} = 942 S/cm at 573 K for x = 0.15). It is important to state that x = 0.15 of VSTO-A shows a maximum electrical conductivity, σ_{max}=1029 S/cm at 573 K which is ~ 9% higher than σ_{max}= 942 S/cm of $Sr_{0.85}La_{0.075}Sm_{0.075}TiO_3$ at the same temperature. This may relate to greater oxide ion diffusion rates through the vacated A-site which permits a greater volume of reduced material throughout the ceramic.

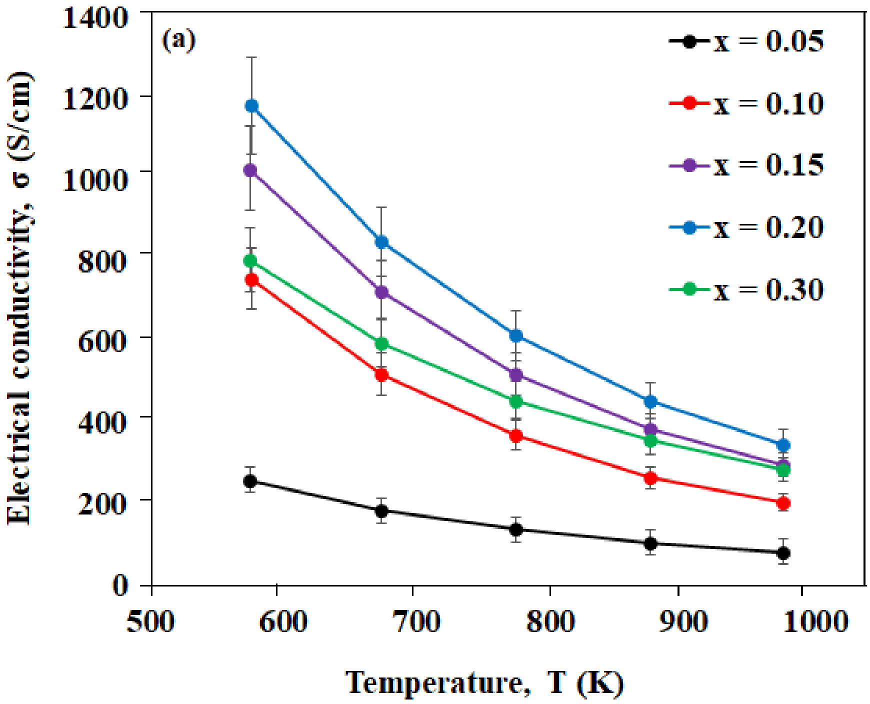

Figure 6.6. Temperature dependence of electrical conductivity, σ for $Sr_{1-3x/2}La_{x/2}Sm_{x/2}TiO_3$; $0.05 \leq x \leq 0.30$ ceramics calcined in air (VSTO-A) at 1573 K for 6 hours and sintered at 1773 K for 6 hours in 5% H_2/N_2.

Seebeck coefficients of all VSTO-A compositions are negative, indicating n-type conduction behaviour. Absolute coefficients for all compositions, Figure 6.7 increase linearly with increasing temperature, showing a metallic behaviour [5]–[7], [14]. $|S|$ values decrease as La-Sm concentration increases, Figure 6.7, possibly due to an increase in the carrier concentration resulting in an increase in electrical conductivity as shown in Figure 6.6. Because of the link of electrical conductivity to carrier concentration and its mobility ($\sigma = ne\mu$, equation 2.22), increase in carrier concentration suggesting metallic behaviour results in a decline in Seebeck coefficient. The $|S|$ value of all samples at high temperature (973 K) falls within the range of 158-255 µV/K.

It is noted however, that these $|S|$ values are higher than the minimum values of Seebeck coefficients (150 -250 µV/K) suggested for a good TE materials [19]. In addition, the Seebeck coefficients obtained are similar to data reported for La-Dy doped $SrTiO_3$ [6], [7] and La-Nb doped $SrTiO_3$ ceramics [4], [20], but lower than the values reported by Han and Song [21] for La-Dy co-doped Sr-deficient $SrTiO_3$ ceramics.

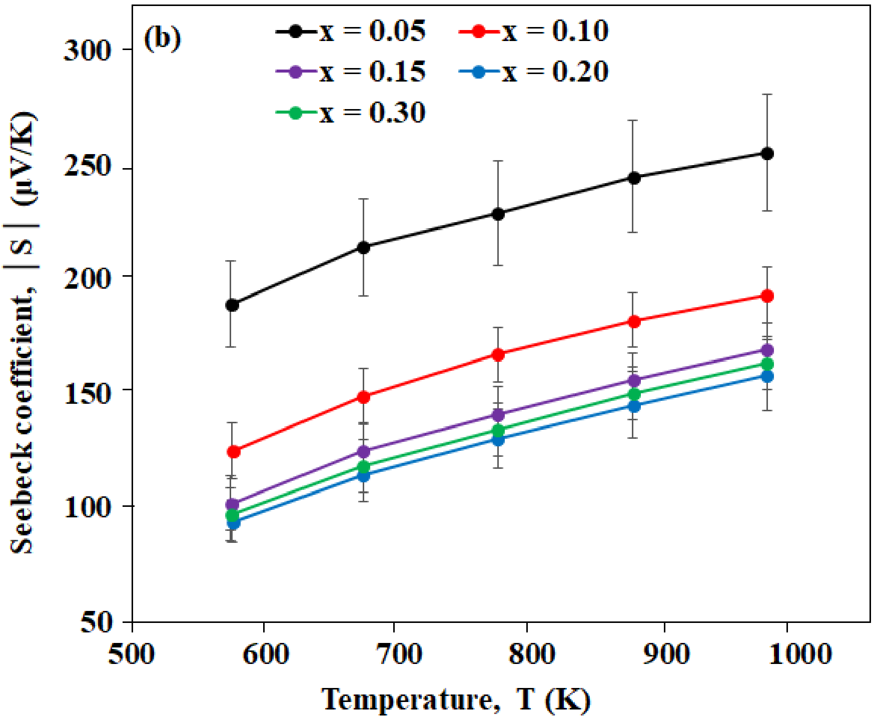

Figure 6.7. Temperature dependence of Seebeck coefficient, │S│ for $Sr_{1-3x/2}La_{x/2}Sm_{x/2}TiO_3$; $0.05 \leq x \leq 0.30$ ceramics calcined in air (VSTO-A) at 1573 K for 6 hours and sintered at 1773 K for 6 hours in 5% H_2/N_2.

Temperature dependence of power factors (PF) for VST-A compositions between 573 and 973 K are shown in Figure 6.8. The PF for samples with La-Sm concentrations ranging from 15 to 30 mol% ($x \geq 0.15$) displays a peak behaviour between 573 and 673 K, suggesting a semiconductor-like mechanism. Above 673 K, the power factors decreased with increasing temperature. For $x \leq 0.10$, the PF decreases in the entire measured temperature range. The maximum PF value of ~ 1185 $\mu W/K^2$ for x = 0.10 at 573 K was obtained. This high PF could be attributed to an optimised │S│ recorded (125-193 μV/K) which is higher than the │S│ values of other compositions except x = 0.05. However, at high temperatures, the PF of x = 0.10 decreased, and could be due to the low σ exhibited, Figure 6.6.

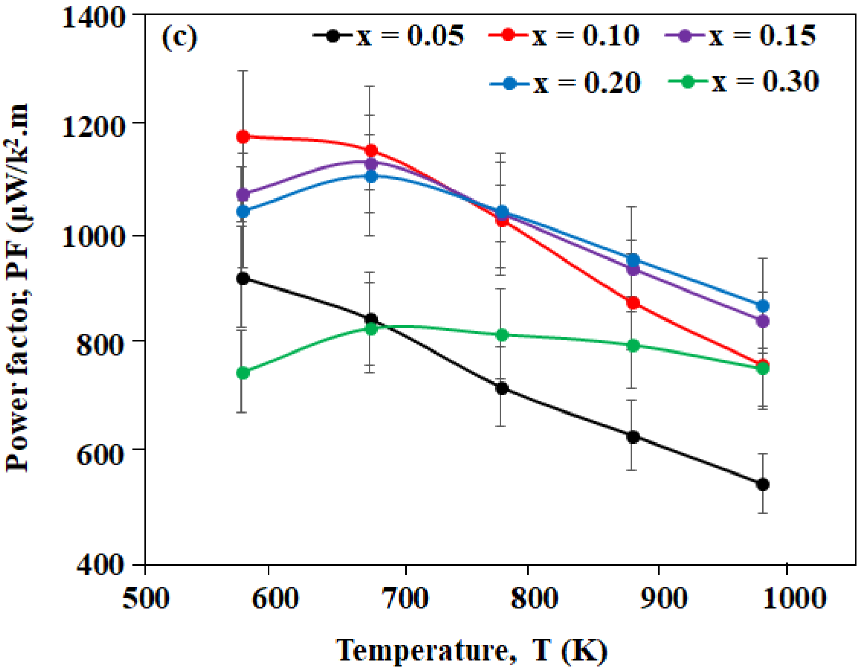

Figure 6.8. Temperature dependence of power factor, PF for $Sr_{1-3x/2}La_{x/2}Sm_{x/2}TiO_3$; $0.05 \leq x \leq 0.30$ ceramics calcined in air (VSTO-A) at 1573 K for 6 hours and sintered at 1773 K for 6 hours in 5% H_2/N_2.

The largest PF at 973 K was ~ 873 μW/K^2 for x = 0.20, and this value is higher than the maximum PF (~ 865 μW/K^2 at 973 K) observed in x = 0.10 of electron La-Sm co-doped $SrTiO_3$ ceramics (Chapter 5). This is due to increasing the electrical conductivity while maintaining a reasonable Seebeck coefficient by La-Sm doping. Based on this, we conclude that electrical transport properties of La-Sm co-doped $SrTiO_3$ is optimised via an A-site vacancy doping mechanism. The PF results obtained in this work are in agreement with most results in the literature for electron La-Yb [5] and La-Dy [6], [7] co-doped $SrTiO_3$ ceramics, but higher than the reported values for Nb-doped $Sr_{0.95}La_{0.05}TiO_3$ ceramics at high temperatures (≥ 973 K) [20].

Although the power factors obtained in this study are not as high as the values observed in La-Nb doped $SrTiO_3$ reported by Wang *et al* [4] and in doped $SrTiO_3$ single crystals [22], [23], the maximum PF recorded is among the high levels in polycrystalline $SrTiO_3$ bulk ceramics.

The total thermal conductivity (k), lattice thermal conductivity (k_L) and electronic thermal conductivity (k_E) of VSTO-A samples are shown in Figures 6.9, 6.10 and 6.11, respectively. The highest k (5.57 W/m. K) at 573 K was observed in x = 0.10, Figure 6.9. In contrast, the lowest k at 573 K was observed in x = 0.30 (3.46 W/m.K), which decreases to a minimum of 2.99 W/m.K for all the compositions at 973 K. Total thermal conductivity decreases with increasing temperature over the measured temperature range, which suggests a typical thermal conduction behaviour of a semiconductor [6] and domination of lattice thermal conductivity [5], Figure 6.10. The high concentration of impurities in the microstructure of x = 0.30 ceramics may have affected the thermal transport, leading to the low k observed. Generally, the reduction of k in doped $SrTiO_3$ ceramics is ascribed to formation of V_O in perovskites, preceded by sintering in reducing atmosphere [16]. At the maximum temperature (973 K), the electronic contribution to the total thermal conductivity was estimated at 0.20 W/m. K (5.1%), 0.49 W/m. K (12.8%), 0.71 W/m. K (18.8%), 0.84 W/m. K (20.9%), 0.68 W/m. K (22.8%) for x = 0.05, 0.10, 0.15, 0.20 and 0.30, respectively. These values confirm that k mainly results from the lattice vibrations (phonon), hence k_L plays a dominant role in k.

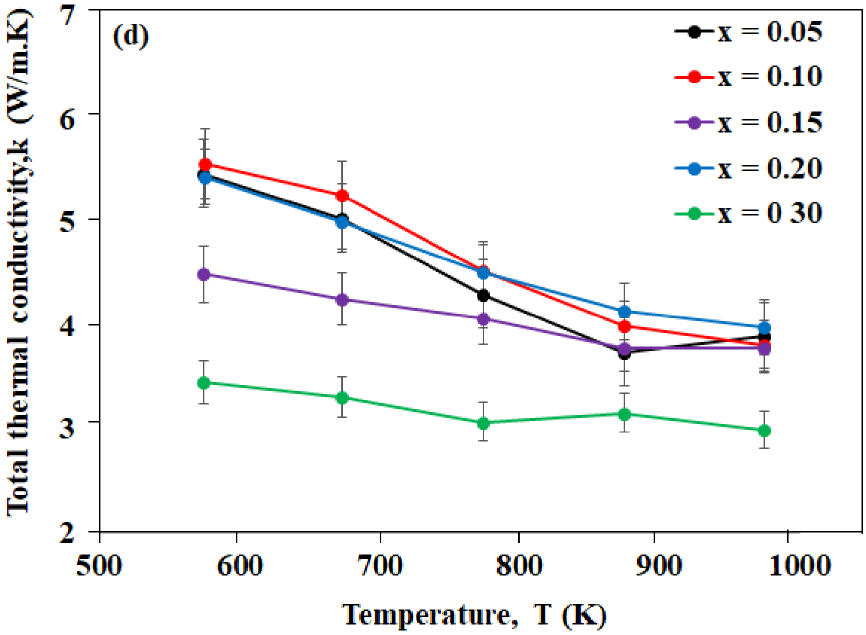

Figure 6.9. Temperature dependence of total thermal conductivity, k for $Sr_{1-3x/2}La_{x/2}Sm_{x/2}TiO_3$; $0.05 \leq x \leq 0.30$ ceramics calcined in air (VSTO-A) at 1573 K for 6 hours and sintered at 1773 K for 6 hours in 5% H_2/N_2.

An increase in La-Sm concentration results in decreasing k_L, Figure 6.10, which indicates increasing lattice defects and shortening of the mean free path (MFP) of phonons resulting to low k [13]. Furthermore, k_L decreases with increasing temperature in all the compositions except the deviation observed for x = 0.05 and 0.15 at 973 K, suggesting a domination by Umklapp phonon scattering [4], [23], [24]. On the other hand, k_E of all compositions, Figure 6.11 shows similar temperature dependence with electrical conductivity and increases with an increase of La-Sm concentration up to x = 0.20 and lowers at x = 0.30. From the results of the thermal transport properties, it can be deduced the reduction in total thermal conductivity caused by La-Sm concentration is mainly attributed to the decrease in k_E, especially at higher temperatures, Figure 6.11.

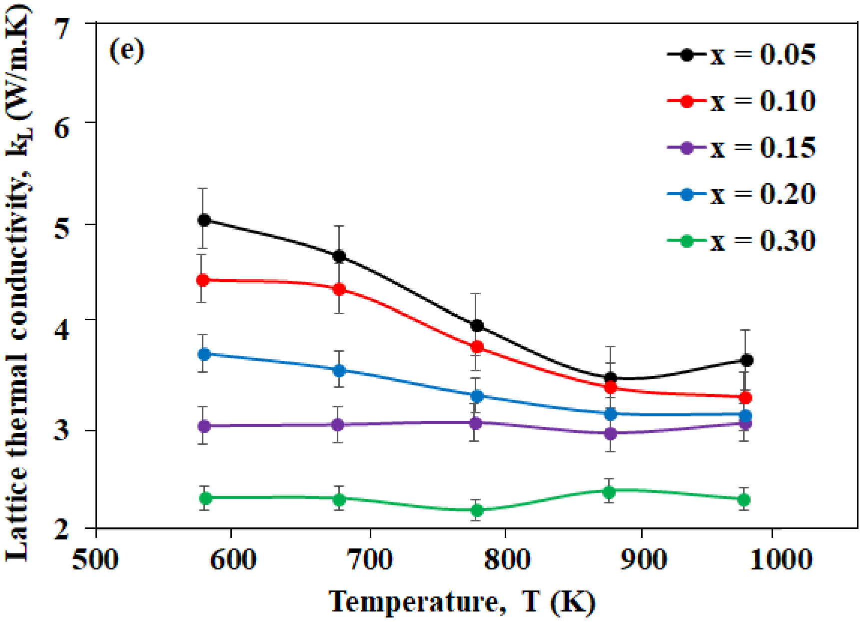

Figure 6.10. Temperature dependence of lattice thermal conductivity, k_L for $Sr_{1-3x/2}La_{x/2}Sm_{x/2}TiO_3$; $0.05 \leq x \leq 0.30$ ceramics calcined in air (VSTO-A) at 1573 K for 6 hours and sintered at 1773 K for 6 hours in 5% H_2/N_2.

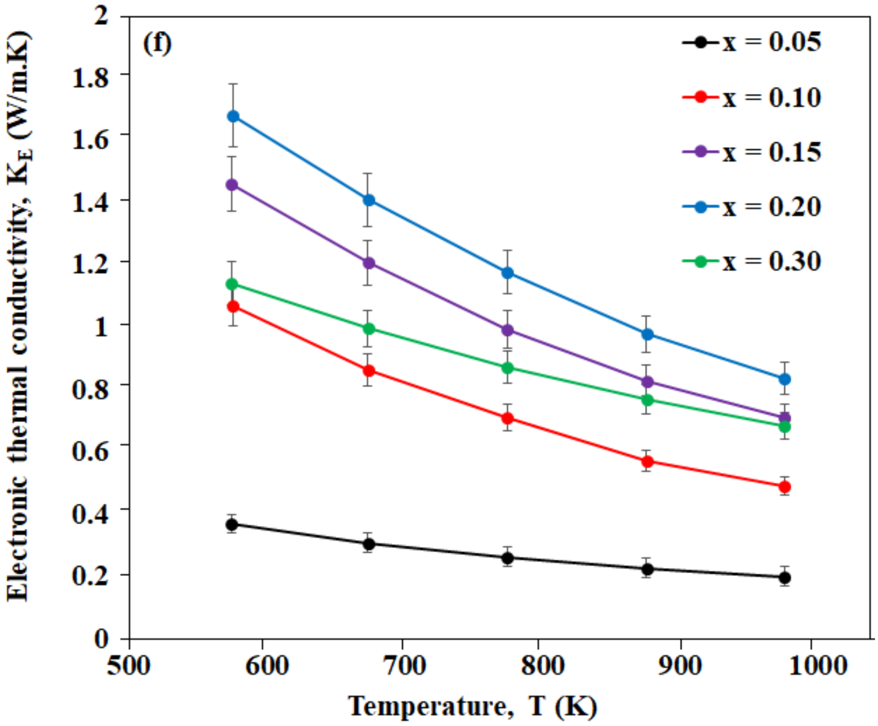

Figure 6.11. Temperature dependence of electronic thermal conductivity, k_L for $Sr_{1-3x/2}La_{x/2}Sm_{x/2}TiO_3$; $0.05 \leq x \leq 0.30$ ceramics calcined in air (VSTO-A) at 1573 K for 6 hours and sintered at 1773 K for 6 hours in 5% H_2/N_2.

Figure 6.12 shows the temperature dependence of figure of merit of all the compositions. ZT increases with increasing temperature over the entire measured temperature range. By optimising the La-Sm doping concentration, x = 0.30 recorded the highest ZT value of 0.25 at 973 K. However, the highest ZT value did not occur in x = 0.20 sample which have both the highest electrical conductivity (350 S/cm at 973 K), Figure 6.6 and power factor (873 $\mu W/K^2.m$ at 973 K), Figure 6.6(c) values as expected. Obviously, the dramatic decrease observed in the k of x = 0.30 sample despite its low PF results in higher ZT values especially at high temperatures (773 – 973 K). This suggests that heavy doping ($x \geq 0.30$) of A-site vacancy $Sr_{1-3x/2}La_{x/2}Sm_{x/2}TiO_3$ ceramics has less effect in enhancing the electrical transport properties especially the power factor.

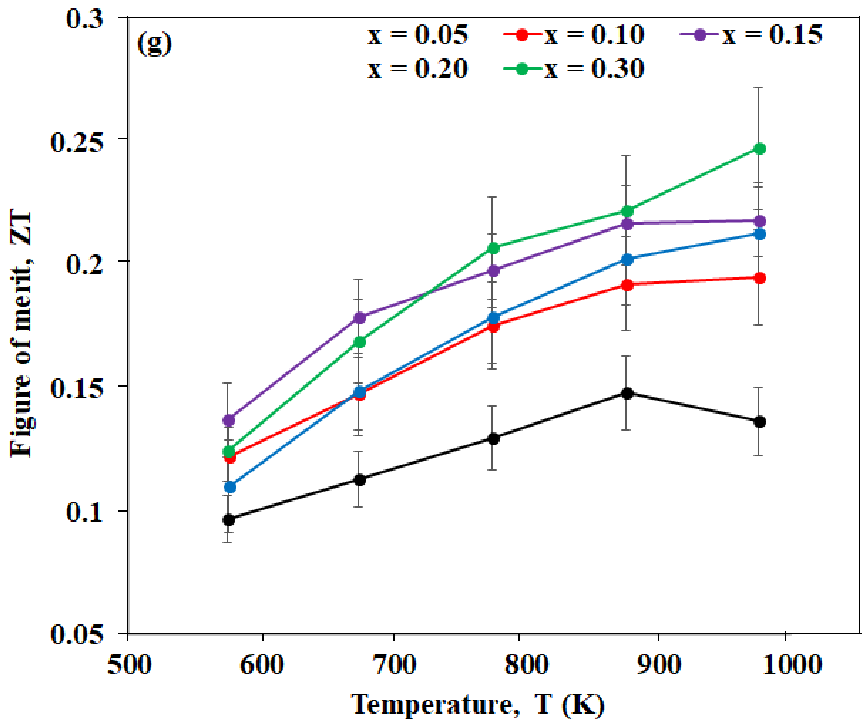

Figure 6.12. Temperature dependence of dimensionless figure of merit, ZT for $Sr_{1-3x/2}La_{x/2}Sm_{x/2}TiO_3$; $0.05 \leq x \leq 0.30$ ceramics calcined in air (VSTO-A) at 1573 K for 6 hours and sintered at 1773 K for 6 hours in 5% H_2/N_2.

6.2.4.2 VSTO-H Series

Temperature dependence of the thermoelectric properties of the $Sr_{1-3x/2}La_{x/2}Sm_{x/2}TiO_3$ (VSTO-H) ceramics sintered at 1773 K for 8 hours in 5% H_2/N_2 gas mixture are shown in Figures 6.13 to 6.20. The ZT, electrical (σ, S, PF) and thermal (k, k_L, k_E) transport properties were measured from 573 to 973 K. The La-Sm doping concentration was observed to have a similar effect on σ, S, and k. Electrical conductivity for all compositions decreases with increasing temperature, implying a metallic conduction behaviour and sharing of a comparable scattering mechanism, Figure 6.13 as reported previously (σ of VSTO-A series) [6], [14]. Further, σ increases with the increase of La-Sm concentration ($0.05 \leq x \leq 0.30$). This trend suggests a better control of the oxygen concentration and a proportional effect of carrier concentration by changing the doping concentration. Therefore, a high concentration of 30 mol% (x = 0.30) resulted in high σ with a maximum value of 1023 S/cm at 573 K.

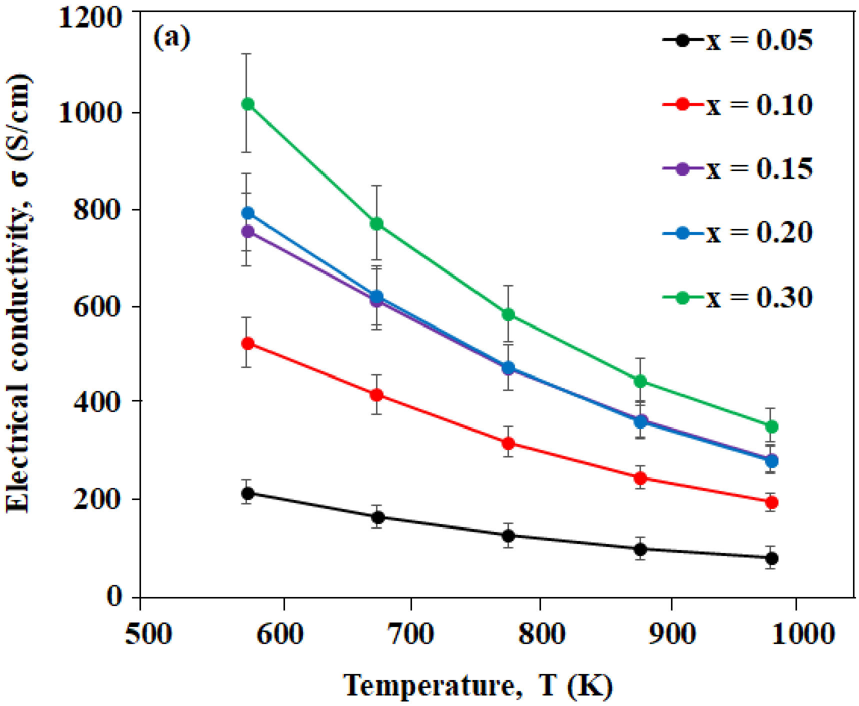

Figure 6.13. Temperature dependence of electrical conductivity, σ for $Sr_{1-3x/2}La_{x/2}Sm_{x/2}TiO_3$; $0.05 \leq x \leq 0.30$ ceramics calcined in 5% H_2/N_2 (VSTO-H) at 1573 K for 6 hours and sintered at 1773 K for 8 hours in 5% H_2/N_2.

A comparative analysis of the σ of VSTO-A, Figure 6.6 and VSTO-H samples shows that the processing atmosphere (whether air or 5% H_2/N_2) has no significant effect on σ at the highest measured temperatures, but variation at low temperatures is observed. For an example, in x = 0.15 compositions, VSTO-A and VSTO-H showed σ values of 1029 S/cm and 758 S/cm, respectively at 573 K. At high temperature (973 K) for the same compositions (x = 0.15), VSTO-A exhibited σ of 298 S/cm, and VSTO-H showed σ = 284 S/cm. This strongly suggests that the bulk conductivity (high temperature conductivity) is the same for a given dopant level (irrespective of processing atmosphere) while grain boundaries or electrical heterogeneities are responsible for the variation in lower temperature conductivity.

Seebeck coefficient shows negative values in the whole temperature range, confirming that all compositions ($0.05 \leq x \leq 0.30$) are n-type. As shown in Figure 6.14, $|S|$ increases with increasing temperature, but decreases with increase in La-Sm concentration, which is in agreement with the reported results, Figure 6.7 [5]–[7], [14]. The metallic behaviour of Seebeck coefficients of VSTO-H sample is better explained using the following equation (equation 2.15) [25] as reported in Chapter 2 of this work:

$$S \simeq \frac{\mathrm{C_{el}}}{\mathrm{q}} = \left(\frac{\mathrm{K_B}}{\mathrm{e}}\right)\frac{\mathrm{K_B T}}{\mathrm{E_F}}$$

The background of the equation shows that carrier concentration and fermi level (E_F) are unchanged relative to temperature (T). The direct relationship of S and T suggests an increase in absolute Seebeck coefficient as temperature increases or vice versa. Another important observation is the inverse relationship of S to charge carrier (q) and E_F, and this implies a decrease in S with increase in carrier concentration as shown in Figure 6.14.

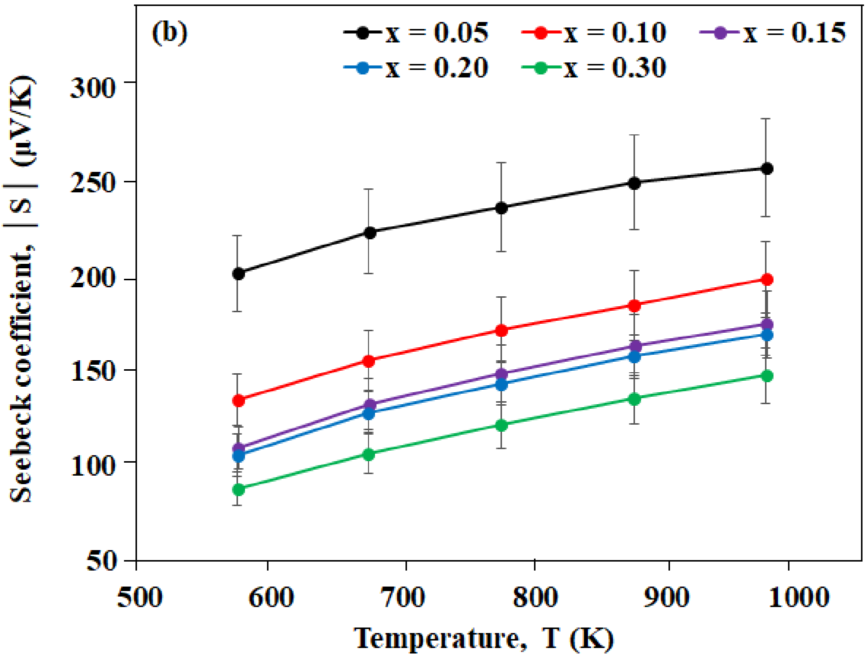

Figure 6.14. Temperature dependence of Seebeck coefficient, |S| for $Sr_{1-3x/2}La_{x/2}Sm_{x/2}TiO_3$; $0.05 \leq x \leq 0.30$ ceramics calcined in 5% H_2/N_2 (VSTO-H) at 1573 K for 6 hours and sintered at 1773 K for 8 hours in 5% H_2/N_2.

Figure 6.15 represents the results of power factor for VSTO-H compositions. The trend and values of results obtained are similar to previously reported data, Figure 6.8. Consequently, processing atmosphere does not have any significant effect on the PF of $Sr_{1-3x/2}La_{x/2}Sm_{x/2}TiO_3$ ceramics especially at high temperatures. This might be the confirmation of the interplay of bulk electrical conductivity at high temperature as discussed previously. As an illustration, x = 0.15 at 973 K showed power factors of 873 and 870 $\mu W/K^2.m$ for VSTO-A and VSTO-H samples, respectively. x = 0.15 showed the maximum display of PF values between 673 and 873 K, with the highest value of ~ 1093 $\mu W/K^2.m$ obtained at 673 K. This could be attributed to the large values of electrical conductivity exhibited.

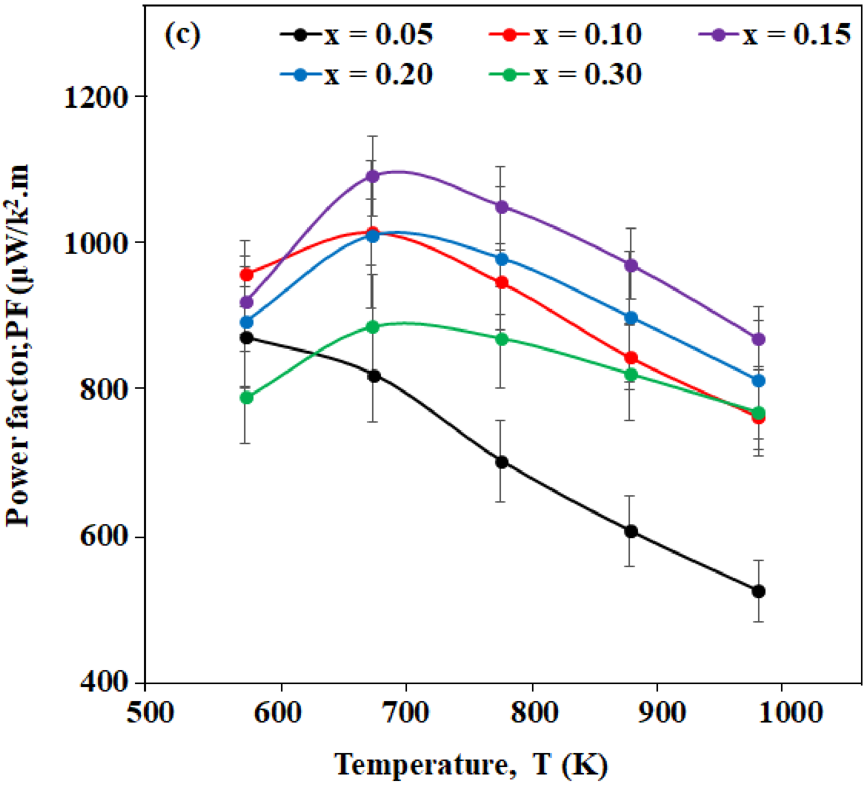

Figure 6.15. Temperature dependence of power factor, PF for $Sr_{1-3x/2}La_{x/2}Sm_{x/2}TiO_3$; $0.05 \leq x \leq 0.30$ ceramics calcined in 5% H_2/N_2 (VSTO-H) at 1573 K for 6 hours and sintered at 1773 K for 8 hours in 5% H_2/N_2.

The thermal transport properties (k, k_L and k_E) of VSTO-H compositions are shown in Figures 6.16 to 6.18. The thermal transport properties of VSTO-H compositions exhibited lower values compared with that of VSTO-A compositions but show similar trend. As discussed previously, processing atmosphere showed little or no effect on the electrical transport properties of $Sr_{1-3x/2}La_{x/2}Sm_{x/2}TiO_3$ ceramics. However, it is evident to state that the effect of processing atmosphere was clearly observed in the thermal transport properties of the compositions.

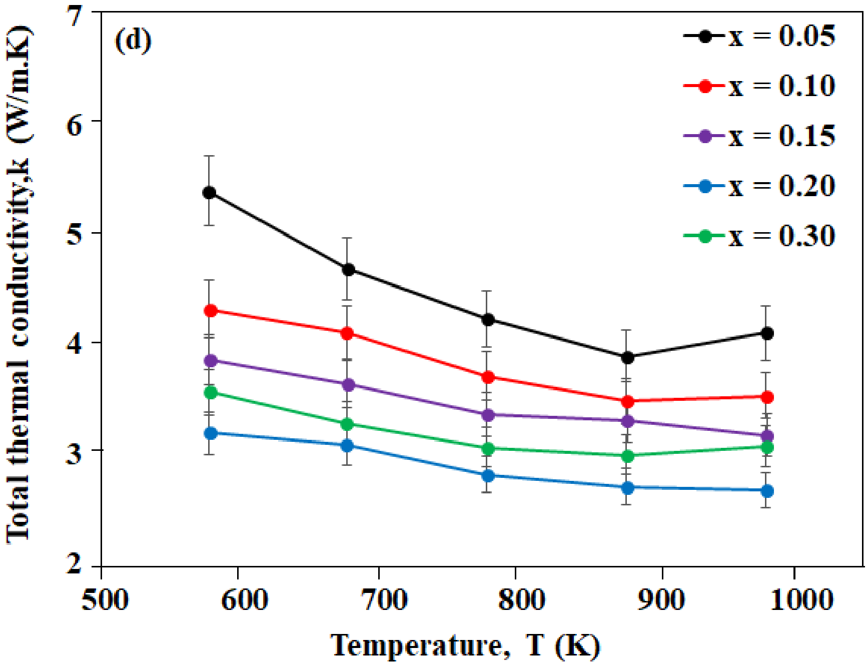

Figure 6.16. Temperature dependence of total thermal conductivity, k for $Sr_{1-3x/2}La_{x/2}Sm_{x/2}TiO_3$; $0.05 \leq x \leq 0.30$ ceramics calcined in 5% H_2/N_2 (VSTO-H) at 1573 K for 6 hours and sintered at 1773 K for 8 hours in 5% H_2/N_2.

The results obtained in the PSD of VSTO-A and VSTO-H powders and grain size of the ceramics were affected by the processing atmosphere, hence the eventual behaviour evidenced in the thermal conductivity. The small mean particle size, d_{50} (4.70 µm) obtained in the PSD of VSTO-H powders compared to that of VSTO-A (6.04 µm) which translated to a reduced grain size obtained in the microstructure of VSTO-H samples as discussed in section 6.2.2 of this work. Reduced grain size or incorporation of large grain boundaries shorten the MFP of phonons by acting as scattering centres [11]. In addition, processing (both calcination and sintering) in reduced atmosphere generate high oxygen vacancies in the lattice. Hence, randomly distributed oxygen vacancies within the lattice restrict phonon propagation in VSTO-H compositions, resulting to a decrease in thermal conductivity [13]. The lowest k (2.67 W/m. K) at 973 K was observed in x = 0.20, which is ~ 11 % lower than the lowest k (2.99 W/m. K at 973 K) obtained in VSTO-A composition. The k value (2.67- 5.50 W/m.K) observed in VSTO-H ceramics is comparable to minimal k values of most doped $SrTiO_3$ ceramics prepared via conventional methods [6], [7], [16], [26] and with metallic/semi -metallic or oxide additives [18], [27], [28]. This significant reduction in k as shown in VSTO-H compositions confirms that strongly reducing conditions are efficient in achieving low thermal conductivity in SSR synthesised $Sr_{1-3x/2}La_{x/2}Sm_{x/2}TiO_3$ ceramics.

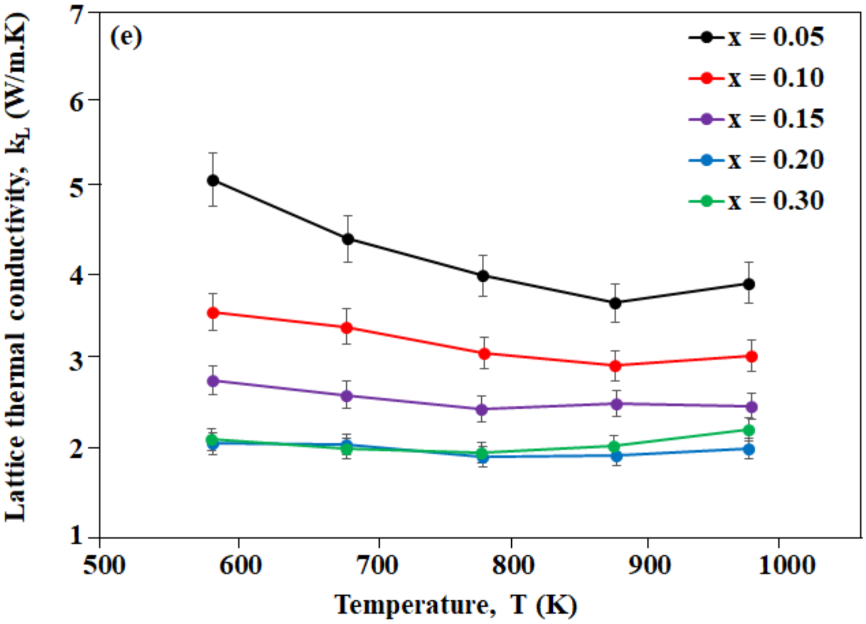

Figure 6.17. Temperature dependence of lattice thermal conductivity, k_L for $Sr_{1-3x/2}La_{x/2}Sm_{x/2}TiO_3$; $0.05 \leq x \leq 0.30$ ceramics calcined in 5% H_2/N_2 (VSTO-H) at 1573 K for 6 hours and sintered at 1773 K for 8 hours in 5% H_2/N_2.

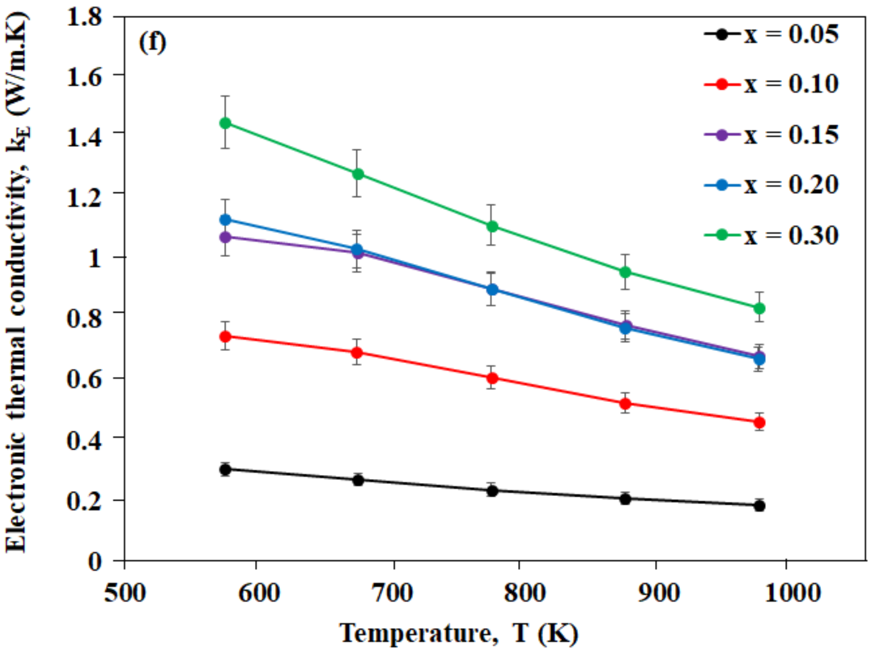

Figure 6.18. Temperature dependence of electronic thermal conductivity, k_L for $Sr_{1-3x/2}La_{x/2}Sm_{x/2}TiO_3$; $0.05 \leq x \leq 0.30$ ceramics calcined in 5% H_2/N_2 (VSTO-H) at 1573 K for 6 hours and sintered at 1773 K for 8 hours in 5% H_2/N_2.

The temperature dependence of dimensionless figure of merit of VSTO-H samples is shown in Figure 6.19. ZT of $x \geq 0.15$ compositions increases with temperature over the entire measured temperature range. In contrast, the ZT of $x \leq 0.10$ compositions increases within 573-873 K temperature range and declines at high temperature (973 K). This could be related to the low electrical conductivity exhibited, Figure 6.13. The ZT increases with increasing La-Sm concentration and reaches a maximum at x = 0.20. A highest ZT value of 0.30 was recorded in x = 0.20 at 973 K, and this could be attributed to its relative low k.

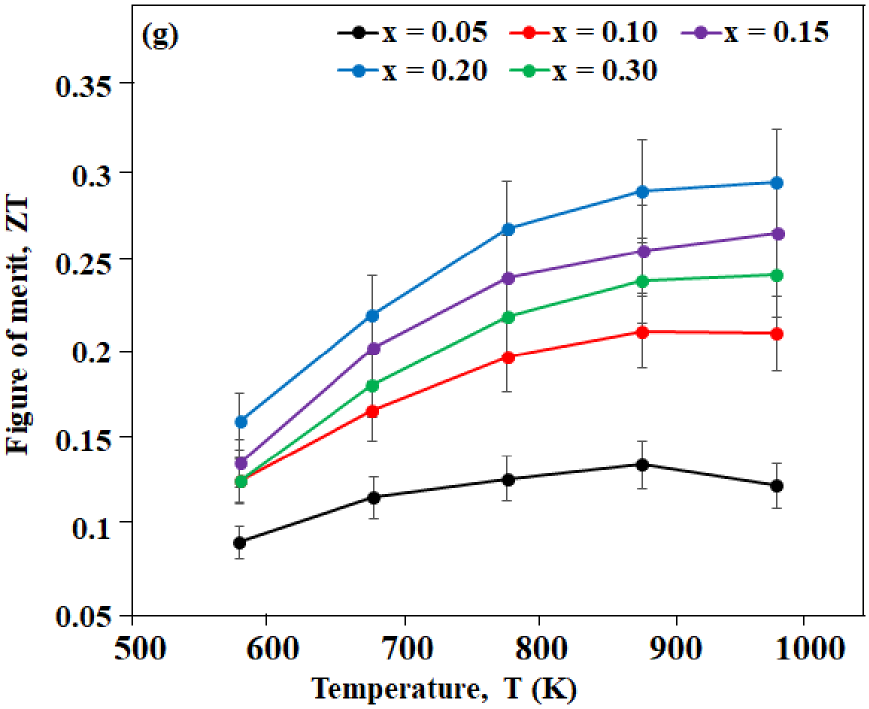

Figure 6.19. Temperature dependence of dimensionless figure of merit, ZT for $Sr_{1-3x/2}La_{x/2}Sm_{x/2}TiO_3$; $0.05 \leq x \leq 0.30$ ceramics calcined in 5% H_2/N_2 (VSTO-H) at 1573 K for 6 hours and sintered at 1773 K for 8 hours in 5% H_2/N_2.

A comparison of ZT values of VSTO-A and VSTO-H ceramics at maximum measured temperature (973 K) relative to La-Sm doping concentration is shown in Figure 6.20. Both samples maintained similar ZT values at low dopant concentration and converged at the maximum doping concentration (x = 0.30). A rapid increase in the ZT of VSTO-H sample was observed in x = 0.15-0.20. The highest ZT, achieved in x = 0.20 of VSTO-H, as already discussed is related to its low k. It is obvious to state that the high concentration of V_O created in this composition (x = 0.20) majorly contributed to the low k and consequent high ZT. This conjecture is supported by the increased lattice parameter observed in the composition as previously reported (Figure 6.2). The lattice expansion observed suggests a decrease in coulombic force or binding energy in the lattice due to creation of V_O accompanied by the formation of the higher ionic radius Ti^{3+} cation [2].

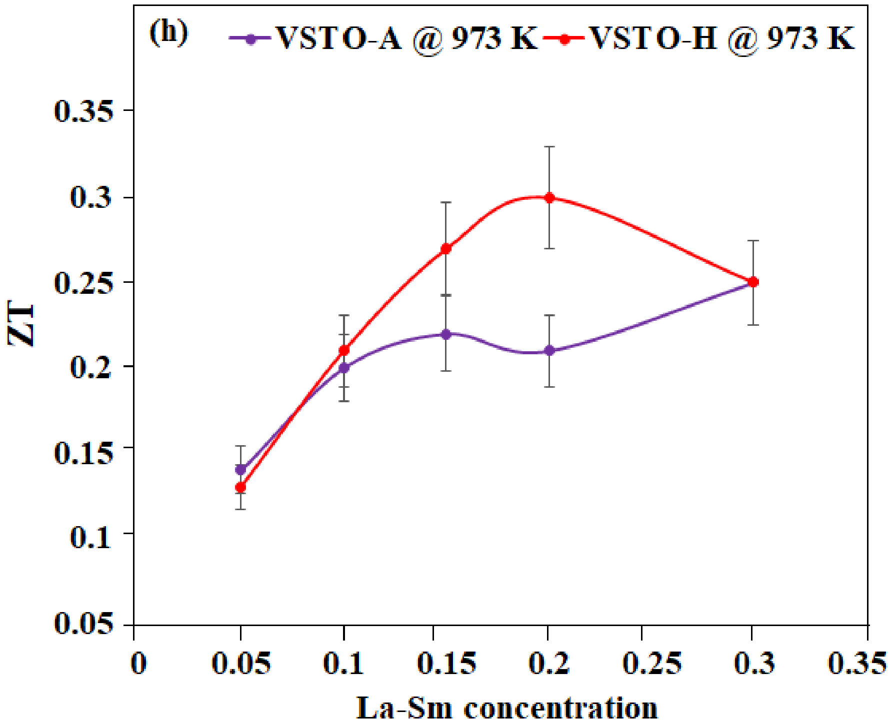

Figure 6.20. A comparison of ZT values of VSTO-A and VSTO-H ceramics relative to La-Sm concentration at 973 K.

In general, the obtained results discussed here show A-site vacancy La-Sm co-doped $SrTiO_3$ TE ceramics can be optimised compared to the electron co-doping mechanism. In $Sr_{1-x}La_{x/2}Sm_{x/2}TiO_3$ samples, a maximum ZT value of 0.24 at 873 K was achieved. As shown in $Sr_{1-3x/2}La_{x/2}Sm_{x/2}TiO_3$ results, enhanced ZT values were obtained with a maximum value of 0.25 for VSTO-A (x = 0.30) and 0.30 for VSTO-H (x = 0.20) at 973 K. This higher ZT value achieved in VSTO-H samples reflects an optimum comprise between reduced k and metallic behaviour of the ceramics without compromising the PF.

6.3 Thermoelectric Study of 20 mol% La-Sm-doped $SrTiO_3$ Ceramics

6.3.1 Introduction

The high ZT (ZT_{max} = 0.30) and appreciable low k (k_{min} = 2.67 W/m. K) achieved in VSTO-H samples are strong indications that processing in strongly reducing conditions can further improve the TE performance of $Sr_{1-3x/2}La_{x/2}Sm_{x/2}TiO_3$. It also confirms introduction of A-site cation vacancies, processing in reduced atmosphere and induced oxygen defects can improve the TE properties of doped $SrTiO_3$ materials. Additionally, microstructure modulation achieved via enhanced processing methods has proved to be a practical approach for enhancing the TE performance of doped ceramics.

Due to the novel research window opened and the highest ZT obtained in x = 0.20 of the La-Sm co-doped $SrTiO_3$, a further step was attempted to enhance its TE properties. The approach involved the modification of the processing temperature and the calcination cycle while maintaining calcination and sintering in 5% H_2/N_2. The structure-property relationships of the new samples are studied, and comparison made with the already discussed 20 mol% of the VSTO-A and VSTO-H samples. These samples are code named 1300A, 1300H, 1350H and 1400H. 1300A and 1300H represent the $SrLa_{0.10}Sm_{0.10}TiO_3$ (electronic doped) and $Sr_{0.70}La_{0.10}Sm_{0.10}TiO_3$ (vacancy doped) ceramics calcined in air and 5% H_2/N_2, respectively at 1300 ^oC (1573 K) for 6 hours and sintered in 5% H_2/N_2 at 1773 K for 6 and 8 hours. Portions of the 1300H calcined powders were recalcined at 1350 or 1400 ^oC for 6 hours in 5% H_2/N_2, and subsequently sintered in the same atmosphere at 1773 K for 8 hours. These samples are named 1350H (calcined at 1573 and 1623 K) and1400H (calcined at 1573 and 1673 K).

6.3.2 Results and discussion

6.3.2.1 Particle Size Distribution

Figure 6.21 represents the particle size distribution of the double calcined $Sr_{0.70}La_{0.10}Sm_{0.10}TiO_3$ (1350H, 1400H) powders after ball milling. All as-milled powders showed no agglomeration and mean particle sizes of ≤ 6 µm and $d_{90} \leq 11$ µm (Table 6.3). Comparing with 1300A and 1300H powders, a significant reduction in d_{50} from 6.04 µm to 4.22 µm (30 % reduction) was observed in 1400H. These small particle sizes confirmed that double calcination at high temperatures in 5%H_2/N_2 contributed in the reduction of the particle sizes of the powders.

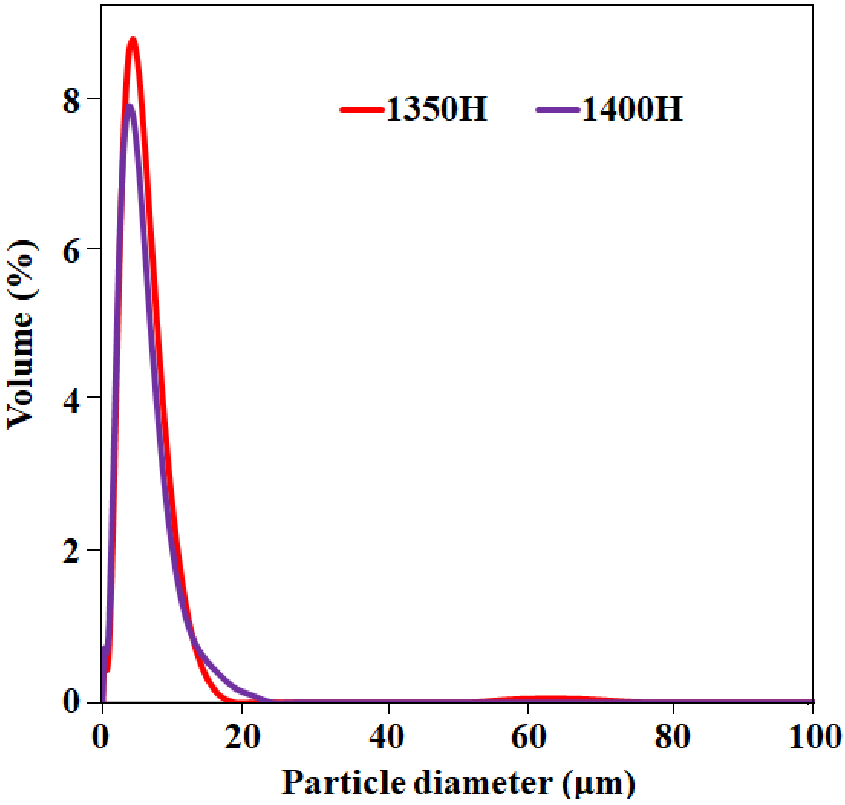

Figure 6.21. Schematic particle size distribution of $Sr_{0.70}La_{0.10}Sm_{0.10}TiO_3$ (1350H and 1400H) calcined powders after 24 hours of ball milling.

Table 6.3. Particle sizes of calcined 20 mol% La-Sm-doped $SrTiO_3$ powders after 24 hours ball milling.

Powder	Calcination conditions			Particle diameter (μm)		
	Atmosphere	Temperature (°C)	Number of cycles	d_{10}	d_{50}	d_{90}
1300A	Air	1300	1	2.93	6.04	11.50
1300H	5%H_2/N_2	1300	1	2.07	4.70	10.80
1350H	5%H_2/N_2	1300,1350	2	1.98	4.53	9.19
1400H	5%H_2/N_2	1300,1400	2	1 .62	4.22	10.20

6.3.2.2 Phase Structure and Microstructure

The XRD patterns of the crushed $SrLa_{0.10}Sm_{0.10}TiO_3$ and $Sr_{0.70}La_{0.10}Sm_{0.10}TiO_3$ ceramics sintered in 5% H_2/N_2 at 1773 K for 6 or 8 hours are shown in Figure 6.22. All the peaks could be indexed on a simple cubic $SrTiO_3$ perovskite with Pm-3m space group. No secondary phase was detected within the detection limit of the diffractometer. The results of the lattice parameters, cell volumes and theoretical density as calculated from the XRD data are shown in Table 6.4, while Figure 6.23 illustrates the behaviour of the lattice parameter relative to processing condition. 1300A sample showed the lowest parameter (3.903 Å), while 1300H exhibited an expanded lattice parameter and reached a maximum value of 3.910 Å, suggesting stripping of more oxygen ions from the lattice and consequent partial reduction of Ti^{4+} to Ti^{3+} ions. For 1350H and 1400H samples, a decrease in lattice parameter (~ 3.907 Å) was observed. No clear reason is adduced for this behaviour, but it could be related to an expansion limit where a further increase in the calcination temperature does not result in a greater concentration of V_O.

Relative density of all samples after sintering was ≥ 96 % (Table 6.4). The SEM images of 1350H and 1400H samples as shown in Figure 6.24 revealed homogenous and dense structures relative to the high relative density in Table 6.4. It is also observed that the microstructure showed a reduced grain sizes consistent with decreased particle diameters of the powders obtained in the particle size distribution test (Table 6.3). The microstructure showed a reduced average grain size of 7- 8 µm with concentration of voids. This shows that double calcination in 5% H_2/N_2 reducing gas at high temperatures has a significant effect on the microstructure of the ceramics.

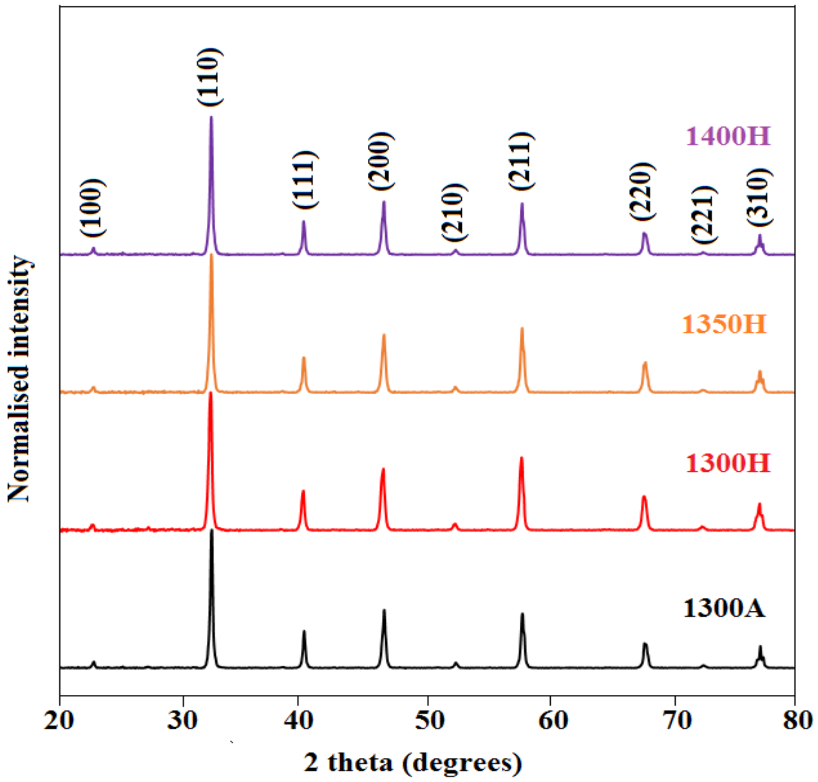

Figure 6.22. Room temperature XRD patterns of crushed $SrLa_{0.10}Sm_{0.10}TiO_3$ and $Sr_{0.70}La_{0.10}Sm_{0.10}TiO_3$ ceramics calcined in air or 5% H_2/N_2 at 1573, 1623 or 1673 K for 6 hours and sintered in 5% H_2/N_2 at 1773 K for 6 or 8 hours.

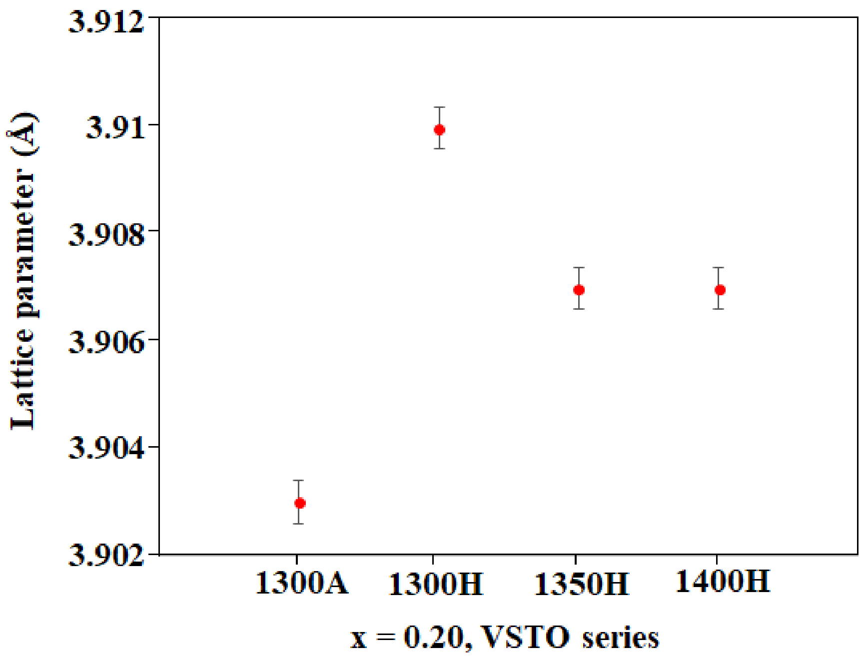

Figure 6.23. Lattice parameter behaviour relative to processing condition of crushed $SrLa_{0.10}Sm_{0.10}TiO_3$ and $Sr_{0.70}La_{0.10}Sm_{0.10}TiO_3$ ceramics calcined in air or 5% H_2/N_2 at 1573, 1623 or 1673 K for 6 hours and sintered in 5% H_2/N_2 at 1773 K for 6 or 8 hours.

Table 6.4. Lattice parameter, cell volume and relative density of 20 mol% La-Sm-doped $SrTiO_3$ ceramics sintered in 5%H_2/N_2 at 1773 K for 6 or 8 hours.

Sample	Lattice parameter (Å) (±0.001 Å)	Cell volume ($Å^3$) (±0.002 $Å^3$)	Relative density (%) (±0.5 %)
1300A	3.903	59.456	98.4
1300H	3.910	59.776	98.7
1350H	3.907	59.639	98.9
1400H	3.907	59.639	96.9

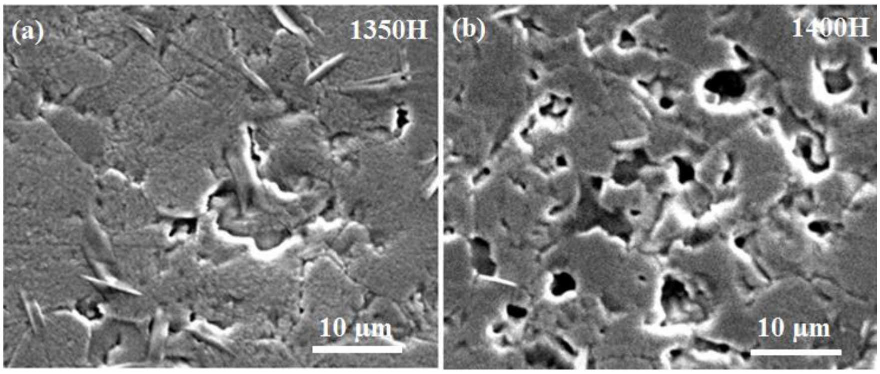

Figure 6.24. SEM micrographs of the surfaces of $Sr_{0.70}La_{0.10}Sm_{0.10}TiO_3$ ceramics double calcined in 5% H_2/N_2 at (a) 1573 and 1623 K (b) 1573 and 1673 K for 6 hours, sintered in 5% H_2/N_2 at 1773 K for 8 hours and thermally etched at 1623 K for 30 minutes.

6.3.2.3 Thermal Behaviour

The thermal stability of 20 mol% La-Sm co-doped $SrTiO_3$ ceramics in air was determined using thermogravimetric analysis (TGA). The TGA results are shown in Figure 6.25. At low temperatures (25 – 500 ^{o}C), a noticeable weight loss (~ 0.2 %) was observed for 1350H and 1400H samples. Such behaviour can mainly be attributed to a chemical reaction (such as thermal decomposition, loss of water of crystallisation, combustion or reduction of oxides) or physical transitions (e.g. vaporisation, evaporation, sublimation, desorption and drying). Within this low temperature range, 1300A and 1300H samples remained stable.

It is worth noting that 1350H and 1400H samples showed a low onset oxidation temperature (500 ^{o}C) when compared to 1300A and 1300H samples as shown in Table 6.5. This could be due to the chemical reaction or physical transitions undergone at low temperatures. However, colour of 1350H and 1400H ceramics after TGA remained black while 1300A and 1300H turned brown and white in appearance, respectively. This suggests that $Sr_{0.70}La_{0.10}Sm_{0.10}TiO_3$ ceramics with improved processing conditions can enhance their stability in air with decreased re-oxidation (small oxidation weight change) as shown in Table 6.5.

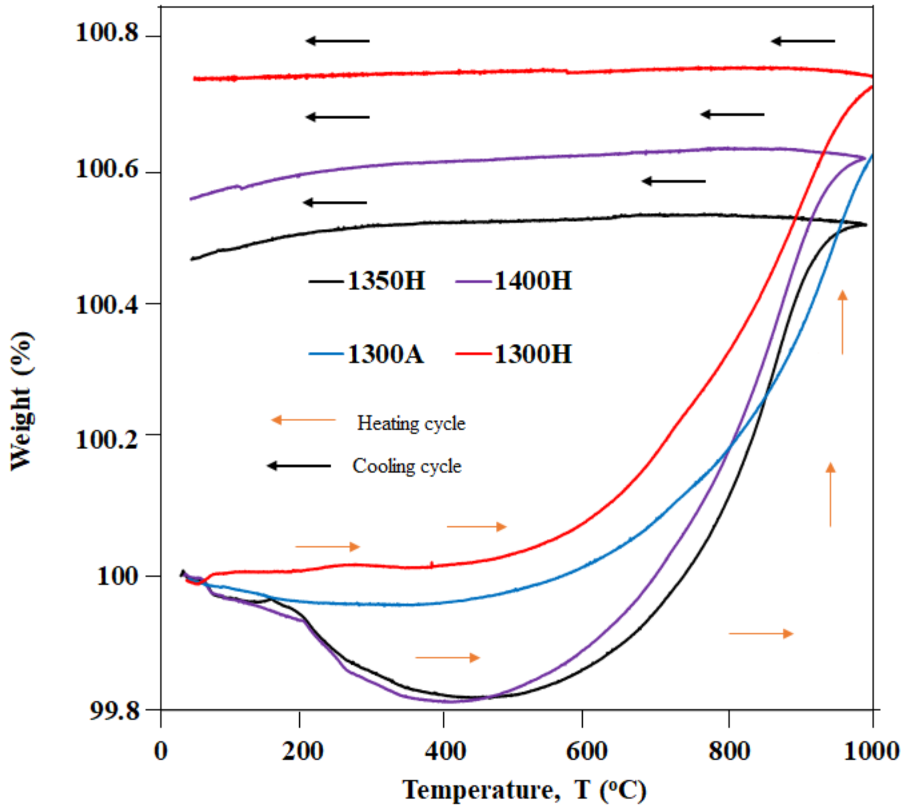

Figure 6.25. Thermogravimetric analysis showing the thermal behaviour in air of 20 mol% La-Sm-doped $SrTiO_3$ ceramics calcined and/or recalcined in air or 5% H_2/N_2 at 1573 -1673 K for 6 hours and sintered in 5% H_2/N_2 at 1773 K for 6-8 hours.

Table 6.5. TGA result showing the weight variation and oxidation onset temperature of 20 mol% La-Sm-doped $SrTiO_3$ ceramics calcined and/or recalcined in air or 5% H_2/N_2 at 1573 -1673 K for 6 hours and sintered in 5% H_2/N_2 at 1773 K for 6-8 hours.

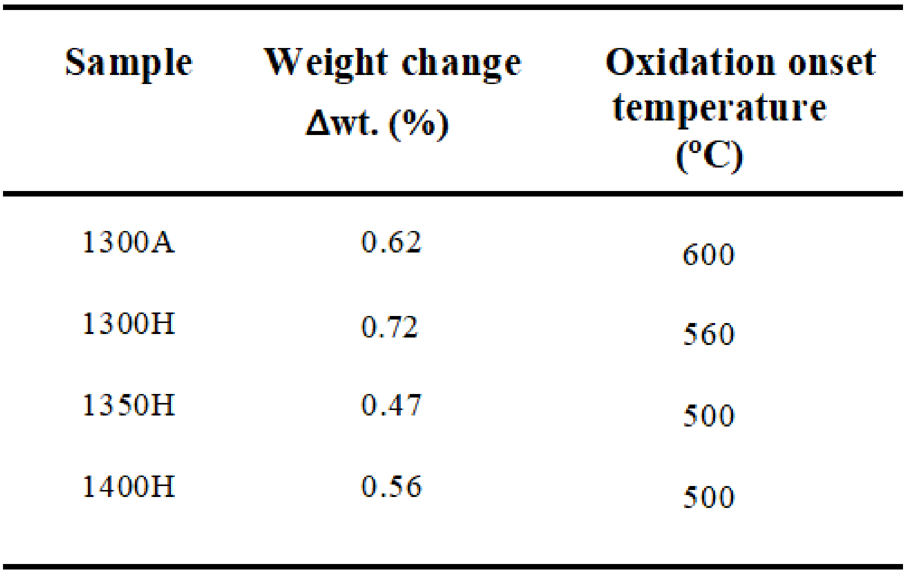

Sample	Weight change Δwt. (%)	Oxidation onset temperature (°C)
1300A	0.62	600
1300H	0.72	560
1350H	0.47	500
1400H	0.56	500

6.3.2.4 Thermoelectric Properties

Figures 6.26 to 6.32 represent the temperature dependence of the thermoelectric properties (σ, │S│, PF, k, kE and ZT) of the $SrLa_{0.10}Sm_{0.10}TiO_3$ and $Sr_{0.70}La_{0.10}Sm_{0.10}TiO_3$ ceramics sintered at 1773 K for 6 or 8 hours in 5%H_2/N_2 gas mixture. In all the samples, electrical conductivity decreases with increasing temperature over the measured temperature range, implying a metallic conductor-like behaviour and display of similar scattering mechanism as discussed previously (Figure 6.26) [6], [14]. It is observed that 1300A and 1400H showed high σ within the measured temperature, and this implies that processing conditions have little or no effect on the electrical properties of 20 mol% $SrTiO_3$ ceramics as studied in this work. 1300A showed the highest σ (1184 S/cm) at 573 K, while at high temperatures (673-973 K) 1400H displayed the highest σ values.

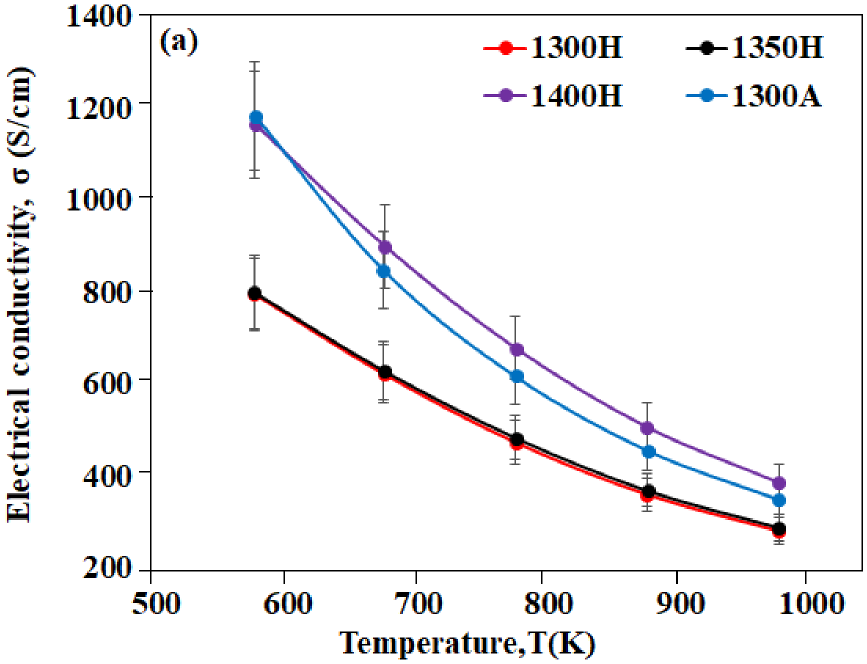

Figure 6.26. Temperature dependence of electrical conductivity, σ for 20 mol% La-Sm-doped $SrTiO_3$ ceramics calcined in air or 5% H_2/N_2 at 1573-1673 K for 6 hours and sintered at 1773 K for 6-8 hours in 5% H_2/N_2.

As highlighted previously, many factors contribute to the electrical conductivity of ceramics, which include doping and processing in reduced atmosphere. Increase in V_O results to increase in an efficient carrier mobility [29]. The more the O^{2-} anions are removed from the lattice, the higher the electrical conductivity.

All samples showed negative Seebeck coefficient values in the whole measured temperature range, indicating n-type degenerate behaviour due to the reducibility of Ti^{4+} to Ti^{3+} ions and eventual release of electrons into the conduction band [30], [31]. As expected, the $|S|$ exhibited metallic behaviour and showed a value ≥ 154 μV/K at 973 K, Figure 6.27. 1400H had the lowest $|S|$ values, and this could be attributed to its high σ.

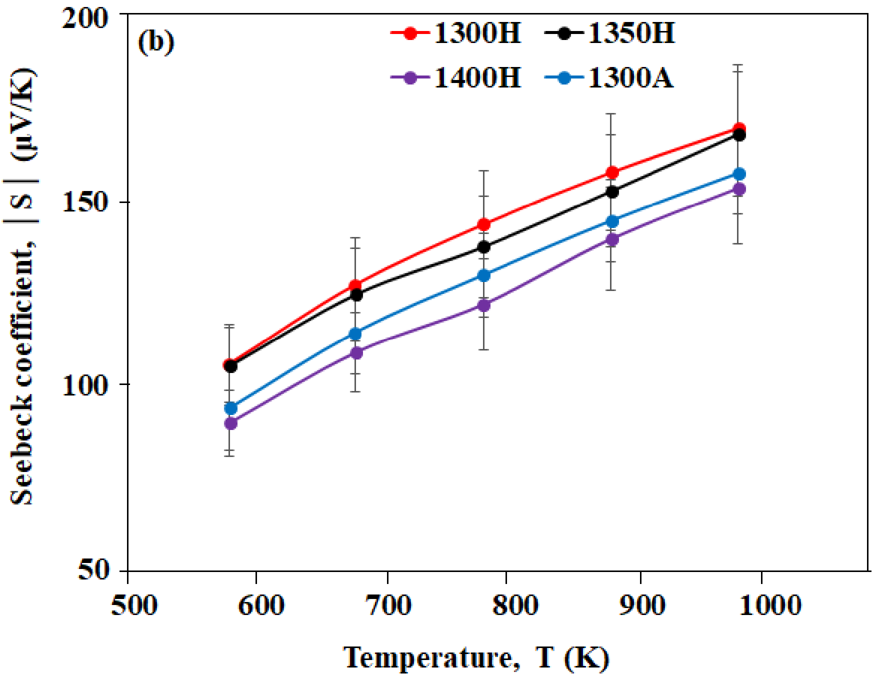

Figure 6.27. Temperature dependence of Seebeck coefficient, │S│ for 20 mol% La-Sm-doped $SrTiO_3$ ceramics calcined in air or 5% H_2/N_2 at 1573-1673 K for 6 hours and sintered at 1773 K for 6-8 hours in 5% H_2/N_2.

The power factors for the different samples (1300A, 1300H, 1350H and 1400H) are presented in Figure 6.28. At low temperatures (573-673), the samples exhibited a peak behaviour, and decreases with increasing temperature between 673 and 973 K. 1300A samples showed the highest PF (~ 1111 $\mu W/K^2.m$) at 573 K. The high PF value is traceable to its highest σ at low temperature (573 K). At $\geq$ 873 K, PF of 1400H exhibited high values than other samples. Therefore, the combination of large σ and moderate │S│ achieved by optimised processing conditions resulted in the large PF observed in 1400H sample at high temperatures.

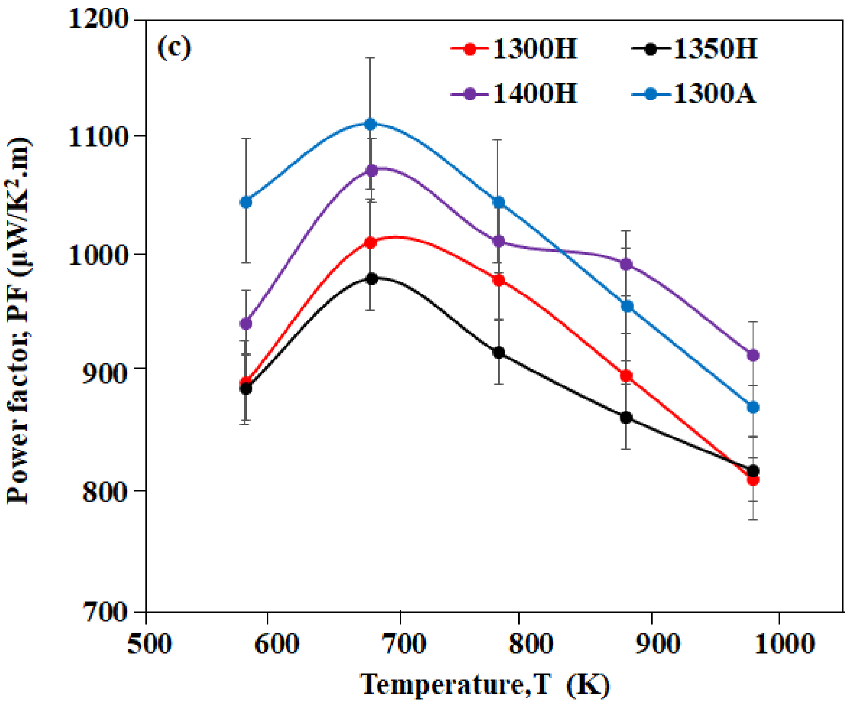

Figure 6.28. Temperature dependence of power factor, PF for 20 mol% La-Sm-doped SrTiO$_3$ ceramics calcined in air or 5% H_2/N_2 at 1573-1673 K for 6 hours and sintered at 1773 K for 6-8 hours in 5% H_2/N_2.

The total thermal conductivity (k) and electronic thermal conductivity (k_E) of the various 20 mol% La-Sm-doped SrTiO$_3$ ceramics are shown in Figures 6.29 and 6.30. A decrease in k with increasing temperature was observed in all samples, suggesting a thermal conduction behaviour with k_L in dominance, commonly found in semiconductors [5], [6]. 1300A sample showed a very high k over the measured temperature range compared to other samples. In contrast, low k was observed in other samples within the measured temperature range and decreased linearly to the smallest value of ~ 2.5 W/m. K at 973 K for 1400H sample, Figure 6.29. This value (2.5 W/m. K) is ~ 6 % lower than the smallest k obtained in VSTO-H compositions (2.67 W/m. K for x = 0.20 at 973 K). The high concentration of voids observed in the microstructure of 1400H sample act as phonon scattering centres and might contribute to the small value of k (2.5 W/m.K).

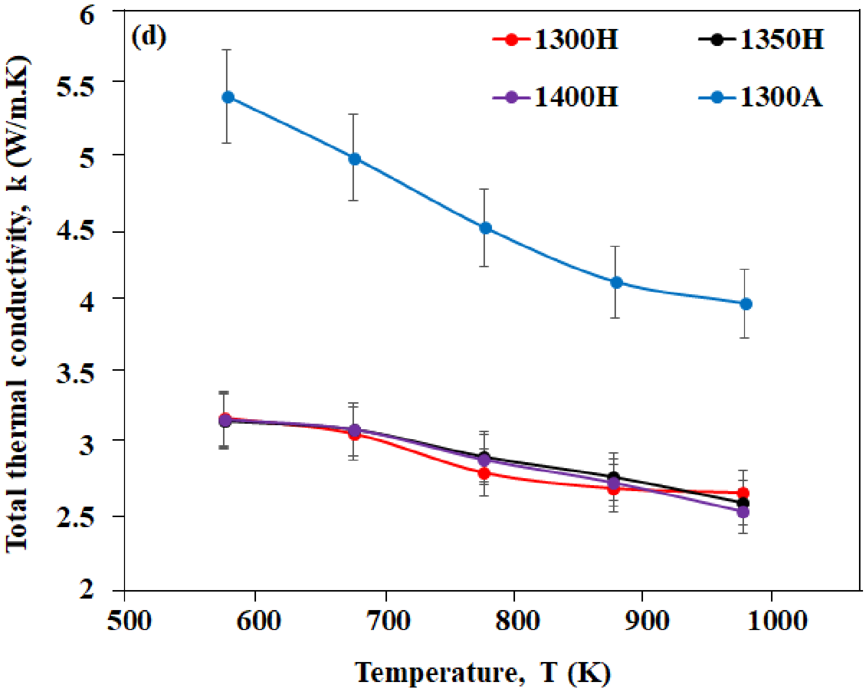

Figure 6.29. Temperature dependence of total thermal conductivity, k for 20 mol% La-Sm-doped $SrTiO_3$ ceramics calcined in air or 5% H_2/N_2 at 1573-1673 K for 6 hours and sintered at 1773 K for 6-8 hours in 5% H_2/N_2.

It is obvious to state that the optimised processing conditions significantly enhanced the thermal transport properties of $Sr_{0.70}La_{0.10}Sm_{0.10}TiO_3$ ceramics. As previously discussed, reduced grain sizes and a significant level of oxygen defects created in the lattice restrict the MFP of phonons, resulting in low k [11]–[13]. The k_E of all samples showed a similar temperature dependence with σ and decreased with an increasing temperature, Figure 6.30. The small values observed in k_E show the main contribution to k comes from k_L, suggesting k_E was controlled efficiently.

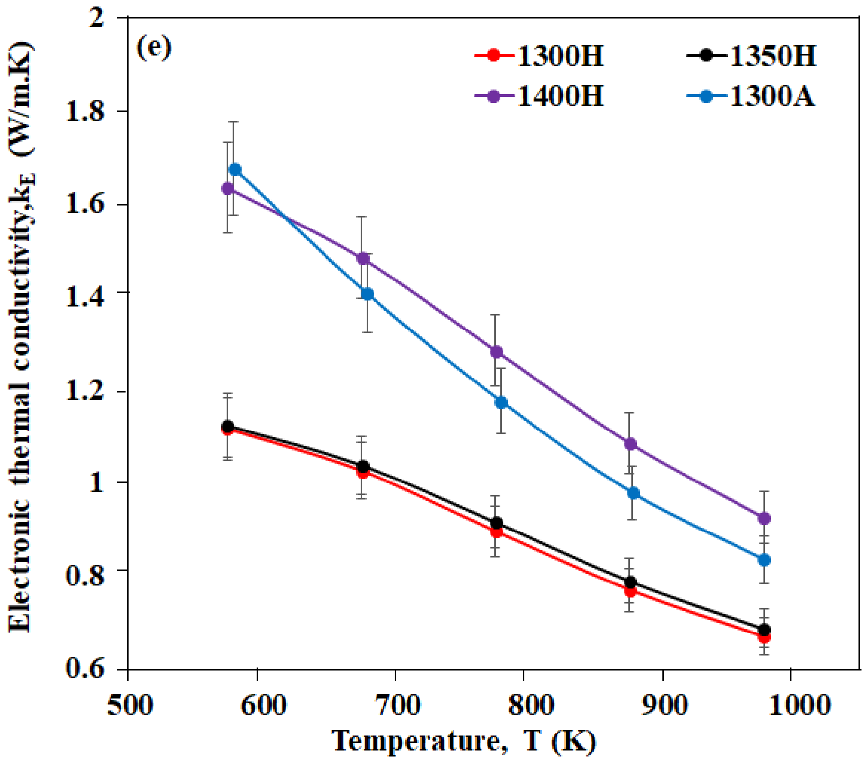

Figure 6.30. Temperature dependence of electronic thermal conductivity, k_E for 20 mol% La-Sm-doped $SrTiO_3$ ceramics calcined in air or 5% H_2/N_2 at 1573-1673 K for 6 hours and sintered at 1773 K for 6-8 hours in 5% H_2/N_2.

By enhancing the processing conditions, a high ZT (0.35) at 973 K, which is 17 % higher than the highest ZT of 0.30 obtained in VSTO-H (x = 0.20) at 973 K was achieved for the 1400H sample, as shown in Figures 6.31- 6.32, respectively. Though, no La-Sm co-doped $SrTiO_3$ has been reported in the literature, the high ZT value of 0.35 at 973 K obtained in this work remains the highest ZT reported in the literature of RE co-doped $SrTiO_3$ at this temperature [5]–[7], [21], [26]. By extrapolation, ZT value of 0.36 - 0.40 at 1000 - 1100 K is achievable in 1400H samples based on the linear trend of ZT values with temperature. The enhancement of ZT is mainly due to reduction of the total thermal conductivity by the reduced grain sizes (containing voids) and increased oxygen vacancies.

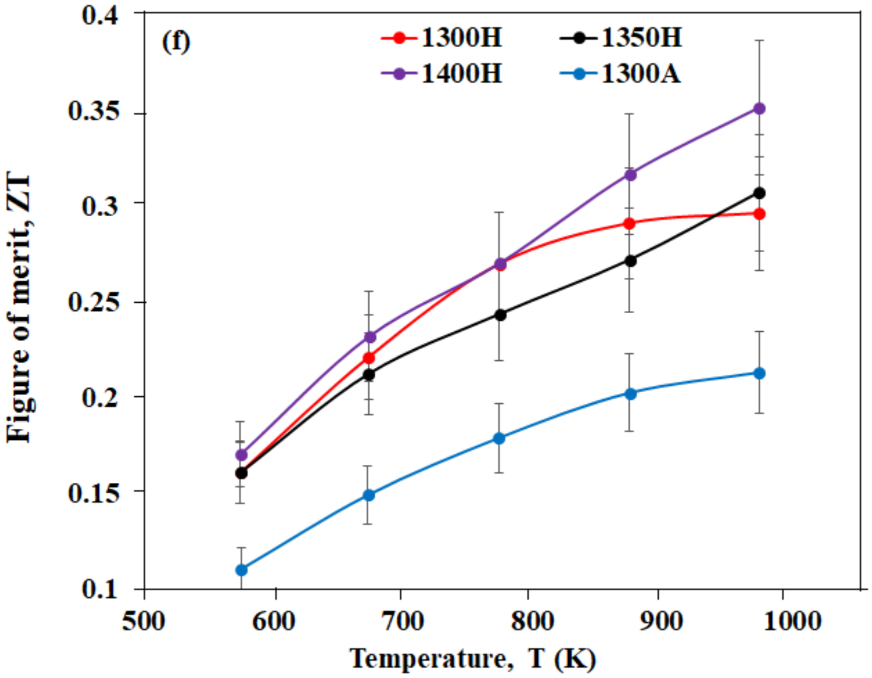

Figure 6.31. Temperature dependence of dimensionless figure of merit, ZT for 20 mol% La-Sm-doped $SrTiO_3$ ceramics calcined in air or 5% H_2/N_2 at 1573-1673 K for 6 hours and sintered at 1773 K for 6-8 hours in 5% H_2/N_2.

Figure 6.32 shows a comparison of ZT values of 1300A, 1300H, 1350H and 1400H ceramics at 573 and 973 K measured temperatures relative to 20 mol% La-Sm concentration. Air calcined samples (1300A) exhibited the lowest ZT value, and ZT increased in 5%H_2/N_2 calcined samples at 1573 K (1300H). As the samples were recalcined in 5%H_2/N_2 at high temperatures (1623-1673 K), an improved ZT was achieved. The highest ZT (0.35) achieved in 1400H as already discussed is related to its low k, which is attributed to the reduced grain sizes and high oxygen vacancies created in the sample.

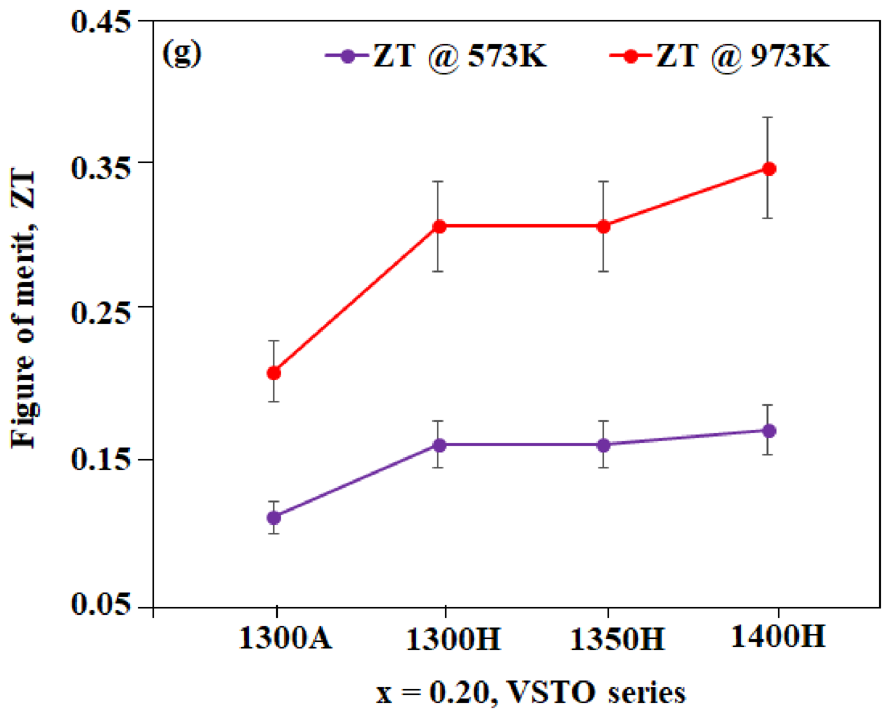

Figure 6.32. Comparison of dimensionless figures of merit, ZT for 20 mol% La-Sm-doped $SrTiO_3$ ceramics relative to La-Sm concentration at 573 and 973 K.

6.4 Conclusion

The combination of the solid-state reaction technique and strongly-reducing processing conditions successfully produced a nanostructured doping in A-site vacancy La-Sm-doped $SrTiO_3$ ceramics. The microstructure-control-approach applied in this work via modified processing (calcination and sintering) conditions has a triple function, viz:

i. La and Sm co-doping increased the carrier concentration, resulting to increase in electrical conductivity.

ii. Though the enhanced processing conditions seem to have a minimal effect on the electrical transport properties, optimised power factors were achieved.

iii. Total thermal conductivity was reduced by introducing complex defect strctures, attributed to atomic-scale La and Sm co-doped, the creation of A-site vacancies and oxygen vacancy contributions.

Upon optimising the electrical transport properties and reducing total thermal conductivity, a higher figure of merit, ZT (0.35) at 973 K was achieved in $Sr_{0.70}La_{0.10}Sm_{0.10}TiO_3$ (1400H) ceramics.

However, the highest ZT (0.35) obtained in this work is still low when compared with the work on $SrTiO_3$ reported by Lu *et al* [8], Lu [32], Kovalevsky *et al* [16] and Wang *et al* [4]. Lu *et al* and Lu conclude that A-site cation vacancies are significant in optimising ZT, hence a high ZT (0.41) at 973 in A-site vacancy La-doped $SrTiO_3$ ceramics is recorded. With this result in comparison to the ZT achieved in this study, one may argue that co-doping has a minimal effect in optimising ZT. In contrast, Wang *et al*, in their recent work reported an optimised ZT values of ≥ 0.6 at 1000-1100 K and ≥ 0.5 at 900-1000 K in 10 mol% La and 10 mol% (La10Nb10) electron co-doped $SrTiO_3$ ceramics. These ZT values (0.50 - 0.60) are higher than the best ZT values (0.38 – 0.41) reported in the literature for single-doped $SrTiO_3$ ceramics [8], [16], [32] and La-Nb doped $SrTiO_3$ assisted with Fe inclusion [27]. Wang *et al* [4] concluded that the combination of hydrothermal synthesis method and efficient sintering led to the optimised ZT.

From this comparative analysis, it is paramount to state that the type of doping mechanism (be it electron or vacancy) adopted plays a role in enhancing the ZT of doped $SrTiO_3$ ceramics but other factors may be more important and an efficient synthesis route with processing in strongly-reducing conditions is suggested to be pivotal in improving the TE performance. Lu *et al* [8] and Lu [32] in their works utilized attrition milling in the synthesis of the starting materials and calcined powders, and obtained small mean particle sizes. Attrition milling is adjudged to be more efficient mixing method than ball milling in reducing particle sizes of ceramic powders [11] and might have contributed to the higher ZT obtained by Lu *et al* and Lu. In another development, Kovalevsky *et al* [16] employed solid state reaction synthesis method and sintering under strongly reducing conditions (10%H_2-90%N_2), resulting to a suppressed k (~ 2.0) and optimised ZT (~ 0.41) at 1073 K for $Sr_{0.9}Dy_{0.1}TiO_{3\pm\delta}$ ceramics.

References

[1] Andrei V. Kovalevsky, Myriam H. Aguirre, Sascha Populoh, Sonia G. Patrício, Nuno M. Ferreira, Sergey M. Mikhalev, Duncan P. Fagg, Anke Weidenkaff, and Jorge R. Frade, "Designing strontium titanate-based thermoelectrics: insight into defect chemistry mechanisms," *J. Mater. Chem. A*, vol. 5, no. 8, pp. 3909–3922, 2017.

[2] Dragos Neagu and John T S Irvine, "Structure and Properties of $La_{0.4}Sr_{0.4}TiO_3$ Ceramics for Use as Anode Materials in Solid Oxide Fuel Cells," *Chem. Mater.*, vol. 22, no. 6, pp. 5042–5053, 2010.

[3] Deepanshu Srivastava, Colin Norman, Feridoon Azough, Marion C. Schafer, Emmanuel Guilmeau, Demie Kepaptsoglou, Quentin M. Ramasse, Giuseppe Nicotrad, and Robert Freer, "Tuning the Thermoelectric Properties of A-site Deficient $SrTiO_3$ Ceramics by Vacancies and Carrier Concentration," *Phys. Chem. Chem. Phys.*, vol. 18, pp. 26475–26486, 2016.

[4] Jun Wang, Bo Yu Zhang, Hui Jun Kang, Yan Li, Xinba Yaer, Jing Feng Li, Qing Tan, Shuai Zhang, Guo Hua Fan, Cheng Yan Liu, Lei Miao, Ding Nan, Tong Min Wang, and Li Dong Zhao, "Record high thermoelectric performance in bulk $SrTiO_3$ via nano-scale modulation doping," *Nano Energy*, vol. 35, no. April, pp. 387–395, 2017.

[5] Hongchao Wang and Chunlei Wang, "Thermoelectric properties of Yb-doped $La_{0.1}Sr_{0.9}TiO_3$ ceramics at high temperature," *Ceram. Int.*, vol. 39, no. 2, pp. 941–946, 2013.

[6] Hong Chao Wang, Chun Lei Wang, Wen Bin Su, Jian Liu, Yi Sun, Hua Peng, and Liang Mo Mei, "Doping effect of La and Dy on the thermoelectric properties of $SrTiO_3$," *J. Am. Ceram. Soc.*, vol. 94, no. 3, pp. 838–842, 2011.

[7] H C Wang, C L Wang, W B Su, J Liu, Y Zhao, H Peng, J L Zhang, M L Zhao, J C Li, N Yin, and L M Mei, "Enhancement of thermoelectric figure of merit by doping Dy in $La_{0.1}Sr_{0.9}TiO_3$ ceramic," *Mater. Res. Bull.*, vol. 45, no. 7, pp. 809–812, 2010.

[8] Zhilun Lu, Huairuo Zhang, Wen Lei, Derek C. Sinclair, and Ian M. Reaney, “High-Figure-of-Merit Thermoelectric La-Doped A-Site-Deficient $SrTiO_3$ Ceramics,” *Chem. Mater.*, vol. 28, no. 3, pp. 925–935, 2016.

[9] Jason H. Chan, Jonathan A. Bock, Hanzheng Guo, Susan Trolier-McKinstry, and Clive A. Randall, “Filled oxygen-deficient strontium barium niobates,” *J. Am. Ceram. Soc.*, vol. 100, no. 2, pp. 774–782, 2017.

[10] J. C Wurst and J. A Nelson, “Lineal Intercept for Measuring Grain Size in Two-Phase Polycrystalline Ceramics,” *J. Am. Ceram. Soc.*, vol. 55, no. 2, p. 109, 1972.

[11] R. Boston, W. L. Schmidt, G. D. Lewin, A. C. Iyasara, Z. Lu, H. Zhang, D. C. Sinclair, and I. M. Reaney, “Protocols for the fabrication, characterization, and optimization of n-type thermoelectric ceramic oxides,” *Chem. Mater.*, vol. 29, no. 1, pp. 265–280, 2017.

[12] Gregor Kieslich, Giacomo Cerretti, Igor Veremchuk, Raphaẽl P. Hermann, Martin Panthӧfer, Juri Grin, and Wolfgang Tremel, “A chemists view: Metal oxides with adaptive structures for thermoelectric applications,” *Phys. Status Solidi Appl. Mater. Sci.*, vol. 213, no. 3, pp. 808–823, 2016.

[13] G. H. Zheng, Z. X. Dai, Y. Q. Dong, F. L. Zan, D. Zou, Y. Q. Ma, and G. Li, “Low thermal conductivity for $Sr_{1-x}La_xTiO_3$,” *Mater. Res. Innov.*, vol. 16, no. 6, pp. 438–441, 2012.

[14] Hiroaki Muta, Ken Kurosaki, and Shinsuke Yamanaka, “Thermoelectric properties of reduced and La-doped single-crystalline $SrTiO_3$,” *J. Alloys Compd.*, vol. 392, no. 1–2, pp. 306–309, 2005.

[15] G J Snyder and E S Toberer, “Complex thermoelectric materials,” *Nat Mater*, vol. 7, no. 2, pp. 105–114, 2008.

[16] A. V. Kovalevsky, A. A. Yaremchenko, S. Populoh, P. Thiel, D. P. Fagg, A. Weidenkaff, and J. R. Frade, “Towards a high thermoelectric performance in rare-earth substituted $SrTiO_3$: effects provided by strongly-reducing sintering conditions,” *Phys. Chem. Chem. Phys.*, vol. 16, no. 48, pp. 26946–26954, 2014.

[17] Adindu C. Iyasara, Whitney L. Schmidt, Rebecca Boston, Derek C. Sinclair, and Ian M. Reaney, “La and Sm Co-doped $SrTiO_{3-\delta}$ Thermoelectric Ceramics,” *Mater. Today Proc.*, vol. 4, no. 12, pp. 12360–12367, 2017.

[18] Dursun Ekren, Feridoon Azough, Ali Gholinia, Sarah J. Day, David Hernandez-Maldonado, Despoina M. Kepaptsoglou, Quentin M. Ramasse, and Robert Freer, “Enhancing the thermoelectric power factor of $Sr_{0.9}Nd_{0.1}TiO_3$ through control of the nanostructure and microstructure,” *J. Mater. Chem. A*, vol. 6, no. 48, pp. 24928–24939, 2018.

[19] Arash Mehdizadeh Dehkordi, “An Experimental Investigation Towards Improvement of Thermoelectric Properties of Strontium Titanate Ceramics,” PhD Thesis, Clemson University, 2014.

[20] H C Wang, C L Wang, W B Su, J Liu, H Peng, J L Zhang, M L Zhao, J C Li, N Yin, and L M Mei, "Substitution effect on the thermoelectric properties of reduced Nb-doped," *J. Alloys Compd.*, vol. 486, pp. 693–696, 2009.

[21] Jiao Han, Qiu Sun, and Ying Song, "Enhanced thermoelectric properties of La and Dy co-doped, Sr-deficient $SrTiO_3$ ceramics," *J. Alloys Compd.*, vol. 705, pp. 22–27, 2017.

[22] T Okuda, K Nakanishi, S Miyasaka, and Y Tokura, "Large Thermoelectric Response of Metallic Perovskite: $Sr_{1-x}La_xTiO_3$ ($0 \leq x \leq 0.1$)," *Phys. Rev. B*, vol. 63, pp. 1131041–1131044, 2001.

[23] Shingo Ohta, Takashi Nomura, Hiromichi Ohta, and Kunihito Koumoto, "High-temperature carrier transport and thermoelectric properties of heavily La- or Nb- doped single crystals," *J. Appl. Phys.*, vol. 97, no. 3, pp. 0341061–0341064, 2005.

[24] Wen Li, Siqi Lin, Xinyue Zhang, Zhiwei Chen, Xiangfan Xu, and Yanzhong Pei, "Thermoelectric Properties of Cu_2SnSe_4 with Intrinsic Vacancy," *Chem. Mater.*, vol. 28, no. 17, pp. 6227–6232, 2016.

[25] T.M. Tritt, "Thermoelectric Materials : Principles , Structure , Properties , and Applications," *Encycl. Mater. Sci. Technol.*, pp. 1–11, 2002.

[26] J. Liu, C. L. Wang, Y. Li, W. B. Su, Y. H. Zhu, J. C. Li, and L. M. Mei, "Influence of rare earth doping on thermoelectric properties of $SrTiO_3$ceramics," *J. Appl. Phys.*, vol. 114, no. 22, 2013.

[27] Deepanshu Srivastava, Colin Norman, Feridoon Azough, Marion C. Schäfer, Emmanuel Guilmeau, and Robert Freer, "Improving the thermoelectric properties of $SrTiO_3$-based ceramics with metallic inclusions," *J. Alloys Compd.*, vol. 731, no. January, pp. 723–730, 2018.

[28] Yue Lin, Colin Norman, Deepanshu Srivastava, Feridoon Azough, Li Wang, Mark Robbins, Kevin Simpson, Robert Freer, and Ian A. Kinloch, "Thermoelectric Power Generation from Lanthanum Strontium Titanium Oxide at Room Temperature through the Addition of Graphene," *ACS Appl. Mater. Interfaces*, vol. 7, no. 29, pp. 15898–15908, 2015.

[29] Zhenguang Shen, Zengying Zhao, Jian Wen, Jingwen Qian, Zhijian Peng, and Xiuli Fu, "Role of Oxygen Vacancies in the Electrical Properties of WO_{3-x} Nano / Microrods with Identical Morphology," vol. 2018, 2018.

[30] M. C. Verbraeken, T. Ramos, K. Agersted, Q. Ma, C. D. Savaniu, B. R. Sudireddy, J. T.S. Irvine, P. Holtappels, and F. Tietz, "Modified strontium titanates: from defect chemistry to SOFC anodes," *RSC Adv.*, vol. 5, no. 2, pp. 1168–1180, 2015.

[31] Yao Ming Wang, Chien Ming Lei, and Horng Yi Chang, "Electrical properties of lanthanum strontium titanates modified by microwave sintering,"

Ferroelectrics, vol. 434, no. 1, pp. 83–90, 2012.

[32] Zhilun Lu, “La doped $SrTiO_3$ Based Oxide Thermoelectrics.,” PhD Thesis, University of Sheffield, 2016.

Chapter 7: $Sr_5LaTi_3Nb_7O_{30}$ and $La_2Ti_2O_7$ Oxide Ceramics

7.1 Introduction

Complex oxide compounds with intricate atomic structures, tunable stoichiometry and intrinsic low thermal conductivity (k) are promising thermoelectric (TE) materials for power generation [1]. Among this class of ceramics, tetragonal tungsten bronze (TTB) and perovskite-like layered structured (PLS) ceramics are of interest due to their intrinsic phonon scattering centres [2], [3] giving rise to low k [4] which may result in an increasing ZT. Unfortunately, they also possess very low electrical conductivity, hence it is a challenge to achieve strong TE performance in these oxides. In this work, the structure and thermoelectric properties of Sm-doped TTB $Sr_5LaTi_3Nb_7O_{30}$ (SLTN) and PLS Nb-doped $La_2Ti_2O_7$ (LTO) ceramics are studied with a view to increasing the electrical conductivity through the use of appropriate dopant/processing strategies.

$Sr_5LaTi_3Nb_7O_{30}$ was investigated via two different doping mechanisms: electron, $Sr_5La_{1-x}Sm_xTi_3Nb_7O_{30}$, $0.00 \leq x \leq 1.00$ (SLTNe) and ionic (vacancy), $Sr_{5-3x/2}LaSm_xTi_3Nb_7O_{30}$, $0.00 \leq x \leq 0.30$ (SLTNv). Nb-doped $La_2Ti_2O_7$ was studied using electron doping mechanism ($La_2Ti_{2-x}Nb_xO_7$; $0.00 \leq x \leq 0.25$).

7.2 Sm-Doped $Sr_5LaTi_3Nb_7O_{30}$ Ceramics: Results and Discussion

7.2.1 Phase Assemblage and Microstructure

Sm-doped $Sr_5LaTi_3Nb_7O_{30}$ compositions (SLTNe and SLTNv) were sintered in air and 5% H_2/N_2 at 1673 K for 6 hours and analysed to confirm the phase assemblage. The resulting room temperature XRD patterns of the crushed ceramics are shown in Figures 7.1, 7.2 and 7.3, respectively. All peaks in air sintered SLTNe compositions, as displayed in Figure 7.1, are indexed with the $Sr_5LaTi_3Nb_7O_{30}$ tetragonal tungsten bronze structure with space group P4/mbm according to the PDF card no. 04-020-0459 [5] and PDF card no. 00-054-0777 (space group, P4bm) [6] for $0.00 \leq x \leq 0.75$ and $x = 1.00$, respectively. No secondary phases were detected.

However, when compositions were sintered in reducing atmosphere using a 5% H_2/N_2 gas mixture (Figures 7.2 and 7.3), significant peaks associated with secondary phases were indexed according to an ideal cubic $SrTiO_3$ perovskite and a weak intensity unknown peak. The presence of these secondary phases ($SrTiO_3$ and the unknown peak) is attributed to structural instability induced by oxygen deficiency [7] resulting from the sintering in the reducing atmosphere (5% H_2/N_2).

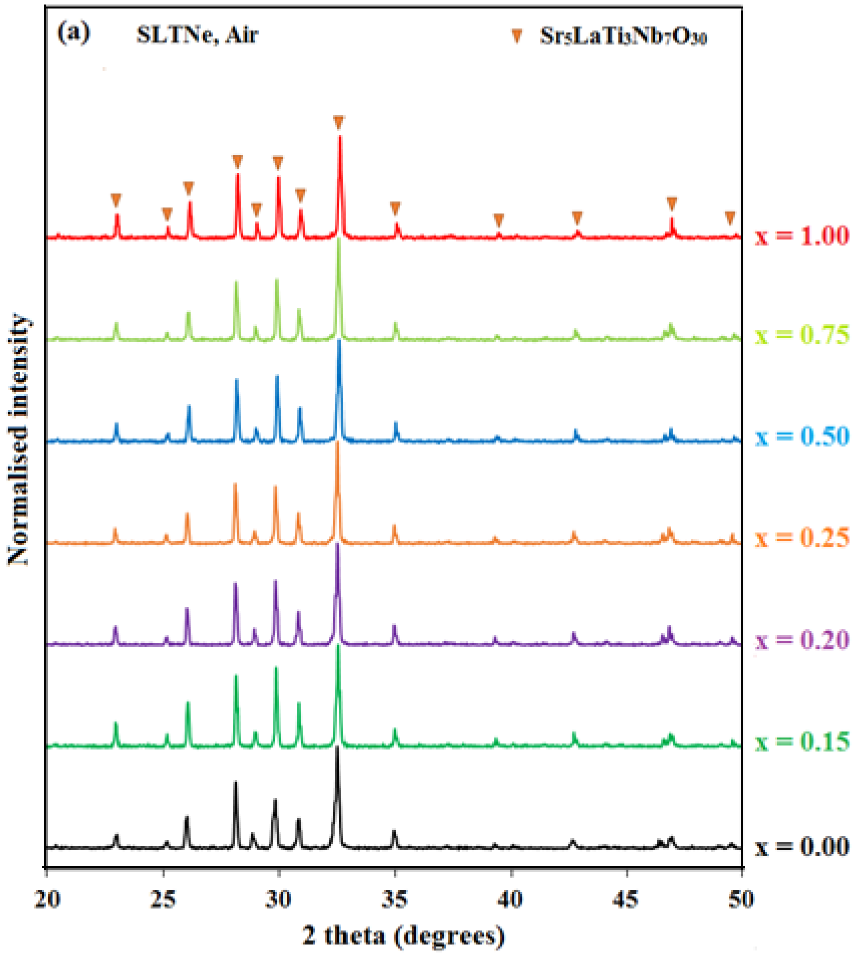

Figure 7.1. Room temperature XRD patterns of crushed $Sr_5La_{1-x}Sm_xTi_3Nb_7O_{30}$; $0.00 \leq x \leq 1.00$ (SLTNe) ceramics sintered in air at 1673 K for 6 hours.

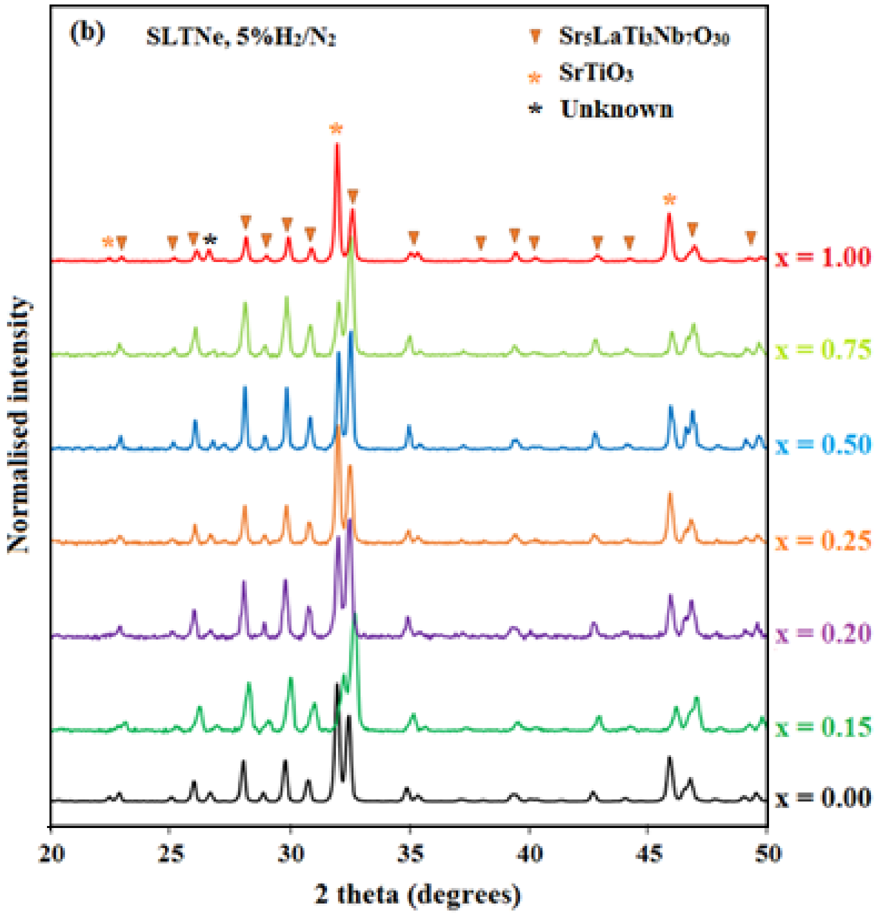

Figure 7.2. Room temperature XRD patterns of crushed $Sr_5La_{1-x}Sm_xTi_3Nb_7O_{30}$; $0.00 \leq x \leq 1.00$ (SLTNe) ceramics sintered in 5% H_2/N_2 at 1673 K for 6 hours.

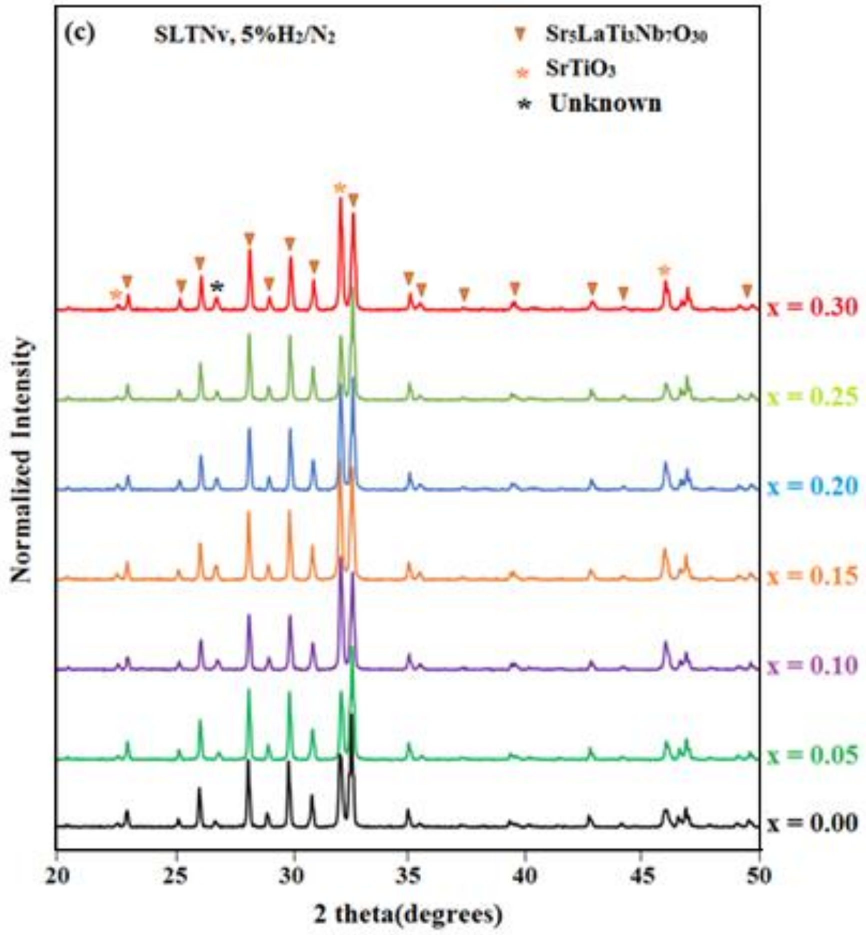

Figure 7.3. Room temperature XRD patterns of crushed $Sr_{5-3x/2}LaSm_xTi_3Nb_7O_{30}$; 0.00 ≤ x ≤ 0.30 (SLTNv) ceramics sintered in 5% H_2/N_2 at 1673 K for 6 hours.

Figures 7.4 and 7.5 display the SEM micrographs of the air and 5% H_2N_2 sintered, thermally etched and carbon coated surfaces of SLTNe (x = 0.00, 0.20, 0.50, 1.00) ceramics. All images of the air sintered ceramics (Figure 7.4) showed homogenous and dense structures consistent with the high average density (5.05 g/cm^3) and absence of secondary phase peaks in XRD spectra. The end member sample (x = 0.00, undoped) had the largest average grain size of 7.4 µm. With increasing x, average grain size decreased to 4.3 µm with rod-like large grains (~ 6 x 2 µm) in x = 1.00.

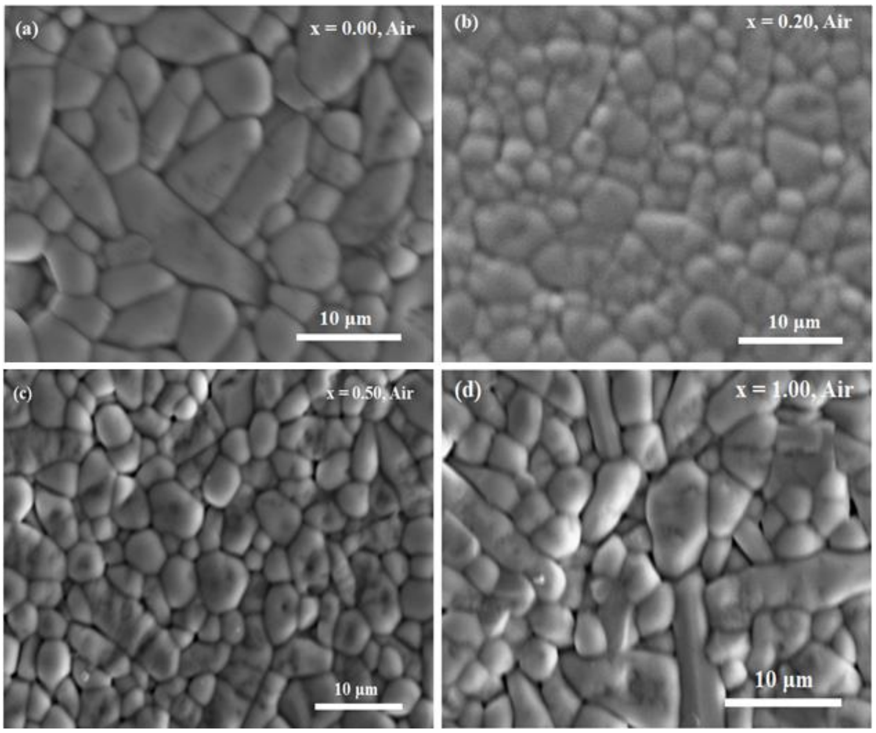

Figure 7.4. SEM micrographs of the surfaces of $Sr_5La_{x-1}Sm_xTi_3Nb_7O_{30}$ (SLTNe); $0.00 \leq x \leq 1.00$ ceramics sintered in air at 1673 K for 6 hours, carbon coated and thermally etched at 1533 K for 30 minutes.

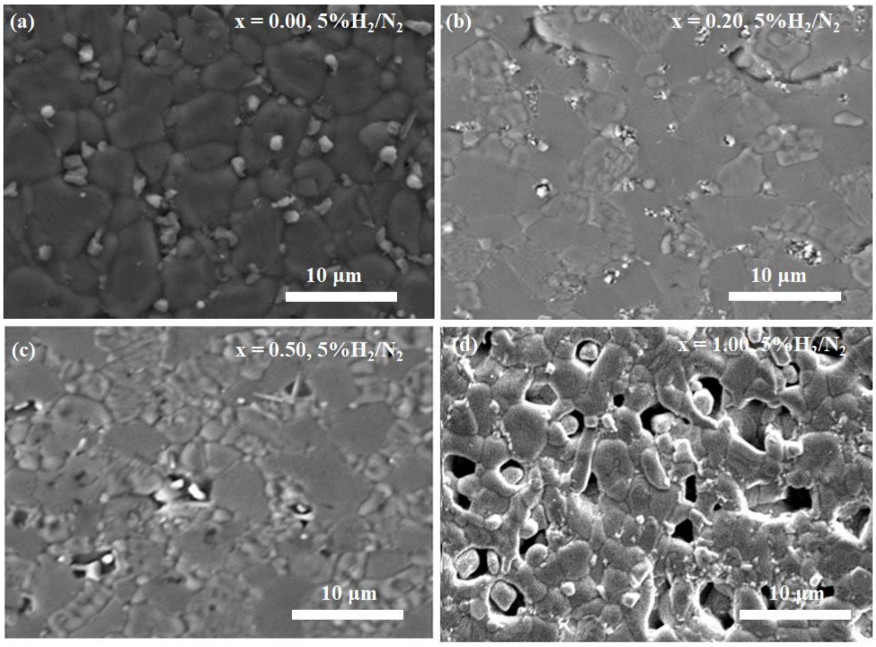

Figure 7.5. SEM micrographs of the surfaces of $Sr_5La_{x-1}Sm_xTi_3Nb_7O_{30}$ (SLTNe); $0.00 \leq x \leq 1.00$ ceramics sintered in 5%H_2N_2 at 1673 K for 6 hours and thermally etched at 1533 K for 30 minutes.

In contrast, SEM images of 5% H_2N_2 sintered samples showed a bimodal grain size distribution as shown in Figure 7.5. The small grains indicated the presence of secondary phase dispersed within the large or coarse grains and at grain boundaries, confirming the presence of secondary phases as identified in XRD patterns, Figures 7.2 - 7.3. The average grain size of the large grains is dependent on the doping concentration. It reduces progressively from 5.1 µm for x = 0.00 to 4.5 µm for x = 0.20, to a minimal value of 4.1 µm for x = 0.50 and increased to 5.0 µm for x = 1.00 sample. The secondary phases are typically 1-2 µm in size.

EDX confirmed the chemical composition of the large grains to be the TTB phase, while the smaller grains of similar contrast are $SrTiO_3$ perovskite with smallest bright grains as Nb-rich oxide as shown in the EDX results and spectra, Figure 7.6, Tables 7.1 and 7.2. The presence of an Nb-rich oxide (most likely Nb_2O_{5-x}) secondary phase is attributed to the reduction. The TTB phase decomposes to a Sm-doped $SrTiO_3$ and Nb_2O_5. The former composition accommodates reduction through the formation of Ti^{3+} on the B-site which is compensated by Sm^{3+} on the A-site. Nb^{5+} is more difficult to reduce and as is expunged from solid solution. However, the formation of Nb^{4+} ions is not excluded in the Nb-rich oxide phase [8], [9]. The presence of these secondary phases has a significant effect on the thermoelectric properties of $Sr_5LaTi_3Nb_7O_{30}$ ceramics as discussed later in this work.

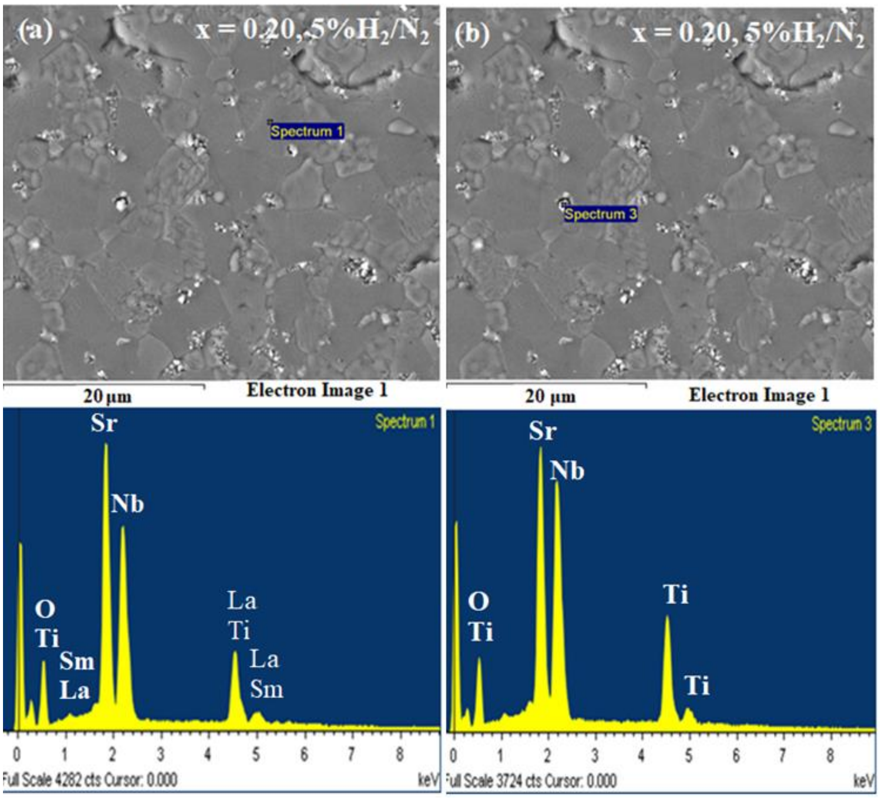

Figure 7.6. SEM image and point EDX trace of $Sr_5La_{0.80}Sm_{0.20}Ti_3Nb_7O_{30}$ ceramic sintered 6 hours in 5% H_2/N_2 at 1673 K from a (a) large grain (spectrum 1) (b) small grain or secondary phase (spectrum 3).

Table 7.1. Point EDX analysis done on the large grain surface (Spectrum 1) of $Sr_5La_{0.80}Sm_{0.20}Ti_3Nb_7O_{30}$ ceramic sintered 6 hours in 5% H_2/N_2 at 1673 K.

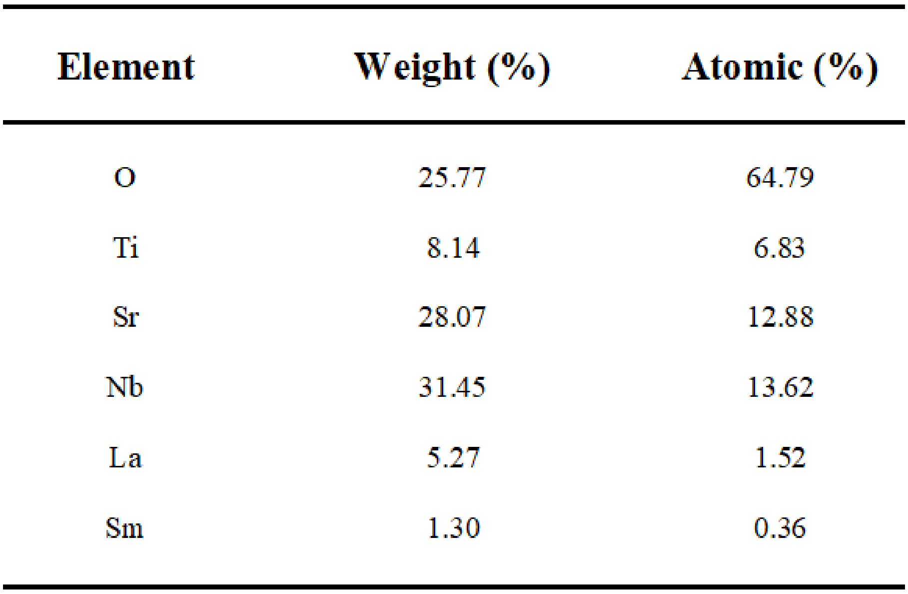

Element	Weight (%)	Atomic (%)
O	25.77	64.79
Ti	8.14	6.83
Sr	28.07	12.88
Nb	31.45	13.62
La	5.27	1.52
Sm	1.30	0.36

Table 7.2. Point EDX analysis done on the small grain surface (Spectrum 3) of $Sr_5La_{0.80}Sm_{0.20}Ti_3Nb_7O_{30}$ ceramic sintered 6 hours in 5% H_2/N_2 at 1673 K.

Element	Weight (%)	Atomic (%)
O	29.12	67.12
Ti	11.14	8.57
Sr	24.74	10.41
Nb	35.00	13.90

7.2.2 Thermoelectric Properties

The thermoelectric results obtained for reduced Sm-doped $Sr_5LaTi_3Nb_7O_{30}$ (SLTNe and SLTNv) ceramics are discussed in the following section. The discussion is divided into three perspectives viz; the electrical transport properties, thermal transport properties and efficiency (ZT) of the ceramics.

Electrical Transport Properties

Figure 7.7 shows the temperature dependence of the electrical conductivity, σ of the $Sr_5La_{1-x}Sm_xTi_3Nb_7O_{30}$ (SLTNe) and $Sr_{5-3x/2}La_xSm_xTi_3Nb_7O_{30}$ (SLTNv) ceramics sintered in 5% H_2/N_2 at 1673 K for 6 hours. The electrical conductivity of all SLTNe samples, except $x = 0.15$ increased with respect to the measuring temperature up to 873 K, and then decreased with a further increase in temperature, Figure 7.7(a). This shows the samples at 573-873 K exhibited semiconducting behaviour, which at 973 K switched to typical metallic behaviour. For $x = 0.15$, σ decreased with increasing temperature over the entire measured temperature range, indicating metallic behaviour as reported previously [10], [11]. The magnitude for the σ of SLTNe samples increased significantly for $x = 0.15$ compared to undoped sample ($x = 0.00$), suggesting that carrier concentration and mobility were affected by doping [12], [13]. With an increase in Sm concentration ($x \geq 0.20$), σ decreased even lower than the un-doped sample ($x = 0.00$). The highest electrical conductivity value (~ 444 S/cm) was obtained in $x = 0.15$ SLTNe sample at 573 K. It is important to state that $x = 0.15$ sample maintained the highest σ in the entire measured temperature range.

The electrical conductivity behaviour of SLTNv samples as shown in Figure 7.7(b) is divided into two parts for discussion purposes. Part I is $x = 0.00$, $x = 0.15$-0.20; part II is $x = 0.05$-0.10, $x \geq 0.25$. In part I, σ increased significantly when compared to part II. The σ of $x = 0.00$; 0.20 and $x = 0.15$ samples exhibited a peak behaviour in the low temperature ranges 573-773 K and 573-873 K, respectively, showing a semiconductor-like behaviour and transits to metallic behaviour (decrease in σ with increasing temperature) at high temperature (973 K) [9], [13]. Similarly, σ of all samples in part II displayed a transition at 873 K, which increased with increasing temperature in 573-873 K temperature range and decreased at high temperature (973 K). Sm-doping of the vacancy compositions (SLTNv) with $x < 0.20$ or > 0.20 reduced σ when compared to un-doped samples ($x = 0.00$), hence the highest σ (~292 S/cm) at 573 K was recorded in $x = 0.20$. As observed from the graph, σ of $x = 0.00$ and $x = 0.20$ ceramics converged at high temperatures (873-973 K). The reason for the maximum σ (292 S/cm) observed in SLTNv when compared to SLTNe (σ_{max} = 444 S/cm at 573 K) is unclear but unlike in perovskite compositions, cation vacancies did not improve σ with respect to electron substitution.

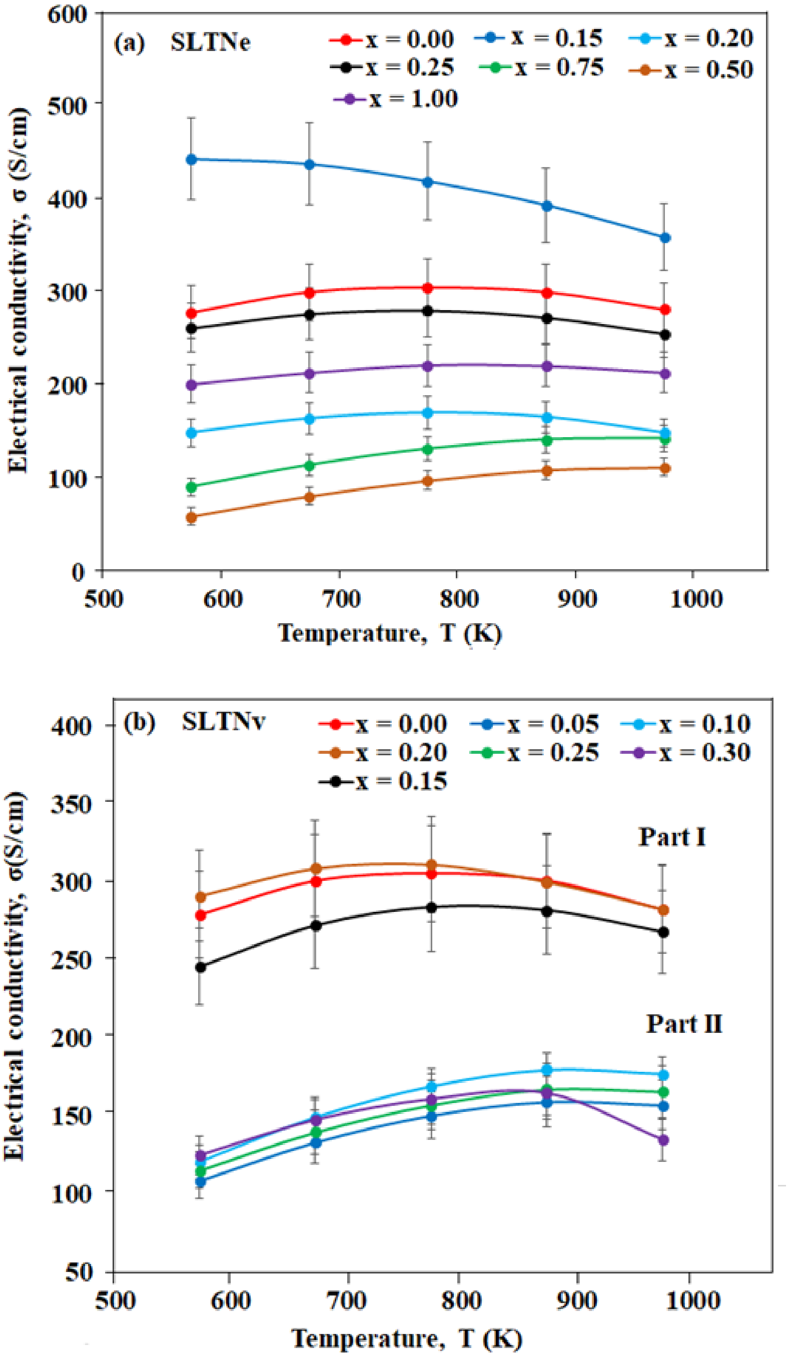

Figure 7.7. Temperature dependence of electrical conductivity for (a) SLTNe, (b) SLTNv samples sintered in 5% H_2/N_2 at 1673 K for 6 hours.

Figure 7.8 shows the absolute Seebeck coefficient, $|S|$ of SLTNe and SLTNv samples as a function of temperature. The Seebeck coefficients of all ceramics are negative, indicating that electrons are the dominant carriers. The Seebeck coefficient increased monotonically with increasing temperature and decreased with increasing σ, showing metallic behaviour. The increase in S with temperature can be associated with an increase in the internal entropy [14]. The highest Seebeck coefficients recorded for SLTNe and SLTNv samples were 179 μV/K (for x = 0.50) and 164 μV/K (for x = 0.30), respectively at 973 K. The high S values exhibited by these compositions (x = 0.50; 0.30) is related to their low σ.

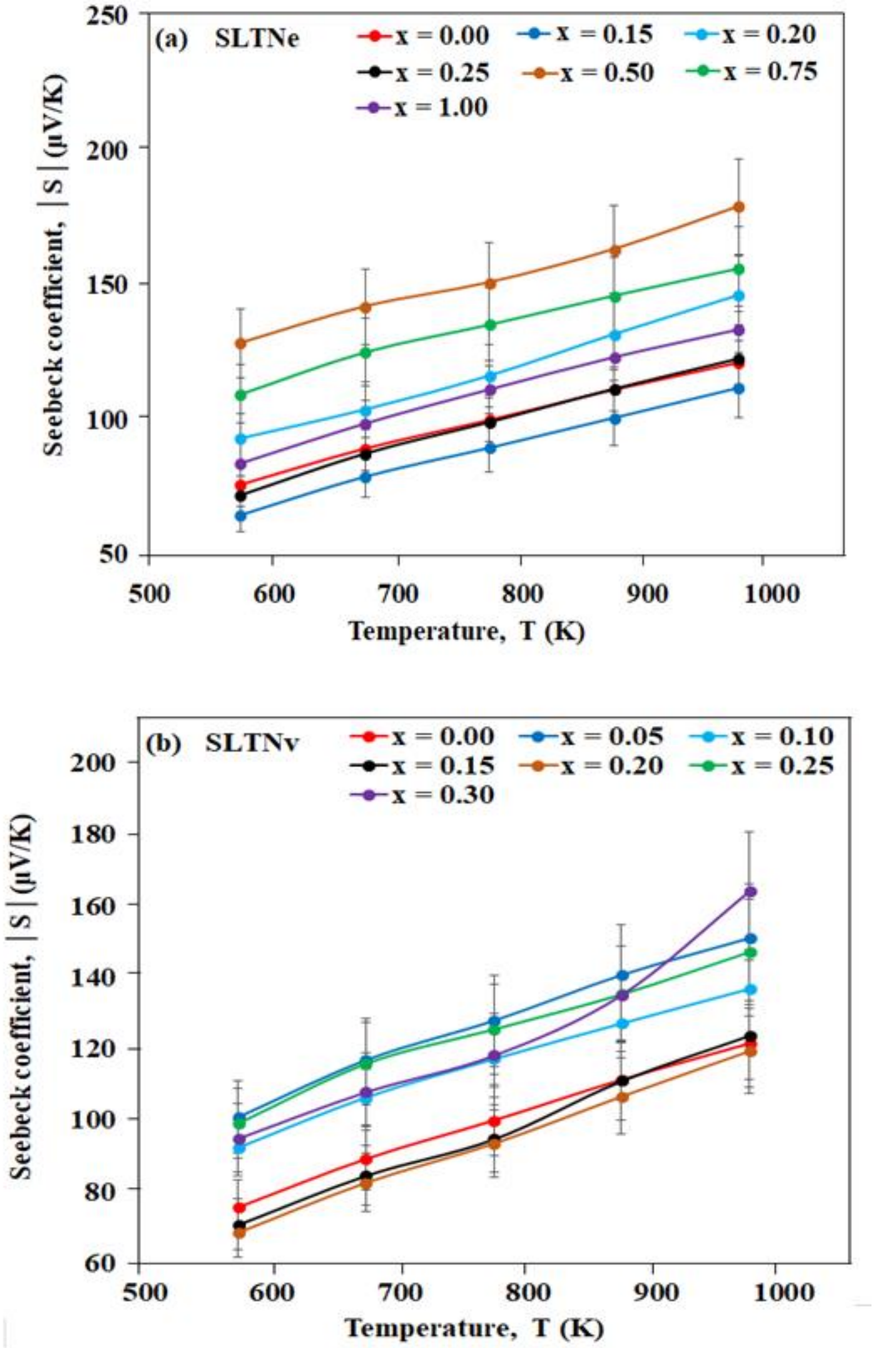

Figure 7.8. Temperature dependence of Seebeck coefficient for (a) SLTNe, (b) SLTNv samples sintered in 5% H_2/N_2 at 1673 K for 6 hours.

The thermoelectric power factor (PF) of SLTNe and SLTNv samples are shown in Figure 7.9. The PF for SLTNe samples, Figure 7.9(a) showed a decrease except x = 0.15 when compared to the undoped ceramic (x = 0.00) due to Sm doping. The highest PF value (451μW/K^2.m) was obtained in x = 0.15 composition at 973 K, and is attributed to its high σ. In contrast, the highest PF value does not occur in x = 0.20 of the vacancy sample (SLTNv) with the highest σ (Figure 7.9b). x = 0.00 (undoped sample) showed the highest PF value, ~ 417 μW/K^2.m at 973 K with x = 0.15 (412 μW/K^2.m) and x = 0.20 (404 μW/K^2.m) power factors close to the maximum PF. The combined effect of the high σ and S obtained in x = 0.00 contributed to its high PF. Though, no TE study has been reported in the literature for $Sr_5LaTi_3Nb_7O_{30}$ TTB, the PF results obtained in this work are higher than the PF results reported for $Sr_xBa_{1-x}Nb_2O_6$ TTB ceramics [9], [15], [16]. It is argued that the presence of secondary phases particularly the conducting $SrTiO_3$ phase in the microstructure might have contributed to the improved PF observed in SLTN ceramics. This assertion is supported by the work of Lu *et al* [17] on La-doped $Sr_3Ti_2O_7$ Ruddlesden-popper (RP) ceramics. They showed that compositions with $SrTiO_3$ secondary phases resulted in high PF. This result suggests that doping $Sr_5LaTi_3Nb_7O_{30}$ ceramics with samarium element and sintered in reducing atmosphere (5% H_2/N_2) can precipitate secondary phases in the lattice which improve the electronic transport properties. It also indicates that the ideal cubic $SrTiO_3$ phases have higher σ than any Sm-doped $Sr_5LaTi_3Nb_7O_{30}$ phase (as discussed in Chapters 5 and 6), and therefore more suitable for TE applications.

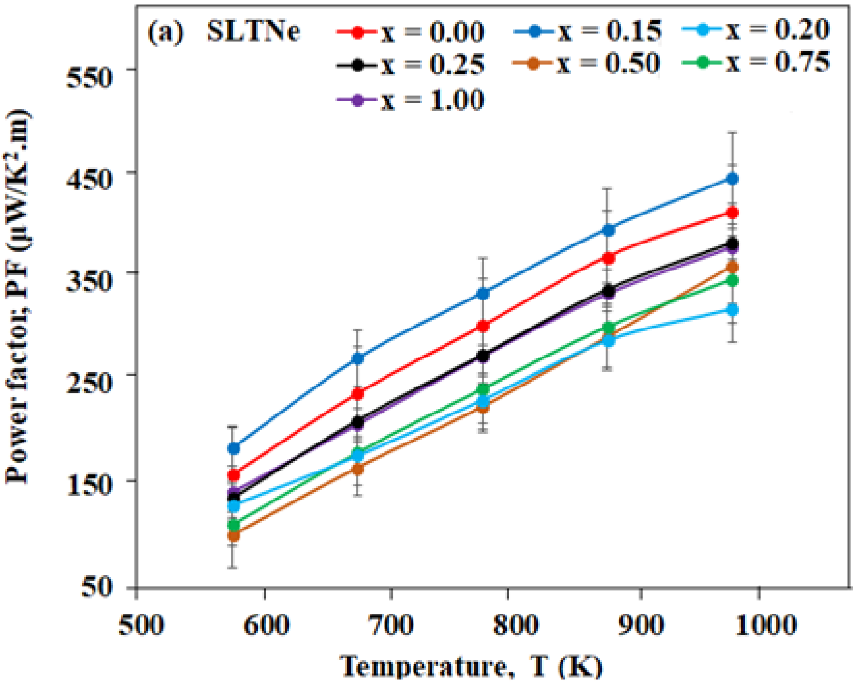

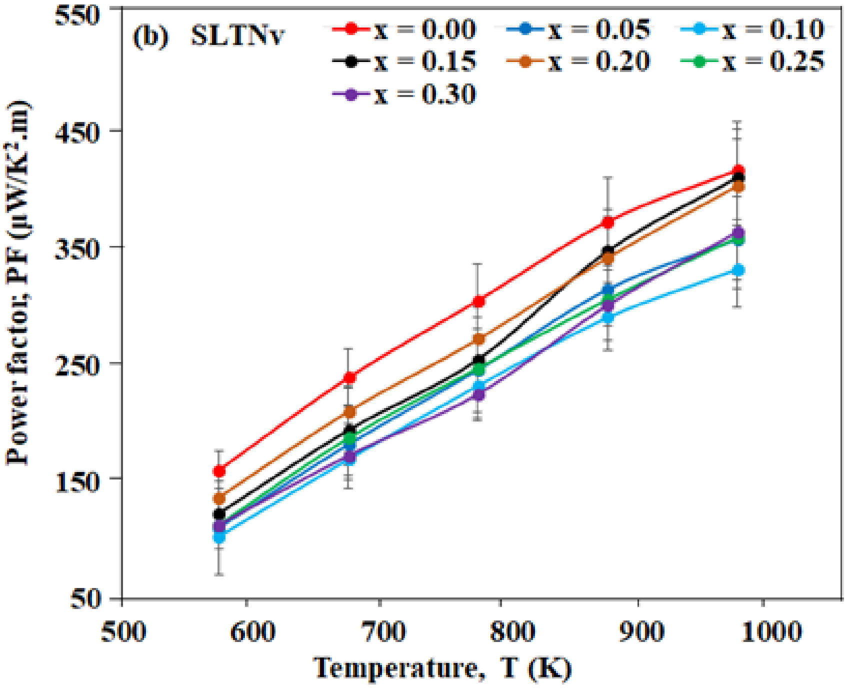

Figure 7.9. Temperature dependence of power factor for (a) SLTNe, (b) SLTNv samples sintered in 5% H_2/N_2 at 1673 K for 6 hours.

Thermal Transport Properties

The total thermal conductivity (k), lattice thermal conductivity (k_L) and electronic thermal conductivity (k_E) of SLTNe and SLTNv samples are shown in Figures 7.10, 7.11 and 7.12, respectively. k and k_L of all the samples vary irregularly with Sm-concentration especially at low temperatures as shown in Figures 7.10 and 7.11. The main reason for this anomaly is unclear but could be due to the influence of numerous factors such as defect scattering and bond angles of the Ti-O, Nb-O octahedra and the changes in phase assemblage as a function of composition. However, at low temperatures, k for most of the compositions increases with temperature. This can be explained as follows [18]. At low temperatures, majority of the thermally excited phonons possess small momentum and it's known as "Normal process (N-process)". As a result, momentum is conserved, hence there is no contribution or effect on net energy, momentum contribution, scattering in heat transport and MFP for k. Thus, k increases with temperature.

Apart from point defects (V_{Sr}, V_O) created in the lattice, the presence of secondary phases ($SrTiO_3$ and Nb_2O_5) in the microstructure influence the thermal conductivity. SLTNv samples exhibited low k values (1.62-3.85 W/m. K) when compared to that of SLTNe samples (2.02 to 4.17 W/m. K) in the whole measured temperature range. This observation suggests the presence of these secondary phase inclusions and the point or vacancy defects act as scattering centres, shorten MFP of phonons and restrict their propagation, resulting in a decrease in k as previously discussed [13], [19], [20]. It is observed that only x = 0.50 (from SLTNe sample) and x = 0.30 (from SLTNv sample) exhibited similar thermal behaviour. k of x = 0.50 and x = 0.30 compositions decreased with increasing temperature over the entire measured temperature range, showing phonon scattering behaviour [9] which is dominated by the Umklapp process (U-process) [13], [21], [22]. The Umklapp process or scattering is the name for several types of scattering that change the momentum of phonons. The U-process occurs usually at high temperatures, and momentum is not conserved, resulting in a net momentum deposition in the scattering process and k being proportional to 1/kT. The lowest k (~ 2.0 W/m. K) obtained in SLTNe sample was observed in x = 0.50 at 973 K, while in SLTNv sample, x = 0.30 showed the lowest k (~ 1.6 W/m. K) at 873 K. The lowest k values are attributed to the Umklapp scattering which not only reduces the k, but also σ (especially at high temperature for SLTNv, x = 0.30) as presented in Figure 7.10.

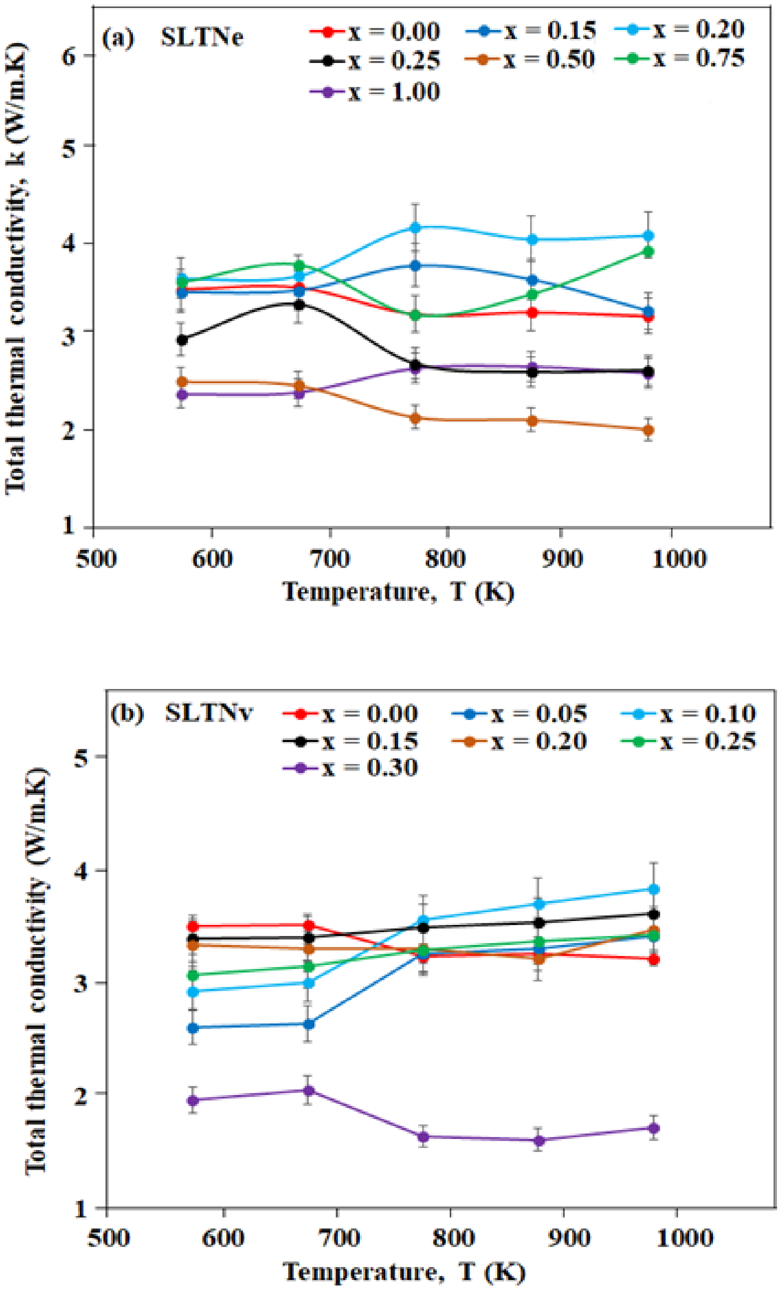

Figure 7.10. Temperature dependence of total thermal conductivity for (a) SLTNe (b) SLTNv samples sintered 6 for hours in 5% H_2/N_2 at 1673 K.

The lattice thermal conductivity (k_L), Figure 7.11 exhibited the same trend as k but with slightly lower values. In general, the decrease in k experienced in SLTNe and SLTNv samples may be linked to an additional phonon scattering resulting from impurities (or secondary phases) evidenced in the SEM images, cation vacancies, oxygen defects and grain boundaries [23]–[25]. The k_E of all samples showed similar temperature dependence with σ and increased with increase in temperature as presented in Figure 7.12. From the small k_E values (19.5-20.6 % of k), the electronic thermal conductivity makes a very small contribution to the total thermal conductivity. Therefore, the decrease of k of the samples is mainly due to the decrease of k_L via enhancement of phonon scattering.

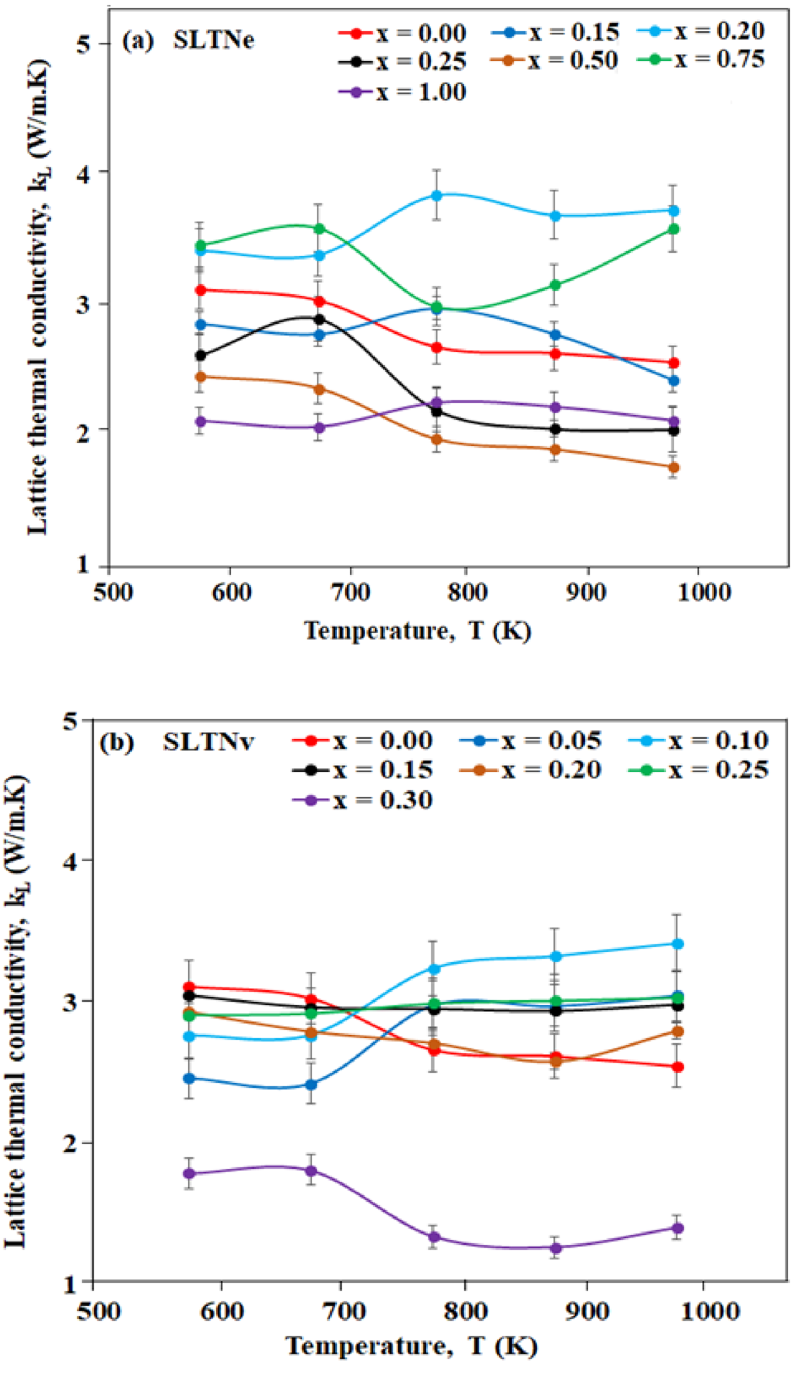

Figure 7.11. Temperature dependence of lattice thermal conductivity for (a) SLTNe (b) SLTNv samples sintered 6 for hours in 5% H_2/N_2 at 1673 K.

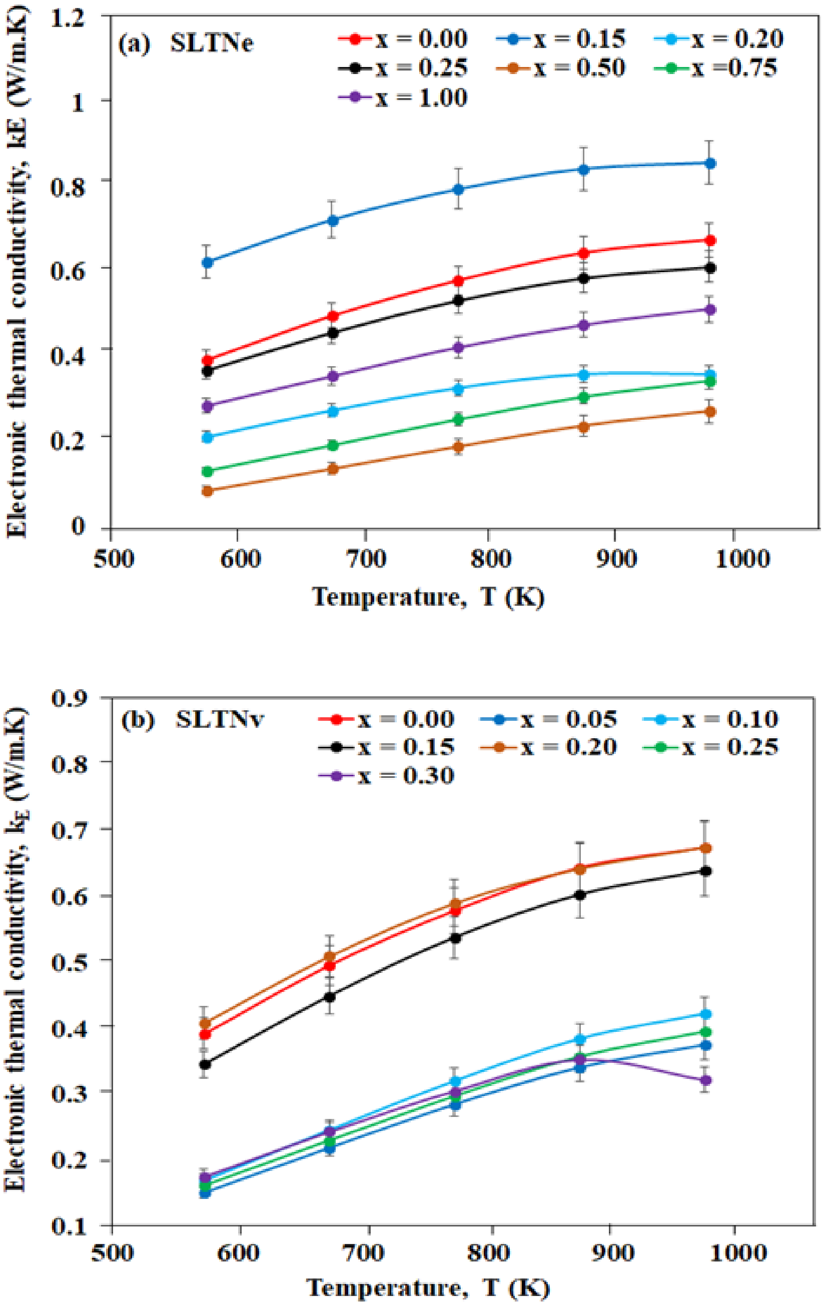

Figure 7.12. Temperature dependence of lattice thermal conductivity for (a) SLTNe (b) SLTNv samples sintered 6 for hours in 5% H_2/N_2 at 1673 K.

Thermoelectric Figure of Merit

The overall thermoelectric performance or efficiency of Sm-doped $Sr_5LaTi_3Nb_7O_{30}$ ceramics studied in this work was measured using the thermoelectric figure of merit (ZT). The thermoelectric figure of merit of SLTNe and SLTNv samples as a function of temperature is shown in Figure 7.13. ZT values of all the samples increased with temperature in the measured temperature range. As previously discussed, Sm-doping, cation vacancy, oxygen-reduction or oxygen vacancy and the secondary phase inclusions evident in the microstructure played a major role in optimising the PF. More so, the significant reduction in k, attributed to a large extent to the multiphase mixtures in the microstructure contributed greatly in the increased ZT recorded in the Sm-doped $Sr_5LaTi_3Nb_7O_{30}$ ceramics.

The ZT values of SLTNe samples reached a maximum of 0.18 at 973 K in the $Sr_5La_{0.50}Sm_{0.50}Ti_3Nb_7O_{30}$ ($x = 0.50$) sample, Figure 7.13(a). However, this highest value of ZT does not occur in $x = 0.15$ composition with the highest σ (Figure 7.7a) and PF, Figure 7.9(a), but from $x = 0.50$ sample composition with the lowest k values. In SLTNv samples, similar trend repeated itself. As shown in Figures 7.7 (b) and 7.9(b), the highest σ and PF were observed in $x = 0.00$ (and $x = 0.20$ at high temperatures) and $x = 0.00$, respectively but could not exhibit the maximum ZT. The highest ZT (~ 0.21) value was observed in $Sr_{4.55}LaSm_{0.30}Ti_3Nb_7O_{30}$ ($x = 0.30$) sample at 973 K (Figure 7.9b). $x = 0.30$ recorded the smallest k value of 1.6 W/m. K at 873 K. The secondary phase inclusions ($SrTiO_3$ and Nb_2O_5) observed in the microstructure and the vacancy defects created (Vsr and V_O) as discussed would have contributed to the enhancement of phonon scattering, resulting in a very low k. The impact of this low k gives an overall increase in ZT.

Overall, the highest ZT (~ 0.21) recorded in this work for the thermoelectric study of Sm-doped $Sr_5LaTi_3Nb_7O_{30}$ was obtained in vacancy doped $Sr_{4.55}LaSm_{0.30}Ti_3Nb_7O_{30}$ ($x = 0.30$) at 973 K. It is obvious to conclude that Sm doping, oxygen-reduction, secondary phase inclusions and cation vacancies created in SLTNv strongly restricted phonon propagation, resulting to the decrease in k (Ref. 13, 19, 20).

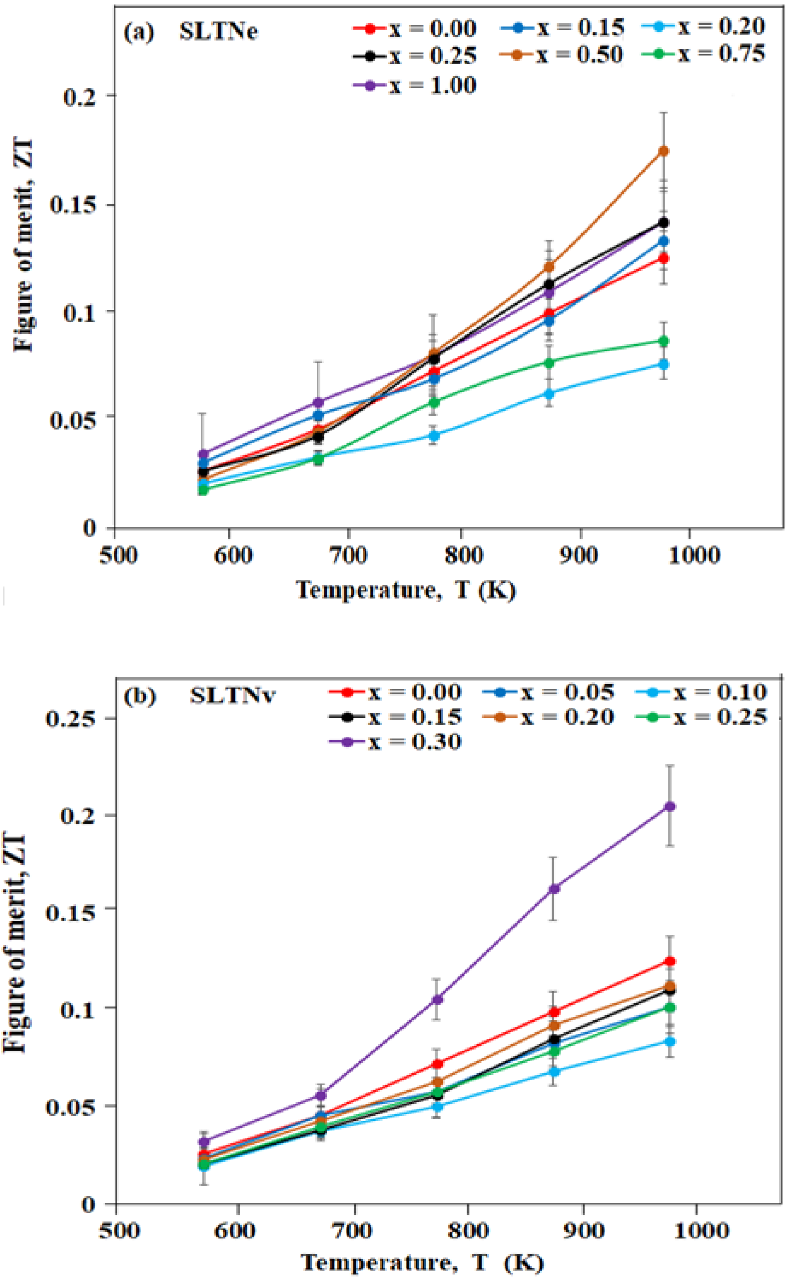

Figure 7.13. Temperature dependence of figure of merit for (a) SLTNe (b) SLTNv samples sintered 6 for hours in 5% H_2/N_2 at 1673 K.

The highest ZT (0.21) reported in this work is comparable to that of $Sr_{1-x}Ba_xNb_2O_6$, 0.21 (at 1073 K) [9] and $Nb_4W_{13}O_{47}$, 0.20 (at 1173 K) [14]. At 973 K, $Sr_{1-x}Ba_xNb_2O_6$ showed a ZT ~ 0.15 which is less that the maximum ZT obtained in this work for SLTNe (ZT_{max} = 0.18) and SLTNv (ZT_{max} = 0.21) at same temperature. In addition, the ZT_{max} is higher than all ZT values achieved for $Sr_{1-x}Ba_xNb_2O_6$ TTBs [15], [16], [26]–[28] and within error with most doped $SrTiO_3$ compositions [29]–[31].

In comparing the thermal behaviour of SLTNe (x = 0.50) and SLTNv (x = 0.30) with maximum ZT values (0.18 for x = 0.50; 0.21 for x = 0.30), as shown in Figure 7.14, x = 0.30 (SLTNv) exhibited the highest ZT values in all the measured temperature range. This result confirms that cation defect (which is absent in SLTNe sample) as previously discussed contributed to the reduction in k and optimised ZT obtained in x = 0.30 (SLTNv). Both x = 0.50 (SLTNe) and x = 0.30 (SLTNv) recorded the same PF (365 $\mu W/K^2.m$) at 973 K, suggesting that the cumulative effect of secondary phase inclusions, Sm-doping and oxygen vacancy on their electronic transport properties is similar. However, they differed in k by 0.29 W/m. K at the same temperature (x = 0.50, 2.02 W/m. K; x = 0.30, 1.73 W/m. K at 973 K), indicating that V_{sr} as an additional scattering centre created in SLTNv samples influenced the k.

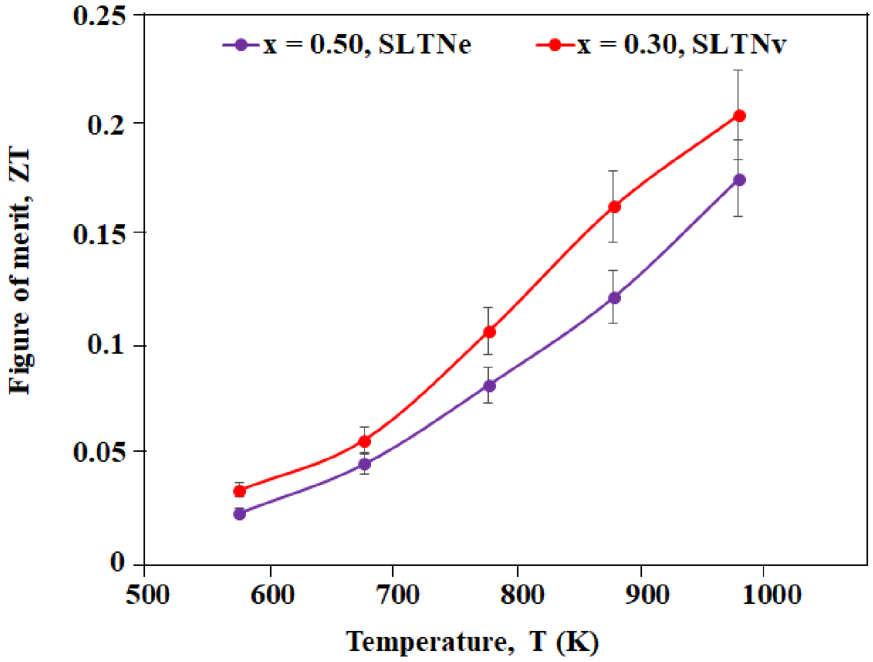

Figure 7.14. Temperature dependence of figure of merit for (a) SLTNe (x =0.50) (b) SLTNv (x = 0.30) samples sintered 6 for hours in 5% H_2/N_2 at 1673 K.

7.3 Nb-Doped $La_2Ti_2O_7$ Ceramics: Results and Discussion

7.3.1 Phase Assemblage and Microstructure

The room temperature XRD patterns of the crushed air and 5%H_2/N_2 sintered $La_2Ti_{2-x}Nb_xO_7$ (LTO) ceramics are shown in Figure 7.15. The phase assemblage was analysed using ICCD Sleve+ PDF-4+ software. The patterns are indexed to a $La_2Ti_2O_7$ monoclinic structure ceramic (space group, $P2_1$) with the lattice constant a = 7.80896(10) Å, b = 5.54608(7) Å, and c = 13.01425(22) Å [32], consistent with those reported in the literature [4], [33]. No secondary phases were detected in any of the compositions within the detection limit of the diffractometer, and the peaks were sharp, suggesting a large particle size according to the Scherrer formula [4].

The bulk and relative density of all compositions for different Nb concentrations are plotted in Figure 7.16. The relative density of all compositions varied progressively from 84 % to 93 %. This implies the bulk density increased with increase in Nb concentration with x = 0.25 showing the maximum sintering density of 5.38 g/cm^3 (93 % of theoretical density, 5.789 g/cm^3) [32]. The SEM images of the 5%H_2/N_2 sintered, thermally etched and carbon coated surfaces for $La_2Ti_{2-x}Nb_xO_7$; $0.00 \leq x \leq 0.25$ ceramics are shown in Figure 7.17. The SEM images revealed homogenous and porous structures consistent with their low relative density of ≤ 93 % and average grain size of ≤ 2 μm. The effect of porosity on the thermoelectric performance of these compositions is unclear. However, some authors have suggested the presence of porosity in the lattice creates discontinuities which act as scattering centres thereby restricting carrier mobility and enhancing phonon scattering [30], [34], [35]. As a result, both σ and k are reduced.

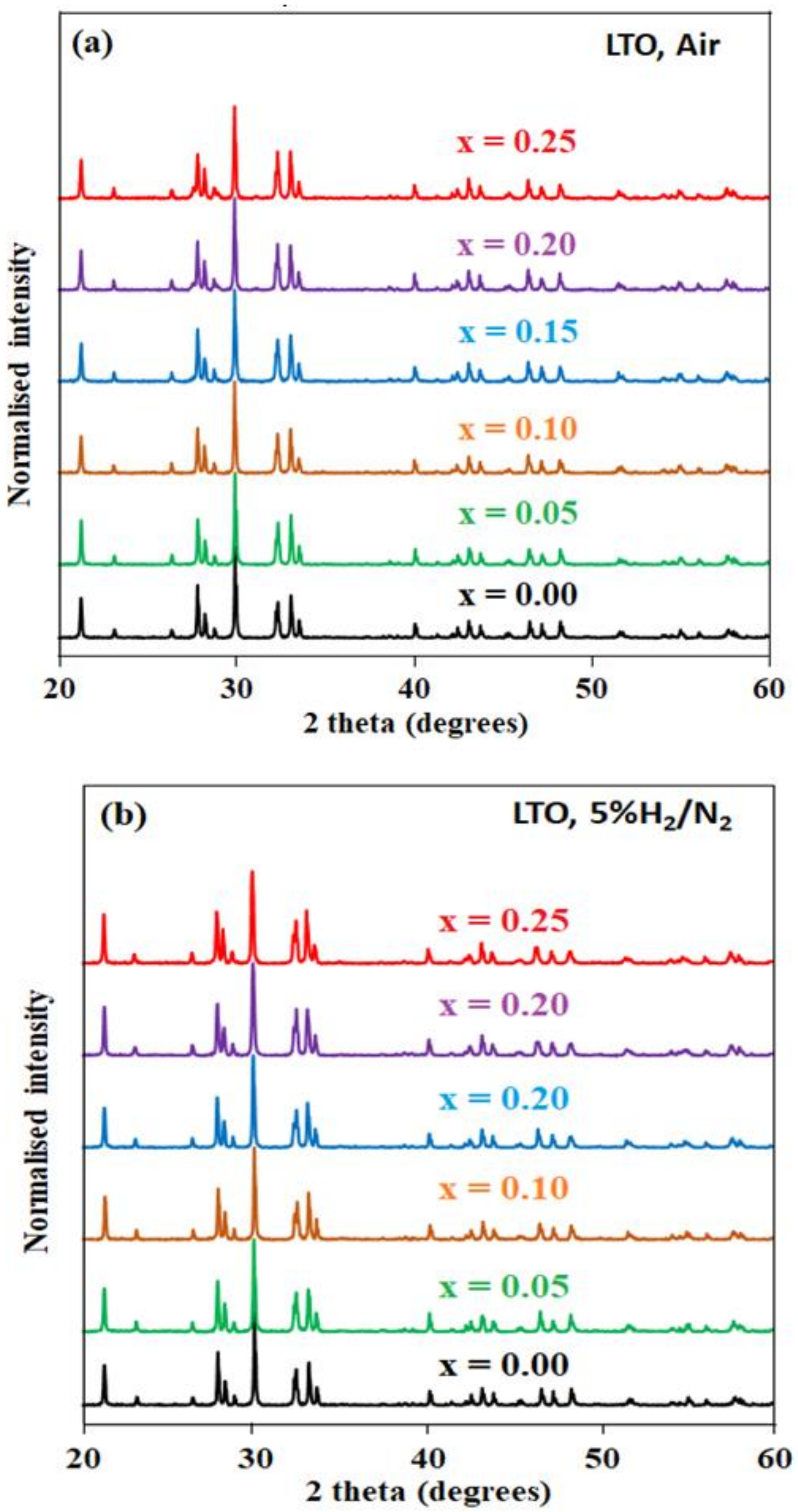

Figure 7.15. Room temperature XRD patterns of crushed ceramics; $La_2Ti_{2-x}Nb_xO_7$ (LTO), $0.00 \leq x \leq 0.25$ sintered 6 hours in (a) air (b) 5% H_2N_2 at 1773K.

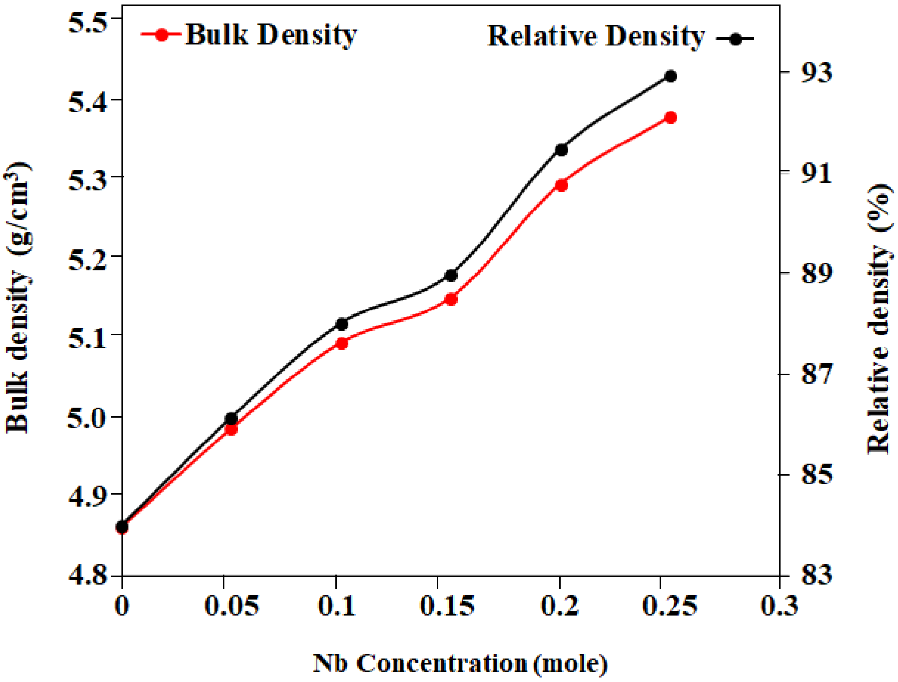

Figure 7.16. The Archimedes measured density of $La_2Ti_{2-x}Nb_xO_7$; $0.00 \leq x \leq 0.25$ ceramics sintered in 5% H_2/N_2 at 1773 K for 6 hours. The uncertainty in density measurement is ± 0.05 %.

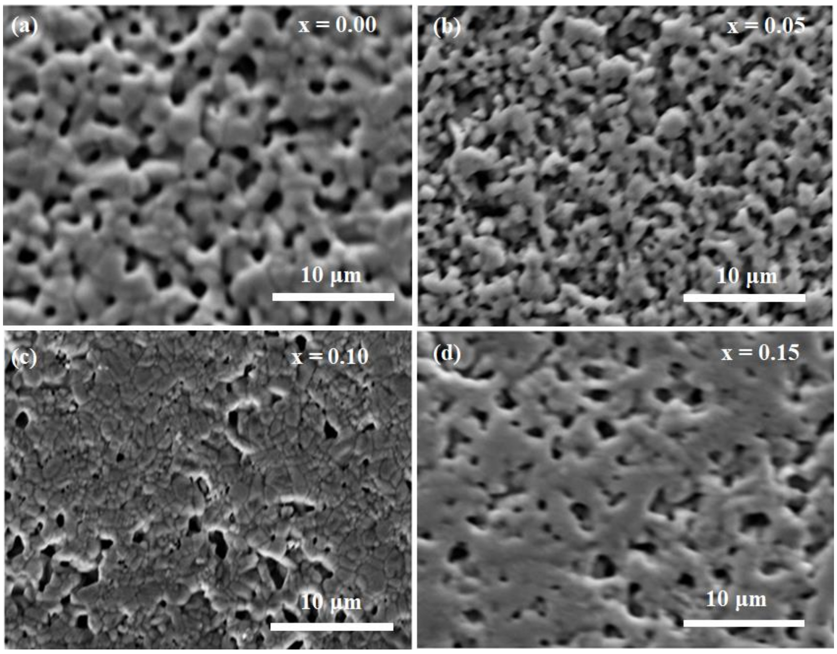

Figure 7.17. SEM micrographs of the surfaces of $La_2Ti_{2-x}Nb_xO_7$ (SLTNe); $0.00 \leq x \leq 0.25$ ceramics sintered 6 hours in 5% H_2/N_2 at 1773 K and thermally etched at 1623 K for 30 minutes.

7.3.2 Thermoelectric Properties

Figures 7.18 to 7.22 show the temperature dependence of the electrical conductivity (σ), absolute Seebeck coefficient (|S|, power factor (PF), total thermal conductivity (k), electronic thermal conductivity (k_E) and dimensionless figure of merit (ZT), respectively for $La_2Ti_{2-x}Nb_xO_7$ ceramic compositions sintered in 5% H_2/N_2 gas mixture at 1773 K for 6 hours. As shown in Figure 7.18, x = 0.00 (undoped $La_2Ti_2O_7$) exhibited the lowest σ in all the measured temperature range, consistent with its lowest density (Figure 7.16). The low σ obtained in x = 0.00 showed that carrier mobility was restricted probably by the inherent heavy pores in the grains. The electrical conductivity increased with Nb doping but inconsistent with dopant (Nb) concentration. x = 0.10 showed the highest σ in all the measured temperature range, reaching a maximum of ~ 2.0 S/cm (200 S/m) at 873 K. This increase in electrical conductivity is attributed to the increase in carrier (electron) concentration due to the substitution of Nb^{5+} for Ti^{4+} which produces electrons. Moreover, V_O introduced by processing in reducing atmosphere increases the carrier concentration, thereby increasing σ [36], [37]. Some authors have also suggested the effect of grain size as a contributory factor to the enhanced σ. Doping has generally been observed to increase grain size, resulting in a reduced grain boundary area and scattering which may enhance the conduction [36]–[38].

σ of all the compositions increased with temperature within 573-873 K, and declined at 973 K. As discussed previously, the compositions at 573-873 K showed semiconducting behaviour and switched to a typical metallic behaviour at high temperature (973 K). The highest σ (200 S/m) at 873 K for $La_2Ti_{1.9}Nb_{0.1}O_7$ obtained in this work is higher than the maximum σ (0.5 S/m) reported in the literature for $La_{1.6}Sr_{0.4}Ti_2O_{6.8\pm\delta}$ ceramic at 573 K [4].

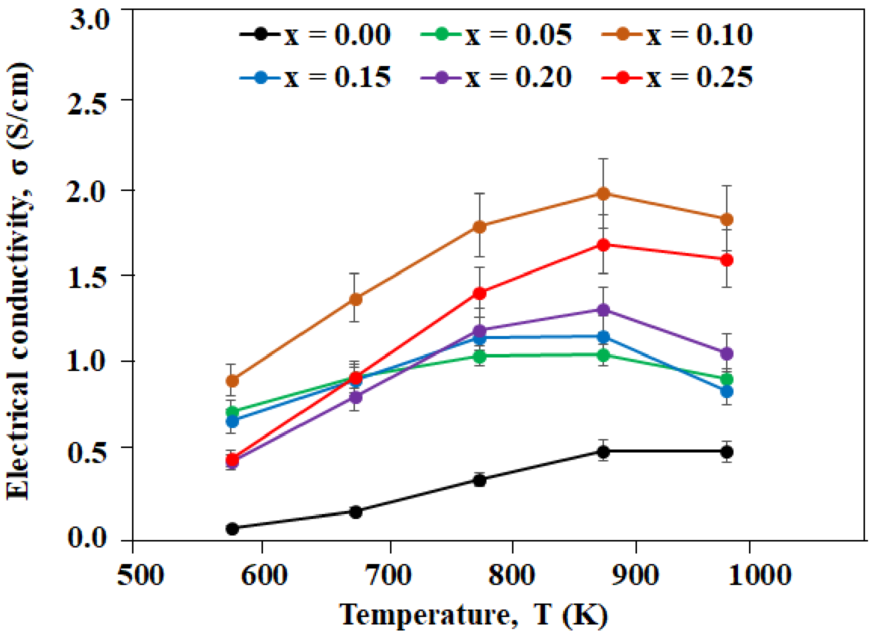

Figure 7.18. Temperature dependence of electrical conductivity for pure and Nb-doped $La_2Ti_2O_7$ ceramics sintered 6 hours in 5% H_2/N_2 at 1773 K.

Figure 7.19 shows the │S│ of $La_2Ti_{2-x}Nb_xO_7$ sample as a function of temperature. S of all ceramics are negative, indicating that electrons are the dominant carriers [37], [39]–[41]. S increased monotonically with increasing temperature in all the measured temperature range. However, the behaviour of S of the sample is inconsistent with Ioffe theory [42] (except x = 0.00 at 973 K), the relationship between S and carrier concentration is given by the following equation [39]:

$$S = \gamma + \ln\frac{1}{n} \qquad 7.1$$

where ϒ and n are the scattering factor and the carrier concentration, respectively. S is inversely proportional to the carrier concentration. This implies that x = 0.00 with the lowest σ (lowest carrier concentration) is expected to show the highest S in all temperatures while x = 0.10 should likewise exhibit the lowest S as a result its high σ in obedience with Ioffe's theory. At the maximum measured temperature (973 K), x = 0.00 as expected exhibited the highest absolute Seebeck coefficient value of ~ 389 µV/K. This value is larger than the Sm-doped $Sr_5LaTi_3Nb_7O_{30}$ values obtained in this work, and in most $SrTiO_3$ samples in the literature [10], [13], [29], [39], [43], [44], but very close to the value of undoped $SrTiO_3$ (393 µV/K at 973 K) reported in this study (Chapter 5).

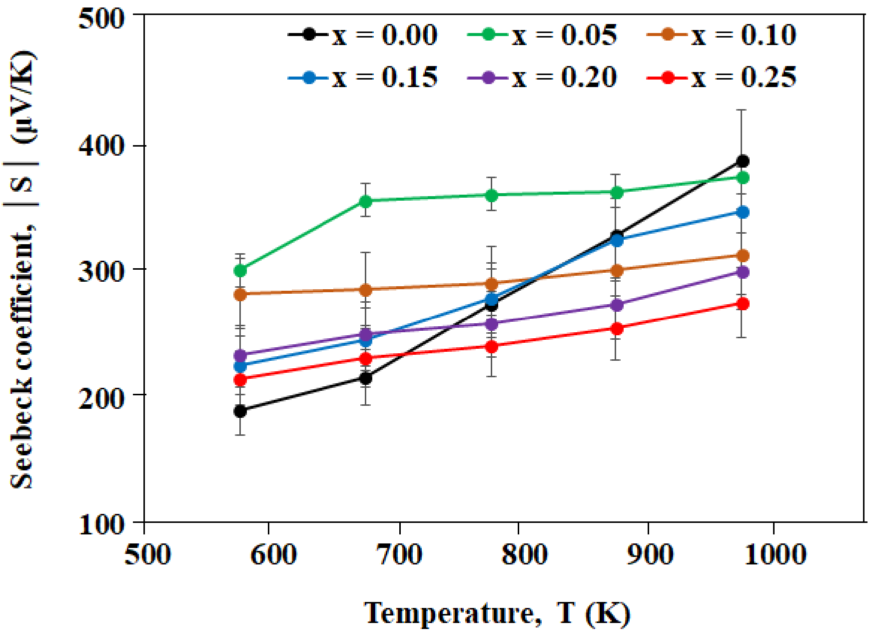

Figure 7.19. Temperature dependence of Seebeck coefficient for pure and Nb-doped $La_2Ti_2O_7$ ceramics sintered 6 hours in 5% H_2/N_2 at 1773 K.

Combining the electrical conductivity and the Seebeck coefficient, the PF of $La_2Ti_{2-x}Nb_xO_7$ sample was determined and shown in Figure 7.20 as a function of temperature. Despite the high Seebeck coefficients (190 - 389 µV/K) exhibited by all the compositions, the PF remained very low (< 20 $\mu W/K^2.m$), due to the low σ (≤ 2.0 S/cm). However, the results obtained showed that the power factors of the Nb-doped compositions ($0.05 \leq x \leq 0.25$) where higher than that of undoped composition (x = 0.00) in all the measured temperature range, due to the enhanced electrical conductivity. x = 0.10 showed a higher PF value especially at high temperatures (773-973 K) than other compositions and recorded the maximum PF value of ~ 18 μW/K^2.m at 973 K.

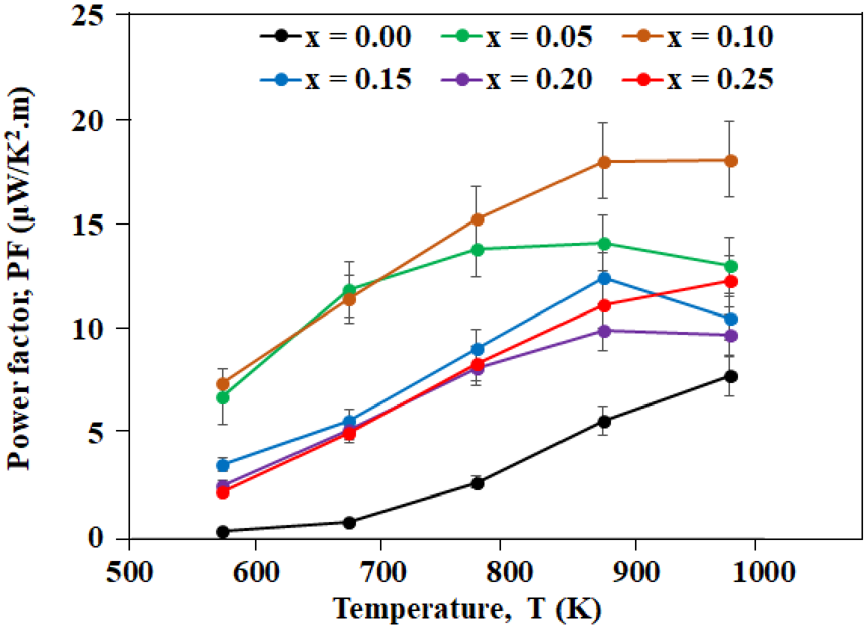

Figure 7.20. Temperature dependence of power factor for pure and Nb-doped $La_2Ti_2O_7$ ceramics sintered 6 hours in 5% H_2/N_2 at 1773 K.

The temperature dependence of the total thermal conductivity, k and the electronic thermal conductivity, k_E of pure and Nb-doped $La_2Ti_2O_7$ ceramics are shown in Figures 7.21. The thermal transport behaviour particularly k of the Nb-doped ceramics is irregular with temperature. This behaviour could be related to the complex interplay of phonon scattering including U and N-processes on the ceramic material. Importantly, the effect of grain size as discussed previously which was presumed to contribute to the enhancement of conduction process affect phonon scattering. Since cation doping of a material increases the grain size thereby promoting carrier (electron) mobility, it could be assumed that phonon propagation as well occurs. As a result, the Nb-doped $La_2Ti_2O_7$ ceramics exhibited a metallic conduction behaviour, which is evidenced in the increased σ and k, respectively.

On the other hand, undoped $La_2Ti_2O_7$ showed the lowest k across the measured temperature range, with a minimum = 1.18 W/m. K at 773-873 K. The reduced relative density observed in $La_2Ti_2O_7$ ceramics indicates an increase in porosity in the microstructure, which significantly affected thermal conductivity. The relation between the k and volume of pores is given in the following equation [45]:

$$k = k_O\left(1 - P^{\frac{2}{3}}\right) \qquad 7.2$$

where k_O is the thermal conductivity of the material without porosity and P is the fraction of pores in the material. The implication of equation 7.2 therefore, is that increase porosity leads to an increase in phonon scattering, resulting in reduction of k. The minimal k value (1.18 W/m.K) obtained in an undoped $La_2Ti_2O_7$ is lower than the value (1.3 W/m.K at 573 K) obtained in the literature for pure $La_2Ti_2O_7$ [4] and comparable to related polycrystalline PLS compounds such as $Bi_4Ti_3O_{12}$ (k ~ 1W/m.K) [4], [46] and $Sr_2Nb_2O_7$ (k = 1.5 W/m.K) [4], [47]. For the Nb-doped $La_2Ti_2O_7$ compositions reported in this work, x = 0.10 showed the highest k value (2.26 W/m. K) at 973 K, while x = 0.05 exhibited the lowest k value of 1. 49 W/m. K at 773 K, attributed to its large unit cell, large atomic mass, crystal anisotropy and complex crystal structure [46], [47].

The electronic thermal conductivity of all LTO compositions showed similar temperature dependence with σ and increased with increase in temperature as presented in Figure 7.21(b). From the small k_E values (≤ 0.0044 W/m. K), it is obvious to state that electronic thermal conductivity makes a very small contribution to the total thermal conductivity. This means that k comes mainly from their lattice thermal conductivity [4], [21].

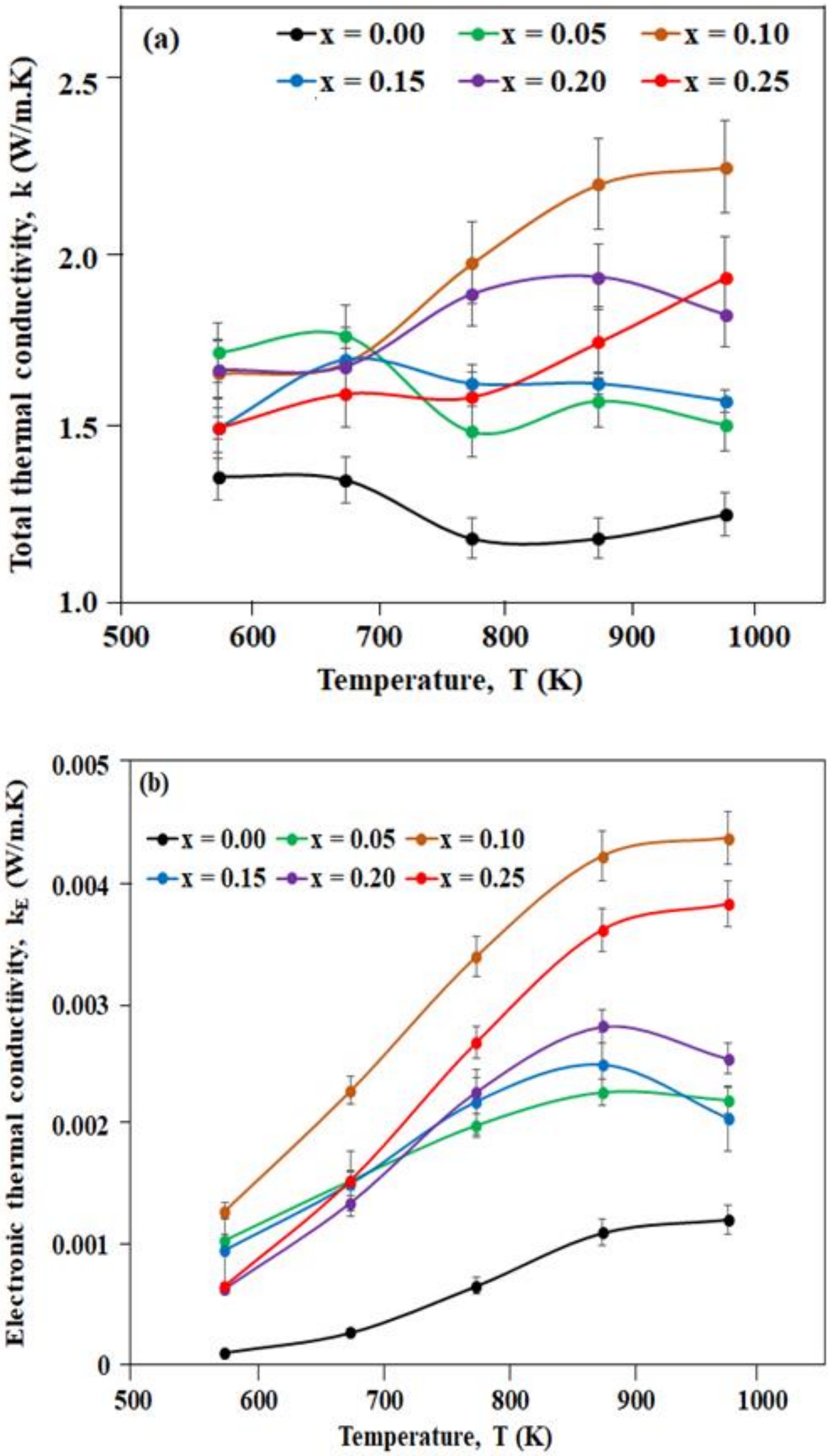

Figure 7.21. Temperature dependence of (a) total thermal conductivity (b) electronic thermal conductivity for pure and Nb-doped $La_2Ti_2O_7$ ceramics sintered 6 hours in 5% H_2/N_2 at 1773 K.

Figure 7.22 shows the temperature dependence of figure of merit (ZT) values for pure and Nb-doped $La_2Ti_2O_7$ ceramics sintered in 5% H_2/N_2 gas mixture at 1773 K for 6 hours. From 573 K up to 873 K (573-873 K), x = 0.00 (pure $La_2Ti_2O_7$) had the lowest ZT values (≤ 0.0045) because of the low electrical conductivity. The combination of a higher σ and S resulted in a relatively high ZT in Nb-doped $La_2Ti_2O_7$ ceramics compared to undoped $La_2Ti_2O_7$. This suggests that the ZT of $La_2Ti_2O_7$ could be increased by a careful tuning with an appropriate dopant such as Nb. As observed from Figure 7.22, the ZT of all the compositions except x = 0.15 increased with increasing temperature within the measured temperature range.

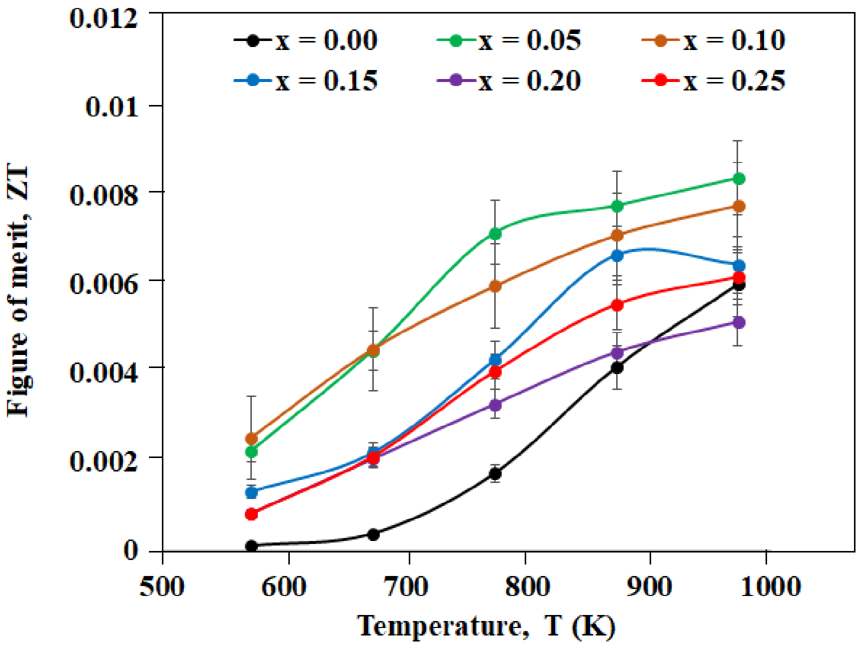

Figure 7.22. Temperature dependence of figure of merit for pure and Nb-doped $La_2Ti_2O_7$ ceramics sintered 6 hours in 5% H_2/N_2 at 1773 K.

The ZT of $La_2Ti_{1.85}Nb_{0.15}O_7$ (x = 0.15) ceramic increased with temperature up to 873 K and decreased at 973 K. Furthermore, in all compositions, x = 0.05 and 0.10 showed a high ZT values at low temperatures (573-673 K), and beyond 673 K, x = 0.05 exhibited the highest values with a maximum ZT of 0.0084 at 973 K. The highest ZT displayed by 5 mol% Nb-doped $La_2Ti_2O_7$ is traceable to the lowest k value recorded at high temperatures (773-973 K) compared to other Nb-doped

$La_2Ti_2O_7$ compositions. x = 0.10 LTO ceramic recorded the highest σ values (Figure 7.18) within the measured temperature and also showed the highest PF at high temperatures (773-973 K), Figure 7.20. With these results, one would have expected x = 0.10 to display the maximum ZT, but its metallic behaviour resulted to increase in k (1.98-2.26 W/m. K) between 773 and 973 K, leading to a drop in ZT. However, the optimised S and low k obtained in Nb-doped $La_2Ti_2O_7$ ceramics are clear indication that $La_2Ti_2O_7$ is a potential oxide thermoelectric material.

7.4 Conclusion

The complex structure and intrinsic low thermal conductivity possessed by $Sr_5LaTi_3Nb_7O_{30}$ TTB and $La_2Ti_2O_7$ PLS oxide ceramics were explored in this study to achieve optimised thermoelectric properties. The combination of cation doping and sintering in reducing atmosphere (5% H_2/N_2) significantly improved the thermoelectric performance. Sm-doping of $Sr_5LaTi_3Nb_7O_{30}$ increased the carrier concentration, which resulted in optimised electrical transport properties (σ, S and PF) obtained. The thermal conductivity of Sm- doped $Sr_5LaTi_3Nb_7O_{30}$ ceramics was reduced through a modulated complex microstructure resulting from Sm-doping, vacancy defects (V_{sr} and V_O) and secondary phase inclusions ($SrTiO_3$ and Nb_2O_5) in the lattice. Overall, a record high ZT value of 0.21 at 973 K was achieved in $Sr_{4.55}LaSm_{0.30}Ti_3Nb_7O_{30}$. However, this high ZT (0.21) obtained for $Sr_5LaTi_3Nb_7O_{30}$ ceramics are still low compared to state-of-art thermoelectric, n-type oxides such as doped $SrTiO_3$ and ZnO, as reported in the literature.

Interestingly, the maximum ZT of 0.21 obtained in this study is higher than most ZT values reported in the literature for La-doped $SrTiO_3$ ceramics [37], [39], [41], [48] and cation doped $CaMnO_3$ n-type ceramics at high temperatures (≥ 900 K) [49]–[52]. For example, in the La- $SrTiO_3$ and Nb-doped $CaMnO_3$ ceramics studied by Shang *et al* [39] and Xu *et al* [49], respectively, a maximum ZT of 0.08 at 679 and 1000 K is obtained. In addition, the ZT = 0.21 at 973 K recorded is comparable to the ZT of Dy-doped n-type $SrTiO_3$ (ZT = 0.22 at 963 K) [41], [48] and Nb-doped $CaMnO_3$ ceramics (ZT = 0.23 at 973 K) [53].

Similarly, improved thermoelectric properties particularly optimised S and reduced k were achieved in $La_2T_2O_7$ ceramics by B-site doping with a heterovalent Nb^{5+} cation. Although the maximum ZT (0.0084) obtained in this study for x = 0.05 LTO at 973 K is very low, optimised S (389 µV/K at 773 K) and minimised k (1.18 W/m. K at 773-873 K) were recorded in undoped $La_2Ti_2O_7$. By doping with Nb^{5+} cation, the carrier concentration was increased, leading to enhanced electrical transport properties and improved ZT. S recorded in all the compositions especially at high temperatures is higher that most of the values achieved in the current oxide state-of- art materials such as BiCuSeO [54]–[58] and $SrTiO_3$ [59]–[61].

In conclusion, TTB, PLS and other structurally related oxides are relatively new classes of thermoelectric oxides, but the results obtained in this project clearly show promising properties. For example, decrease in grain size, presence of secondary phases and pores can contribute to a decrease in k, leading to improved ZT. Therefore, effective control of the microstructure and relative density can promote the efficiency of TE materials and devices. From the developmental history of thermoelectrics, the research on oxides is relatively young [62], and there is no doubt that progress is evident in the near future. In the words of Vining [63] as reported by Kieslich *et al*[1], thermoelectric research is not expected to proffer solution to all the world energy problems but only anticipated to make a more committed contributions than in the past.

References

[1] Gregor Kieslich, Giacomo Cerretti, Igor Veremchuk, Raphaȅl P. Hermann, Martin Panthöfer, Juri Grin, and Wolfgang Tremel, “A chemists view: Metal oxides with adaptive structures for thermoelectric applications,” *Phys. Status Solidi Appl. Mater. Sci.*, vol. 213, no. 3, pp. 808–823, 2016.

[2] Frank Krumeich, “Order and Disorder in Niobium Tungsten Oxides of the Tetragonal Tungsten Bronze Type,” *Acta Crystallogr. Sect. B Struct. Sci.*, vol. 54, no. 3, pp. 240–249, 1998.

[3] Christophe P. Heinrich, Matthias Schrade, Giacomo Cerretti, Ingo Lieberwirth, Patrick Leidich, Andreas Schmitz, Harald Fjeld, Eckhard Mueller, Terje G. Finstad, Truls Norby, and Wolfgang Tremel, "Tetragonal tungsten bronzes $Nb_{8-x}W_{9+x}O_{47-\delta}$: optimization strategies and transport properties of a new n-type thermoelectric oxide," *Materials Horizons*, vol. 2, no. 5, pp. 519–527, 2015.

[4] Jibran Khaliq, Li Chunchun, Chen Kan, Shi Baogui, Ye Haitao, Antonio M. Grande, Haixue Yan, and Michael J. Reece, "Reduced thermal conductivity by nanoscale intergrowths in perovskite like layered structure $La_2Ti_2O_7$," *J. Appl. Phys.*, vol. 117, no. 7, pp. 2–8, 2015.

[5] Xiao Li Zhu, Kun Li, Muhammad Asif Rafiq, Xiao Qiang Liu, and Xiang Ming Chen, "Relaxor nature in lead-free $Sr_5LaTi_3Nb_7O_{30}$ tetragonal tungsten bronze ceramics," *J. Appl. Phys.*, vol. 114, no. 12, 2013.

[6] H Zhang, L Fang, T H Huang, H X Liu, R Z Yuan, and R Dronskowski, "Structural and dielectric properties of ferroelectric $Sr_4R_2Ti_4Nb_6O_{30}$ (R = Sm and Nd) ceramics," *Journal of Materials Science*, vol. 40, pp. 529–531, 2005.

[7] Bao Li Deng, Xiao Li Zhu, Xiao Qiang Liu, and Xiang Ming Chen, "Effects of oxygen-deficiency on crystal structure, dielectric and ferroelectric properties in $Sr_5SmTi_{3+2x}Nb_{7-2x}O_{30-x}$ with tungsten bronze structure," *RSC Adv.*, vol. 7, no. 44, pp. 27370–27376, 2017.

[8] Yi Li, Jian Liu, Chun-Lei Wang, Wen-Bin Su, Yuan-Hu Zhu, Ji-Chao Li, and Liang-Mo Mei, "Thermoelectric properties of $Sr_{0.61}Ba_{0.39}Nb_2O_{6-\delta}$ ceramics in different oxygen-reduction conditions," *Chinese Phys. B*, vol. 24, no. 4, p. 047201, 2015.

[9] Yi Li, Jian Liu, Zhen Wang, Yu Cheng Zhou, Chunlei Wang, Jichao Li, Yuanhu Zhu, Maokui Li, and Liangmo Mei, "Effects of fluorine doping on thermoelectric properties of $Sr_{0.61}Ba_{0.39}Nb_2O_6$ ceramics," *Phys. Scr.*, vol. 90, no. 2, 2015.

[10] Hong Chao Wang, Chun Lei Wang, Wen Bin Su, Jian Liu, Yi Sun, Hua Peng, and Liang Mo Mei, "Doping effect of La and Dy on the thermoelectric properties of $SrTiO_3$," *J. Am. Ceram. Soc.*, vol. 94, no. 3, pp. 838–842, 2011.

[11] Hiroaki Muta, Ken Kurosaki, and Shinsuke Yamanaka, "Thermoelectric properties of reduced and La-doped single-crystalline $SrTiO_3$," *J. Alloys Compd.*, vol. 392, no. 1–2, pp. 306–309, 2005.

[12] G J Snyder and E S Toberer, "Complex thermoelectric materials," *Nat Mater*, vol. 7, no. 2, pp. 105–114, 2008.

[13] Jun Wang, Bo Yu Zhang, Hui Jun Kang, Yan Li, Xinba Yaer, Jing Feng Li, Qing Tan, Shuai Zhang, Guo Hua Fan, Cheng Yan Liu, Lei Miao, Ding Nan, Tong Min Wang, and Li Dong Zhao, "Record high thermoelectric performance in bulk $SrTiO_3$ via nano-scale modulation doping," *Nano Energy*, vol. 35, no. April, pp. 387–395, 2017.

[14] G. Cerretti, M. Schrade, X. Song, B. Balke, H. Lu, T. Weidner, I. Lieberwirth, M. Panthöfer, T. Norby, and W. Tremel, "Thermal stability and enhanced thermoelectric properties of the tetragonal tungsten bronzes $Nb_{8-x}W_{9+x}O_{47}$ ($0 < x < 5$)," *J. Mater. Chem. A*, vol. 5, no. 20, pp. 9768–9774, 2017.

[15] Christopher S. Dandeneau, "Defect Chemistry and Thermoelectric Behavior of n-type $(Sr_xBa_{1-x})Nb_2O_6$," PhD Thesis, University of Washington, 2015.

[16] Yi Li, Jian Liu, Chun Lei Wang, Wen Bin Su, Yuan Hu Zhu, Ji Chao Li, and Liang Mo Mei, "Effects of Oxygen-Reduction on Thermoelectric Properties of $Sr_{0.61}Ba_{0.39}Nb_2O_6$ Ceramics," *Mater. Sci. Forum*, vol. 787, no. December, pp. 210–214, 2014.

[17] Zhilun Lu, Derek C. Sinclair, Ian M. Reaney, and X. Tan, "The Influence of La Doping and Heterogeneity on the Thermoelectric Properties of $Sr_3Ti_2O_7$ Ceramics," *J. Am. Ceram. Soc.*, vol. 99, no. 2, pp. 515–522, 2016.

[18] David Spiteri, "Understanding phonon scattering and predicting thermal conductivity from molecular dynamics simulation," PhD Thesis, University of Bristol, 2015.

[19] G. H. Zheng, Z. X. Dai, Y. Q. Dong, F. L. Zan, D. Zou, Y. Q. Ma, and G. Li, "Low thermal conductivity for $Sr_{1-x}La_xTiO_3$," *Mater. Res. Innov.*, vol. 16, no. 6, pp. 438–441, 2012.

[20] Jiao Han, Qiu Sun, Wenxu Li, and Ying Song, "Microstructure and thermoelectric properties of $La_{0.1}Dy_{0.1}Sr_xTiO_3$ ceramics," *Ceram. Int.*, vol. 43, no. 7, pp. 5557–5563, 2017.

[21] Shingo Ohta, Takashi Nomura, Hiromichi Ohta, and Kunihito Koumoto, "High-temperature carrier transport and thermoelectric properties of heavily La- or Nb- doped single crystals," *J. Appl. Phys.*, vol. 97, no. 3, pp. 0341061–0341064, 2005.

[22] Wen Li, Siqi Lin, Xinyue Zhang, Zhiwei Chen, Xiangfan Xu, and Yanzhong Pei, "Thermoelectric Properties of Cu_2SnSe_4 with Intrinsic Vacancy," *Chem. Mater.*, vol. 28, no. 17, pp. 6227–6232, 2016.

[23] Kanishka Biswas, Jiaqing He, Ivan D. Blum, Chun I. Wu, Timothy P. Hogan, David N. Seidman, Vinayak P. Dravid, and Mercouri G. Kanatzidis, "High-performance bulk thermoelectrics with all-scale hierarchical architectures," *Nature*, vol. 489, no. 7416, pp. 414–418, 2012.

[24] Bo Qiu, Hua Bao, Gengqiang Zhang, Yue Wu, and Xiulin Ruan, "Molecular dynamics simulations of lattice thermal conductivity and spectral phonon mean free path of PbTe: Bulk and nanostructures," *Comput. Mater. Sci.*, vol. 53, no. 1, pp. 278–285, 2012.

[25] Yifeng Wang, Kyoichi Fujinami, Ruizhi Zhang, Chunlei Wan, Ning Wang, Yaoshuai Ba, and Kunihito Koumoto, "Interfacial thermal resistance and thermal conductivity in nanograined $SrTiO_3$," *Appl. Phys. Express*, vol. 3, no.

3, pp. 1–3, 2010.

[26] Yi Li, Jian Liu, Chun-Lei Wang, Wen-Bin Su, Yuan-Hu Zhu, Ji-Chao Li, and Liang-Mo Mei, “Thermoelectric properties of $Sr_{0.61}Ba_{0.39}Nb_2O_{6-\delta}$ ceramics in different oxygen-reduction conditions,” *Chinese Phys. B*, vol. 24, no. 4, p. 047201, 2015.

[27] Yi Li, Jian Liu, Yaqi Hou, Yacui Zhang, Yucheng Zhou, Wenbin Su, Yuanhu Zhu, Jichao Li, and Chunlei Wang, “Thermal conductivity and thermoelectric performance of $Sr_xBa_{1-x}Nb_2O_6$ ceramics at high temperatures,” *Scr. Mater.*, vol. 109, pp. 80–83, 2015.

[28] Soonil Lee, Jonathan A. Bock, Susan Trolier-McKinstry, and Clive A. Randall, “Ferroelectric-thermoelectricity and Mott transition of ferroelectric oxides with high electronic conductivity,” *J. Eur. Ceram. Soc.*, vol. 32, no. 16, pp. 3971–3988, 2012.

[29] H C Wang, C L Wang, W B Su, J Liu, Y Zhao, H Peng, J L Zhang, M L Zhao, J C Li, N Yin, and L M Mei, “Enhancement of thermoelectric figure of merit by doping Dy in $La_{0.1}Sr_{0.9}TiO_3$ ceramic,” *Mater. Res. Bull.*, vol. 45, no. 7, pp. 809–812, 2010.

[30] Adindu C. Iyasara, Whitney L. Schmidt, Rebecca Boston, Derek C. Sinclair, and Ian M. Reaney, “La and Sm Co-doped $SrTiO_{3-\delta}$ Thermoelectric Ceramics,” *Mater. Today Proc.*, vol. 4, no. 12, pp. 12360–12367, 2017.

[31] Deepanshu Srivastava, Colin Norman, Feridoon Azough, Marion C. Schäfer, Emmanuel Guilmeau, and Robert Freer, “Improving the thermoelectric properties of $SrTiO_3$-based ceramics with metallic inclusions,” *J. Alloys Compd.*, vol. 731, no. January, pp. 723–730, 2018.

[32] Elizabeth J. Harvey, Sharon E. Ashbrook, Gregory R. Lumpkin, and Simon A. T. Redfern, “Characterisation of the $(Y_{1-x}La_x)_2Ti_2O_7$ system by powder diffraction and nuclear magnetic resonance methods,” *J. Mater. Chem.*, vol. 16, no. 48, pp. 4665–4674, 2006.

[33] N. Zhang, Q. J. Li, S. G. Huang, Y. Yu, J. Zheng, C. Cheng, and C. C. Wang, “Dielectric relaxations in multiferroic $La_2Ti_2O_7$ ceramics,” *J. Alloys Compd.*, vol. 652, pp. 1–8, 2015.

[34] Chang Sun Park, Min Hee Hong, Hyung Hee Cho, and Hyung Ho Park, “Effect of mesoporous structure on the Seebeck coefficient and electrical properties of $SrTi_{0.8}Nb_{0.2}O_3$,” *Appl. Surf. Sci.*, vol. 409, pp. 17–21, 2017.

[35] Min Hee Hong, Chang Sun Park, Sangwoo Shin, Hyung Hee Cho, Won Seon Seo, Young Soo Lim, Jung Kun Lee, and Hyung Ho Park, “Effect of surfactant concentration variation on the thermoelectric properties of mesoporous ZnO,” *J. Nanomater.*, vol. 2013, pp. 1–6, 2013.

[36] Peng Peng Shang, Bo Ping Zhang, Yong Liu, Jing Feng Li, and Hong Min Zhu, “Preparation and thermoelectric properties of la-doped $SrTiO_3$

ceramics," *J. Electron. Mater.*, vol. 40, no. 5, pp. 926–931, 2011.

[37] Iqbal Mahmud, Man-Soon Yoon, Il-Ho Kim, Moon-Kwan Choi, and Soon-Chul Ur, "Thermoelectric properties of the ceramic oxide Sr_{1-x} La_xTiO_3," *J. Korean Phys. Soc.*, vol. 68, no. 1, pp. 35–40, 2016.

[38] B. R. Sudireddy and K. Agersted, "Sintering and Electrical Characterization of La and Nb Co-doped $SrTiO_3$ Electrode Materials for Solid Oxide Cell Applications," *Fuel Cells*, vol. 14, no. 6, pp. 961–965, 2014.

[39] Peng Peng Shang, Bo Ping Zhang, Jing Feng Li, and Ning Ma, "Effect of sintering temperature on thermoelectric properties of La-doped $SrTiO_3$ ceramics prepared by sol-gel process and spark plasma sintering," *Solid State Sci.*, vol. 12, no. 8, pp. 1341–1346, 2010.

[40] R. Venkatasubramanian, E. Siivola, T. Colpitts, and B. O'Quinn, "Thin-film thermoelectric devices with high room-temperature figures of merit," *Nature*, vol. 413, no. 6856, pp. 597–602, 2001.

[41] Jiao Han, Qiu Sun, and Ying Song, "Enhanced thermoelectric properties of La and Dy co-doped, Sr-deficient $SrTiO_3$ceramics," *J. Alloys Compd.*, vol. 705, pp. 22–27, 2017.

[42] A.F. Ioffe, *Semiconductor Thermoelements and Thermoelectric Cooling*. Infosearch Ltd, 1957.

[43] J. Liu, C. L. Wang, Y. Li, W. B. Su, Y. H. Zhu, J. C. Li, and L. M. Mei, "Influence of rare earth doping on thermoelectric properties of $SrTiO_3$ ceramics," *J. Appl. Phys.*, vol. 114, no. 22, 2013.

[44] Hongchao Wang and Chunlei Wang, "Thermoelectric properties of Yb-doped $La_{0.1}Sr_{0.9}TiO_3$ ceramics at high temperature," *Ceram. Int.*, vol. 39, no. 2, pp. 941–946, 2013.

[45] Sung-Hwan Bae, Jun-Young Cho, O-Jong Kwon, Hyun Koo, Chan Park, Sejin Yoon, Jin-Sang Kim, Seunghyun Ahn, and Jae-Yeol Kim, "The Effect of Grain Size and Density on the Thermoelectric Properties of Bi_2Te_3-PbTe Compounds," *J. Electron. Mater.*, vol. 42, no. 12, pp. 3390–3396, 2013.

[46] Yang Shen, David R. Clarke, and Paul A. Fuierer, "Anisotropic thermal conductivity of the Aurivillus phase, bismuth titanate ($Bi_4Ti_3O_{12}$): A natural nanostructured superlattice," *Appl. Phys. Lett.*, vol. 93, no. 10, pp. 10–13, 2008.

[47] Taylor D. Sparks, Paul A. Fuierer, and David R. Clarke, "Anisotropic thermal diffusivity and conductivity of La-doped strontium niobate $Sr_2Nb_2O_7$," *J. Am. Ceram. Soc.*, vol. 93, no. 4, pp. 1136–1141, 2010.

[48] Hiroaki Muta, Ken Kurosaki, and Shinsuke Yamanaka, "Thermoelectric properties of rare earth doped $SrTiO_3$," *J. Alloys Compd.*, vol. 350, no. 1–2, pp. 292–295, 2003.

[49] D. Srivastava, F. Azough, R. Freer, E. Combe, R. Funahashi, D. M. Kepaptsoglou, Q. M. Ramasse, M. Molinari, S. R. Yeandel, J. D. Baran, and S. C. Parker, "Crystal structure and thermoelectric properties of Sr-Mo substituted $CaMnO_3$: A combined experimental and computational study," *J. Mater. Chem. C*, vol. 3, no. 47, pp. 12245–12259, 2015.

[50] Yuan Hu Zhu, Wen Bin Su, Jian Liu, Yu Cheng Zhou, Jichao Li, Xinhua Zhang, Yanling Du, and Chun Lei Wang, "Effects of Dy and Yb co-doping on thermoelectric properties of $CaMnO_3$ ceramics," *Ceram. Int.*, vol. 41, no. 1, pp. 1535–1539, 2015.

[51] Romy Löhnert, Michael Stelter, and Jörg Töpfer, "Evaluation of soft chemistry methods to synthesize Gd-doped $CaMnO_{3-\delta}$ with improved thermoelectric properties," *Mater. Sci. Eng. B Solid-State Mater. Adv. Technol.*, vol. 223, pp. 185–193, 2017.

[52] Hongchao Wang and Chunlei Wang, "Synthesis of Dy doped $Yb_{0.1}Ca_{0.9}MnO_3$ ceramics with a high relative density and their thermoelectric properties," *Mater. Res. Bull.*, vol. 47, no. 9, pp. 2252–2256, 2012.

[53] Yuanhu Zhu, Chunlei Wang, Wenbin Su, Jichao Li, Jian Liu, Yanling Du, and Liangmo Mei, "High-temperature thermoelectric performance of $Ca_{0.96}Dy_{0.02}RE_{0.02}MnO_3$ ceramics (RE=Ho, Er, Tm)," *Ceram. Int.*, vol. 40, no. 10, pp. 15531–15536, 2014.

[54] J. P. Carmo, Joaquim Antunes, M. F. Silva, J. F. Ribeiro, L. M. Goncalves, and J. H. Correia, "Characterization of thermoelectric generators by measuring the load-dependence behavior," *Meas. J. Int. Meas. Confed.*, vol. 44, no. 10, pp. 2194–2199, 2011.

[55] Qiang Li, Zhiwei Lin, and Juan Zhou, "Thermoelectric materials with potential high power factors for electricity generation," *J. Electron. Mater.*, vol. 38, no. 7, pp. 1268–1272, 2009.

[56] S Kumar and U Schwingenschlo, "Lattice thermal conductivity in layered BiCuSeO," *Phys. Chem. Chem. Phys.*, vol. 18, pp. 19158–19164, 2016.

[57] Yong Liu, Li-dong Zhao, Yaochun Liu, Jinle Lan, Wei Xu, Fu Li, Bo-ping Zhang, and David Berardan, "Remarkable Enhancement in Thermoelectric Performance of BiCuSeO," *J. Am. Chem. Soc.*, vol. 133, pp. 20112–20115, 2011.

[58] Fu Li, Jing-Feng Li, Li-Dong Zhao, Kai Xiang, Yong Liu, Bo-Ping Zhang, Yuan-Hua Lin, Ce-Wen Nana, and Hong-Min Zhu, "Polycrystalline BiCuSeO Oxides as a Potential Thermoelectric Material," *Energy Environ. Sci.*, vol. 5, pp. 7188–7195, 2012.

[59] S. Bhattacharya, A. Mehdizadeh Dehkordi, S. Tennakoon, R. Adebisi, J. R. Gladden, T. Darroudi, H. N. Alshareef, and T. M. Tritt, "Role of phonon scattering by elastic strain field in thermoelectric $Sr_{1-x}Y_xTiO_{3-\delta}$," *J. Appl. Phys.*, vol. 115, no. 22, 2014.

[60] Kunihito Koumoto, Yifeng Wang, Ruizhi Zhang, Atsuko Kosuga, and Ryoji Funahashi, “Oxide Thermoelectric Materials: A Nano Structuring Approach,” *Annu. Rev. Mater. Res.*, vol. 40, pp. 363–394, 2010.

[61] Arash Mehdizadeh Dehkordi, Sriparna Bhattacharya, Taghi Darroudi, Jennifer W Gra, Udo Schwingenschlo, Husam N Alshareef, and Terry M Tritt, “Large Thermoelectric Power Factor in Pr-Doped $SrTiO_3$ −,” *Chem. Mater.*, vol. 26, no. 7, p. 2478−2485, 2014.

[62] Michitaka Ohtaki, Kazuhiko Araki, and Kiyoshi Yamamoto, “High thermoelectric performance of dually doped ZnO ceramics,” *J. Electron. Mater.*, vol. 38, no. 7, pp. 1234–1238, 2009.

[63] Cronin B Vining, “An inconvenient truth about thermoelectrics ,” *Nature. Mater.*, vol. 8 , no. 2, pp. 83–85, 2009.

Chapter 8: General Discussion

8.1 Discussion

In light of the limitations associated with non-oxide thermoelectric materials [1], ceramics based on transition metal oxide are considered to be viable alternatives [2]–[4]. However, n-type oxides remain inferior when compared to p-type oxides owing to their low PF and ZT values. With this in mind, $SrTiO_3$, a potential TE n-type oxide together with $Sr_5LaTi_3Nb_7O_{30}$ and $La_2Ti_2O_7$ were investigated. The complex crystal structures, tunable composition/stoichiometry and intrinsic low k inherent in perovskites, TTBs [5]–[7] and PLS [8] ceramics motivated this study.

8.1.1 La-Sm Doped $SrTiO_3$ Ceramics

Electron La-Sm co-doping $SrTiO_3$ (ESTO) followed by sintering 6 hours in 5% H_2/N_2 at 1773 K enhanced ZT (especially the ≤ 0.15 compositions) due to the relatively high PF and low k. x = 0.15 recorded the highest ZT value of 0.24 at 873 K due to a reduced k and a high σ of 942 S/cm at 573 K. At ≥ 0.20, a switch from metallic to semiconducting behaviour was observed, hence σ decreases. x = 0.20 achieved the smallest k (3.0 W/m. K) at 973 K. The minimum k is attributed in part to the presence of porosity and secondary phase in the microstructure which agrees with the reported phase assemblage and microstructure. Some authors have suggested the pores and second phase inclusions restrict carrier mobility and enhance phonon scattering, resulting in a reduction in σ [9], [10] and k [10].

The maximum figure of merit, ZT_{max} (0.24) obtained for x = 0.15 of the ESTO samples is higher than many reported ZT values for electron doped and reduced polycrystalline strontium titanates such as $Sr_{0.9}Dy_{0.1}TiO_3$ (ZT = 0.22 at 573 K) [11]–[13], $Sr_{0.92}La_{0.08}TiO_3$ (ZT = 0.22 at 800 K) and $SrTi_{0.90}Ta_{0.1}TiO_3$ (ZT = 0.17 at 1045 K) [13]; and comparable to Sm-doped $SrTiO_3$ (ZT = 0.24, 1073 K) [11]. In light of the promising results achieved in ESTO samples and building on work by

Lu *et al* [13] and Lu [14], doped $SrTiO_3$ ceramics batched with A-site vacancies (VSTO) were studied in two different calcination conditions; air (VSTO-A) and 5% H_2/N_2 calcined (VSTO-H) followed by sintering in 5% H_2/N_2. The TE properties of VSTO-A ceramics, particularly electrical transport properties, showed significant improvement with respect to ESTO ceramics. The maximum power factor (PF_{max}) achieved in VSTO-A was 873 $\mu W/K^2.m$ at 973 K for x = 0.20, higher than that (865 $\mu W/K^2.m$ at 973 K) achieved for x = 0.10 (ESTO) ceramics. x = 0.30 (VSTO-A) with the minimum k (2.99 W/m. K) exhibited the highest ZT value 0.25 (only 0.01 higher than maximum ZT of ESTO) at 973 K. The further reducing conditions applied in VSTO-H ceramics decreased the thermal conductivity [15] without compromising PF. Smaller grain size combined with V_O resulted in reduced k [16] and optimised ZT. The minimum k (2.67 W/m. K) and maximum ZT (0.30) were recorded in x = 0.20 (VSTO-H) ceramics at 973 K.

The highest ZT (0.30) achieved in 20 mol% of VSTO-H ceramics revealed the impact of processing cation-doped $SrTiO_3$ ceramics using strong reducing conditions. Application of double calcination in 5% H_2/N_2 for vacancy x = 0.20 composition, first at 1573 K and finally at high temperatures (1623 or 1673 K) prior to sintering at 1773 K for 8 hours (increased dwell time) was suggested to be a suitable option to further reduce k and optimise the ZT. 1400H (x = 0.20) composition calcined at 1573 and 1673 k, respectively achieved the smallest k (2.5 W/m. K) and a maximum ZT value of 0.35 at 973 K. As already stated in Chapter six, this maximum ZT (0.35) achieved in this work for $SrTiO_3$ is the highest ZT reported for RE co-doped $SrTiO_3$ at 973 K in the literature [1], [17]–[20].

8.1.2 Sm-Doped $Sr_5LaTi_3Nb_7O_{30}$ Ceramics

Electronic Sm-doped $Sr_5LaTi_3Nb_7O_{30}$ (SLTNe) ceramics sintered in reducing atmosphere (5%H_2/N_2) showed improved TE properties. A maximum PF of 451 $\mu W/K^2.m$ was achieved in x = 0.15 at 973 K, attributed to its high σ. At x = 0.50, a minimum k (~2.0 W/m. K) was observed resulting in the highest ZT (0.18) at 973 K. The low k observed in SLTNe ceramics is attributed in part to the presence of impurities (secondary phases), reduced grain sizes and oxygen defects created in the lattice (Chapter 7) [21]–[23].

In a bid to optimise ZT and following on from the work on perovskite structured ceramics, ionic (vacancy) Sm-doped $Sr_5LaTi_3Nb_7O_{30}$ (SLTNv) ceramics were studied. Phonon scattering from cation vacancies, oxygen defects and secondary phase inclusions ($SrTiO_3$ and Nb_2O_5) observed in the microstructure restricted carrier mobility and phonon propagation [15], hence low σ (σ_{max} = 292 S/cm at 573 for x = 0.20) compared to SLTNe samples and low k was achieved. Overall, a maximum σ (292 S/cm at 573 K for x = 0.20), smallest k (1.6 W/m. K) and a highest ZT value of 0.21 at 973 K for x = 0.30 were recorded. The improved ZT from 0.18 (SLTNe) to a maximum ZT of 0.21(SLTNv) could be attributed to the smallest k (1.6 W/m.K) obtained as a result of the increased concentration of scatter centres (V_{Sr}, V_O and secondary phase inclusions). In addition, the promising PF values probably relate to the presence of doped, reduced $SrTiO_3$ secondary phases following the arguments made by Lu *et al* for RP-structured compositions [14].

8.1.2 Nb-Doped $La_2Ti_2O_7$ Ceramics

Reduced Nb-doped $La_2Ti_2O_7$ (LTO) ceramics were studied. The pure $La_2Ti_2O_7$ exhibited the lowest k, 1.18 W/m. K at 773-873 K and the maximum Seebeck coefficient, S (389 μV/K at 973 K). All doped compositions showed an increase in σ and k, attributed to metallic behaviour due to an increase in carrier concentration and creation of oxygen vacancies [24], [25]. x = 0.10 showed the highest PF (18 μW/K^2.m) at 973 K, resulting from its high σ (σ_{max} = 0.2 S/cm at 873 K) and moderate S. The highest ZT (0.0084) was recorded in x = 0.05 compositions at 973 K partially due to its low k value. Generally, Nb-doped $La_2Ti_2O_7$ ceramics exhibited very low TE properties especially σ, PF and ZT which are not suitable for TE applications. However, the high S (≥ 190 μV/K) and low k (≤ 2.26 W/m. K) recorded are a manifestation of the TE potential of Nb-doped $La_2Ti_2O_7$ ceramics.

References

[1] J. Liu, C. L. Wang, Y. Li, W. B. Su, Y. H. Zhu, J. C. Li, and L. M. Mei, "Influence of Rare Earth Doping on Thermoelectric Properties of $SrTiO_3$ Ceramics," *J. Appl. Phys.*, vol. 114, no. 22, 2013.

[2] Kunihito Koumoto and Ichiro Terasaki, "Complex Oxide Materials for Thermoelectric Applications," *MRS Bull.*, vol. 31, no. March, pp. 206–210, 2006.

[3] Jing Feng Li, Wei Shu Liu, Li Dong Zhao, and Min Zhou, "High-Performance Nanostructured Thermoelectric Materials," *NPG Asia Mater.*, vol. 2, no. 4, pp. 152–158, 2010.

[4] Ti R Ta, R R Sun, X Y Qin, L L Li, D Li, N N Wang, J Zhang, and Q Q Wang, "Transport and Thermoelectric Properties of $Sr_3(Ti_{0.95}R_{0.05})_2O_7$ (R = Ta, Nb, W) Oxides," vol. 3, pp. 0–8, 2012.

[5] Gebru Zerihun, Gaoshang Gong, Shuai Huang, and Songliu Yuan, "Dielectric and Relaxor Ferroelectric Properties of $Sr_4CaLaTi_3Nb_7O_{30}$ Tetragonal Tungsten Bronze Ceramics," *Ceram. Int.*, vol. 41, no. 9, pp. 12426–12431, 2015.

[6] M R Ranga Raju, R N P Choudhary, and H R Rukmini, "Diffuse Phase Transition in $Sr_5RTi_3Nb_7O_{30}$ (R = La, Nd, Sm, Gd and Dy) Ferroelectric Ceramics," *Ferroelectrics*, vol. 325, no. 1, pp. 25–32, 2005.

[7] M R Ranga Raju and R N P Choudhary, "Diffuse Phase Transition in $Sr_5RTi_3Nb_7O_{30}$ (R=La, Nd and Sm)," *J. Phys. Chem. Solids*, vol. 64, no. 5, pp. 847–853, 2003.

[8] Jibran Khaliq, Li Chunchun, Chen Kan, Shi Baogui, Ye Haitao, Antonio M. Grande, Haixue Yan, and Michael J. Reece, “Reduced Thermal Conductivity by Nanoscale Intergrowths in Perovskite Like Layered Structure $La_2Ti_2O_7$,” *J. Appl. Phys.*, vol. 117, no. 7, pp. 2–8, 2015.

[9] Jun Wang, Bo Yu Zhang, Hui Jun Kang, Yan Li, Xinba Yaer, Jing Feng Li, Qing Tan, Shuai Zhang, Guo Hua Fan, Cheng Yan Liu, Lei Miao, Ding Nan, Tong Min Wang, and Li Dong Zhao, “Record High Thermoelectric Performance in Bulk $SrTiO_3$ Via Nano-Scale Modulation Doping,” *Nano Energy*, vol. 35, no. April, pp. 387–395, 2017.

[10] Chang Sun Park, Min Hee Hong, Hyung Hee Cho, and Hyung Ho Park, “Effect of Mesoporous Structure on the Seebeck Coefficient and Electrical Properties of $SrTi_{0.8}Nb_{0.2}O_3$,” *Appl. Surf. Sci.*, vol. 409, pp. 17–21, 2017.

[11] A. V. Kovalevsky, A. A. Yaremchenko, S. Populoh, P. Thiel, D. P. Fagg, A. Weidenkaff, and J. R. Frade, “Towards a High Thermoelectric Performance in Rare-Earth Substituted $SrTiO_3$: Effects Provided by Strongly-Reducing Sintering Conditions,” *Phys. Chem. Chem. Phys.*, vol. 16, no. 48, pp. 26946–26954, 2014.

[12] A. V. Kovalevsky, A. A. Yaremchenko, S. Populoh, A. Weidenkaff, and J. R. Frade, “Effect of A-Site Cation Deficiency on the Thermoelectric Performance of Donor-Substituted Strontium Titanate,” *J. Phys. Chem. C*, vol. 118, no. 9, pp. 4596–4606, 2014.

[13] Zhilun Lu, Huairuo Zhang, Wen Lei, Derek C. Sinclair, and Ian M. Reaney, “High-Figure-of-Merit Thermoelectric La-Doped A-Site-Deficient $SrTiO_3$ Ceramics,” *Chem. Mater.*, vol. 28, no. 3, pp. 925–935, 2016.

[14] Zhilun Lu, “La doped $SrTiO_3$ Based Oxide Thermoelectrics.,” PhD Thesis, University of Sheffield, 2016.

[15] G. H. Zheng, Z. X. Dai, Y. Q. Dong, F. L. Zan, D. Zou, Y. Q. Ma, and G. Li, “Low Thermal Conductivity for $Sr_{1-x}La_xTiO_3$,” *Mater. Res. Innov.*, vol. 16, no. 6, pp. 438–441, 2012.

[16] R. Boston, W. L. Schmidt, G. D. Lewin, A. C. Iyasara, Z. Lu, H. Zhang, D. C. Sinclair, and I. M. Reaney, “Protocols for the Fabrication, Characterization, and Optimization of n-Type Thermoelectric Ceramic Oxides,” *Chem. Mater.*, vol. 29, no. 1, pp. 265–280, 2017.

[17] Hongchao Wang and Chunlei Wang, “Thermoelectric Properties of Yb-Doped $La_{0.1}Sr_{0.9}TiO_3$ Ceramics at High Temperature,” *Ceram. Int.*, vol. 39, no. 2, pp. 941–946, 2013.

[18] Hong Chao Wang, Chun Lei Wang, Wen Bin Su, Jian Liu, Yi Sun, Hua Peng, and Liang Mo Mei, "Doping Effect of La and Dy on the Thermoelectric Properties of $SrTiO_3$," *J. Am. Ceram. Soc.*, vol. 94, no. 3, pp. 838–842, 2011.

[19] H C Wang, C L Wang, W B Su, J Liu, Y Zhao, H Peng, J L Zhang, M L Zhao, J C Li, N Yin, and L M Mei, "Enhancement of Thermoelectric Figure of Merit by Doping Dy in $La_{0.1}Sr_{0.9}TiO_3$ Ceramic," *Mater. Res. Bull.*, vol. 45, no. 7, pp. 809–812, 2010.

[20] Jiao Han, Qiu Sun, and Ying Song, "Enhanced Thermoelectric Properties of La and Dy Co-Doped, Sr-Deficient $SrTiO_3$ Ceramics," *J. Alloys Compd.*, vol. 705, pp. 22–27, 2017.

[21] Kanishka Biswas, Jiaqing He, Ivan D. Blum, Chun I. Wu, Timothy P. Hogan, David N. Seidman, Vinayak P. Dravid, and Mercouri G. Kanatzidis, "High-Performance Bulk Thermoelectrics with All-Scale Hierarchical Architectures," *Nature*, vol. 489, no. 7416, pp. 414–418, 2012.

[22] Bo Qiu, Hua Bao, Gengqiang Zhang, Yue Wu, and Xiulin Ruan, "Molecular Dynamics Simulations of Lattice Thermal Conductivity and Spectral Phonon Mean Free Path of PbTe: Bulk and Nanostructures," *Comput. Mater. Sci.*, vol. 53, no. 1, pp. 278–285, 2012.

[23] Yifeng Wang, Kyoichi Fujinami, Ruizhi Zhang, Chunlei Wan, Ning Wang, Yaoshuai Ba, and Kunihito Koumoto, "Interfacial Thermal Resistance and Thermal Conductivity in Nanograined $SrTiO_3$," *Appl. Phys. Express*, vol. 3, no. 3, pp. 1–3, 2010.

[24] Peng Peng Shang, Bo Ping Zhang, Yong Liu, Jing Feng Li, and Hong Min Zhu, "Preparation and Thermoelectric Properties of La-Doped $SrTiO_3$ Ceramics," *J. Electron. Mater.*, vol. 40, no. 5, pp. 926–931, 2011.

[25] Iqbal Mahmud, Man-Soon Yoon, Il-Ho Kim, Moon-Kwan Choi, and Soon-Chul Ur, "Thermoelectric Properties of the Ceramic Oxide $Sr_{1-x}La_xTiO_3$," *J. Korean Phys. Soc.*, vol. 68, no. 1, pp. 35–40, 2016.

Chapter 9: Conclusions

In this research, conventional solid-state reaction, aliovalent doping mechanisms and reducing conditions were employed to study the thermoelectric performance of La-Sm co-doped $SrTiO_3$, Sm- and Nb-doped $Sr_5LaTi_3Nb_7O_{30}$ and $La_2Ti_2O_7$ n-type ceramics.

Air sintered La-Sm doped $SrTiO_3$ samples appeared white or pale yellow after sintering, indicating insulating behaviour and could not be measured for TE properties. The synthesis method and processing conditions are beneficial for distinguishing electron and A-site vacancy (ionic) compensation mechanisms in La-Sm co-doped $SrTiO_3$ compositions. For the electron doped $SrTiO_3$ compositions (ESTO), the electrical conductivity reached a peak (942 S/cm at 573 K) for $x = 0.15$. At $x \geq 0.20$, a switch from metallic to semiconducting behaviour was observed, which is attributed to the solid solubility limit, structural phase transitions [1]–[3], and/or presence of pores and secondary phases which are consistent with the observed microstructure.

For A-site vacancy La-Sm doped $SrTiO_3$ (VSTO) samples, the solubility limit was higher and improved σ and ZT were obtained compared to electron doped samples. With the improved TE results achieved in VSTO ceramics, it became apparent that processing in strongly reducing conditions could lead to optimized ZT. This is as a result of the effective phonon scattering in the oxygen deficient ceramics formed upon reduction, leading to suppressed k. The ZT value of 0.35 recorded for $Sr_{0.7}La_{0.1}Sm_{0.1}TiO_3$ (1400H) at 973 K remains the highest ZT reported in the literature for RE co-doped $SrTiO_3$.

The crystal structure of a material influences the TE properties. The phase transition from ideal cubic to tetragonal for $RE_{0.1}Sr_{0.9}TiO_3$ ceramics as reported by Kovalevsky *et al* [1] suggests that the enhanced ZT observed is associated with distortion of TiO_6 octahedra, leading to reduction in k and improved conductivity along Ti-O-Ti bonds. The authors maintain that decrease in the radii of the RE cations results in the distorted TiO_6 octahedra.

In contrast, the data generated from La-Sm co-doped $SrTiO_3$ in this work suggests that co-doping postponed to higher values of x the distortion to tetragonal from the ideal cubic structure of $SrTiO_3$ as reported in Sm-doped $SrTiO_3$ [1], [2]. It may be concluded that understanding of the mechanism behind the non-distortion of La-Sm doped $SrTiO_3$ is complex and depends on a number of factors such as cation vacancies, Ti^{3+}, V_O and A-site ion ionic radius. However, a further study as recommended in Chapter 10 (Future work) of this report will actually help to establish a reliable position.

Comparison of the lattice parameter of ESTO and VSTO samples in this study reveals the impact of strongly-reducing processing conditions on the TE performance. The lattice parameter of ESTO (with $x \leq 0.20$) and VSTO-A compositions sintered in 5% H_2/N_2 decreased with increase in x, consistent with the substitution of Sr^{2+} ion (1.44 Å in CN 12) with the smaller RE cations (La^{3+}, 1.36 Å in CN 12; Sm^{3+}, 1.24 Å in CN 12) as previously discussed [ref 5-8, chapter 6]. For VSTO-H compositions sintered in 5% H_2/N_2, the lattice parameter increased from x = 0.05 to 0.20 and declined at x > 0.20. As already discussed, the increase is attributed to a decrease in Coulombic force in the lattice, leading to loss of oxygen ions (V_O) and formation of unequal mixed oxidation states (Ti^{3+}/Ti^{4+}) on the B-site. This trend of increase in lattice parameter relative to x observed in VSTO-H samples is in agreement with previous works of Sahini *et al* [4], Lu *et al* [3] and [5] for $Ba_{0.5}Sr_{0.5}Co_{0.8}Fe_{0.2}O_3$, $Sr_{1-3x/2}La_xTiO_3$ and $Sr_{1-x}La_{x/3}Ti_{1-x}Nb_xO_3$ perovskites, respectively. The partial reduction of Ti^{4+} to Ti^{3+} cations creates V_O in the matrix. As already discussed, V_O is a point defect and contributes in enhancing phonon scattering thereby lowering k. Therefore, the cumulative effect of V_O and Ti^{3+} ions induced by strongly-reducing processing conditions is suggested to have contributed to the high ZT values recorded in VSTO-H samples.

This study also demonstrated the effect of processing conditions on the grain size of samples, and the general impact on the TE properties. ESTO samples exhibited large grain size, low solubility, inherent pores at high x and subsequent poor TE properties when compared to VSTO samples.

The observation is in agreement with the suggestion in the literature (see also Chapter 5 of this project) that $SrTiO_3$ ceramics with A-site vacancies are more likely to improve the TE properties via enhanced phonon scattering and reduced k. Therefore, as established by previous authors in the literature (and as discussed therein), the combination of cation and anion (oxygen) vacancies in $SrTiO_3$ help to improve PF and reduce k. Between VSTO-A and VSTO-H samples, processing conditions have been established as having little or no effect on the electronic transport properties of the samples. Other factors such as carrier concentration, bulk conductivity (high temperature conductivity and grain boundaries or electrical heterogeneities might play significant role. For example, VSTO-A (x = 0.15) showed σ = 298 S/cm (at 973 K), while VSTO-H (x = 0.15) exhibited σ = 284 S/cm (at 973 K). The effect of strongly-reducing conditions was felt on the thermal transport properties. The results of the PSD of the powders and grain size of VSTO-H ceramics are smaller than the values of VSTO-A (as discussed in Chapters 4 and 6). The minimum k values for VSTO-H and VSTO-A samples are 2.50 W/m.K (x = 0.20, 1400H) and 2.99 W/m.K (x = 0.30), respectively at 973 K. This, therefore, suggests that calcination and sintering (strongly reducing atmosphere) in 5% H_2/N_2 generates high V_O concentration, which serves as restriction to phonon propagation, resulting in low k. Consequently, high ZT values are observed in VSTO-H samples.

The 5% H_2/N_2 sintered Sm-doped $Sr_5LaTi_3Nb_7O_{30}$ ceramics contain phase mixtures of TTB with $SrTiO_3$ perovskite and Nb_2O_5. Reduced $SrTiO_3$ compositions are known to have a high PF and k might be optimised by phonon scattering within a mixed phase assemblage as posited by Lu *et al* [6]. The presence of secondary phases may thus contribute to enhanced thermoelectric performance. Samples with A-site vacancies (SLTNv) have the lowest electrical conductivity and smallest thermal conductivity but showed the highest ZT value. This observation is contrary to perovskite compositions where cation vacancies improve the PF.

For Nb-doped $La_2Ti_2O_7$ ceramics, the TE results obtained are not suitable for thermoelectric applications. Nb-doped compositions of $La_2Ti_2O_7$ showed better properties than the undoped compositions suggesting that cation doping has the potential to improve the TE properties. Therefore, the impact of Nb-doping on

$La_2Ti_2O_7$ ceramics in improving the TE performance opens a new window for exploring LTO and other related perovskite-like layered compounds.

Overall, this investigation established the influence of microstructural modification, strongly-reducing processing conditions and secondary phases on the thermoelectric properties of La-Sm co-doped $SrTiO_3$ and Sm-doped $Sr_5LaTi_3Nb_7O_{30}$ ceramics. The significant effect of cation vacancies, oxygen deficiencies and generation of high ionic radius Ti^{3+}/Nb^{4+} electronic defects were identified as the main contributing factors in improving the electronic transport properties. Phonon scattering at grain boundaries, presence of secondary phases and point defects (e.g. V_{Sr}, V_O, voids and pores) hindered the MFP of phonons and depressed the phonon group velocity within the lattice. The net effect, therefore, is reduced thermal conductivity and improved ZT values. This processing route could provide a guide to the synthesis of future targeted oxides for TE applications.

References

[1] A. V. Kovalevsky, A. A. Yaremchenko, S. Populoh, P. Thiel, D. P. Fagg, A. Weidenkaff, and J. R. Frade, “Towards a high thermoelectric performance in rare-earth substituted $SrTiO_3$: effects provided by strongly-reducing sintering conditions,” *Phys. Chem. Chem. Phys.*, vol. 16, no. 48, pp. 26946–26954, 2014.

[2] Adindu C. Iyasara, Whitney L. Schmidt, Rebecca Boston, Derek C. Sinclair, and Ian M. Reaney, “La and Sm Co-doped $SrTiO_{3-\delta}$ Thermoelectric Ceramics,” *Mater. Today Proc.*, vol. 4, no. 12, pp. 12360–12367, 2017.

[3] Zhilun Lu, Huairuo Zhang, Wen Lei, Derek C. Sinclair, and Ian M. Reaney, “High-Figure-of-Merit Thermoelectric La-Doped A-Site-Deficient $SrTiO_3$ Ceramics,” *Chem. Mater.*, vol. 28, no. 3, pp. 925–935, 2016.

[4] M. G. Sahini, J. R. Tolchard, K. Wiik, and T. Grande, “High temperature X-ray diffraction and thermo-gravimetrical analysis of the cubic perovskite $Ba_{0.5}Sr_{0.5}Fe_{0.2}O_{3-\delta}$ under different atmospheres,” *Dalt. Trans.*, vol. 44, no. 23, pp. 10875–10881, 2015.

[5] Deepanshu Srivastava, “Effect of Processing Conditions and Second-Phase Additives on Thermoelectric Properties of $SrTiO_3$ Based Ceramics,” PhD Thesis, The University of Manchester, 2016.

[6] Zhilun Lu, Derek C. Sinclair, Ian M. Reaney, and X. Tan, “The Influence of La Doping and Heterogeneity on the Thermoelectric Properties of $Sr_3Ti_2O_7$ Ceramics,” *J. Am. Ceram. Soc.*, vol. 99, no. 2, pp. 515–522, 2016.

Chapter 10: Future Work

For La-Sm co-doped $SrTiO_3$ (STO) ceramics, the ideal cubic structure was maintained in all compositions, contrary to the work reported by Kovalevsky *et al* [1] where a tetragonal phase was achieved for single Sm-doped $SrTiO_3$ ceramics ($Sr_{0.9}Sm_{0.1}TiO_{3\pm\delta}$). Further diffraction analysis (e.g. electron or neutron) is recommended. This will help to establish whether co-doping has actually stifled the distortion or reduced its scale length below the detection limit of the x-ray diffractometer. Generally, a detailed microstructural and crystallographic study using transmission electron microscope (TEM) and/or scanning transmission electron microscope (STEM) to determine the distribution (short vs. long range order) of A-site defects and tilt phase transitions in La-Sm co-doped $SrTiO_3$ ceramics is paramount.

Cation doping, processing in reducing atmosphere and oxygen loss result in improved electrical conductivity due to an increase in carrier concentration. Hall Effect measurements are suggested to determine the actual amount of carrier concentration and mobility generated. This will be a practical guide to evaluate the electronic conduction of the materials. Freeman *et al* [2] studied by simulation (modelling) the effect of oxygen loss on the electronic conduction of A-site vacancy La-doped $BaTiO_3$. Such a study is suggested for La-Sm doped $SrTiO_3$ and by extension on other n-type oxides investigated in this project. In so doing, the highest electronic conductivity observed for A-site vacancy compositions compared to electronic doped compositions would be quantitatively explained.

Calcination of mixed powders of A-site vacancy La-Sm doped $SrTiO_3$ (VSTO) in 5% H_2/N_2 instead of air, prior to sintering in 5% H_2/N_2 led to more oxygen loss which resulted in optimized TE properties. The same processing method is suggested for other potential n-type oxides studied in this work. If combined with attrition milling, as reported by Lu *et al* [3] and Lu [4] and in combination with spark plasma sintering (SPS) dense small grained microstructures with a large volume fraction of grain boundaries might be obtained. As a result, the MFP of phonons would be shortened, and TE performance improved by lowering the thermal conductivity without compromising the electrical conductivity.

Finally, a holistic study of RE A-site vacancy co-doped and/or A-site (and B-site) electron doped $SrTiO_3$ ceramics prepared by the combination of hydrothermal method and strong reducing processing condition may further enhance the TE properties obtained. A similar work has been reported recently for $Sr_{0.9}La_{0.1}Ti_{0.9}Nb_{0.1}O_3$ ceramics [5] in which a ZT (> 0.6) at 1000 K is achieved.

References

[1] A. V. Kovalevsky, A. A. Yaremchenko, S. Populoh, P. Thiel, D. P. Fagg, A. Weidenkaff, and J. R. Frade, "Towards a High Thermoelectric Performance in Rare-Earth Substituted $SrTiO_3$: Effects Provided by Strongly-Reducing Sintering Conditions," *Phys. Chem. Chem. Phys.*, vol. 16, no. 48, pp. 26946–26954, 2014.

[2] Colin L. Freeman, James A. Dawson, Hung Ru Chen, Liubin Ben, John H. Harding, Finlay D. Morrison, Derek C. Sinclair, and Anthony R. West, "Energetics of Donor-Doping, Metal Vacancies, and Oxygen-Loss in A-Site Rare-Earth-Doped $BaTiO_3$," *Adv. Funct. Mater.*, vol. 23, no. 31, pp. 3925–3928, 2013.

[3] Zhilun Lu, Huairuo Zhang, Wen Lei, Derek C. Sinclair, and Ian M. Reaney, "High-Figure-of-Merit Thermoelectric La-Doped A-Site-Deficient $SrTiO_3$ Ceramics," *Chem. Mater.*, vol. 28, no. 3, pp. 925–935, 2016.

[4] Zhilun Lu, "La Doped $SrTiO_3$ Based Oxide Thermoelectrics.," PhD Thesis, University of Sheffield, 2016.

[5] Jun Wang, Bo Yu Zhang, Hui Jun Kang, Yan Li, Xinba Yaer, Jing Feng Li, Qing Tan, Shuai Zhang, Guo Hua Fan, Cheng Yan Liu, Lei Miao, Ding Nan, Tong Min Wang, and Li Dong Zhao, "Record High Thermoelectric Performance in Bulk $SrTiO_3$ via Nano-Scale Modulation Doping," *Nano Energy*, vol. 35, no. April, pp. 387–395, 2017.